

INFORMATION TO USERS

This manuscript has been reproduced from the microfilm master. UMI films the text directly from the original or copy submitted. Thus, some thesis and dissertation copies are in typewriter face, while others may be from any type of computer printer.

The quality of this reproduction is dependent upon the quality of the copy submitted. Broken or indistinct print, colored or poor quality illustrations and photographs, print bleedthrough, substandard margins, and improper alignment can adversely affect reproduction.

In the unlikely event that the author did not send UMI a complete manuscript and there are missing pages, these will be noted. Also, if unauthorized copyright material had to be removed, a note will indicate the deletion.

Oversize materials (e.g., maps, drawings, charts) are reproduced by sectioning the original, beginning at the upper left-hand corner and continuing from left to right in equal sections with small overlaps. Each original is also photographed in one exposure and is included in reduced form at the back of the book.

Photographs included in the original manuscript have been reproduced xerographically in this copy. Higher quality 6" x 9" black and white photographic prints are available for any photographs or illustrations appearing in this copy for an additional charge. Contact UMI directly to order.

UMI

A Bell & Howell Information Company
300 North Zeeb Road, Ann Arbor MI 48106-1346 USA
313/761-4700 800/521-0600

MEASURING THE TRANSVERSE RMS EMITTANCE AND RMS PULSE LENGTH
OF A SHORT PULSE, PHOTOINJECTOR PRODUCED ELECTRON BEAM WITH
THE SECOND MOMENT OF ITS IMAGE CHARGE

By

Steven J. Russell

A DISSERTATION

Submitted to
Michigan State University
in partial fulfillment of the requirements
for the degree of

DOCTOR OF PHILOSOPHY

Department of Physics and Astronomy

1998

UMI Number: 9909362

UMI Microform 9909362
Copyright 1998, by UMI Company. All rights reserved.

**This microform edition is protected against unauthorized
copying under Title 17, United States Code.**

UMI
300 North Zeeb Road
Ann Arbor, MI 48103

ABSTRACT

MEASURING THE TRANSVERSE RMS EMITTANCE AND RMS PULSE LENGTH OF A SHORT PULSE. PHOTOINJECTOR PRODUCED ELECTRON BEAM WITH THE SECOND MOMENT OF ITS IMAGE CHARGE

By

Steven J. Russell

Radio frequency, photo-cathode injectors are a recent development in the electron accelerator community. They work by placing a small, photo-emissive surface inside a radio frequency accelerating cavity. Electrons are stripped from the photo-cathode with a pulsed laser and immediately accelerated by the cavity fields. These photoinjectors enable the creation of high charge, short pulse length beams. However, they also create problems for the electron beam diagnostics. A photoinjector accelerates the electrons to relativistic velocities very quickly. As a result, the beam does not have time to come to equilibrium. Its spatial distribution will be unknown and cannot be well approximated by a Gaussian. Therefore, diagnostic techniques can make no assumptions about the beam's spatial distribution. A class of diagnostics that fulfill this requirement look at the image charge "wake" generated in the metal walls of the beam pipe as the electron beam passes. These devices are generically known as beam position monitors and are normally used to measure the first moment of the image charge signal, thereby determining the position of the beam's center. However, coupled with a good knowledge of the beam line, they are also capable of determining the rms emittance of the beam by measuring the second moment of the image charge signal. In addition, when used in tandem with a deflecting

cavity, beam position monitors can also be used to perform a measurement of the beam pulse length. Both of these measurements are independent of the beam's spatial distribution, making them ideal for photoinjectors. Described here is their theory and implementation.

To my parents

Jack and Pat

ACKNOWLEDGMENTS

I extend my thanks to the Michigan State University physics department and the members of LANSCE-9 at Los Alamos National Laboratory. To Dr. Bruce Carlsten, for his guidance, encouragement and supervision during my thesis work. I owe a great debt of gratitude. I doubt he knew what he was getting into. I owe special thanks to Dr. Brad Sherrill for being my liaison to Michigan State and for remembering who I am. I thank Dr. Rich Sheffield for bringing me into Los Alamos in the first place. I thank Steve Gierman, Dr. Doug Gilpatrick and Dr. Eric Nelson for very helpful discussions. I thank Mike Webber, John Plato, Scott Volz, Boyd Sherwood, Marty Milder, Ron Sturgis, Dr. Ron Cooper and Dr. Doug Fulton for putting the accelerator together and keeping it running. I thank Dr. Dinh Nguyen, John Power, Brad Shurter and Dr. David Oro for providing valuable assistance and equipment. I thank Drs. Martin Berz, Jack Bass, Ray Brock and Edwin Kashy for their service on my Ph. D. guidance committee.

I thank my family for their support. I especially thank my parents, Jack and Pat, for everything they have given me. My uncle Gary and aunt Elaine I thank for support and friendship during my stay in Los Alamos. I thank my sister and brother, Ann and Tim, for making my life better.

I also thank Molly, for her love and inspiration.

I am also grateful to Michigan State University for the financial support they have given me during my graduate study and Los Alamos National Laboratory for the opportunity to perform my research.

TABLE OF CONTENTS

LIST OF TABLES	xi
LIST OF FIGURES	xii
INTRODUCTION	1
I.1 Background.....	1
I.2 Measuring emittance.....	4
I.3 Measuring pulse length.....	8
I.4 Beam position monitors.....	9
I.5 Implementation of measurements.....	11
 CHAPTER 1	
BEAM PARAMETERS MEASURED BY BEAM POSITION MONITORS	16
1.1 Introduction.....	16
1.2 Notation.....	16
1.3 Physical description of BPMs.....	17
1.4 Image charge	19
1.5 Model of BPM coupling to image charge.....	20
1.6 Beam information provided by BPM.....	23
 CHAPTER 2	
MEASURING EMITTANCE WITH BEAM POSITION MONITORS.....	26
2.1 Introduction.....	26
2.2 Emittance	26
2.3 Measuring the emittance	30
2.4 Stability of emittance measurement.....	32
2.5 Figure of merit for matrix equation stability.....	33
2.6 Finding a stable implementation of Miller's measurement	37
2.6.1 Poor implementations of Miller's emittance measurement	37
2.6.2 Singular equations and strong coupling.....	41
2.6.3 Stable implementation of Miller's measurement.....	43
2.6.4 Numerical examples.....	45

CHAPTER 3	
MEASURING THE RMS PULSE LENGTH WITH FAST DEFLECTING CAVITY AND BEAM POSITION MONITOR	51
3.1 Introduction.....	51
3.2 Trajectory change of a single electron at fast deflector exit	53
3.2.1 Field components.....	53
3.2.2 Conversion of field components to Cartesian coordinates.....	55
3.2.3 Equations of motion.....	56
3.3 Measuring the rms length squared of the electron beam bunches	59
3.3.1 Fast deflector off.....	60
3.3.2 Fast deflector on.....	61
3.3.3 Measuring bunch length.....	65
3.4 Calibration of measurement.....	66
3.5 Estimate of measurement resolution.....	66
3.6 Effect of BPM rotated with respect to fast deflector cavity.....	69
3.6.1 Pulse length measurement.....	69
3.6.2 Calibration.....	72
 CHAPTER 4	
CALIBRATING BEAM A POSITION MONITOR	74
4.1 Introduction.....	74
4.2 Simulating a relativistic beam.....	74
4.3 Mapping the BPM.....	76
4.4 Fitting the map data	76
4.4.1 Centroid calibration	79
4.4.2 Quadrupole calibration.....	84
4.5 Simulating a diffuse beam	88
4.5.1 Interpolation versus measurement	91
4.5.2 Check of BPM accuracy for measuring $\langle x^2 \rangle - \langle y^2 \rangle$	93
4.6 Concerns with calibration method	95
 CHAPTER 5	
EXPERIMENTAL RESULTS.....	98
5.1 Introduction.....	98
5.2 Experimental apparatus and data acquisition.....	98
5.2.1 Experimental apparatus.....	98
5.2.2 Capturing BPM signals.....	101
5.2.3 Analyzing digitized BPM signals	101
5.3 Stability experiment	104
5.3.1 Shot-to-shot stability.....	105
5.3.2 Average stability	110
5.4 Experiments to check BPM calibration	111
5.5 Emittance measurements	117
5.5.1 Single emittance measurement	118

5.5.2 On the question of beam scraping.....	127
5.5.3 Emittance versus bunch charge.....	133
5.5.4 Emittance versus magnetic field.....	134
CONCLUSION.....	141
APPENDIX A	
CHARGE DISTRIBUTION INDUCED ON INNER SURFACE OF BEAM	
PIPE DUE TO RELATIVISTIC ELECTRON BEAM.....	
A.1 Introduction.....	144
A.2 Solution in beam frame.....	144
A.3 Surface charge distribution in lab frame.....	154
A.4 Relativistic approximation.....	157
APPENDIX B	
SURFACE CHARGE DISTRIBUTION ON INNER SURFACE OF	
CYLINDRICAL METAL PIPE DUE TO AN INFINITE LINE CHARGE	
INSIDE THE PIPE AND PARALLEL TO ITS AXIS.....	
B.1 Introduction.....	160
B.2 Constant potential surfaces due to two infinite line charges in free space.....	160
B.3 Electric potential from infinite line charge inside an infinite metal pipe.....	163
B.4 Surface charge distribution from infinite line charge inside infinite metal pipe.....	166
B.4.1 Image charge distribution.....	166
B.4.2 Expansion of image charge distribution in Fourier series.....	167
APPENDIX C	
VOLTAGE SIGNAL GENERATED ON OSCILLOSCOPE FROM	
BEAM POSITION MONITOR SIGNAL TRANSMITTED THROUGH	
TRANSMISSION LINE.....	
C.1 Introduction.....	169
C.2 General Solution.....	169
C.2.1 Solution to circuit model.....	169
C.2.2 Expression for beam current.....	172
C.2.3 Solution.....	175
C.3 Approximate solution for short beam pulse.....	175
C.4 Gaussian beam.....	176
APPENDIX D	
EXPANSION OF BPM SIGNAL AMPLITUDE IN CARTESIAN COORDINATES.....	
D.1 Introduction.....	179
D.2 Expansion of amplitude in Cartesian coordinates.....	179
D.2.1 Expansion of summation term in Cartesian coordinates.....	180
D.2.2 Expressing amplitude as a sum of moments.....	181

APPENDIX E	
FIRST ORDER CALCULATION OF THE TRAJECTORY OF AN ELECTRON DUE TO IDEAL FAST DEFLECTOR FIELDS.....	185
E.1 Introduction	185
E.2 Electric and magnetic fields of fast deflector	185
E.3 Transformation of fields to Cartesian coordinates	187
E.4 Demonstration of dominant field.....	193
E.5 Solution to the first order equations of motion.....	196
E.6 Electron position and divergence at exit of fast deflector cavity.....	198
 APPENDIX F	
COVARIANCE MATRIX AND THE STANDARD ERROR IN THE CALCULATION OF THE EMITTANCE	201
F.1 Introduction.....	201
F.2 Estimating measurement errors	202
F.3 Covariance matrix.....	207
F.4 Estimated error in calculation of the emittance	209
 REFERENCES	215

LIST OF TABLES

Table 3-1: Value of $a_1^2 \langle \phi_z^2 \rangle$ vs. drift length, d. and the FWHM pulse length of the beam	70
Table 4-1: Table comparing the values of \bar{x} , \bar{y} and $\langle x^2 \rangle - \langle y^2 \rangle$ as measured by a BPM to their actual values for several simulated, diffuse beams.....	94
Table 5-1: Average measured value of $\langle x^2 \rangle - \langle y^2 \rangle$, predicted value of $\langle x^2 \rangle - \langle y^2 \rangle$ (from fit) and the difference between them for each quadrupole setting in emittance measurement for charge equal to approximately 0.2 nC/bunch.....	123
Table 5-2: Same as Table 5-1, but measurements 2, 3, 5 and 19 are all discarded because of beam scraping	126
Table 5-3: Value of $\langle x^2 \rangle - \langle y^2 \rangle$ from simulation, predicted value of $\langle x^2 \rangle - \langle y^2 \rangle$ (from fit) and the difference between them for each quadrupole setting in simulated emittance measurement with beam pipe.....	131
Table 5-4: Values of the RMS beam parameters for different fits in simulated emittance measurements.....	132

LIST OF FIGURES

Figure I-1: Schematic of SPA photoinjector.....	13
Figure I-2: Schematic of SPA beam line	14
Figure I-3: a) Schematic of magnetic chicane. b) Energy versus beam bunch length from simulation.	15
Figure I-1: Schematic of beam position monitor cross section. The beam will travel along the z axis. out of the page	18
Figure I-2: Circuit model of BPM electrode coupling to electron beam. C_p is the capacitance of the BPM electrode. Z_c is the characteristic impedance of the transmission line. i_b represents the image induced image charge from the passing electron beam.....	21
Figure 2-1: The x phase space of the SPA beam from simulation.....	28
Figure 2-2: Schematic of beam line for implementation of emittance measurement using only drifts	38
Figure 2-3: Schematic of beam line consisting of quadrupole magnet, drift and BPM.....	40
Figure 2-4: Schematic of beam line consisting of a triplet followed by a beam position monitor	44
Figure 3-1: Illustration of fast deflector cavity streaking a beam bunch	52
Figure 3-2: Schematic of fast deflector cavity	54
Figure 3-3: BPM rotated with respect to the x and y axes defined by the fast deflector fields	71

Figure 4-1: Schematic of pulsed wire apparatus for calibrating BPM.....	75
Figure 4-2: Maps of the a) right ($\theta = 0^\circ$) and b) left ($\theta = 180^\circ$) electrodes of a BPM	77
Figure 4-3: Maps of the a) top ($\theta = 90^\circ$) and b) bottom ($\theta = 270^\circ$) electrodes of a BPM	78
Figure 4-4: a) R_x versus actual x position of wire. b) R_x versus x position of wire as calculated by fitted equation.....	81
Figure 4-5: a) R_y versus actual y position of wire. b) R_y versus y position of wire as calculated by fitted equation.....	82
Figure 4-6: a) Difference between actual x position of wire and that calculated from the fitted equation versus radial position of the wire. b) Difference between actual y position of wire and that calculated from the fitted equation versus the radial position of the wire.....	83
Figure 4-7: a) Plot of the difference between actual value of $x^2 - y^2$ and its calculated value using the fit of Equation (4-6) . and b) using Equation (4-7).....	87
Figure 4-8: Schematic showing grid points for simulation of diffuse beam with a single pulsed wire	90
Figure 4-9: a) Plot of $\langle x^2 \rangle - \langle y^2 \rangle$ versus Q for a number of simulated beams ($\bar{x} = \bar{y} = 0$) using the apparatus in Figure 4-1. b) Identical to a) except that the responses of the BPM electrodes for the individual grid points are interpolated from BPM maps	92
Figure 4-10: Plot of the difference between the actual value of $\langle x^2 \rangle - \langle y^2 \rangle$ and that calculated from the BPM signals in mm^2 for a single simulated beam as it is move radial outward from the BPM center	97
Figure 5-1: Schematic of end section of SPA beam line	99
Figure 5-2: Schematic of data acquisition system for capturing BPM signals	102

Figure 5-3: Voltage versus time signal from BPM electrode for a typical beam shot. There are two full beam bunches and part of a third displayed.....	103
Figure 5-4: a) Intensity (sum of four BPM electrodes) versus successive beam shots. b) $\langle x^2 \rangle - \langle y^2 \rangle$ versus successive beam shots	107
Figure 5-5: a) x position of beam center versus successive beam shots. b) y position of beam center versus successive beam shots	108
Figure 5-6: a) Average intensity (sum of four BPM electrodes) of beam bunch versus measurement number. b) Average value of $\langle x^2 \rangle - \langle y^2 \rangle$ versus measurement number. Each measurement is the average over 99 consecutive beam shots	112
Figure 5-7: a) Average value of x position of beam bunch center versus measurement number. b) Average value of y position of beam bunch center versus measurement number. Each measurement is the average over 99 consecutive beam shots	113
Figure 5-8: a) Another example of the average intensity (sum of four BPM electrodes) of a beam bunch versus measurement number. b) Another example of the average value of $\langle x^2 \rangle - \langle y^2 \rangle$ versus measurement number	114
Figure 5-9: a) Quadrupole moment versus $\bar{x}^2 - \bar{y}^2$. The slope of the fit line is 0.95 ± 0.021 . b) $\langle x^2 \rangle - \langle y^2 \rangle$ versus measurement number for the same data points shown in a). Each point is the average of 99 beam shots	116
Figure 5-10: $\bar{\bar{A}}$ matrix associated with settings for quadrupoles in Figure 5-1 used to measure the electron beam emittance	120
Figure 5-11: Average beam intensity (sum of four BPM electrodes) at BPM versus measurement number for emittance measurement a charge equal to approximately 0.2 nC/bunch	122
Figure 5-12: Intensity vs. measurement number for simulated emittance measurement.....	130

Figure 5-13: A plot of normalized emittance versus bunch charge	135
Figure 5-14: Emittance versus magnetic field on photo-cathode	140
Figure A-1: Relativistic electron beam pulse in metal pipe: a) cross sectional view. b) longitudinal view	145
Figure A-2: Lab and beam frame for relativistic electron beam bunch traveling down beam pipe	155
Figure B-1: Two infinite line charges parallel to the z axis with charge per unit length λ and $-\lambda$, respectively	161
Figure B-2: Infinite line charge inside an infinite metal pipe	164
Figure C-1: Circuit model of BPM electrode coupling to electron beam. C_p is the capacitance of the BPM electrode. Z_c is the characteristic impedance of the transmission line. i_b represents the image induced image charge from the passing electron beam.....	170
Figure C-2: The function $e^{-\frac{1}{2} \left(\frac{\omega}{\beta c} \sigma \right)^2}$ vs. frequency for a 6 mm, or 20 ps, FWHM long electron pulse.....	178
Figure E-1: Schematic of fast deflector cavity.....	186
Figure E-2: a) $J_1(k_{11}r)$ (blue) and $\frac{k_{11}r}{2}$ (red) versus radius. b) $J_2(k_{11}r)$ (blue) and $\frac{1}{8}(k_{11}r)^2$ (red) versus radius	191
Figure E-3: $\left(1 - \frac{x_{11}^2}{4a^2} x^2\right)$ vs. x (cm)	192
Figure E-4: $\left \frac{\Delta\gamma}{\gamma} \right $ vs. x (cm) for an 8 MeV electron	195

INTRODUCTION

I.1 Background

In 1984 the Strategic Defense Initiative (SDI) was officially launched. Its stated goal was to develop weapons capable of destroying nuclear missiles in flight, creating an impenetrable shield around United States interests. Since the technology to develop such a system was not in existence, substantial funding was provided to the scientific and engineering community towards its development.

As SDI got under way, it was not clear what final form the weaponry of SDI would take and many potential solutions were pursued. Of particular interest were the high powered laser programs. Fast and precise, lasers were a perfect fit to SDI if laser systems of sufficient power could be developed. The free electron laser (FEL) was one candidate that held great potential to satisfy SDI needs[1].

Although a rigorous description is quite complicated[2], FELs are conceptually simple devices. A high energy beam of electrons is directed down the axis of an alternating magnetic field. In this field, the electrons move back and forth across the path of their initial trajectory, generating light that can be used to amplify a conventional laser beam or to create a coherent light beam inside a resonator cavity.

At the time that SDI came into being, FELs had been in existence for a little over a decade[3]. However, this was the first time that significant resources were applied

toward their development. Because their physics can be described classically, powerful simulations were developed that indicated fantastic performance was possible using FELs. In fact, two machines boasting an average laser power to be measured in megawatts and operating over a broad range of wavelengths were proposed[1]. However, in the end, neither of these devices were constructed. SDI came to a halt and FEL funding was sharply curtailed.

The SDI program advanced the knowledge of FELs very rapidly in a short time. FELs still hold great promise as high powered, tunable light sources and the knowledge gained during the frenetic SDI years has proved very valuable. Although in hindsight it is apparent that the attempts to build the huge, mega-watt machines was premature, many other technical advancements that came out of the programs of the past are still very much alive. Of particular importance to the electron accelerator community was the invention of the radio-frequency (rf) photoinjector[4], [5].

Throughout the history of FELs, it has been apparent that the success of an FEL experiment depends strongly upon the quality of the electron beam used to drive the device. This fact was further underscored for those who worked in the SDI FEL programs. Therefore, there was a significant effort to advance electron accelerator technology to achieve better beams.

The electron source, as one might imagine, is a very important part of any electron accelerator. For many years, the only choice was to use a thermionic cathode[6]. This is a simple device where the cathode material is heated to the point that electrons on its surface obtain enough energy to overcome the material work function. Immersed in a static electric field, the electrons are accelerated as they boil off the cathode surface to

form a dc beam. Since high energy accelerators are pulsed devices, this dc beam of electrons is not appropriate for immediate injection into the accelerator. First, a pulsed structure that matches that of the accelerator is imposed. This is done by bunching the beam with time varying electric fields. Only then are the electrons accelerated to high energy.

Although thermionic cathodes are very reliable, they severely limit the command one has over the shape of the electron beam that is injected into the accelerator. While being bunched, the electrons are at low energy and the repulsive force between them works against the bunching process. The end result is that an electron beam from a thermionic injector will approach an equilibrium shape[6]. Although not obvious, experimentally this means that the spatial distribution of the beam will be very nearly Gaussian. The combination of low energy and repulsive space charge force will wash out any other structure that might be dictated.

The rf photoinjector was invented by Richard Sheffield and John Fraser[4], [5] as an alternative to the thermionic injector for rf accelerators. The idea was based on the lasertron concept[7]. Instead of a heated filament, the photoinjector uses a photo-cathode as its electron source. The photo-cathode is a photo-emissive surface located inside the accelerator. A short pulse, high energy laser impinges upon the photo-cathode, stripping electrons from the cathode surface. Once free, the electrons are quickly accelerated to relativistic velocities.

The inventors of the photoinjector had two powerful insights. First, they realized that our ability to manipulate pulsed laser light is much greater than our ability to manipulate pulsed electron beams. By using a laser to make the electron beam, much of this greater

capability is transferred, improving our capacity to impose a desired initial shape for the electron beam. Second, since the electron beam is already bunched, the photo-cathode can be placed inside the first cell of the accelerator. Here, the very high electric fields accelerate the electrons to relativistic velocities over a distance an order of magnitude shorter than that required by a thermionic injector. Therefore, because of relativistic effects, much of the original structure of each electron beam is preserved. This allows a great deal of control over the spatial distribution of the final electron beam. No longer is a Gaussian-like shape inevitable.

The ability to control the final beam distribution, at least partially, is the most significant advancement that the photoinjector brings to the electron accelerator community. Employing this control wisely can improve the beam quality and enable longitudinal compression of the electron beam that is much more effective than what can be achieved with a thermionic beam[8]. However, this also creates new challenges for the beam diagnostics. Because the beam is no longer Gaussian-like and because our control over its shape is not complete, we can no longer make accurate assumptions about the spatial distribution of the beam[9], [10]. Therefore, it is important that our diagnostics make no assumptions about the beam distribution.

I.2 Measuring emittance

Each electron in a beam bunch is described by six coordinates: the three spatial coordinates and their associated momentum. Taken as a whole, the bunch occupies a six dimensional volume. Ideally, we could know the beam distribution in this six dimensional phase space at any given time. However, the ability to make such a

measurement has not yet been realized. Instead, we look at projections.

If a screen is inserted into the beam path we see the projection of the six dimensional phase space onto the x, y plane. This is a very useful diagnostic that tells us the transverse shape of the beam at a given point in its transport. However, the projections onto the x and y phase spaces tell even more. These are the planes with one axis defined by the position coordinate and the other by the respective momentum. In principle, knowledge of these projections at any given point in the beam transport allows us to determine the shape of the beam at any other point in the beam-line if the focusing forces are linear[6].

There are schemes for mapping out the complete transverse phase space of an electron beam using slit and collector type schemes[9]. However, for high charge beams with energies of more than a few MeV, it is questionable how efficacious these methods are. The slit, which is used to select slices of the beam while blocking the rest, becomes less effective as the beam energy increases. The electrons start to punch through the material that is meant to stop them and at the same time produce copious x-rays. This results in a large amount of noise in the collector necessitating some scheme for subtracting the background out of the desired signal. At high charge and high energy this becomes difficult.

For higher energy electron beams, complete maps of the transverse phase spaces are usually abandoned in favor of an envelope description. This simplifies the measurement greatly and still provides useful information. In this scheme, the x and y phase spaces are characterized by the x and y root-mean-square (rms) emittances defined by

$$\varepsilon_x \equiv \sqrt{\langle x^2 \rangle \langle x'^2 \rangle - \langle xx' \rangle^2}$$

and

$$\varepsilon_y \equiv \sqrt{\langle y^2 \rangle \langle y'^2 \rangle - \langle yy' \rangle^2}.$$

The angled brackets indicate an average over the beam distribution. The x and y divergencies, x' and y' , are proportional to the x and y momenta for relativistic electron beams. In the x phase space, the three numbers, $\langle x^2 \rangle$, $\langle x'^2 \rangle$ and $\langle xx' \rangle$, describe an ellipse. The emittance is the area of this ellipse divided by the number π . The meaning of the y emittance is similar.

From the rms emittance, we can define the normalized rms emittances as

$$\varepsilon_{xn} \equiv \beta\gamma\varepsilon_x$$

and

$$\varepsilon_{yn} \equiv \beta\gamma\varepsilon_y$$

where β and γ are the usual relativistic parameters associated with the average energy of the beam. The normalized emittance is a useful metric because it has the property that it is a conserved quantity in a linear focusing channel with acceleration[6]. Because of this property, it is an excellent indicator of unwanted nonlinear processes. Also, the emittance is to charged particle optics what wavelength is to light optics: it provides a fundamental limit on how tightly a beam can be focused and indicates how fast it will diverge from that focus. Since the main goal is often to pack as many electrons as possible into a given area, normalized emittance is widely used as a metric for beam quality. Accelerator facilities will always quote normalized emittance as a standard for machine performance.

A typical procedure for determining the rms emittance is to measure $\langle x^2 \rangle$ and $\langle y^2 \rangle$ at several points in a linear focusing channel. If, for example, we wanted to know the rms x emittance, $\langle x^2 \rangle$ would be measured in at least three different beam line locations. This results in a set of three, or more, linear equations that can be solved for $\langle x^2 \rangle$, $\langle x'^2 \rangle$ and $\langle xx' \rangle$. Similarly, we could measure $\langle y^2 \rangle$ and obtain $\langle y^2 \rangle$, $\langle y'^2 \rangle$ and $\langle yy' \rangle$.

Measuring $\langle x^2 \rangle$ and $\langle y^2 \rangle$ can be a challenging task. A common method would be to insert a screen in the beam path. This screen can have a phosphor coating that generates an optical image of the beam spot. A series of mirrors and lenses is then used to direct the beam spot image to a camera where it can be captured.

If the beam spot image were perfect, a direct numerical integration would give $\langle x^2 \rangle$ and $\langle y^2 \rangle$. For a real image, however, integration is a poor option. There are two main reasons that it fails: image noise and the limited dynamic range of the camera. Noise spikes in the image, whatever their origin, are always positive. That is the nature of the measurement, there is never a negative intensity. Because integration sums the intensities, the noise will add together, causing substantial error. The limited dynamic range, on the other hand, will cause some of the beam image to be lost. Away from the bright central core of the beam, the light generated by the electrons is too faint for the camera to see. This might seem unimportant since a faint image indicates a low electron density. However, because the area is large, the total number of electrons in these faint regions can be a large fraction of the total number in the beam. Leaving them out of an integration would also result in a large error.

Instead of integrating the image, the problem can be greatly simplified by assuming that the beam has a particular type of distribution. Then, the obtained beam image can be fit to this distribution and $\langle x^2 \rangle$ and $\langle y^2 \rangle$ fall out naturally. Noise spikes essentially have no affect on the fit and the central region of the beam image is enough information for this type of processing if the distribution assumption is a good one. Thermionic beams, with their Gaussian nature, are ideal candidates for this technique and accurate values for $\langle x^2 \rangle$ and $\langle y^2 \rangle$ result. For photoinjector beams, however, the distribution is not known. Any distribution assumption, Gaussian or otherwise, will generally be a poor one. Inaccurate values for $\langle x^2 \rangle$ and $\langle y^2 \rangle$ are the consequence. In turn, because it depends upon these values, poor estimates of the rms emittance result.

1.3 Measuring pulse length

Measuring the length of the beam pulse is another pressing diagnostic problem. Recently, photoinjector beams of substantial charge have been compressed to lengths of less than 0.3 mm[8]. Traveling at nearly the speed of light, this is less than 1 picosecond in time. Diagnostics with such time resolution are hard to come by and often expensive. An economical solution to this problem utilizes a radio frequency (rf) cavity and a simple screen[8].

A cylindrical cavity operating in its TM_{110} mode will produce a time varying, magnetic dipole field. If a beam pulse is directed down its axis and its arrival and the phase of the cavity fields are synchronized correctly, the head and tail of the pulse will be kicked in opposite directions while the trajectory of the beam center remains unchanged.

This will spread the beam in one dimension. By placing a screen downstream from the cavity (called a fast deflector), the increase in width that results can be measured. In turn, this will give the length of the beam pulse.

This technique is quite good for low charge beams. As the charge per pulse is increased, however, its effectiveness breaks down. After passing through the fast deflector cavity, the beam continues to expand as it drifts. Therefore, the increase in beam width will be greater the longer the beam is allowed to drift. When the beam pulses are very short, it is important that this drift be of sufficient length to obtain the necessary resolution. At the same time, how tightly the beam can be focused at the position of the screen is lessened the longer it is allowed to drift, especially for high charge beams because of the repulsive space charge force. From a practical point of view this is important because a large beam spot at the screen results in a low signal to noise ratio, making it difficult to measure any width change. At low charge, this is not an issue. However, as the charge per bunch is increased, the goal of adequate resolution and a tightly focused spot become mutually exclusive.

1.4 Beam position monitors

The term beam position monitor (BPM) refers to a generic class of devices that determine the position of a charged particle beam's center. They work by coupling to the electromagnetic fields that accompany the beam. One particular class of these devices sees the image charge that these fields induce in the metal of the beam pipe walls.

A dual axis BPM of this type is a BPM that measures both the x and y positions of the beam center. Without going into too much detail now, it will consist of four

electrodes placed on the inner beam pipe wall at 90 degree intervals. What will be shown in Chapter 1 is that, when combined properly, the four electrode signals measure four beam properties: the total charge in the beam, the x and y center positions of the beam and the value of $\langle x^2 \rangle - \langle y^2 \rangle$. When the beam pulses are very short, as is the case for our photoinjector beam, the determination of these quantities is independent of the beam's spatial distribution.

BPMs have been used for quite some time for measuring the beam position[11]. They have not been used extensively to determine $\langle x^2 \rangle - \langle y^2 \rangle$. However, knowledge of this quantity can be exploited to measure both the rms emittance of the beam and the rms pulse length.

To measure the emittance, we perform essentially the same measurement as was described earlier. It was first proposed by Miller et. al.[12] to measure $\langle x^2 \rangle - \langle y^2 \rangle$, instead of $\langle x^2 \rangle$ or $\langle y^2 \rangle$, at various points in a well characterized, linear focusing channel. If this is done at least six times, a set of linear equations results and we can solve for $\langle x^2 \rangle$, $\langle x'^2 \rangle$, $\langle xx' \rangle$, $\langle y^2 \rangle$, $\langle y'^2 \rangle$ and $\langle yy' \rangle$, determining both the x and y rms emittances.

The measurement of the pulse length is also the same as described before, but with the screen replaced by a BPM. By measuring the value of $\langle x^2 \rangle - \langle y^2 \rangle$ before and after the cavity is turned on, it can be shown that the difference between the two measurements will produce the rms length of the beam pulse. The advantage that the BPM brings to the method is that, unlike the screen, a good focus is not necessary at the BPM location. This allows us to increase the drift, and therefore the resolution, between the BPM and the

cavity indefinitely as long as the beam does not intercept the beam pipe walls.

I.5 Implementation of measurements

The Sub-picosecond Accelerator (SPA) facility at Los Alamos National Laboratory is an 8 MeV, rf photoinjector operating at a frequency of 1300 MHz[13]. Its primary mission is to explore the uses and dynamics of compressed electron beams. State of the art in this field. SPA is capable of compressing electron pulses containing more than 1 nC of charge to sub-picosecond lengths with a magnetic chicane[8]. In its previous incarnation, the SPA photoinjector was the electron source for the High Brightness Accelerator FEL (HIBAF) facility[14]. Schematics of the important components of the SPA facility are shown in Figure I-1, I-2 and I-3.

The chicane, shown in Figure I-3a, is a series of four dipole magnets whose field orientations are such that an electron will travel a path through them like that shown in the figure. Utilizing the unique capabilities of the photoinjector, electron beam pulses of an appropriate length are injected into the accelerating structure at a phase in the rf cycle so that an energy versus phase correlation is introduced. This energy slope, shown in Figure I-3b, is largely linear and is such that the electrons in the front of the beam bunch have lower energy than those at the back. Because of their lower energy, the electrons at the front of the pulse are directed along a bigger arc through the chicane than those at the back. Therefore, they travel a greater distance. If the energy slope and initial bunch length are chosen correctly, the particles at the back of the bunch will catch those at the front as the beam exits the chicane, compressing the beam.

Compression technology is an important issue in the electron accelerator community. The delivery of large amounts of charge in small volumes is a critical ability for both applications and fundamental research. However, recent work has predicted an unfortunate degradation of rms emittance as a bunched beam passes through a bend[15]. Since a chicane is a series of bends, it is very likely that, at the same time it compresses the beam, it causes serious harm to its quality. What is needed are the tools to perform the relevant measurements of the SPA beam properties.

The two diagnostic techniques described here will fill important diagnostic needs for SPA, if they prove practical. What is presented here is the theory and implementation of the rms emittance measurement using BPMs and the theory behind the rms pulse length measurement using a cylindrical cavity and a BPM.

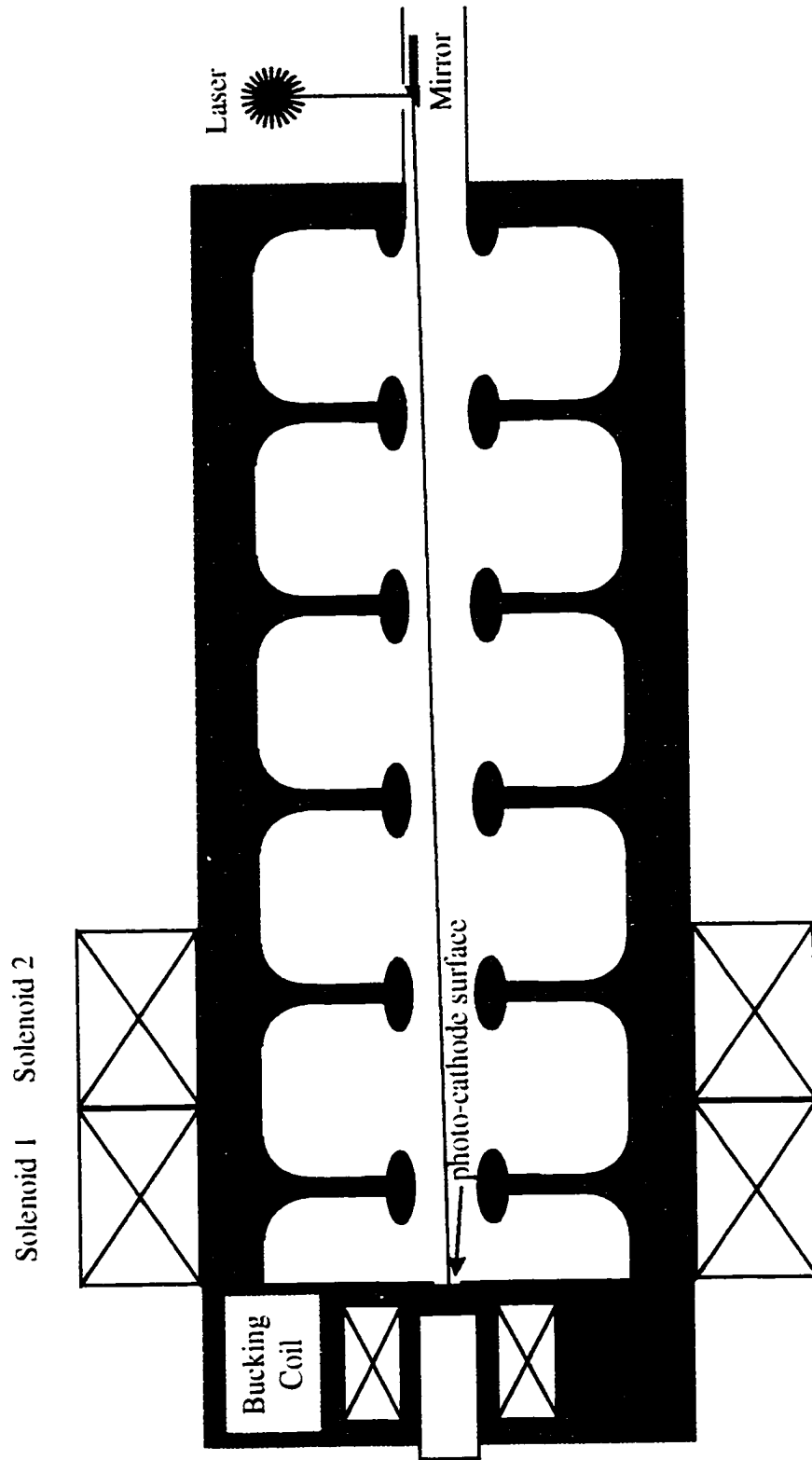


Figure I-1: Schematic of SPA photoinjector.

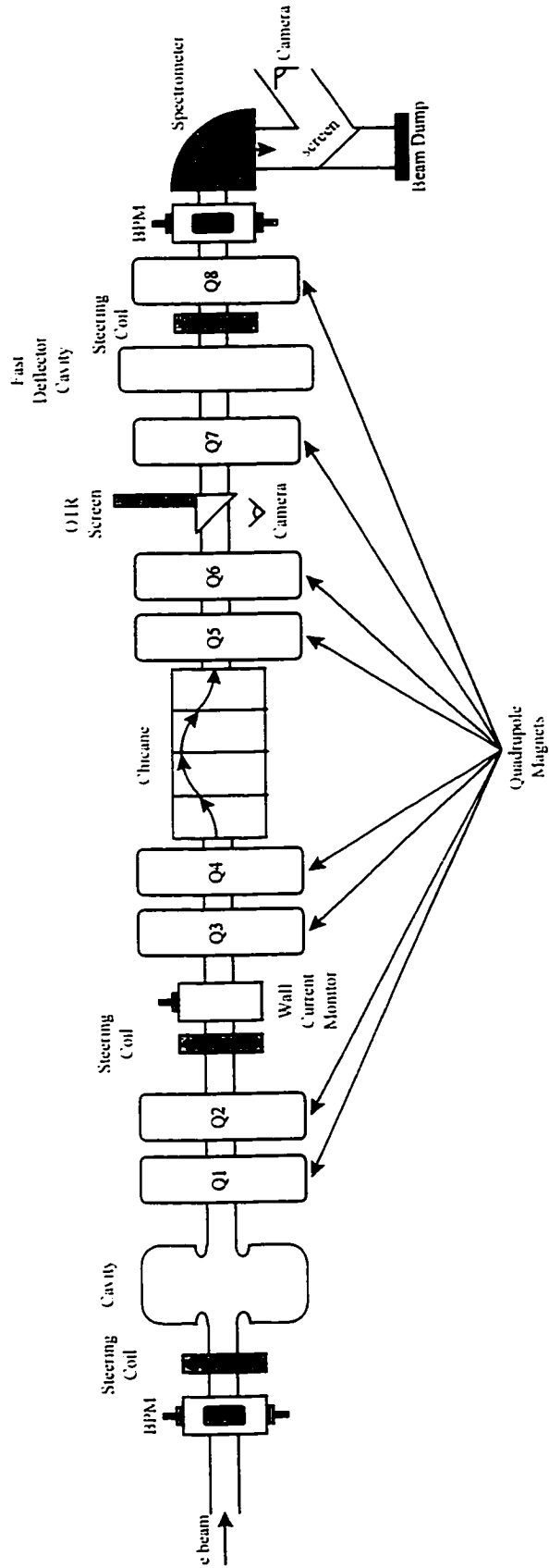
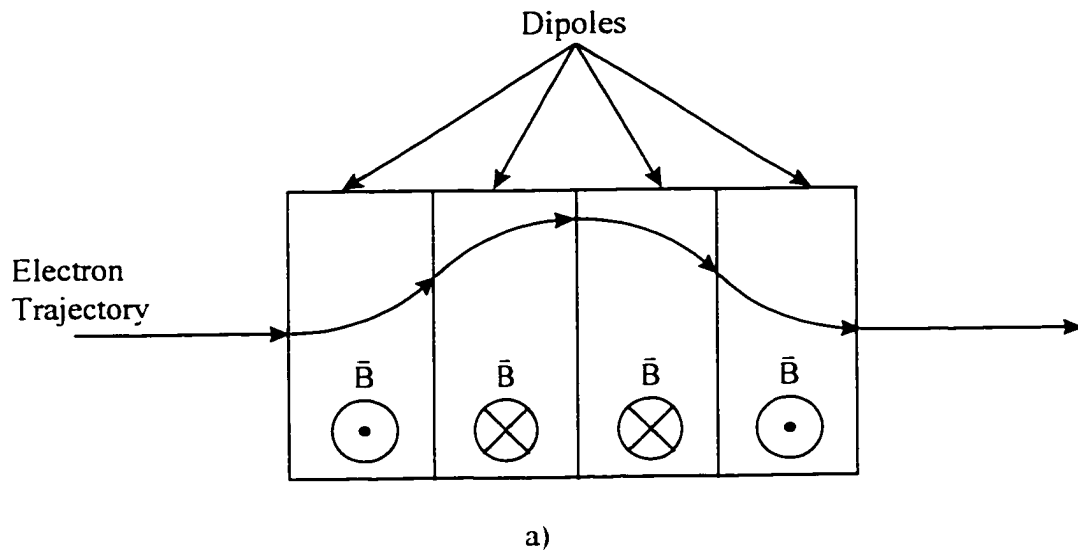
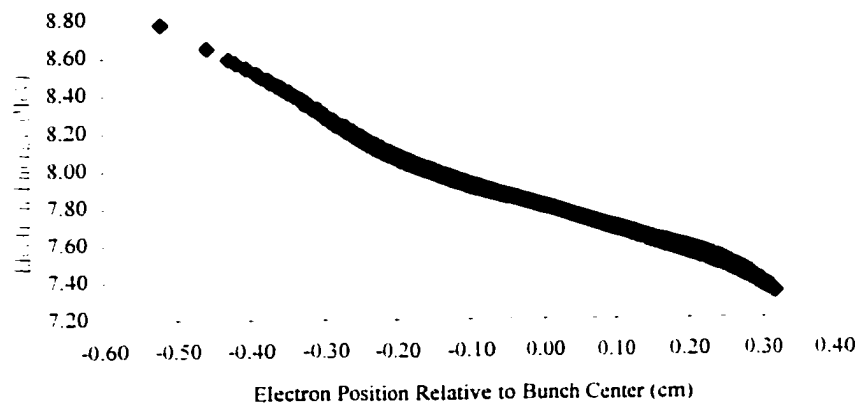


Figure I-2: Schematic of SPA beam line.



Electron Energy vs. Position in Bunch From Simulation



b)

Figure I-3: a) Schematic of magnetic chicane. b) Energy versus beam bunch length from simulation.

Chapter 1

BEAM PARAMETERS MEASURED BY BEAM POSITION MONITORS

1.1 Introduction

Before beginning any other discussion, it is important to demonstrate what it is that BPMs measure. A complete understanding of the signals they produce and how they can be exploited to obtain important beam parameters is presented in this chapter.

1.2 Notation

Before proceeding, a brief statement concerning notation is in order. Throughout this document, quantities will be averaged over the electron beam distribution. This will be done in two ways. The first is called an ensemble average. This is the average of a quantity over the beam distribution in the coordinate system whose origin corresponds to the center of the beam. An ensemble average is denoted by angled brackets:

$$\langle \text{quantity} \rangle \equiv \frac{\iiint_{\text{Origin corresponds to beam center}} \text{quantity} \times \rho(\bar{x}) dV}{\iiint_{\text{Origin corresponds to beam center}} \rho(\bar{x}) dV} \quad (1-1)$$

where $\rho(\bar{x})$ describes the electron beam's spatial distribution. By definition

$$\langle x \rangle = \langle y \rangle = \langle z \rangle = 0.$$

The second way in which the average of the beam distribution is taken defines the transverse, or xy , origin to correspond with the center of the beam pipe. The longitudinal, or z , origin corresponds to the longitudinal center of the beam bunch. This average is important when describing the signals produced by the BPM. This average will be referred to as a BPM average and is denoted in the following way:

$$\langle \text{quantity} \rangle_{\text{BPM}} \equiv \frac{\iiint \text{quantity} \times \rho(\bar{x}) dV}{\iiint \rho(\bar{x}) dV} \quad (1-2)$$

xy origin corresponds to beam pipe center, z origin to beam bunch center

The BPM averages of x and y yield the x and y position of the center of the beam with respect to the beam pipe and

$$\langle z \rangle_{\text{BPM}} = 0.$$

1.3 Physical description of BPMs

The BPMs employed on SPA are dual axis, capacitive type probes that differentiate the beam image charge[16]. Physically, they are short sections of beam pipe in which 3.2 mm long slots that subtend an angle of 45° have been cut out of the beam pipe walls. Metal electrode are inserted into the gaps created by the cutouts. Somewhat smaller than the slots and electrically isolated from the rest of the BPM, the electrodes are slightly inset from the pipe wall. They are placed at 90° intervals around the pipe circumference: two on the x axis and two on the y axis. Figure 1-1 is a schematic of the BPM geometry.

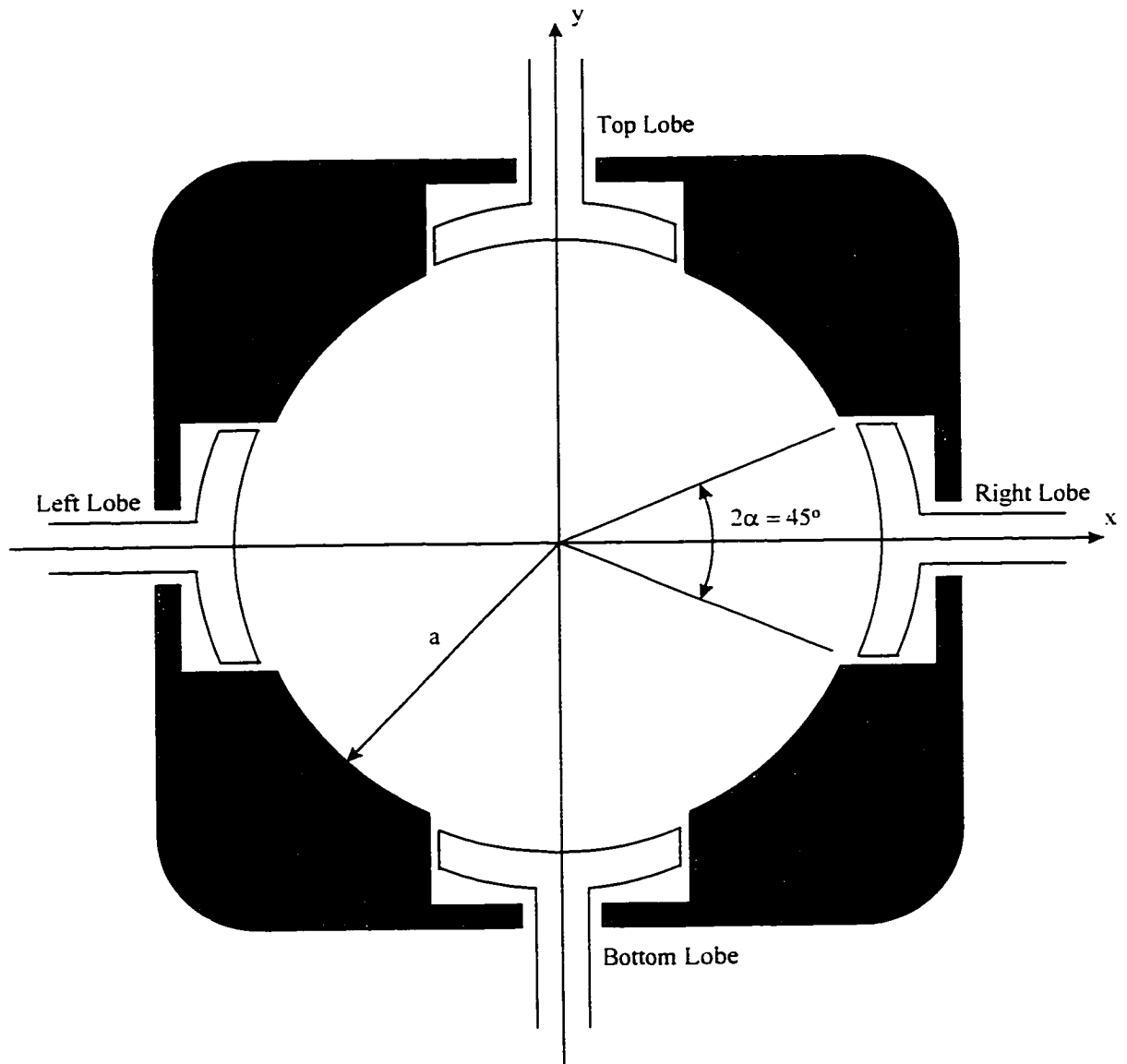


Figure 1-1: Schematic of BPM cross section. The beam will travel along the z axis, out of the page.

1.4 Image charge

As an electron beam bunch travels down the z axis (out of the page in Figure 1-1) it is accompanied by a "wake" of image charge in the beam pipe walls. The distribution of the image charge depends upon the shape of the beam bunch.

Assuming that the BPM electrodes introduce a negligible perturbation, the image charge distribution that they see can be well represented by the analytical result obtained for a smooth metal wall. For a bunch of charge moving at a relativistic velocity along the z axis of the pipe, this is

$$\sigma(\theta, z, t) = \frac{-\gamma}{\pi a^2} \int_V \rho_L(r', \theta', z', t) \sum_{n=0}^{\infty} a_n \cos[n(\theta - \theta')] \left[\sum_{m=1}^{\infty} \frac{J_n\left(x_{nm} \frac{r'}{a}\right)}{J_n(x_{nm})} e^{-\frac{x_{nm}}{a} z - z'} \right] d^3x'$$

where

$$a_n = \begin{cases} \frac{1}{2}, & n = 0 \\ 1, & n \neq 0 \end{cases} \quad (1-3)$$

The radius of the beam pipe is a, the x_{nm} 's are the Bessel function zeros and γ is the usual relativistic parameter. The beam bunch has a density distribution function $\rho_L(r, \theta, z, t)$ in the lab frame. (See Appendix A)

When the beam is highly relativistic a useful approximation can be made. One definition of the Dirac delta function is

$$\delta(x - x') \equiv \lim_{\epsilon \rightarrow 0} \frac{e^{-\frac{|x-x'|}{\epsilon}}}{2\epsilon}.$$

Making the definition

$$\varepsilon \equiv \frac{a}{\gamma X_{nm}}$$

gives

$$e^{-\gamma \frac{X_{nm}}{a} z-z'} = \frac{a}{\gamma X_{nm}} \frac{e^{-\frac{z-z'}{a} \gamma X_{nm}}}{a} = 2 \frac{a}{\gamma X_{nm}} \frac{e^{-\frac{z-z'}{\varepsilon}}}{2\varepsilon}.$$

When γ is large one can make the approximation

$$e^{-\gamma \frac{X_{nm}}{a} z-z'} \cong 2 \frac{a}{\gamma X_{nm}} \delta(z-z'). \quad (1-4)$$

Substituting (1-4) into (1-3) gives

$$\sigma(\theta, z, t) \cong \frac{-1}{2\pi a} \int_{\text{area of pipe}} \rho_L(r', \theta', z, t) \left\{ 1 + 2 \sum_{n=1}^{\infty} \left(\frac{r'}{a} \right)^n \cos[n(\theta - \theta')] \right\} r' dr' d\theta'. \quad (1-5)$$

The geometrical term in parentheses is the distribution function for an infinite line charge inside a cylindrical pipe. (See Appendix B) This is a result of the well known "pan-caking" effect. When the beam bunch is relativistic, the electric field lines are almost perpendicular to the direction of motion.

1.5 Model of BPM coupling to image charge

The coupling of the BPM electrodes to the beam image charge can be modeled by the circuit in Figure 1-2[17]. The image charge is represented by the current, i_b . Z_c is the characteristic impedance of the transmission line and C_p is the capacitance of the BPM electrodes. In the frequency domain, this model is accurate up to approximately 2 GHz[16].

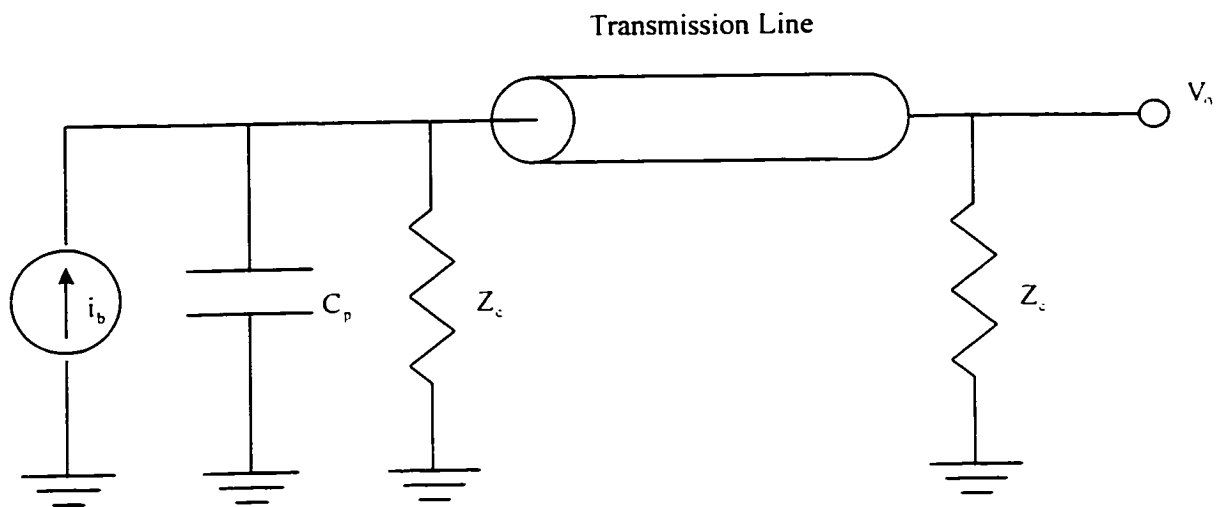


Figure 1-2: Circuit model of BPM electrode coupling to electron beam. C_p is the capacitance of the BPM electrode. Z_c is the characteristic impedance of the transmission line. i_b represents the image induced image charge from the passing electron beam.

The signal generated by a BPM electrode travels down a transmission line to where an oscilloscope displays the resulting voltage signal. Because our beam bunches are very short, a large part of the signal content is at very high frequencies. Since the model is inaccurate above 2 GHz, low-pass filters are placed on the oscilloscope inputs in order to ensure that we are far from that regime. The end result is that the original signal is modified significantly by the time it is displayed on the oscilloscope. Therefore, transfer functions are assigned in the frequency domain: $\sigma(\omega)$ for the transmission line and $A(\omega)$ for the combination low pass filter and oscilloscope.

As already mentioned, the electron beam bunches on SPA are quite short. The maximum expected full width at half maximum length (FWHM) is 6 mm, or 20 ps. Under these conditions the beam bunch is essentially a delta function longitudinally for all frequencies of interest. Taking this into account and using the circuit model in Figure 1-2 and the expression for the image charge given in equation (1-5), the voltage signal seen by the oscilloscope is

$$v_{\text{osc}}(t) = \frac{1}{4\pi^2} \int_{\text{area of pipe}} da' \int_{-\infty}^{\infty} dz' \rho_L(r', \theta', z') \left\{ 2\alpha + 4 \sum_{n=1}^{\infty} \left(\frac{r'}{a} \right)^n \frac{\sin n\alpha}{n} \cos[n(\theta - \theta')] \right\} \\ \otimes \int_{-\infty}^{\infty} \frac{e^{-j\frac{\omega}{\beta c} z_0}}{2\pi} \left(1 - e^{-j\frac{\omega}{\beta c} L} \right) \frac{Z_c \sigma(\omega) A(\omega)}{1 + j\omega C_p Z_c} e^{j\omega t} d\omega. \quad (1-6)$$

where L is the length of the electrode and z_0 its longitudinal position. (See Appendix C)

Without knowledge of the form of the transfer functions $\sigma(\omega)$ and $A(\omega)$ or the values for the various constants, the shape of the time signal cannot be predicted. However this does not present a problem. As will be shown, it is the amplitude of the

time signal that provides the useful information about the electron beam.

1.6 Beam information provided by BPM

The amplitude of the time function in (1-6) is given by

$$A = \frac{1}{4\pi^2} \int_{\text{area of pipe}} da' \int_{-\infty}^{\infty} dz' \rho_L(r', \theta', z') \left\{ 2\alpha + 4 \sum_{n=1}^{\infty} \left(\frac{r'}{a} \right)^n \frac{\sin n\alpha}{n} \cos[n(\theta - \theta')] \right\}. \quad (1-7)$$

The term in parentheses can be expanded and converted to Cartesian coordinates. (See Appendix D) Then, the integral can be taken over each term in (1-7) yielding

$$\begin{aligned} A = \frac{q}{4\pi^2} & \left\{ 2\alpha + \frac{4 \sin \alpha}{a} (\bar{x} \cos \theta + \bar{y} \sin \theta) \right. \\ & + \frac{2 \sin 2\alpha}{a^2} \left[(\langle x^2 \rangle_{\text{BPM}} - \langle y^2 \rangle_{\text{BPM}}) \cos 2\phi + 2 \langle xy \rangle_{\text{BPM}} \sin 2\phi \right] \\ & + \frac{4 \sin 3\alpha}{3 a^3} \left[(\langle x^3 \rangle_{\text{BPM}} - 3 \langle xy^2 \rangle_{\text{BPM}}) \cos 3\phi + (3 \langle x^2 y \rangle_{\text{BPM}} - \langle y^3 \rangle_{\text{BPM}}) \sin 3\phi \right] \\ & \left. + O\left(\frac{1}{a^4}\right) \right\}. \quad (\text{See Appendix D}) \end{aligned} \quad (1-8)$$

The x and y coordinates of the beam center with respect to the beam pipe are given by \bar{x} and \bar{y} respectively.

The BPM electrodes are placed every 90 degrees around the circumference of the beam pipe at 0, 90, 180 and 270 degrees. Substituting these values for θ into (1-8) gives

$$\begin{aligned} A(\theta = 0) \equiv A_R = \frac{q}{4\pi^2} & \left\{ 2\alpha + \frac{4 \sin \alpha}{a} \bar{x} + \frac{2 \sin 2\alpha}{a^2} (\langle x^2 \rangle_{\text{BPM}} - \langle y^2 \rangle_{\text{BPM}}) \right. \\ & \left. + \frac{4 \sin 3\alpha}{3 a^3} (\langle x^3 \rangle_{\text{BPM}} - 3 \langle xy^2 \rangle_{\text{BPM}}) + O\left(\frac{1}{a^4}\right) \right\}. \end{aligned} \quad (1-9)$$

$$A(\theta = \pi) \equiv A_L = \frac{q}{4\pi^2} \left\{ 2\alpha - \frac{4 \sin \alpha}{a} \bar{x} + \frac{2 \sin 2\alpha}{a^2} (\langle x^2 \rangle_{\text{BPM}} - \langle y^2 \rangle_{\text{BPM}}) - \frac{4 \sin 3\alpha}{3 a^3} (\langle x^3 \rangle_{\text{BPM}} - 3\langle xy^2 \rangle_{\text{BPM}}) + O\left(\frac{1}{a^4}\right) \right\}. \quad (1-10)$$

$$A\left(\theta = \frac{\pi}{2}\right) \equiv A_T = \frac{q}{4\pi^2} \left\{ 2\alpha + \frac{4 \sin \alpha}{a} \bar{y} - \frac{2 \sin 2\alpha}{a^2} (\langle x^2 \rangle_{\text{BPM}} - \langle y^2 \rangle_{\text{BPM}}) - \frac{4 \sin 3\alpha}{3 a^3} (3\langle x^2 y \rangle_{\text{BPM}} - \langle y^3 \rangle_{\text{BPM}}) + O\left(\frac{1}{a^4}\right) \right\}. \quad (1-11)$$

and

$$A\left(\theta = \frac{3\pi}{2}\right) \equiv A_B = \frac{q}{4\pi^2} \left\{ 2\alpha - \frac{4 \sin \alpha}{a} \bar{y} - \frac{2 \sin 2\alpha}{a^2} (\langle x^2 \rangle_{\text{BPM}} - \langle y^2 \rangle_{\text{BPM}}) + \frac{4 \sin 3\alpha}{3 a^3} (3\langle x^2 y \rangle_{\text{BPM}} - \langle y^3 \rangle_{\text{BPM}}) + O\left(\frac{1}{a^4}\right) \right\}. \quad (1-12)$$

The subscripts R, L, T, and B identify the right, left, top and bottom lobes respectively (Figure 1-1). It is easily shown that the charge in the bunch is given by

$$q = \frac{\pi^2}{2\alpha} (A_R + A_L + A_T + A_B) \text{ to order } \frac{(\text{beam size})^4}{a^4}. \quad (1-13)$$

and that the centroid locations are given by

$$\bar{x} = a \frac{\alpha}{2 \sin \alpha} \frac{A_R - A_L}{A_R + A_L} \text{ to order } \frac{(\text{beam size})^3}{a^3}. \quad (1-14)$$

$$\bar{y} = a \frac{\alpha}{2 \sin \alpha} \frac{A_T - A_B}{A_T + A_B} \text{ to order } \frac{(\text{beam size})^3}{a^3}. \quad (1-15)$$

The last bit of information that can be extracted is the quadrupole moment, given by

$$\langle x^2 \rangle_{\text{BPM}} - \langle y^2 \rangle_{\text{BPM}} = \frac{a^2 \alpha}{\sin 2\alpha} \frac{A_R + A_L - A_T - A_B}{A_R + A_L + A_T + A_B} \text{ to order } \frac{(\text{beam size})^4}{a^4}. \quad (1-16)$$

In Appendix D it is shown that

$$\langle x^2 \rangle_{\text{BPM}} - \langle y^2 \rangle_{\text{BPM}} = \langle x^2 \rangle - \langle y^2 \rangle + \bar{x}^2 - \bar{y}^2.$$

Since \bar{x} and \bar{y} are determined by (1-14) and (1-15), equation (1-16) is essentially a measure of $\langle x^2 \rangle - \langle y^2 \rangle$.

Chapter 2

MEASURING EMITTANCE WITH BEAM POSITION MONITORS

2.1 Introduction

This chapter will first give a definition of the x and y rms emittances and briefly discuss why they are important. It will then move on to describe the theory behind the BPM emittance measurement. Ending the chapter is a valuable discussion of the numerical characteristics of this diagnostic.

There is a strong tendency for this emittance measurement to be numerically unstable. If the technique is implemented improperly, the measurement errors in the BPM data are amplified greatly in the fitting process. The last part of this chapter addresses this problem and describes how it is avoided.

2.2 Emittance

Each electron in a beam bunch is described by six coordinates: the three transverse coordinates and their associated momentum. Taken as a whole, the bunch describes a six dimensional volume. The x and y rms emittances are derived from the projections of this six dimensional volume onto the x and y phase spaces.

The x phase space is two dimensional with one axis defined by the x position and the other by the x momentum. The definition of the y phase space is similar. In charged

particle beam dynamics, the momentum is replaced by the divergence[6]. The x divergence, written as x' , is the angle that the electron makes with the z axis in the x plane. It is related to the x momentum according to the equation

$$p_x = \gamma m v_x = \gamma m \frac{dx}{dt} = \gamma m \frac{dz}{dt} \frac{dx}{dz} = \gamma m c \frac{v_z}{c} x' = \beta \gamma m c x'$$

where β and γ are the usual relativistic parameters, c is the speed of light and m is the electron mass. If the energy spread within each electron bunch is small, then the value of $\beta\gamma$ will essentially be a constant within the beam bunch and x' will be equivalent to p_x . The same relationship exists between y' and p_y . Using the divergence facilitates the formulation of the beam dynamics as an optical, or geometrical, system.

A numerical computation of the x phase space of the SPA beam as it exits the accelerator is shown in Figure 2-1. The superimposed ellipse is defined by the ensemble averages $\langle x^2 \rangle$, $\langle xx' \rangle$ and $\langle x'^2 \rangle$. The equation for this ellipse can be written as

$$\beta_x x^2 - \alpha_x xx' + \gamma_x x'^2 = \pi \epsilon_x.$$

The first three constants, or Twiss parameters, are given by

$$\beta_x \equiv \frac{\langle x^2 \rangle}{\epsilon_x},$$

$$\alpha_x \equiv \frac{\langle xx' \rangle}{\epsilon_x}$$

and

$$\gamma_x \equiv \frac{\langle x'^2 \rangle}{\epsilon_x} [18].$$

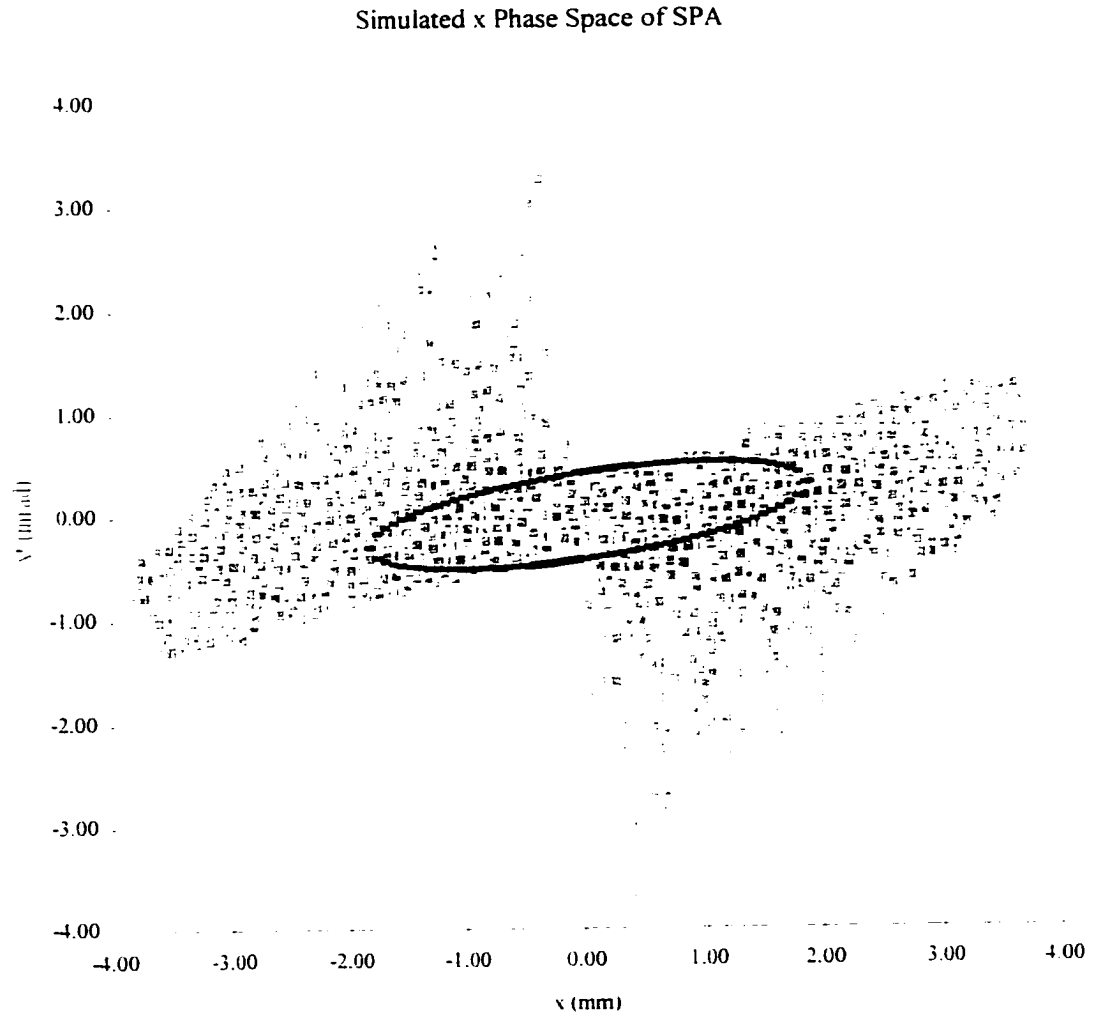


Figure 2-1: The x phase space of the SPA beam from simulation.

They have the property that

$$\beta_x \gamma_x - \alpha_x^2 = 1.$$

The rms x emittance, ϵ_x , is given by

$$\epsilon_x \equiv \sqrt{\langle x^2 \rangle \langle x'^2 \rangle - \langle xx' \rangle^2}. \quad (2-1)$$

It is the area of ellipse divided by the number π . Equivalently, the rms y emittance is given by

$$\epsilon_y \equiv \sqrt{\langle y^2 \rangle \langle y'^2 \rangle - \langle yy' \rangle^2}. \quad (2-2)$$

It can be shown that the normalized rms emittances, defined as

$$\epsilon_{xn} \equiv \beta \gamma \epsilon_x \quad (2-3)$$

and

$$\epsilon_{yn} \equiv \beta \gamma \epsilon_y \quad (2-4)$$

where $\beta \gamma$ is the relativistic parameter associated with the average beam energy, are conserved quantities in a linear focusing system with acceleration[6]. Therefore, any change in the value of the normalized x and y rms emittances are necessarily due to nonlinear processes in the beam transport. For this reason, knowledge of the normalized rms emittances is a valuable diagnostic. Changes in their value, unforeseen or otherwise, can indicate misaligned focusing elements, nonlinear interactions and other undesirable effects.

The normalized rms emittance is also a valuable measure of beam quality. The beam will be at a focus in x when the value of α_x is zero. When this is true,

$$\beta_x = \frac{1}{\gamma_x}.$$

Substituting the definitions for β_x and γ_x into this equation yields

$$\langle x^2 \rangle = \frac{\varepsilon_x^2}{\langle x'^2 \rangle}.$$

In essence, the emittance indicates how tightly a beam can be focused and how quickly it will diverge from that focus.

2.3 Measuring the emittance

Roger Miller et. al. first proposed using BPMs in a non-intercepting emittance probe[12]. Later, it was demonstrated that this technique measures the rms emittance without reference to the spatial distribution of the beam[19]. Because of the difficulties photoinjectors present for diagnostics[9], [10], this technique is ideal for SPA.

The transverse motion of a single charged particle traveling down a linear focusing channel can be characterized by a set of linear equations. The final particle parameters, at the end of the channel, are related to the initial parameters, at the beginning of the channel, by the matrix equation

$$\begin{pmatrix} x_f \\ x'_f \\ y_f \\ y'_f \end{pmatrix} = \begin{bmatrix} R_{11} & R_{12} & 0 & 0 \\ R_{21} & R_{22} & 0 & 0 \\ 0 & 0 & R_{33} & R_{34} \\ 0 & 0 & R_{43} & R_{44} \end{bmatrix} \begin{pmatrix} x_i \\ x'_i \\ y_i \\ y'_i \end{pmatrix} [6].$$

The transfer matrix is determined by mapping the electric and magnetic fields of the focusing elements. A focusing channel that consists of quadrupole magnets and drifts will be linear. The section of beam line that is used to measure the emittance on SPA

consists of only these two elements.

It is easily shown that

$$\begin{aligned} \langle x^2 \rangle_f - \langle y^2 \rangle_f = & (R_{11})^2 \langle x^2 \rangle_i + 2R_{11}R_{12} \langle xx' \rangle_i + (R_{12})^2 \langle x'^2 \rangle_i \\ & - (R_{33})^2 \langle y^2 \rangle_i - 2R_{33}R_{34} \langle yy' \rangle_i - (R_{34})^2 \langle y'^2 \rangle_i \quad [12], \end{aligned}$$

where the f subscript refers to the BPM location and the i subscript to the focusing channel entrance. Changing the transfer matrix m times, where $m \geq 6$, and measuring $\langle x^2 \rangle_f - \langle y^2 \rangle_f$ for each change, results in the matrix equation

$$\bar{\bar{\mathbf{A}}} \bar{\mathbf{x}} = \bar{\mathbf{b}} \quad (2-5)$$

where

$$\bar{\bar{\mathbf{A}}} \equiv \begin{bmatrix} \left[(R_{11})^2 \right]_1 & \left[2R_{11}R_{12} \right]_1 & \left[(R_{12})^2 \right]_1 & - \left[(R_{33})^2 \right]_1 & - \left[2R_{33}R_{34} \right]_1 & - \left[(R_{34})^2 \right]_1 \\ \left[(R_{11})^2 \right]_2 & \left[2R_{11}R_{12} \right]_2 & \left[(R_{12})^2 \right]_2 & - \left[(R_{33})^2 \right]_2 & - \left[2R_{33}R_{34} \right]_2 & - \left[(R_{34})^2 \right]_2 \\ \vdots & \vdots & \vdots & \vdots & \vdots & \vdots \\ \left[(R_{11})^2 \right]_m & \left[2R_{11}R_{12} \right]_m & \left[(R_{12})^2 \right]_m & - \left[(R_{33})^2 \right]_m & - \left[2R_{33}R_{34} \right]_m & - \left[(R_{34})^2 \right]_m \end{bmatrix} \quad (2-6)$$

$$\bar{\mathbf{x}} \equiv \begin{pmatrix} \langle x^2 \rangle_i \\ \langle xx' \rangle_i \\ \langle x'^2 \rangle_i \\ \langle y^2 \rangle_i \\ \langle yy' \rangle_i \\ \langle y'^2 \rangle_i \end{pmatrix}$$

and

$$\bar{\mathbf{b}} \equiv \begin{pmatrix} \left[\langle x^2 \rangle_f - \langle y^2 \rangle_f \right]_1 \\ \left[\langle x^2 \rangle_f - \langle y^2 \rangle_f \right]_2 \\ \vdots \\ \left[\langle x^2 \rangle_f - \langle y^2 \rangle_f \right]_m \end{pmatrix}.$$

Solving for $\bar{\mathbf{x}}$, in the least squares sense, estimates the rms beam parameters $\langle x^2 \rangle_i$, $\langle x'^2 \rangle_i$, $\langle xx' \rangle_i$, $\langle y^2 \rangle_i$, $\langle y'^2 \rangle_i$ and $\langle yy' \rangle_i$. In turn, we can estimate the x and y emittances at the start of the focusing channel using (2-1) and (2-2).

2.4 Stability of emittance measurement

Because $\bar{\mathbf{b}}$ in (2-5) is determined by measurement, there will be errors associated with it. These errors propagate to the estimate of $\bar{\mathbf{x}}$. How accurate this estimate will be depends upon the stability of the matrix equation.

Consider the true value of $\bar{\mathbf{x}}$ as existing at the bottom of a potential well. $\bar{\mathbf{A}}$ determines the shape of that well. When the stability of the matrix equation is good, the well is deep with sheer walls and it is difficult for the errors in $\bar{\mathbf{b}}$ to move the estimated value of $\bar{\mathbf{x}}$ far from the true value of $\bar{\mathbf{x}}$. However, if the stability of the matrix equation is poor, the well will be very shallow and the errors in $\bar{\mathbf{b}}$ will push the estimated value of $\bar{\mathbf{x}}$ far from the true value of $\bar{\mathbf{x}}$.

A matrix equation's stability is inherent and cannot be improved using clever data processing techniques. However, stability is also relative. The stability demanded of the matrix equation depends upon how accurately $\bar{\mathbf{b}}$ is measured and how precisely we need

to know \bar{x} . Because the emittance of the SPA beam is small, the accuracy demanded of the BPM measurements for typical implementations of Miller's method was more than we could achieve. A realization of Miller's technique was required that was stable enough to tolerate a BPM's limited precision.

The question of stability can arise in any diagnostic technique that involves linear equations, sometimes rendering a clever measurement approach useless. However, there is often enough flexibility in the way a given measurement can be implemented so that this problem is avoided. Miller's technique is such a measurement. The approach for finding a stable implementation of Miller's method that is outlined here may be applicable to other diagnostics.

2.5 Figure of merit for matrix equation stability

In this section, a measure for the stability of a general matrix equation is derived. This metric will be used in the next section to compare different implementations of Miller's emittance measurement.

Consider the general matrix equation,

$$\bar{\bar{A}}\bar{x} = \bar{b},$$

where $\bar{\bar{A}}$ has m rows and n columns, \bar{x} has dimension n and \bar{b} has dimension m .

Assume that $m \geq n$ and $\bar{\bar{A}}$ has rank n . The least squares solution for \bar{x} is

$$\bar{x} = \left(\bar{\bar{A}}^T \bar{\bar{A}} \right)^{-1} \bar{\bar{A}}^T \bar{b} = \bar{\bar{A}}^+ \bar{b}. \quad (2-6)$$

$\left(\bar{\bar{A}}^T \bar{\bar{A}} \right)^{-1} \bar{\bar{A}}^T$ is the pseudo-inverse[20] of $\bar{\bar{A}}$ and is denoted by $\bar{\bar{A}}^+$.

To measure the stability of the matrix equation, a relationship between the errors in $\bar{\mathbf{b}}$ and the resulting errors in $\bar{\mathbf{x}}$ needs to be established. Assuming that the errors in $\bar{\mathbf{b}}$ are normal and have value $\pm\sigma$, an upper bound on the errors for the estimates of the elements of $\bar{\mathbf{x}}$ is established.

The matrix $\bar{\bar{\mathbf{A}}}$ can be factored into three matrices called the singular value decomposition of $\bar{\bar{\mathbf{A}}}$ [20]:

$$\bar{\bar{\mathbf{A}}} = \bar{\bar{\mathbf{Q}}}_1 \bar{\bar{\Sigma}} \bar{\bar{\mathbf{Q}}}_2^T. \quad (2-7)$$

$\bar{\bar{\mathbf{Q}}}_1$ is an m by m orthogonal matrix. Like $\bar{\bar{\mathbf{A}}}$, $\bar{\bar{\Sigma}}$ is an m by n matrix. Its first n entries along the main diagonal are $\sqrt{\lambda_i}$, where the λ_i 's are the eigenvalues of the matrix $\bar{\bar{\mathbf{A}}}^T \bar{\bar{\mathbf{A}}}$, and all other elements are zero. $\bar{\bar{\mathbf{Q}}}_2$ is an n by n orthogonal matrix whose columns are the n orthonormal eigenvectors, $\bar{\bar{\mathbf{v}}}_i$, of $\bar{\bar{\mathbf{A}}}^T \bar{\bar{\mathbf{A}}}$.

Using (2-7), the pseudo-inverse of $\bar{\bar{\mathbf{A}}}$ can be written as

$$\bar{\bar{\mathbf{A}}}^+ = \bar{\bar{\mathbf{Q}}}_2 \bar{\bar{\Sigma}}^+ \bar{\bar{\mathbf{Q}}}_1^T.$$

Because they are orthogonal, the inverses of $\bar{\bar{\mathbf{Q}}}_1$ and $\bar{\bar{\mathbf{Q}}}_2$ are their transposes. $\bar{\bar{\Sigma}}^+$ is the pseudo-inverse of $\bar{\bar{\Sigma}}$ and is an n by m matrix with the first n entries along its main diagonal given by

$$\frac{1}{\sqrt{\lambda_i}}$$

and all other elements zero [20]. Writing $\bar{\mathbf{b}}$ as

$$\bar{\mathbf{b}} = \bar{\mathbf{b}}_0 + \bar{\mathbf{e}}_b.$$

where $\bar{\mathbf{b}}_0$ is the ideal value of $\bar{\mathbf{b}}$ and $\bar{\mathbf{e}}_b$ is an error vector. the error in $\bar{\mathbf{x}}$ is given by

$$\bar{\mathbf{e}}_x = \bar{\mathbf{Q}}_2 \bar{\Sigma}^{-1} \bar{\mathbf{Q}}_1^T \bar{\mathbf{e}}_b. \quad (2-8)$$

The exact form of $\bar{\mathbf{e}}_b$ is unknown. However, the elements of $\bar{\mathbf{e}}_b$ are estimated to have magnitude σ , the error in the measurements that determine $\bar{\mathbf{b}}$. Therefore, the approximate magnitude of $\bar{\mathbf{e}}_b$ is given by

$$|\bar{\mathbf{e}}_b| = \sqrt{\bar{\mathbf{e}}_b \cdot \bar{\mathbf{e}}_b} \cong \sqrt{m\sigma^2} = \sigma\sqrt{m}$$

and the approximate value of $\bar{\mathbf{e}}_b$ can be written as

$$\bar{\mathbf{e}}_b \cong \sigma\sqrt{m}\hat{\mathbf{u}}.$$

where $\hat{\mathbf{u}}$ is some unit vector that is unknown. Substituting this into (2-8) gives

$$\bar{\mathbf{e}}_x \cong \sigma\sqrt{m}\bar{\mathbf{Q}}_2 \bar{\Sigma}^{-1} \bar{\mathbf{Q}}_1^T \hat{\mathbf{u}}.$$

Because $\bar{\mathbf{Q}}_1$ is orthogonal, its transpose will only rotate $\hat{\mathbf{u}}$ into some other unit vector, $\hat{\mathbf{u}}'$. Therefore,

$$\bar{\mathbf{e}}_x \cong \sigma\sqrt{m}\bar{\mathbf{Q}}_2 \bar{\Sigma}^{-1} \hat{\mathbf{u}}'. \quad (2-9)$$

Like $\hat{\mathbf{u}}$, $\hat{\mathbf{u}}'$ is unknown. However, it is assumed that the measurement errors in $\bar{\mathbf{b}}$ are random. Therefore, the elements of $\hat{\mathbf{u}}'$, on average, have magnitude $1/\sqrt{m}$. Recalling the definition of $\bar{\Sigma}^{-1}$ and $\bar{\mathbf{Q}}_2$, (2-9) becomes

$$\bar{\mathbf{e}}_x \cong \sigma \sqrt{m} \begin{bmatrix} v_{11} & v_{21} & \cdot & \cdot & \cdot & v_{n1} \\ v_{12} & v_{22} & \cdot & \cdot & \cdot & v_{n2} \\ \cdot & \cdot & \cdot & \cdot & \cdot & \cdot \\ \cdot & \cdot & \cdot & \cdot & \cdot & \cdot \\ \cdot & \cdot & \cdot & \cdot & \cdot & \cdot \\ v_{1n} & v_{2n} & \cdot & \cdot & \cdot & v_{nn} \end{bmatrix} \begin{pmatrix} \pm \frac{1}{\sqrt{m\lambda_1}} \\ \pm \frac{1}{\sqrt{m\lambda_2}} \\ \cdot \\ \cdot \\ \cdot \\ \pm \frac{1}{\sqrt{m\lambda_n}} \end{pmatrix}.$$

where v_{ij} is the j^{th} element of the i^{th} eigenvector of $\bar{\mathbf{A}}^T \bar{\mathbf{A}}$. Doing the matrix multiplication and adding in quadrature gives

$$e_{xj} \cong \sigma \sqrt{\sum_{i=1}^n \frac{v_{ij}^2}{\lambda_i}} \quad (2-10)$$

where e_{xj} is the error in the j^{th} element of $\bar{\mathbf{x}}$.

Since the eigenvectors $\bar{\mathbf{v}}_i$ are orthonormal, the maximum value of any given element is 1. Therefore, from (2-10), the maximum magnitude for any particular e_{xj} is

$$\frac{\sigma}{\sqrt{\lambda_{\min}}}.$$

It is not unreasonable, then, to define a figure of merit (FOM) to measure the stability of the matrix equation.

$$\text{FOM} = \frac{1}{\sqrt{\lambda_{\min}}}. \quad (2-11)$$

where λ_{\min} is the smallest eigenvalue of $\bar{\mathbf{A}}^T \bar{\mathbf{A}}$.

It should be pointed out that the FOM as defined here is only a useful tool if one is aware that it does depend upon the units chosen for the vector $\bar{\mathbf{x}}$. For instance, if we choose mm and mrad for our length and angle units in Miller's method, we are making

the choice that an error of $\pm 1 \text{ mm}^2$ (in $\langle x^2 \rangle_i$ and $\langle y^2 \rangle_i$) is as severe as an error of $\pm 1 \text{ mrad}^2$ (in $\langle x'^2 \rangle_i$ and $\langle y'^2 \rangle_i$) and as severe as an error of $\pm 1 \text{ mm mrad}$ (in $\langle xx' \rangle_i$ and $\langle yy' \rangle_i$). If we wish to measure $\langle x^2 \rangle_i$ and $\langle y^2 \rangle_i$ to $\pm 0.1 \text{ mm}^2$ and $\langle x'^2 \rangle_i$ and $\langle y'^2 \rangle_i$ to $\pm 0.1 \text{ mrad}^2$, then this choice of units is appropriate. However, if we wish to determine $\langle x^2 \rangle_i$ and $\langle y^2 \rangle_i$ to $\pm 0.1 \mu\text{m}^2$ and $\langle x'^2 \rangle_i$ and $\langle y'^2 \rangle_i$ to $\pm 0.1 \text{ rad}^2$, then choosing mm and mrad will cause the FOM to provide inaccurate information when comparing different implementations of Miller's method.

2.6 Finding a stable implementation of Miller's measurement

This section will first present naïve attempts at implementing Miller's emittance measurement that fail. It will then move on to discuss near singular equations and coupling, the cornerstones of making Miller's method stable. At the end, three numerical examples from SPA are presented and are compared using the figure of merit derived in the last section.

2.6.1 Poor implementations of Miller's emittance measurement

Figure 2-2 shows a schematic of a very simple attempt to implement Miller's measurement: several BPMs separated by drifts. The number of BPMs, m , is at least six. The linear transfer matrix for a drift is

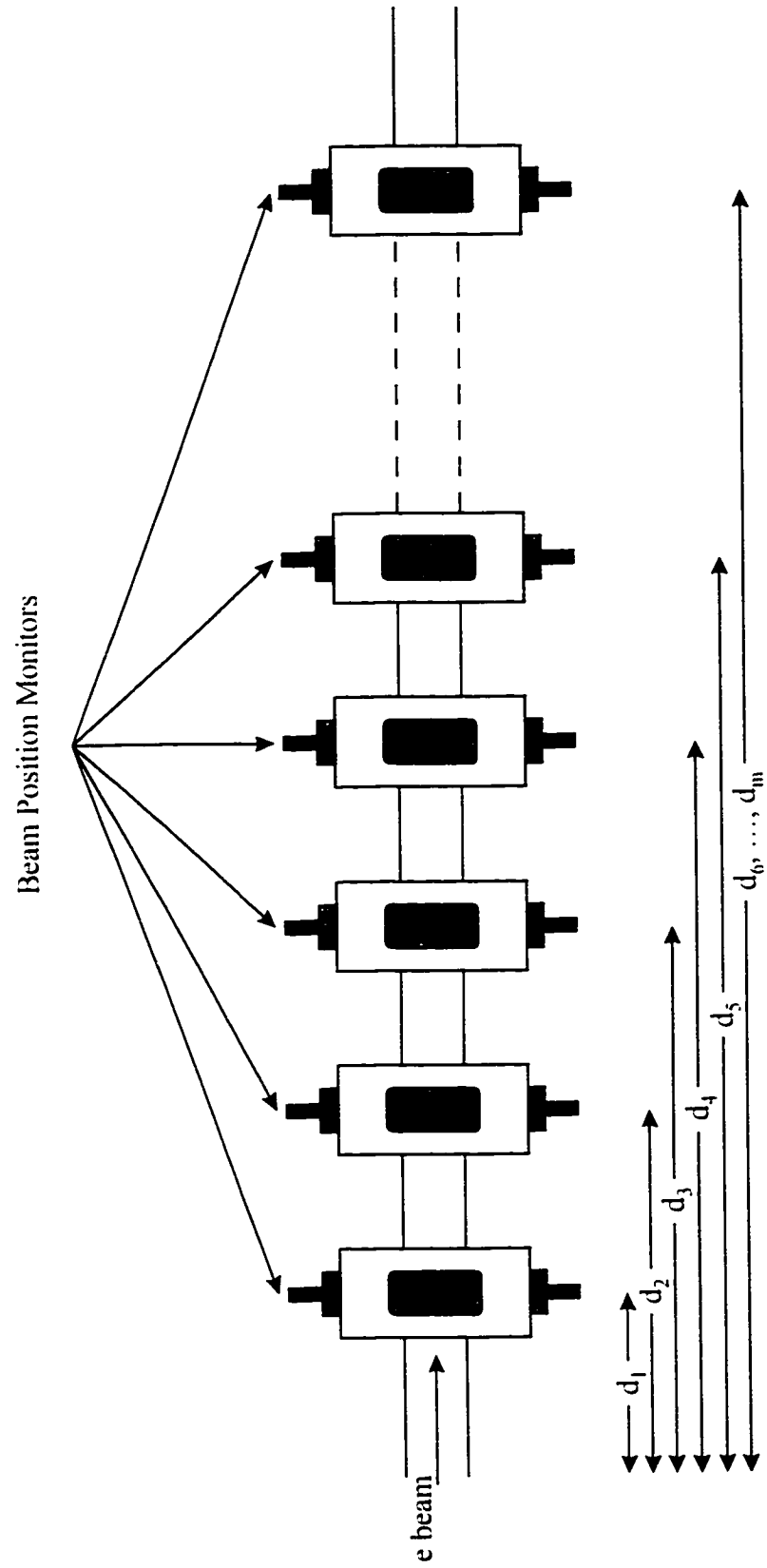


Figure 2-2: Schematic of beam line for implementation of emittance measurement using only drifts.

$$\bar{\bar{\mathbf{R}}}_d = \begin{bmatrix} 1 & d & 0 & 0 \\ 0 & 1 & 0 & 0 \\ 0 & 0 & 1 & d \\ 0 & 0 & 0 & 1 \end{bmatrix},$$

where d is the length of the drift. From (2-6), then.

$$\bar{\bar{\mathbf{A}}} = \begin{bmatrix} 1 & 2d_1 & d_1^2 & -1 & -2d_1 & -d_1^2 \\ 1 & 2d_2 & d_2^2 & -1 & -2d_2 & -d_2^2 \\ \cdot & \cdot & \cdot & \cdot & \cdot & \cdot \\ \cdot & \cdot & \cdot & \cdot & \cdot & \cdot \\ \cdot & \cdot & \cdot & \cdot & \cdot & \cdot \\ 1 & 2d_m & d_m^2 & -1 & -2d_m & -d_m^2 \end{bmatrix}.$$

The second three columns are linearly dependent upon the first three columns and it is readily obvious that this $\bar{\bar{\mathbf{A}}}$ is singular and the matrix equation has no solution. Therefore, the emittance cannot be measured by BPMs separated by drifts.

Figure 2-3 shows a schematic of a second configuration that often already exists in an accelerator beam line: a single quadrupole magnet followed by a drift and a BPM. The quadrupole magnet acts like a lens that focuses in one direction and defocuses in the other. Although a thick lens formula is more accurate, it is assumed that the effect of the quadrupole can be approximated by a thin lens. The transfer matrix for a thin lens that focuses in one direction and defocuses in the other is

$$\bar{\bar{\mathbf{R}}}_{\text{lens}} = \begin{bmatrix} 1 & 0 & 0 & 0 \\ -1/f & 1 & 0 & 0 \\ 0 & 0 & 1 & 0 \\ 0 & 0 & 1/f & 1 \end{bmatrix},$$

where f is the focal length of the quadrupole. The total transfer matrix of the drift/lens combination is given by

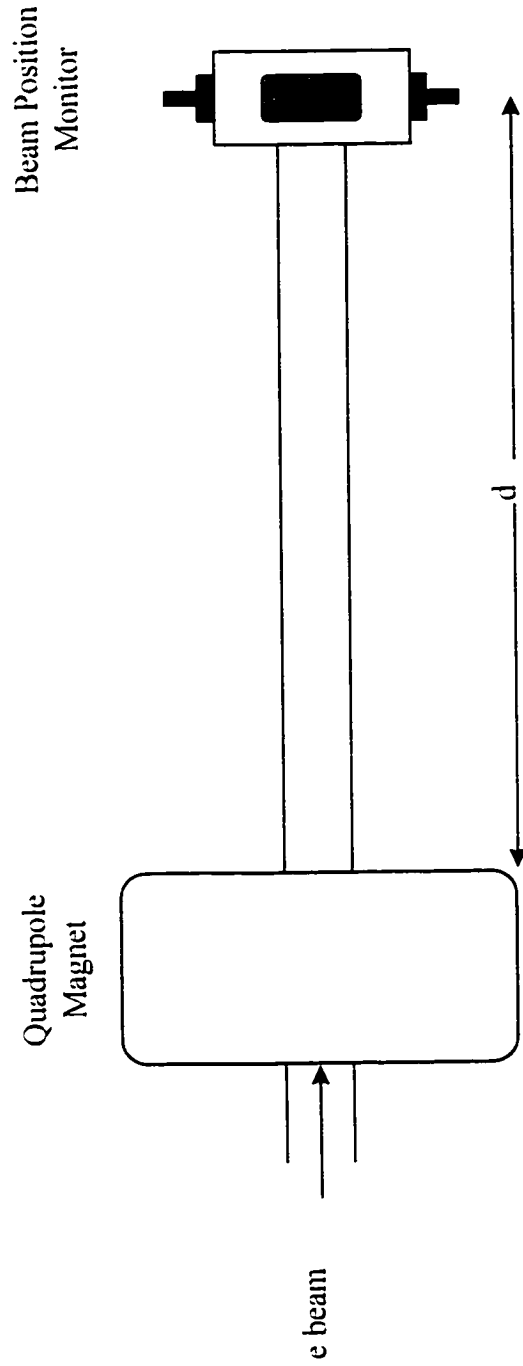


Figure 2-3: Schematic of beam line consisting of quadrupole magnet, drift and BPM.

$$\bar{\mathbf{R}}_{\text{tot}} = \bar{\mathbf{R}}_d \bar{\mathbf{R}}_{\text{lens}} = \begin{bmatrix} 1 - d/f & d & 0 & 0 \\ -1/f & 1 & 0 & 0 \\ 0 & 0 & 1 + d/f & d \\ 0 & 0 & 1/f & 1 \end{bmatrix}$$

Using (2-6) and varying the focusing strength of the quadrupole m times, where $m \geq 6$, results in

$$\bar{\mathbf{A}} = \begin{bmatrix} \left(1 - \frac{d}{f_1}\right)^2 & 2d\left(1 - \frac{d}{f_1}\right) & d^2 & -\left(1 + \frac{d}{f_1}\right)^2 & -2d\left(1 + \frac{d}{f_1}\right) & -d^2 \\ \left(1 - \frac{d}{f_2}\right)^2 & 2d\left(1 - \frac{d}{f_2}\right) & d^2 & -\left(1 + \frac{d}{f_2}\right)^2 & -2d\left(1 + \frac{d}{f_2}\right) & -d^2 \\ \cdot & \cdot & \cdot & \cdot & \cdot & \cdot \\ \cdot & \cdot & \cdot & \cdot & \cdot & \cdot \\ \left(1 - \frac{d}{f_m}\right)^2 & 2d\left(1 - \frac{d}{f_m}\right) & d^2 & -\left(1 + \frac{d}{f_m}\right)^2 & -2d\left(1 + \frac{d}{f_m}\right) & -d^2 \end{bmatrix}$$

Because column three and column six are linearly dependent, this matrix is also singular.

If the thick lens formula is used to describe the quadrupole magnet, $\bar{\mathbf{A}}$ in the second example would not be singular. However, it would be close to singular and the matrix equation would be very unstable. What these two examples illustrate is that stable configurations of Miller's measurement do not necessarily occur naturally. Typically, they must be searched out.

2.6.2 Singular equations and strong coupling

Finding a stable implementation of Miller's emittance measurement is a somewhat informal process. Although the figure of merit, (2-11), will indicate whether or not a given configuration is good enough, it does not disclose how a stable implementation is to be found. That task requires some trial and error.

There are two aspects to consider when searching for a stable matrix equation. The first has already been discussed: avoid nearly singular matrix equations. To do this, first consider what control is available over the elements of the matrix $\bar{\bar{A}}$. For instance, in Miller's technique assume that we can implement the measurement in such a way as to allow transfer matrices with the following four characteristics: in the first, the elements R_{12} , R_{33} and R_{34} are zero, in the second, R_{11} , R_{33} and R_{34} are zero, in the third, R_{11} , R_{12} and R_{34} are zero and in the fourth, R_{11} , R_{12} and R_{33} are zero. Substituting these into (2-6) gives

$$\bar{\bar{A}} = \begin{bmatrix} \left[(R_{11})^2 \right]_1 & 0 & 0 & 0 & 0 & 0 \\ 0 & 0 & \left[(R_{12})^2 \right]_2 & 0 & 0 & 0 \\ 0 & 0 & 0 & -\left[(R_{33})^2 \right]_3 & 0 & 0 \\ 0 & 0 & 0 & 0 & 0 & -\left[(R_{34})^2 \right]_4 \\ \left[(R_{11})^2 \right]_5 & \left[2R_{11}R_{12} \right]_5 & \left[(R_{12})^2 \right]_5 & -\left[(R_{33})^2 \right]_5 & -\left[2R_{33}R_{34} \right]_5 & -\left[(R_{34})^2 \right]_5 \\ \left[(R_{11})^2 \right]_6 & \left[2R_{11}R_{12} \right]_6 & \left[(R_{12})^2 \right]_6 & -\left[(R_{33})^2 \right]_6 & -\left[2R_{33}R_{34} \right]_6 & -\left[(R_{34})^2 \right]_6 \end{bmatrix}. \quad (2-12)$$

The first four rows are perpendicular to each other. The settings for the last two rows are now easily chosen to avoid a singular matrix.

The second aspect to be considered when searching for a stable matrix equation is the coupling of the desired parameters. Good coupling is when $\bar{\bar{A}}\bar{x}$ is much larger than the error in the measurement of \bar{b} . For the matrix equation to be sufficiently stable, each of the initial parameters, $\langle x^2 \rangle$, $\langle x'^2 \rangle$, $\langle xx' \rangle$, $\langle y^2 \rangle$, $\langle y'^2 \rangle$ and $\langle yy' \rangle$, must couple strongly to the final value of $\langle x^2 \rangle - \langle y^2 \rangle$ in at least one of the measurements.

Consider the motion of an electron in the fields of a quadrupole magnet. As it passes through the magnetic field of the quadrupole, the strength of the field that the electron

sees depends upon the electron's position in the magnet aperture. The resulting change in the electron's trajectory will be strongly dependent upon its initial position in the quadrupole field and much less dependent upon its initial direction, or divergence. Therefore, the final value of $\langle x^2 \rangle - \langle y^2 \rangle$ will depend very little upon the initial values of $\langle x'^2 \rangle$ and $\langle y'^2 \rangle$ but very much on the initial values of $\langle x^2 \rangle$ and $\langle y^2 \rangle$. A quadrupole magnet will provide strong coupling between the initial values $\langle x^2 \rangle$ and $\langle y^2 \rangle$, and the final value of $\langle x^2 \rangle - \langle y^2 \rangle$.

The transfer matrix for a drift of length d has

$$R_{12} = R_{34} = d.$$

R_{12} and R_{34} in the total transfer matrix of the beam line determine the coupling of the initial values $\langle x'^2 \rangle$ and $\langle y'^2 \rangle$. Therefore, long drifts tend to amplify the coupling of the initial values of $\langle x'^2 \rangle$ and $\langle y'^2 \rangle$ to the final value of $\langle x^2 \rangle - \langle y^2 \rangle$.

2.6.3 Stable implementation of Miller's measurement

Taking into consideration near singular matrices and coupling, an excellent implementation of Miller's emittance measurement is that shown as a schematic in Figure 2-4: a triplet followed by a BPM. The triplet consists of three quadrupoles separated by roughly equal drifts. Having two quadrupoles ensures enough control over the transfer matrix elements to avoid a nearly singular matrix equation. The third quadrupole adds another degree of freedom to guarantee satisfactory coupling of the initial values of $\langle x^2 \rangle$ and $\langle y^2 \rangle$ to the final value of $\langle x^2 \rangle - \langle y^2 \rangle$. Sufficient coupling of the initial values of

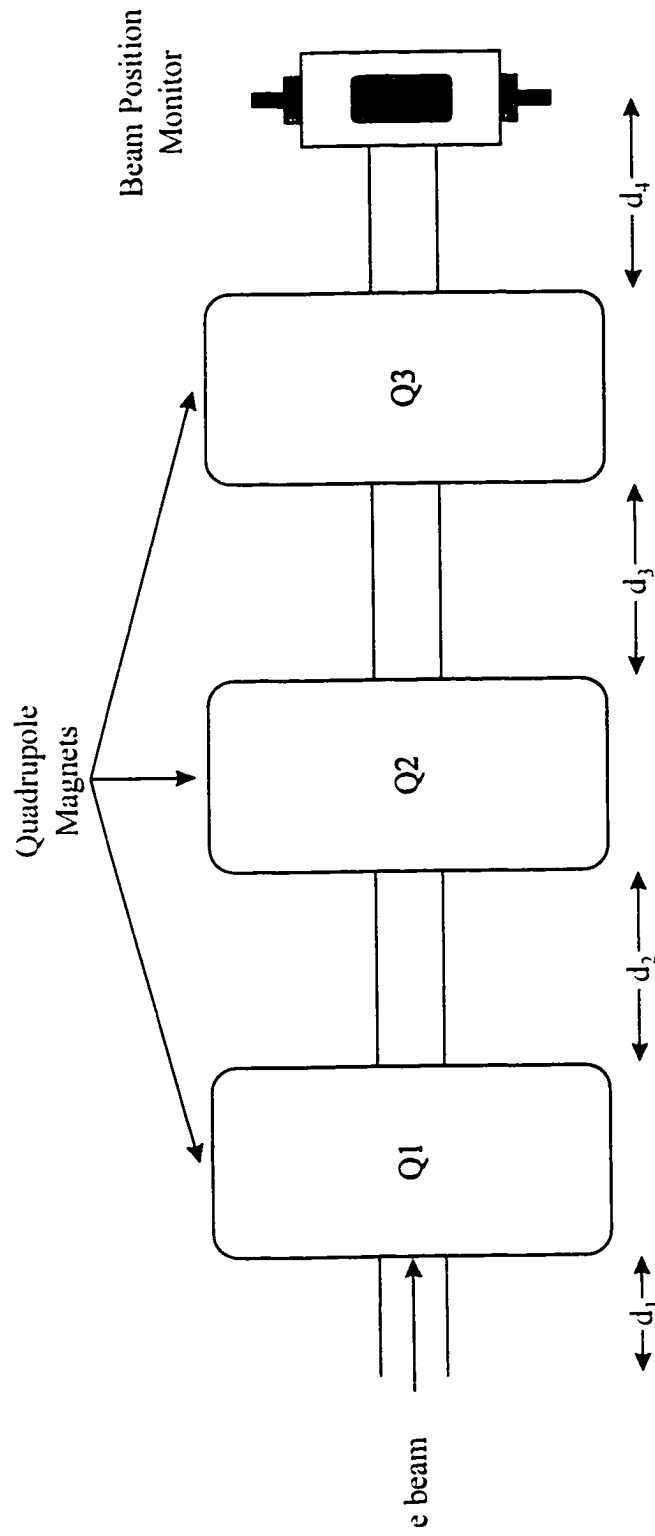


Figure 2-4: Schematic of beam line consisting of a triplet followed by a beam position monitor.

$\langle x'^2 \rangle$ and $\langle y'^2 \rangle$ to the final value of $\langle x^2 \rangle - \langle y^2 \rangle$ is assured by making the drift lengths between the quadrupoles long enough.

2.6.4 Numerical examples

To demonstrate the effectiveness of the triplet configuration, three numerical examples using the parameters from SPA are presented and compared.

The values for the drifts in Figure 2-4 are

$$d_1 = 83.1 \text{ mm.}$$

$$d_2 = 326.75 \text{ mm.}$$

$$d_3 = 425.2 \text{ mm}$$

and

$$d_4 = 236.6 \text{ mm.}$$

The quadrupole magnets are electromagnetic and have an effective length of 86 mm. The beam energy is 8 MeV. From simulations of SPA with the code PARMELA[21], the values of the beam parameters at the end of the accelerator for a 3 nC beam are

$$\langle x^2 \rangle = 7.05 \text{ mm}^2.$$

$$\langle xx' \rangle = -3.15 \text{ mm mrad.}$$

$$\langle x'^2 \rangle = 1.52 \text{ mrad}^2.$$

$$\langle y^2 \rangle = 0.50 \text{ mm}^2.$$

$$\langle yy' \rangle = -0.59 \text{ mm mrad}$$

and

$$\langle y'^2 \rangle = 2.29 \text{ mrad}^2.$$

The emittance can be calculated from the parameters using (2-1) and (2-2) giving

$$\varepsilon_x = 1.25 \pi \text{ mm mrad}.$$

and

$$\varepsilon_y = 0.892 \pi \text{ mm mrad}.$$

It is expected that the BPM will measure the value of $\langle x^2 \rangle - \langle y^2 \rangle$ to $\sigma = \pm 0.5 \text{ mm}^2$.

Six quadrupole settings will be used in each example. According to simulation, each setting transports the beam past the BPM location. The transfer matrices are calculated using the linear beam transport code Trace3D[22].

The first example is a redux of Figure 2-2 using only the last quadrupole in Figure 2-4. This time, however, the proper transfer matrix for the quadrupole magnet is used, not the thin lens approximation. The second example employs all three quadrupoles in Figure 2-4 with random field strengths. In the third example the matrix is made stable using the concepts discussed previously.

In example one, three arbitrary values for the current in the third quadrupole are chosen. The signs of the three currents are then reversed to get to six settings. A typical result is

$$\bar{\mathbf{A}} = \begin{bmatrix} 3.6529 & 1.3725 & 0.1289 & -0.0260 & -0.0927 & -0.0828 \\ 2.7403 & 1.1553 & 0.1218 & -0.1466 & -0.2275 & -0.0882 \\ 1.9742 & 0.9526 & 0.1149 & -0.3720 & -0.3739 & -0.0940 \\ 0.0260 & 0.0927 & 0.0828 & -3.6529 & -1.3725 & -0.1289 \\ 0.1466 & 0.2275 & 0.0882 & -2.7403 & -1.1553 & -0.1218 \\ 0.3720 & 0.3739 & 0.0940 & -1.9742 & -0.9526 & -0.1149 \end{bmatrix}.$$

Calculating the eigenvectors and eigenvalues of $\bar{\bar{A}}^T \bar{\bar{A}}$ and using (2-11) results in

$$\text{FOM} = \frac{1}{\sqrt{\lambda_{\min}}} = 3.05 \times 10^4.$$

The expected errors in the estimated values for the beam parameters are, from (2-10),

$$\text{err}_{x^2} = \pm 190 \text{ mm}^2.$$

$$\text{err}_{xx'} = \pm 2.0 \times 10^3 \text{ mm mrad}.$$

$$\text{err}_{y^2} = \pm 1.1 \times 10^4 \text{ mrad}^2.$$

$$\text{err}_{y^2} = \pm 190 \text{ mm}^2.$$

$$\text{err}_{yy'} = \pm 2.0 \times 10^3 \text{ mm mrad}$$

and

$$\text{err}_{y^2} = \pm 1.1 \times 10^4 \text{ mrad}^2.$$

Obviously, when compared to the actual values of the beam parameters, these errors are completely unacceptable. Also note that the magnitudes of the two largest errors are approximately σ times the FOM.

For the second example, six settings were chosen at random, using all three quads at least once. A typical result is

$$\bar{\bar{A}} = \begin{bmatrix} 0.0104 & -0.1505 & 0.5419 & -4.6088 & -8.3564 & -3.7879 \\ 0.0191 & 0.3555 & 1.6529 & -0.6651 & -1.3695 & -0.7049 \\ 7.5388 & 8.5015 & 2.3968 & -0.4586 & 1.5146 & -1.2506 \\ 0.5010 & -0.3159 & 0.4098 & -0.1028 & -1.4157 & -4.8723 \\ 0.0550 & 0.2471 & 0.2776 & -3.3319 & -8.0093 & -4.8132 \\ 3.6529 & 8.7298 & 5.2157 & -0.0260 & -0.1450 & -0.2025 \end{bmatrix}.$$

Again calculating the eigenvectors and eigenvalues of $\bar{\bar{A}}^T \bar{\bar{A}}$, (2-11) yields

$$\text{FOM} = 3.0.$$

From (2-10), the expected errors in the parameter estimates are

$$\text{err}_{x^2} = \pm 0.71 \text{ mm}^2.$$

$$\text{err}_{xx} = \pm 0.53 \text{ mm mrad}.$$

$$\text{err}_{y^2} = \pm 0.41 \text{ mrad}^2.$$

$$\text{err}_{y^2} = \pm 1.05 \text{ mm}^2.$$

$$\text{err}_{yy} = \pm 0.66 \text{ mm mrad}$$

and

$$\text{err}_{y^2} = \pm 0.33 \text{ mrad}^2.$$

This is much better than the first example. However, the errors are still bigger than some of the beam parameters. Again, note that the largest expected error is approximately σ times the FOM.

In the third example, the six settings were carefully chosen to make the matrix stable.

In this case, the matrix $\bar{\bar{A}}$ is

$$\bar{\bar{A}} = \begin{bmatrix} 0.0000 & 0.0000 & 4.7779 & -0.0454 & 0.0000 & 0.0000 \\ 0.0454 & 0.0000 & 0.0000 & 0.0000 & 0.0000 & -4.7779 \\ 0.0178 & 0.0000 & 0.0000 & -8.9987 & 0.0000 & 0.0000 \\ 8.9987 & 0.0000 & 0.0000 & -0.0178 & 0.0000 & 0.0000 \\ 0.0003 & 0.0096 & 0.0887 & -4.3470 & -10.2809 & -6.0787 \\ 4.3470 & 10.2809 & 6.0787 & 0.0003 & 0.0096 & 0.0887 \end{bmatrix}.$$

Calculating the eigenvectors and eigenvalues of $\bar{\bar{A}}^T \bar{\bar{A}}$, (2-11) yields

$$\text{FOM} = 0.25.$$

From (2-10), the expected errors in the estimated parameters are

$$\text{err}_{x^2} = \pm 0.056 \text{ mm}^2 .$$

$$\text{err}_{xx'} = \pm 0.070 \text{ mm mrad} .$$

$$\text{err}_{y^2} = \pm 0.105 \text{ mrad}^2 .$$

$$\text{err}_{y^2} = \pm 0.056 \text{ mm}^2 .$$

$$\text{err}_{yy'} = \pm 0.070 \text{ mm mrad}$$

and

$$\text{err}_{y'^2} = \pm 0.105 \text{ mrad}^2 .$$

These errors are very reasonable and much better than the previous two examples. Once again, the magnitudes of the two largest errors are approximately σ times the FOM.

In the examples, the FOM, together with the expected error in the BPM measurements, provides an accurate indicator of the maximum expected error. Therefore, the ratio of the FOMs is a good comparison of each implementation. Taking the ratio of FOM for examples one and three gives

$$\frac{\text{FOM}_{\text{Ex. 1}}}{\text{FOM}_{\text{Ex. 3}}} = 1.22 \times 10^5 .$$

The ratio for examples two and three gives

$$\frac{\text{FOM}_{\text{Ex. 2}}}{\text{FOM}_{\text{Ex. 3}}} = 12.0 .$$

So, although the BPM measurements are equally accurate, the estimates of $\langle x^2 \rangle$, $\langle x'^2 \rangle$,

$\langle xx' \rangle$, $\langle y^2 \rangle$, $\langle y'^2 \rangle$ and $\langle yy' \rangle$ from the third example are an order of magnitude better than the estimates from the second example and five orders of magnitude better than the estimates from the first. This is a significant improvement.

It should be noted that the nature of the matrix equation is not the only factor that limits the accuracy of Miller's emittance measurement. I do not want to imply that its accuracy can be improved without bound by rearranging the quadrupoles or increasing their strength. Quadrupole settings that cause the beam to intercept the beam pipe walls, chromatic aberrations due to energy spread in the beam, imperfections in the quadrupole fields, space charge forces and other factors also limit the performance of Miller's measurement. The matrix stability is only one facet of the problem.

There are many measurements that require that a set of linear equations be solved. If this question of stability is an issue, considerable gains can often be realized if the problem has sufficient flexibility. Techniques that might seem hopeless can be salvaged and the accuracy of proven measurements can be made better.

Chapter 3

MEASURING THE RMS PULSE LENGTH WITH FAST DEFLECTING CAVITY AND BEAM POSITION MONITOR

3.1 Introduction

In this chapter a technique is describe for measuring the rms length of the SPA electron beam bunches using an rf cavity and a BPM. Figure 3-1 demonstrates the principle behind the measurement. The fast deflecting cavity is designed to operate in a TM_{110} mode. In this mode the electric and magnetic fields are dominated by a time varying, magnetic dipole field. When an electron beam bunch passes through the cavity and the phase of the cavity fields is set properly, the front and tail of the bunch are deflected in opposite directions while the trajectory of the bunch center remains unchanged. This "streaking" effect causes the beam width to increase as the bunch drifts away from the cavity. The rate of the width increase is dependent upon the longitudinal length of the beam pulse. If the cavity fields are orientated properly, this increase will occur in mainly one plane, x or y. Measuring the position of the beam center and its quadrupole moment, $\langle x^2 \rangle_{\text{BPM}} - \langle y^2 \rangle_{\text{BPM}}$, with the BPM when the deflecting cavity is on and when it is off determines the rms length of the beam bunch.

The rms length of the beam bunch is defined as the ensemble average $\langle z^2 \rangle$. It will prove convenient to replace the longitudinal coordinate, z, with a phase angle, ϕ_z . This

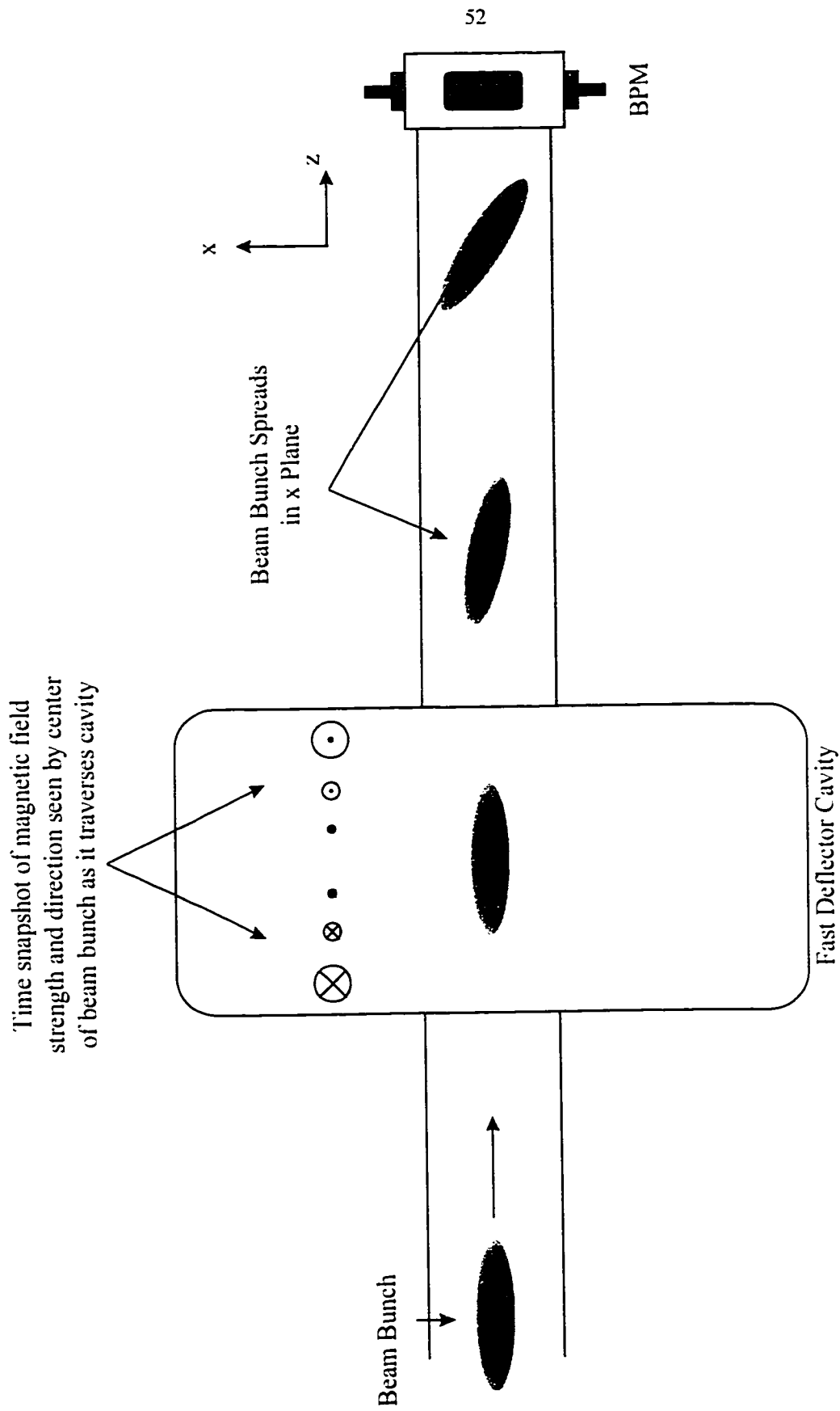


Figure 3-1: Illustration of fast deflector cavity streaking a beam bunch.

phase angle is referenced to the wavelength of the rf frequency of the fast deflecting cavity. The rms length can then be written as

$$\langle \phi_z^2 \rangle = \left(\frac{2\pi}{\lambda_{rf}} \right)^2 \langle z^2 \rangle = \left(\frac{2\pi f}{c} \right)^2 \langle z^2 \rangle. \quad (3-1)$$

The frequency of the cavity is f and the speed of light is c .

3.2 Trajectory change of a single electron at fast deflector exit

To start off the discussion, this section presents the change in trajectory of a single, relativistic electron as it travels through the fields of the fast deflector cavity. This calculation is to first order.

The results of this section are essentially a summary of a more complete derivation presented in Appendix E. It begins by demonstrating that the dominant field in the cavity is a time varying magnetic dipole field. Then, using only this field, the simple equation of motion is solved in the appropriate coordinates.

3.2.1 Field components

The fast deflector is a cylindrical cavity that operates in a TM_{110} mode. A schematic is shown in Figure 3-2. The ideal electric and magnetic fields are

$$E_z = E_0 J_1(k_{11}r) \cos\theta \cos(\omega t + \phi),$$

$$B_r = \omega \frac{a^2}{x_{11}^2 r c^2} E_0 J_1(k_{11}r) \sin\theta \sin(\omega t + \phi)$$

and

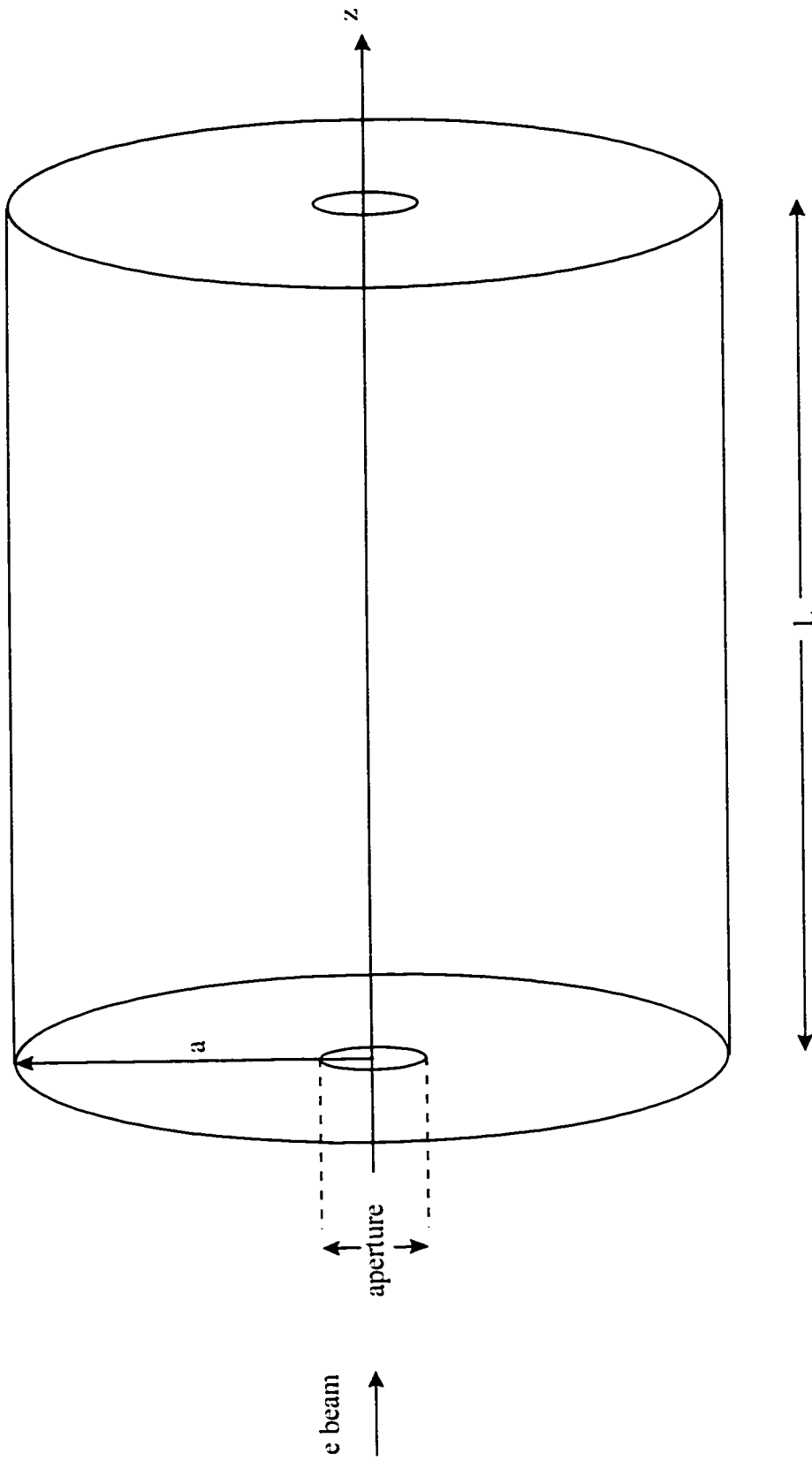


Figure 3-2: Schematic of fast deflector cavity.

$$B_{\theta} = \omega \frac{a}{x_{11}c^2} E_0 J_1'(k_{11}r) \cos\theta \sin(\omega t + \phi).$$

All other field components are zero. The constant k_{11} is defined as

$$k_{11} \equiv \frac{x_{11}}{a}$$

where x_{11} , equal to 3.8317, is the first zero of the first Bessel function and a is the radius of the cavity. The angular frequency, ω , is given by

$$\omega = 2\pi f$$

where the frequency, f , is 1300 MHz for our cavity. The relationship between the angular frequency and the geometrical properties of the cavity is

$$\omega = k_{11}c.$$

Therefore, the cavity radius is

$$a = \frac{x_{11}c}{\omega} = \frac{x_{11}c}{2\pi f} = 0.14 \text{ m}.$$

The length of the cavity, L , is independent of frequency and on SPA measures 14.48 cm. The maximum amplitude of the electric field, E_0 , is 24 MV/m, from measurement. The kinetic energy of the electrons as they enter the cavity will be approximately 8 MeV. The aperture of the cavity, the opening that the beam travels through, is one inch in diameter, or 1.27 cm in radius.

3.2.2 Conversion of field components to Cartesian coordinates

Using the relationships

$$\hat{r} = \hat{x} \cos\theta + \hat{y} \sin\theta$$

and

$$\hat{\theta} = -\hat{x} \sin \theta + \hat{y} \cos \theta .$$

the electric and magnetic fields can be converted to Cartesian coordinates, giving

$$E_z = E_0 J_1(k_{11} r) \cos \theta \cos(\omega t + \phi) .$$

$$B_x = \frac{a\omega}{x_{11}c^2} J_2(k_{11} r) E_0 \sin 2\theta \sin(\omega t + \phi)$$

and

$$B_y = \frac{\omega a}{x_{11}c^2} E_0 \left(\frac{a}{x_{11}r} J_1(k_{11} r) - J_2(k_{11} r) \cos^2 \theta \right) \sin(\omega t + \phi) .$$

Since the beam is limited to the transverse region defined by the aperture of the fast deflector cavity, these expressions are well approximated by

$$E_z \cong E_0 \frac{k_{11}}{2} x \cos(\omega t + \phi) .$$

$$B_x \cong \frac{\omega x_{11}}{4ac^2} E_0 xy \sin(\omega t + \phi)$$

and

$$B_y \cong \frac{\omega a}{2x_{11}c^2} E_0 \sin(\omega t + \phi) . \quad (\text{See Appendix E}) \quad (3-2)$$

3.2.3 Equations of motion

Of the three field components, B_y is dominant. In the aperture region, the magnitude of the ratio of B_x to B_y is

$$\left| \frac{B_x}{B_y} \right| \leq \frac{\frac{\omega x_{11}}{8ac^2} E_0 x_{\max} y_{\max}}{\frac{\omega a}{2x_{11}c^2} E_0} = \frac{x_{11}^2 r_{\max}^2}{2a^2} = \frac{(3.8317)^2 (1.27\text{cm})^2}{4(14.0\text{cm})^2} = 0.03.$$

showing that B_x can be ignored to first order. The electric field along the axis can be shown to produce a relative change in an electron's energy of less than four percent for an 8 MeV beam. (See Appendix E) In most cases it will be much smaller than this, allowing the electric field to be ignored as well.

To first order, then, the only equation of motion that is of consequence is

$$\gamma m \ddot{x} = e z \frac{\omega a}{2x_{11}c^2} E_0 \sin(\omega t + \phi).$$

Using the relationships

$$\frac{d}{dt} = \frac{dz}{dt} \frac{d}{dz} = \dot{z} \frac{d}{dz} = \beta c \frac{d}{dz}$$

and

$$t = \frac{z}{\beta c}, \quad (3-3)$$

where z equal to zero is defined as the entrance to the fast deflector cavity, gives

$$x'' = \frac{e}{\beta \gamma m c} \frac{\omega a}{2x_{11}c^2} E_0 \sin\left(\frac{\omega z}{\beta c} + \phi\right).$$

This equation can easily be integrated to give the divergence and position of the electron as it moves through the fast deflector cavity:

$$x'(z) = -\frac{e}{\gamma m} \frac{a}{2x_{11}c^2} E_0 \cos\left(\frac{\omega z}{\beta c} + \phi\right) + c_1 \quad (3-4)$$

and

$$x(z) = -\frac{e}{\gamma m} \frac{a}{2x_{11}c^2} E_0 \frac{\beta c}{\omega} \sin\left(\frac{\omega z}{\beta c} + \phi\right) + c_1 z + c_2. \quad (3-5)$$

where

$$c_1 = x'_i + \frac{e}{\gamma m} \frac{a}{2x_{11}c^2} E_0 \cos\phi \quad (3-6)$$

and

$$c_2 = x_i + \frac{e}{\gamma m} \frac{a}{2x_{11}c^2} E_0 \frac{\beta c}{\omega} \sin\phi. \quad (3-7)$$

The values of x and x' at the entrance to the fast deflector are x_i and x'_i , respectively.

The change in the electron's trajectory caused by the action of the fast deflector cavity can be found by setting z equal to L , the length of the cavity, in (3-4) and (3-5), resulting in

$$x_L = x(L) = -\frac{e}{\gamma m} \frac{a}{2x_{11}c^2} E_0 \frac{\beta c}{\omega} \sin\left(\frac{\omega L}{\beta c} + \phi\right) + c_1 L + c_2 \quad (3-8)$$

and

$$x'_L = x'(L) = -\frac{e}{\gamma m} \frac{a}{2x_{11}c^2} E_0 \cos\left(\frac{\omega L}{\beta c} + \phi\right) + c_1. \quad (3-9)$$

It will prove useful to rewrite the phase angle, ϕ , as

$$\phi = \phi_0 + \Delta\phi + \phi_z.$$

The angle $\phi_0 + \Delta\phi$ is defined as the phase of the beam bunch center with respect to the cavity fields. The angle $\Delta\phi$ is included for calibration purposes. Its magnitude is defined to be much less than one. The angle ϕ_z is defined as the phase of a particular electron in the bunch with respect to $\phi_0 + \Delta\phi$.

As mentioned in Chapter 1, the beam bunches on SPA are 6 mm FWHM in length or

less. This is a time duration of 20 ps. At the frequency 1300MHz. then. the magnitude of ϕ_z will be

$$|\phi_z| \leq (10 \text{ ps})(2\pi f) = 0.082 .$$

Therefore.

$$|\Delta\phi + \phi_z| \ll 1 .$$

Substituting (3-6) and (3-7) into (3-8) and (3-9). this condition makes the following approximation possible:

$$\begin{aligned} x_L \cong x_i + Lx'_i + \frac{e}{\gamma m} \frac{a}{2x_{i1}c^2} E_0 \frac{\beta c}{\omega} \left\{ \sin \phi_0 + \frac{\omega L}{\beta c} \cos \phi_0 - \sin \left(\frac{\omega L}{\beta c} + \phi_0 \right) \right. \\ \left. + (\Delta\phi + \phi_z) \left[\cos \phi_0 - \frac{\omega L}{\beta c} \sin \phi_0 - \cos \left(\frac{\omega L}{\beta c} + \phi_0 \right) \right] \right\} . \end{aligned} \quad (3-10)$$

and

$$\begin{aligned} x'_L \cong x'_i + \frac{e}{\gamma m} \frac{a}{2x_{i1}c^2} E_0 \left\{ \cos \phi_0 - \cos \left(\frac{\omega L}{\beta c} + \phi_0 \right) \right. \\ \left. + (\Delta\phi + \phi_z) \left[\sin \left(\frac{\omega L}{\beta c} + \phi_0 \right) - \sin \phi_0 \right] \right\} . \text{ (See Appendix E)} \end{aligned} \quad (3-11)$$

3.3 Measuring the rms length of the electron beam bunches

After exiting the fast deflector. the electron beam will travel down a section of beam pipe to the location of the BPM. It will be assumed that this region is a linear focusing channel so that a linear transfer matrix can be assigned.

$$\bar{\bar{\mathbf{R}}} = \begin{bmatrix} R_{11} & R_{12} & 0 & 0 \\ R_{21} & R_{22} & 0 & 0 \\ 0 & 0 & R_{33} & R_{34} \\ 0 & 0 & R_{43} & R_{44} \end{bmatrix}.$$

Using $\bar{\bar{\mathbf{R}}}$, and equations (3-10) and (3-11), it can be shown that the rms length of the electron beam bunches can be determined by measuring the values of \bar{x} and \bar{y} , according to (1-14) and (1-15), and $\langle x^2 \rangle_{\text{BPM}} - \langle y^2 \rangle_{\text{BPM}}$, according to equation (1-16), with the BPM in Figure 3-1 when the fast deflector is on and when it is off.

3.3.1 Fast deflector off

When the fast deflector cavity is turned off, it is nothing more than a section of drift. Therefore, the total transfer matrix between the entrance to the cavity and the location of the BPM is

$$\bar{\bar{\mathbf{R}}}_T = \begin{bmatrix} R_{11} & R_{12} & 0 & 0 \\ R_{21} & R_{22} & 0 & 0 \\ 0 & 0 & R_{33} & R_{34} \\ 0 & 0 & R_{43} & R_{44} \end{bmatrix} \begin{bmatrix} 1 & L & 0 & 0 \\ 0 & 1 & 0 & 0 \\ 0 & 0 & 1 & L \\ 0 & 0 & 0 & 1 \end{bmatrix}$$

$$\bar{\bar{\mathbf{R}}}_T = \begin{bmatrix} R_{11} & R_{12} + LR_{11} & 0 & 0 \\ R_{21} & R_{22} + LR_{21} & 0 & 0 \\ 0 & 0 & R_{33} & R_{34} + LR_{33} \\ 0 & 0 & R_{43} & R_{44} + LR_{43} \end{bmatrix}.$$

Therefore, the final parameters of a single electron at the location of the BPM will be

$$\begin{pmatrix} x_f \\ x'_f \\ y_f \\ y'_f \end{pmatrix}_{\text{case 1}} = \begin{bmatrix} R_{11} & R_{12} + LR_{11} & 0 & 0 \\ R_{21} & R_{22} + LR_{21} & 0 & 0 \\ 0 & 0 & R_{33} & R_{34} + LR_{33} \\ 0 & 0 & R_{43} & R_{44} + LR_{34} \end{bmatrix} \begin{pmatrix} x_i \\ x'_i \\ y_i \\ y'_i \end{pmatrix}.$$

Doing the matrix multiplication yields

$$(x_f)_{\text{FD Off}} = R_{11}x_i + (R_{12} + LR_{11})x'_i \quad (3-12)$$

and

$$(y_f)_{\text{FD Off}} = R_{33}y_i + (R_{34} + LR_{33})y'_i. \quad (3-13)$$

The BPM in Figure 3-1 will be used to measure \bar{x} , \bar{y} and $\langle x^2 \rangle_{\text{BPM}} - \langle y^2 \rangle_{\text{BPM}}$ at the BPM location. That is,

$$(\bar{x}_f)_{\text{FD Off}} = \langle (x_f)_{\text{FD Off}} \rangle_{\text{BPM}} \quad (3-14)$$

$$(\bar{y}_f)_{\text{FD Off}} = \langle (y_f)_{\text{FD Off}} \rangle_{\text{BPM}} \quad (3-15)$$

and

$$\begin{aligned} \langle (x_f^2)_{\text{FD Off}} \rangle_{\text{BPM}} - \langle (y_f^2)_{\text{FD Off}} \rangle_{\text{BPM}} &= \langle (x_f^2)_{\text{FD Off}} \rangle - \langle (y_f^2)_{\text{FD Off}} \rangle \\ &\quad + (\bar{x}_f)_{\text{FD Off}}^2 - (\bar{y}_f)_{\text{FD Off}}^2. \end{aligned} \quad (3-16)$$

3.3.2 Fast deflector on

When the fast deflector cavity is on, the values of \bar{x} , \bar{y} and $\langle x^2 \rangle_{\text{BPM}} - \langle y^2 \rangle_{\text{BPM}}$ will change. To calculate that change, start by noticing that, according to the approximate equations of motion, the cavity fields will have no effect in the y plane of motion. The fast deflector is still a drift of length L . Therefore, the results for the y center of the beam

are identical to those for the first case.

$$(y_f)_{\text{FD On}} = R_{33}y_i + (R_{33} + LR_{34})y'_i$$

or

$$(y_f)_{\text{FD On}} = (y_f)_{\text{FD Off}}. \quad (3-17)$$

Therefore, the BPM will measure

$$(\bar{y}_f)_{\text{FD On}} = (\bar{y}_f)_{\text{FD Off}}. \quad (3-18)$$

In the x plane, we must use equations (3-10) and (3-11). The values of x and x' at the location of the BPM are given by

$$\begin{pmatrix} x_f \\ x'_f \end{pmatrix} = \begin{bmatrix} R_{11} & R_{12} \\ R_{21} & R_{22} \end{bmatrix} \begin{pmatrix} x_L \\ x'_L \end{pmatrix}.$$

Doing the matrix multiplication yields

$$\begin{aligned} (x_f)_{\text{FD On}} = & R_{11}x_i + (R_{12} + LR_{11})x'_i + \frac{e}{\gamma m} \frac{a}{2x_{11}c^2} E_0 \left\{ R_{11} \frac{\beta c}{\omega} \left[\sin \phi_0 + \frac{\omega L}{\beta c} \cos \phi_0 \right. \right. \\ & \left. \left. - \sin \left(\frac{\omega L}{\beta c} + \phi_0 \right) \right] + R_{12} \left[\cos \phi_0 - \cos \left(\frac{\omega L}{\beta c} + \phi_0 \right) \right] + (\Delta \phi + \phi_z) \left\{ R_{11} \frac{\beta c}{\omega} \left[\cos \phi_0 \right. \right. \right. \\ & \left. \left. - \frac{\omega L}{\beta c} \sin \phi_0 - \cos \left(\frac{\omega L}{\beta c} + \phi_0 \right) \right] + R_{12} \left[\sin \left(\frac{\omega L}{\beta c} + \phi_0 \right) - \sin \phi_0 \right] \right\} \right\}. \quad (3-19) \end{aligned}$$

Making the definitions

$$\begin{aligned}
a_1 \equiv \frac{e}{\gamma m} \frac{a}{2x_{11}c^2} E_0 \left\{ R_{11} \frac{\beta c}{\omega} \left[\cos\phi_0 - \frac{\omega L}{\beta c} \sin\phi_0 - \cos\left(\frac{\omega L}{\beta c} + \phi_0\right) \right] \right. \\
\left. + R_{12} \left[\sin\left(\frac{\omega L}{\beta c} + \phi_0\right) - \sin\phi_0 \right] \right\} \quad (3-20)
\end{aligned}$$

and

$$\begin{aligned}
a_2 \equiv \frac{e}{\gamma m} \frac{a}{2x_{11}c^2} E_0 \left\{ R_{11} \frac{\beta c}{\omega} \left[\sin\phi_0 + \frac{\omega L}{\beta c} \cos\phi_0 - \sin\left(\frac{\omega L}{\beta c} + \phi_0\right) \right] \right. \\
\left. + R_{12} \left[\cos\phi_0 - \cos\left(\frac{\omega L}{\beta c} + \phi_0\right) \right] \right\}. \quad (3-21)
\end{aligned}$$

simplifies (3-19) to

$$(x_f)_{\text{FD On}} = R_{11}x_i + (R_{12} + LR_{11})x'_i + a_1(\Delta\phi + \phi_z) + a_2.$$

Using equation (3-12) this becomes

$$(x_f)_{\text{FD On}} = (x_f)_{\text{FD Off}} + a_1(\Delta\phi + \phi_z) + a_2. \quad (3-22)$$

Therefore, the BPM will measure

$$\langle \bar{x}_f \rangle_{\text{FD On}} = \langle (x_f)_{\text{FD On}} \rangle_{\text{BPM}} = \langle (x_f)_{\text{FD Off}} \rangle_{\text{BPM}} + \langle a_1 \Delta\phi \rangle_{\text{BPM}} + \langle a_1 \phi_z \rangle_{\text{BPM}} + \langle a_2 \rangle_{\text{BPM}}.$$

Since ϕ_z is proportional to z ,

$$\langle \phi_z \rangle_{\text{BPM}} = 0.$$

Therefore,

$$\langle \bar{x}_f \rangle_{\text{FD On}} = \langle \bar{x}_f \rangle_{\text{FD Off}} + a_1 \Delta\phi + a_2. \quad (3-23)$$

To find $\langle x^2 \rangle_{\text{BPM}} - \langle y^2 \rangle_{\text{BPM}}$ at the BPM location with the fast deflector on, first square

(3-17) and (3-22) then subtract the results to obtain

$$\begin{aligned} (x_f^2)_{\text{FD On}} - (y_f^2)_{\text{FD On}} &= (x_f^2)_{\text{FD Off}} + 2\left[(x_f)_{\text{FD Off}}\right]a_1(\Delta\phi + \phi_z) + 2\left[(x_f)_{\text{FD Off}}\right]a_2 \\ &\quad + a_1^2(\Delta\phi^2 + 2\Delta\phi\phi_z + \phi_z^2) + 2a_1(\Delta\phi + \phi_z)a_2 + a_2^2 - (y_f^2)_{\text{FD Off}}. \end{aligned}$$

Taking the BPM average of this expression yields

$$\begin{aligned} \langle (x_f^2)_{\text{FD On}} \rangle_{\text{BPM}} - \langle (y_f^2)_{\text{FD On}} \rangle_{\text{BPM}} &= \langle (x_f^2)_{\text{FD Off}} \rangle_{\text{BPM}} - \langle (y_f^2)_{\text{FD Off}} \rangle_{\text{BPM}} \\ &\quad + 2a_1\Delta\phi\langle (x_f)_{\text{FD Off}} \rangle_{\text{BPM}} + 2a_1\langle (x_f)_{\text{FD Off}} \phi_z \rangle_{\text{BPM}} + 2a_2\langle (x_f)_{\text{FD Off}} \rangle_{\text{BPM}} \\ &\quad + a_1^2\Delta\phi^2 + 2a_1^2\Delta\phi\langle \phi_z \rangle_{\text{BPM}} + a_1^2\langle \phi_z^2 \rangle_{\text{BPM}} + 2a_1a_2\Delta\phi + 2a_1a_2\langle \phi_z \rangle_{\text{BPM}} + a_2^2. \end{aligned}$$

Using (3-14), (3-15) and (3-16), and realizing that

$$\langle (x_f)_{\text{FD Off}} \phi_z \rangle = 0$$

gives

$$\begin{aligned} \langle (x_f^2)_{\text{FD On}} \rangle_{\text{BPM}} - \langle (y_f^2)_{\text{FD On}} \rangle_{\text{BPM}} &= \langle (x_f^2)_{\text{FD Off}} \rangle - \langle (y_f^2)_{\text{FD Off}} \rangle + (\bar{x}_f)_{\text{FD Off}}^2 - (\bar{y}_f)_{\text{FD Off}}^2 \\ &\quad + 2a_1\Delta\phi(\bar{x}_f)_{\text{FD Off}} + 2a_2(\bar{x}_f)_{\text{FD Off}} + a_1^2\Delta\phi^2 + a_1^2\langle \phi_z^2 \rangle_{\text{BPM}} + 2a_1a_2\Delta\phi + a_2^2. \\ \langle (x_f^2)_{\text{FD On}} \rangle_{\text{BPM}} - \langle (y_f^2)_{\text{FD On}} \rangle_{\text{BPM}} &= \langle (x_f^2)_{\text{FD Off}} \rangle - \langle (y_f^2)_{\text{FD Off}} \rangle \\ &\quad + \left[(\bar{x}_f)_{\text{FD Off}} + a_1\Delta\phi + a_2 \right]^2 - (\bar{y}_f)_{\text{FD Off}}^2 + a_1^2\langle \phi_z^2 \rangle_{\text{BPM}}. \end{aligned}$$

Using (3-18) and (3-23), this becomes

$$\begin{aligned} \langle (x_f^2)_{\text{FD On}} \rangle_{\text{BPM}} - \langle (y_f^2)_{\text{FD On}} \rangle_{\text{BPM}} &= \langle (x_f^2)_{\text{FD Off}} \rangle - \langle (y_f^2)_{\text{FD Off}} \rangle \\ &\quad + (\bar{x}_f)_{\text{FD On}}^2 - (\bar{y}_f)_{\text{FD On}}^2 + a_1^2\langle \phi_z^2 \rangle_{\text{BPM}}. \end{aligned}$$

Now, because ϕ_z is a longitudinal coordinate and because the longitudinal origin defined in the ensemble average, equation (1-1), is the same as that defined in the BPM average.

equation (1-2) . we have

$$\langle \phi_z^2 \rangle_{\text{BPM}} = \langle \phi_z^2 \rangle .$$

Therefore

$$\begin{aligned} \langle (x_f^2)_{\text{FD On}} \rangle_{\text{BPM}} - \langle (y_f^2)_{\text{FD On}} \rangle_{\text{BPM}} &= \langle (x_f^2)_{\text{FD Off}} \rangle - \langle (y_f^2)_{\text{FD Off}} \rangle \\ &+ (\bar{x}_f)_{\text{FD On}}^2 - (\bar{y}_f)_{\text{FD On}}^2 + a_1^2 \langle \phi_z^2 \rangle . \end{aligned} \quad (3-24)$$

3.3.3 Measuring bunch length

Using the six measured quantities given in (3-14). (3-15). (3-16). (3-18). (3-23) and (3-24). we can define the following quantities:

$$M_{\text{FD Off}} \equiv \langle (x_f^2)_{\text{FD Off}} \rangle_{\text{BPM}} - \langle (y_f^2)_{\text{FD Off}} \rangle_{\text{BPM}} - (\bar{x}_f)_{\text{FD Off}}^2 + (\bar{y}_f)_{\text{FD Off}}^2 \quad (3-25)$$

and

$$M_{\text{FD On}} \equiv \langle (x_f^2)_{\text{FD On}} \rangle_{\text{BPM}} - \langle (y_f^2)_{\text{FD On}} \rangle_{\text{BPM}} - (\bar{x}_f)_{\text{FD On}}^2 + (\bar{y}_f)_{\text{FD On}}^2 . \quad (3-26)$$

Subtracting these two expressions yields

$$M_{\text{FD On}} - M_{\text{FD Off}} = a_1^2 \langle \phi_z^2 \rangle .$$

Therefore

$$\langle \phi_z^2 \rangle = \frac{M_{\text{FD On}} - M_{\text{FD Off}}}{a_1^2} . \quad (3-27)$$

Recall that, from (3-1). $\langle \phi_z^2 \rangle$ is equivalent to the rms length of the electron beam bunches.

3.4 Calibration of measurement

To calibrate this measurement, the value of a_1 , defined in (3-20), must be determined. This is done easily by measuring the position of the beam in the BPM aperture while shifting the phase of the fast deflector cavity.

When measuring the bunch length, the phase of the cavity fields is set so that the center of the beam is very near the center of the BPM. By shifting this phase slightly, the value of $\Delta\phi$ is changed, steering the x coordinate of the beam according to (3-23):

$$\left(\bar{x}_f\right)_{\text{FD On}} = \left(\bar{x}_f\right)_{\text{FD Off}} + a_1\Delta\phi + a_2.$$

By making measurements of \bar{x} for two values of $\Delta\phi$ we get

$$\bar{x}_1 = \left(\bar{x}_f\right)_{\text{FD Off}} + a_1\Delta\phi_1 + a_2 \quad (3-28)$$

and

$$\bar{x}_2 = \left(\bar{x}_f\right)_{\text{FD Off}} + a_1\Delta\phi_2 + a_2. \quad (3-29)$$

Therefore, by measuring \bar{x}_1 , \bar{x}_2 and $\Delta\phi_1 - \Delta\phi_2$, we have

$$a_1 = \frac{\bar{x}_1 - \bar{x}_2}{\Delta\phi_1 - \Delta\phi_2}. \quad (3-30)$$

3.5 Estimate of measurement resolution

The resolution of this measurement depends upon several factors: how much power can be put into the fast deflector cavity before it breaks down, the accuracy of the BPM and the nature of the transfer matrix between the fast deflector and the location of the BPM. However, by making some reasonable assumptions, it is possible to obtain an estimate of the technique's resolution.

Assume that the region between the fast deflector cavity and the BPM is nothing more than a drift. Therefore,

$$R_{11} = 1$$

and

$$R_{12} = d$$

where d is the length of the drift. From (3-20), then,

$$a_1 = \frac{e}{\gamma m} \frac{a}{2x_{11}c^2} E_0 \left\{ \frac{\beta c}{\omega} \left[\cos \phi_0 - \frac{\omega L}{\beta c} \sin \phi_0 - \cos \left(\frac{\omega L}{\beta c} + \phi_0 \right) \right] \right. \\ \left. + d \left[\sin \left(\frac{\omega L}{\beta c} + \phi_0 \right) - \sin \phi_0 \right] \right\} \quad (3-31)$$

When measuring the beam bunch length, the phase of the fast deflector cavity fields is set so that the beam is nearly centered in the BPM aperture. This condition is satisfied when the y magnetic field given by (3-2) is zero when the center of the beam bunch arrives at the center of the cavity. Using (3-3), (3-2) can be rewritten as

$$B_y = \frac{\omega a}{2x_{11}c^2} E_0 \sin \left(\frac{\omega z}{\beta c} + \phi_0 \right)$$

where $\Delta\phi$ and ϕ_z have been set to zero. At the center of the cavity,

$$z = \frac{L}{2}.$$

Therefore, B_y is zero when

$$\phi_0 = -\frac{\omega L}{2\beta c}.$$

Substituting this into (3-31) gives

$$\begin{aligned}
a_1 &= \frac{e}{\gamma m} \frac{a}{2x_{11}c^2} E_0 \left\{ \frac{\beta c}{\omega} \left[\cos\left(-\frac{\omega L}{2\beta c}\right) - \frac{\omega L}{\beta c} \sin\left(-\frac{\omega L}{2\beta c}\right) - \cos\left(\frac{\omega L}{\beta c} - \frac{\omega L}{2\beta c}\right) \right] \right. \\
&\quad \left. + d \left[\sin\left(\frac{\omega L}{\beta c} - \frac{\omega L}{2\beta c}\right) - \sin\left(-\frac{\omega L}{2\beta c}\right) \right] \right\} \\
&= \frac{e}{\gamma m} \frac{a}{2x_{11}c^2} E_0 \left\{ \frac{\beta c}{\omega} \left[\cos\left(\frac{\omega L}{2\beta c}\right) + \frac{\omega L}{\beta c} \sin\left(\frac{\omega L}{2\beta c}\right) - \cos\left(\frac{\omega L}{2\beta c}\right) \right] \right. \\
&\quad \left. + d \left[\sin\left(\frac{\omega L}{2\beta c}\right) + \sin\left(\frac{\omega L}{2\beta c}\right) \right] \right\} \\
a_1 &= \frac{e}{\gamma m} \frac{a}{2x_{11}c^2} E_0 \sin\left(\frac{\omega L}{2\beta c}\right) \left(\frac{\beta c}{\omega} + 2d\right) \tag{3-32}
\end{aligned}$$

As mentioned at the start of this chapter, the maximum value of E_0 is 24 MV/m. A kinetic energy of 8 MeV yields

$$\gamma = 16.63.$$

Looking up the other constants and substituting them into (3-32) gives

$$a_1 = 0.051 \times (0.037 \text{ meters} + 2.0 \times d). \tag{3-33}$$

SPA is capable of compressing the electron beam bunches from 6 mm in length to less than 0.3 mm in length. These are FWHM measurements. Expressing these distances in time yields a compression from 20 ps to less than 1 ps.

The longitudinal distribution of the beam bunches is unknown. However, for the sake of this estimate, and for simplicity, we will assume that it is Gaussian. Therefore, the relationship between the FWHM and the rms length of the beam bunch is

$$\text{FWHM} = 2.35\sqrt{\langle z^2 \rangle}.$$

Using (3-1) this becomes

$$\langle \phi_z^2 \rangle = (1.22 \times 10^{-5}) \times [\text{FWHM (in picoseconds)}]^2 . \quad (3-34)$$

Table 3-1 shows the estimated value of $a_1^2 \langle \phi_z^2 \rangle$ using (3-33) and (3-34) for various beam pulse lengths versus the length of the drift after the fast deflector cavity. It is expected that the BPM will have an accuracy of $\pm 0.5 \text{ mm}^2$. Therefore, with a drift length of two meters, a one picosecond resolution is feasible.

3.6 Effect of BPM rotated with respect to fast deflector cavity

As a final note it should be mentioned that it is not always easy to align the BPM and fast deflector. Therefore, the BPM will often be rotated slightly with respect to the x and y axes defined by the cavity fields. As will be shown, as long as the angle of rotation is small, this is not a significant effect.

3.6.1 Pulse length measurement

If the BPM is rotated as shown in Figure 3-3, then a point in the BPM frame is related to a point in the fast deflector frame by

$$x_{\text{BPM Frame}} = x \cos \alpha + y \sin \alpha \quad (3-35)$$

and

$$y_{\text{BPM Frame}} = -x \sin \alpha + y \cos \alpha . \quad (3-36)$$

When the BPM is not rotated with respect to the fast deflector, it was previously shown in equation (3-27) that the rms pulse length squared is given by

Table 3-1: Value of $a_1^2 \langle \phi_z^2 \rangle$ vs. drift length, d , and the FWHM pulse length of the beam.

d (in meters)	FWHM of Beam Pulse (in picoseconds)			
	20	10	1	0.1
0.5	13.65 mm ²	3.41 mm ²	0.0341 mm ²	0.000341 mm ²
1.0	52.67 mm ²	13.17 mm ²	0.1317 mm ²	0.001317 mm ²
1.5	117.1 mm ²	29.28 mm ²	0.2928 mm ²	0.002928 mm ²
2.0	206.9 mm ²	51.73 mm ²	0.5173 mm ²	0.005173 mm ²

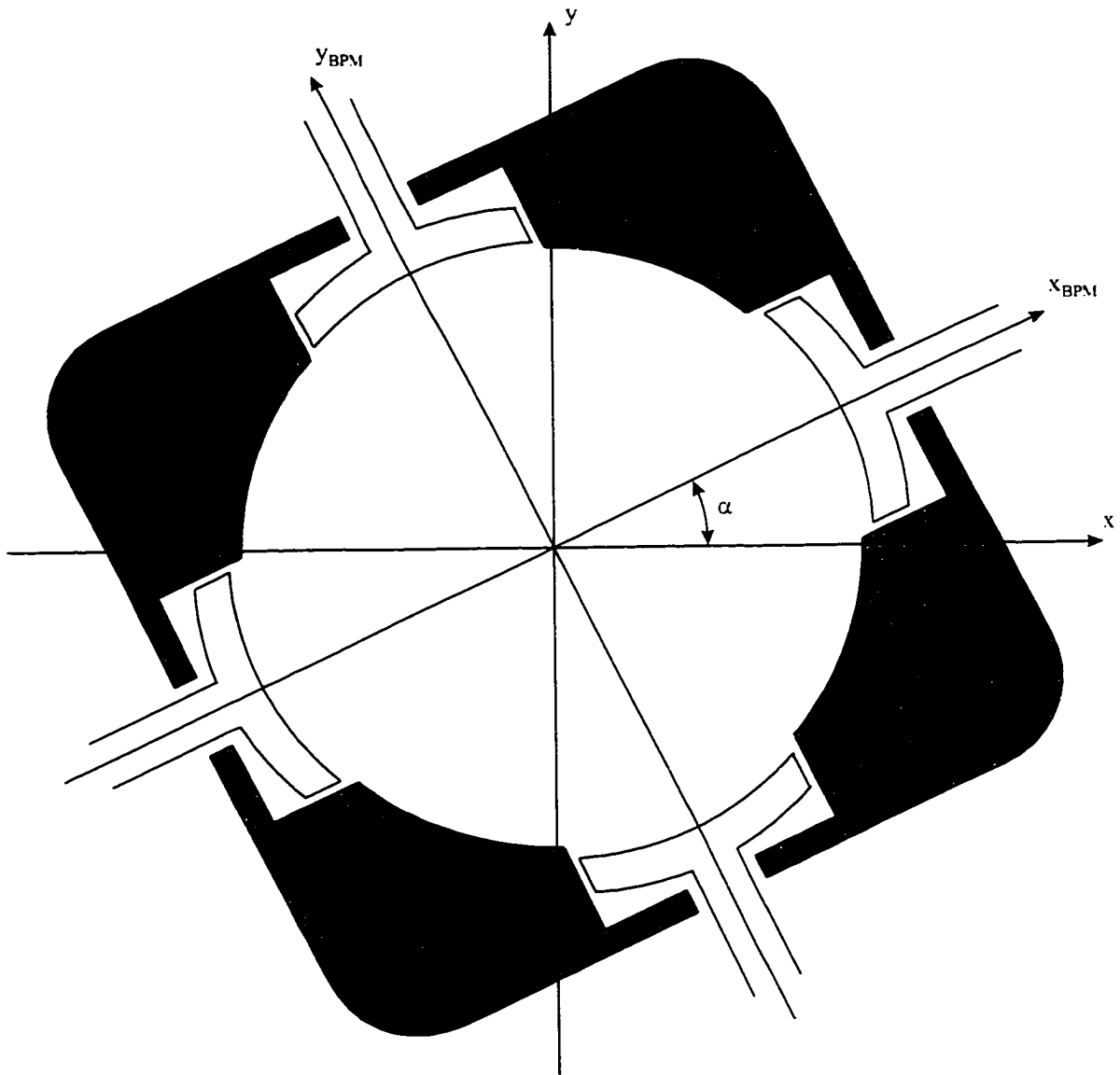


Figure 3-3: BPM rotated with respect to the x and y axes defined by the fast deflector fields.

$$\langle \phi_z^2 \rangle = \frac{M_{\text{FD On}} - M_{\text{FD Off}}}{a_1^2}$$

where $M_{\text{FD Off}}$ and $M_{\text{FD On}}$ are defined in (3-25) and (3-26) respectively. When the BPM is rotated, it is easily shown using (3-35) and (3-36) that this equation is modified to

$$\langle \phi_z^2 \rangle = \frac{M_{\text{FD On}} - M_{\text{FD Off}}}{a_1^2 (\cos^2 \alpha - \sin^2 \alpha)}.$$

The definitions of $M_{\text{FD Off}}$ and $M_{\text{FD On}}$ do not change. Therefore, small rotations will have no significant effect.

3.6.2 Calibration

The calibration with the rotated BPM proceeds just as before. However, instead of just measuring the x position of the beam when the phase of the cavity fields is shifted, as in (3-28) and (3-29), the y position must also be measured. Using (3-35) and (3-36), this results in the four measurements

$$\bar{x}_1 = (\bar{x}_r)_{\text{FD Off}} + (a_1 \Delta\phi_1 + a_2) \cos \alpha, \quad (3-37)$$

$$\bar{y}_1 = (\bar{y}_r)_{\text{FD Off}} + (a_1 \Delta\phi_1 + a_2) \sin \alpha, \quad (3-38)$$

$$\bar{x}_2 = (\bar{x}_r)_{\text{FD Off}} + (a_1 \Delta\phi_2 + a_2) \cos \alpha \quad (3-39)$$

and

$$\bar{y}_2 = (\bar{y}_r)_{\text{FD Off}} + (a_1 \Delta\phi_2 + a_2) \sin \alpha. \quad (3-40)$$

Keeping track of the phase shift $\Delta\phi_1 - \Delta\phi_2$, (3-37), (3-38), (3-39) and (3-40) yield

$$a_1 = \frac{\bar{x}_1 - \bar{x}_2}{(\Delta\phi_1 - \Delta\phi_2)\cos\alpha}$$

where

$$\alpha = \text{Arc tan}\left(\frac{\bar{x}_1 - \bar{x}_2}{\bar{y}_2 - \bar{y}_1}\right).$$

Chapter 4

CALIBRATING A BEAM POSITION MONITOR

4.1 Introduction

In general, a real BPM will have flaws in its construction. The electrodes will not be identical and the actual image charge distribution will be perturbed from its ideal. For these reasons, each BPM needs to be calibrated to understand its response and to demonstrate that we can measure the desired beam quantities with accuracy.

To calibrate a BPM, a thin wire is placed inside its aperture. A current signal on the wire simulates a relativistic, pencil beam[23]. Since the position of this wire can be controlled very accurately, the response of the BPM versus wire/beam position can be mapped. From this map, accurate calibrations of the BPM are established.

4.2 Simulating a relativistic beam

A schematic of the calibration apparatus is shown in Figure 4-1. A thin wire antenna is threaded down the axis of the BPM. Short sections of beam pipe are attached to either end of the BPM to maintain the proper boundary conditions. The wire is attached at one end to the center conductor of a coaxial cable and at the other is soldered to a ball bearing. The ball bearing is held in place by a magnet on the base of the apparatus, stretching the wire taut. The position of the wire in the x, y plane is determined by two

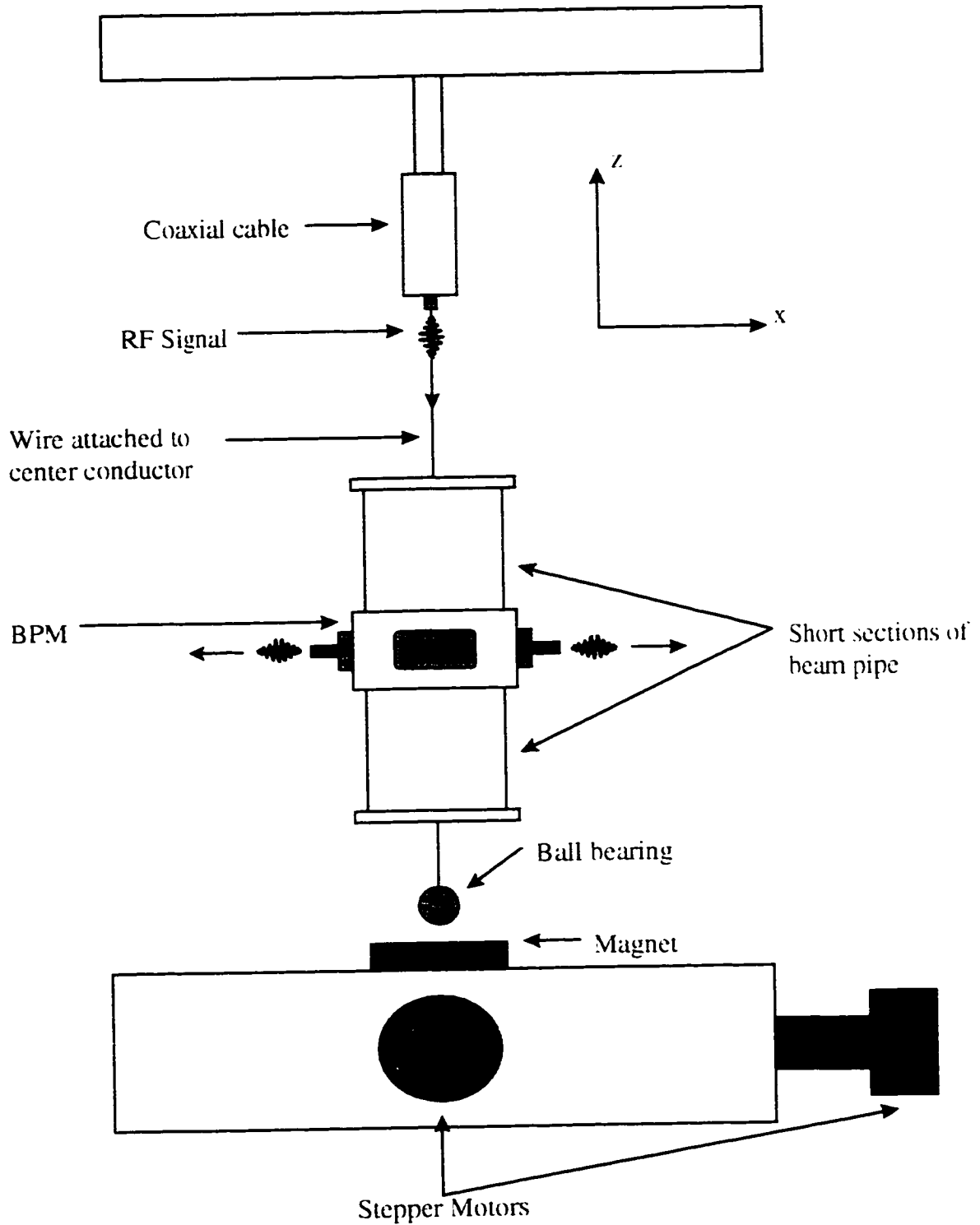


Figure 4-1: Schematic of pulsed wire apparatus for calibrating BPM.

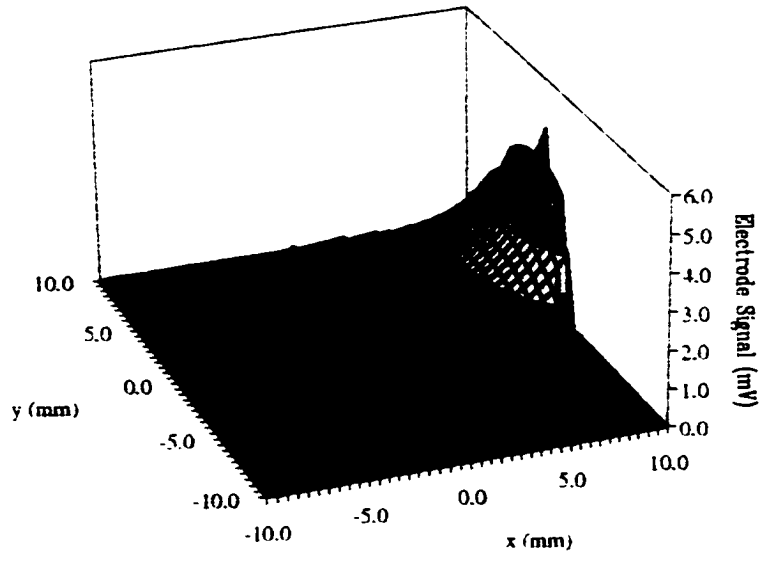
two stepper motors, one on each axis, controlled by a Macintosh™ computer running LabView® from National Instruments™. To simulate a highly relativistic beam, an rf sine wave signal is generated on the wire.

4.3 Mapping the BPM

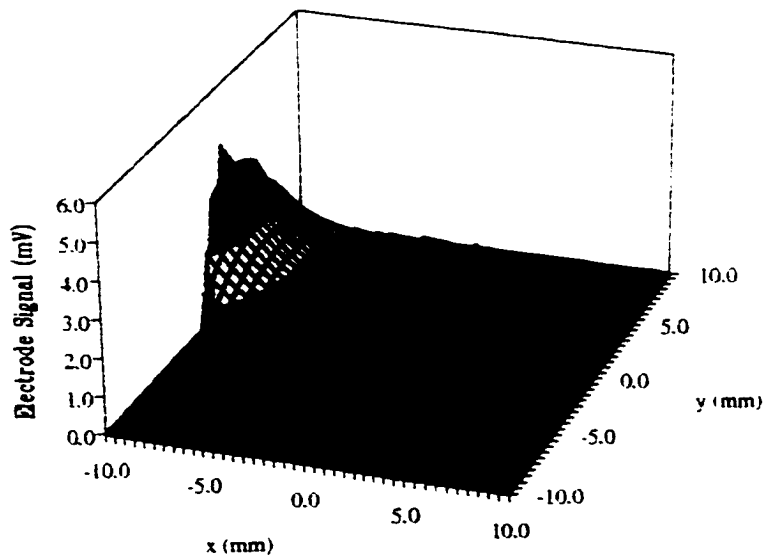
When mapping a BPM, the center of its aperture is found first. Moving the wire along the x axis in the plus and minus directions until it just makes electrical contact with the BPM wall locates the x center of the BPM. Likewise, the y center can be found. Once the wire is positioned in the aperture center, the stepping motors are zeroed and the response of each of the four electrodes is measured with the rf signal on versus wire position within the BPM aperture. Typical maps for the electrodes are shown in Figures 4-2 and 4-3. These show the amplitude of the signal induced in the BPM electrodes versus the position of the wire.

4.4 Fitting the map data

Once the map data has been taken, it can be used to find a calibration for the BPM. By fitting the proper equations to the map data, calibrations for measuring the position of the beam center and for measuring the quadrupole moment, $\langle x^2 \rangle_{\text{BPM}} - \langle y^2 \rangle_{\text{BPM}}$, are found.

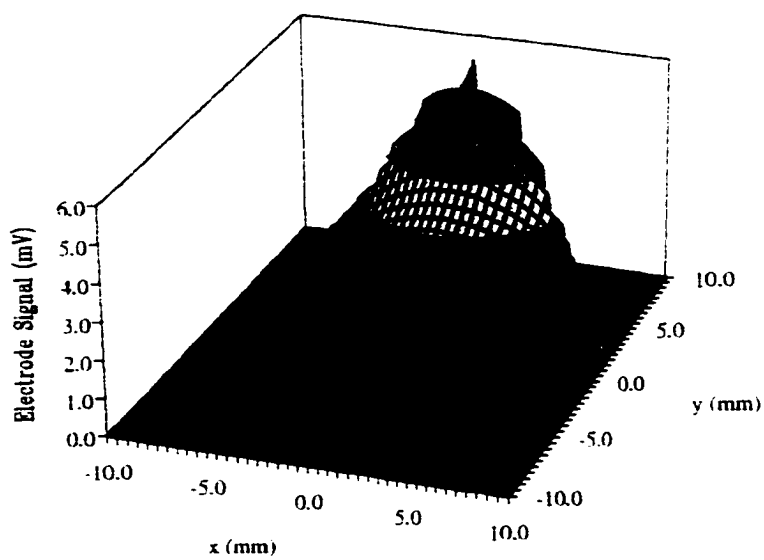


a) Right electrode

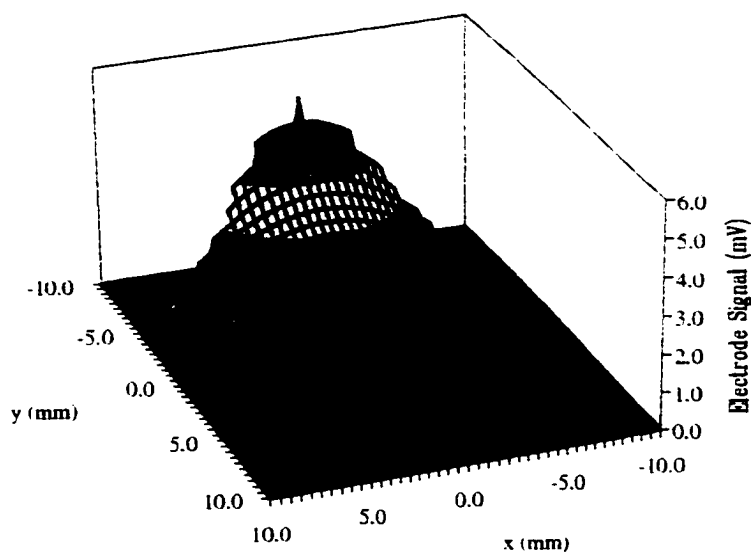


b) Left electrode

Figure 4-2: Maps of the a) right ($\theta = 0^\circ$) and b) left ($\theta = 180^\circ$) electrodes of a BPM.



a) Top electrode



b) Bottom electrode

Figure 4-3: Maps of the a) top ($\theta = 90^\circ$) and b) bottom ($\theta = 270^\circ$) electrodes of a BPM.

4.4.1 Centroid calibration

To calibrate the BPM to measure the beam center, the proper equation must be fit to the map data. Naïvely, one might use equations like (1-14) and (1-15). However, this is unwise. These equations assume an ideal BPM, but as was mentioned at the start of this chapter, a real BPM will be flawed. The four electrodes will have slightly different angular widths and each will have a slightly different capacitance, causing each to couple to the beam differently.

It is simple to derive equations similar to (1-14) and (1-15) that take into account the differences between the BPM electrodes. When this is done and the results are used to fit the BPM map data the results are quite good. However, even better results are obtained if the following equations are used:

$$x = x_0 + S_x R_x + S_x^3 R_x^3 + S_{xy} R_x R_y^2 \quad (4-1)$$

and

$$y = y_0 + S_y R_y + S_y^3 R_y^3 + S_{yx} R_y R_x^2 \quad (4-2)$$

where x_0 , S_x , S_x^3 , S_{xy} , y_0 , S_y , S_y^3 , and S_{yx} are all fitted constants. The values of R_x and R_y are defined as

$$R_x \equiv 20 \text{Log} \left(\frac{A_R}{A_L} \right) \quad (4-3)$$

and

$$R_y \equiv 20 \text{Log} \left(\frac{A_T}{A_B} \right). \quad (4-4)$$

This is a strange set of equations and it is not at all obvious why they should be

preferred. Their origin comes from the electronics used to process the BPM signals. In larger machines there are often several hundred BPMs being monitored at all times. In these situations it proves to be advantageous to do as much processing of the BPM signals with analog electronics as possible before they are sent to the control system. There are different schemes for accomplishing this task[24] and one of these naturally measures the quantities in (4-3) and (4-4)[25], [26]. The expressions in (4-1) and (4-2) were developed to take advantage of this fact and, as it turns out, give very good results for the beam position[24], [27].

Fitting (4-1) and (4-2) to the BPM map data results in the following values for the constants:

$$x_0 = 0.122 \text{ mm.}$$

$$S_x = 0.374 \text{ mm.}$$

$$S_{x'} = -0.000072 \text{ mm.}$$

$$S_{xy'} = 0.00023 \text{ mm.}$$

$$y_0 = -0.034 \text{ mm.}$$

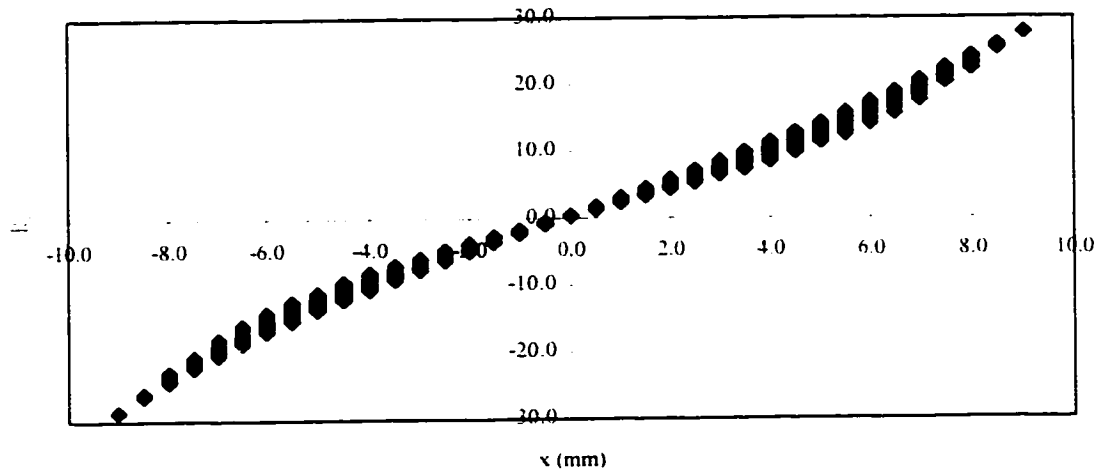
$$S_y = 0.373 \text{ mm.}$$

$$S_{y'} = -0.000070 \text{ mm}$$

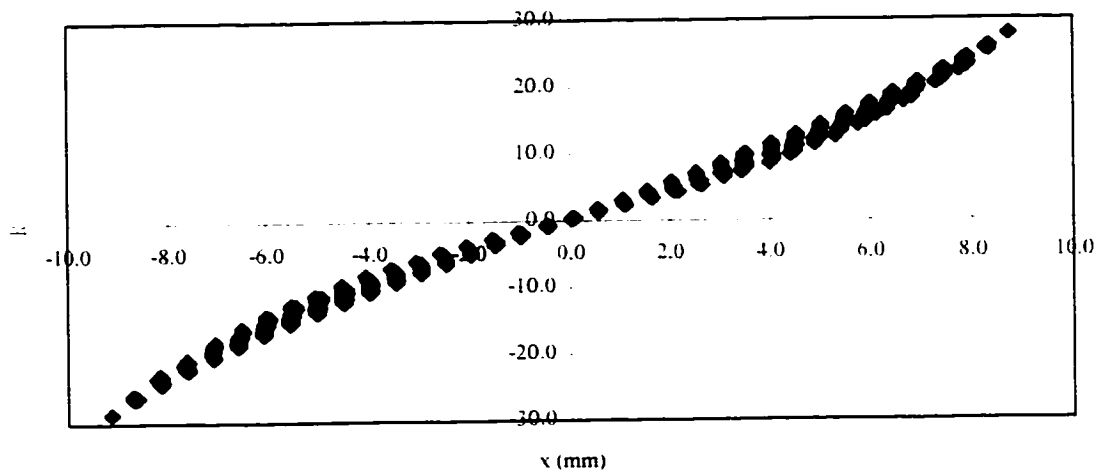
and

$$S_{yx'} = 0.00022 \text{ mm.}$$

Figures 4-4, 4-5 and 4-6 show how effective this fit is. Figure 4-4a shows a plot of R_x versus the x position of the wire. Figure 4-4b shows the same plot but with the x position

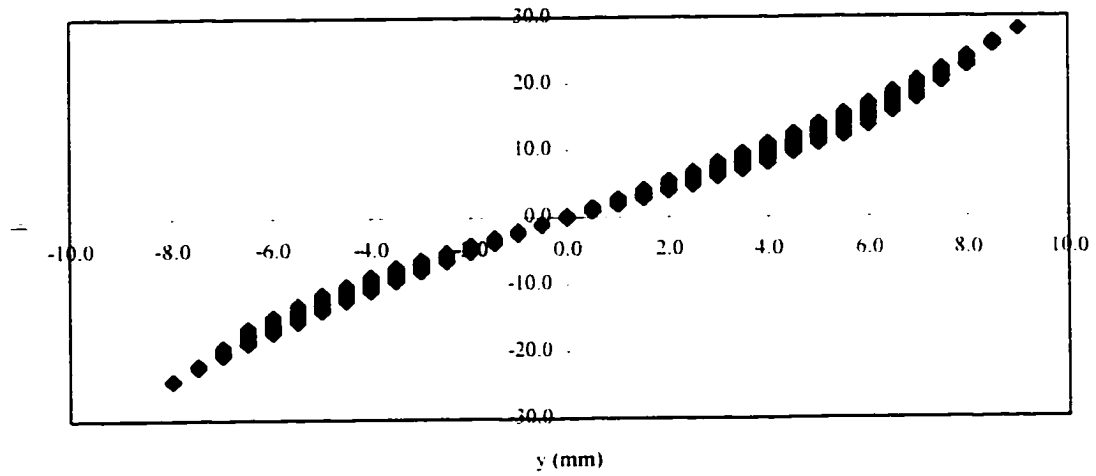
R_x vs. Actual x Position of Wire

a)

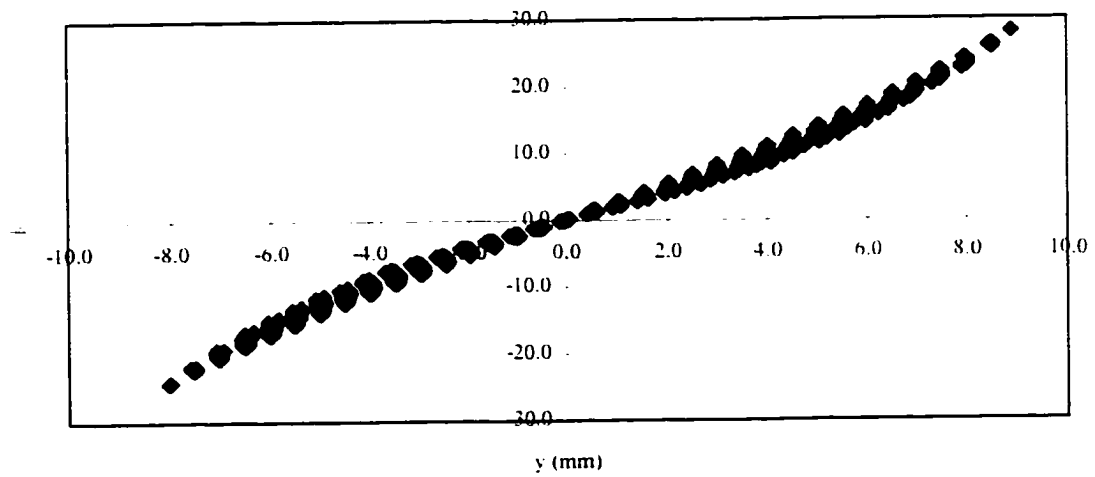
 R_x vs. x Position of Wire From Fit

b)

Figure 4-4: a) R_x versus actual x position of wire. b) R_x versus x position of wire as calculated by fitted equation.

R_y vs. Actual y Position of Wire

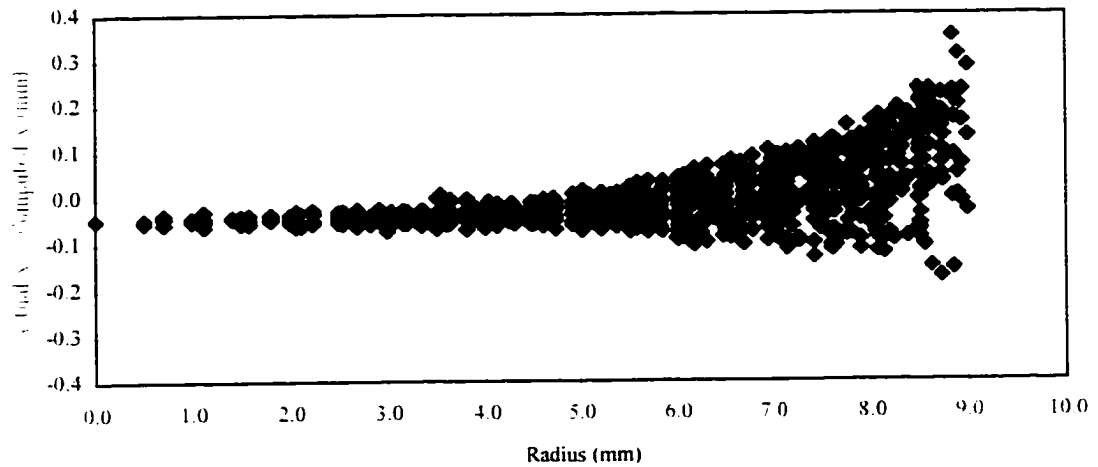
a)

 R_y vs. y Position of Wire From Fit

b)

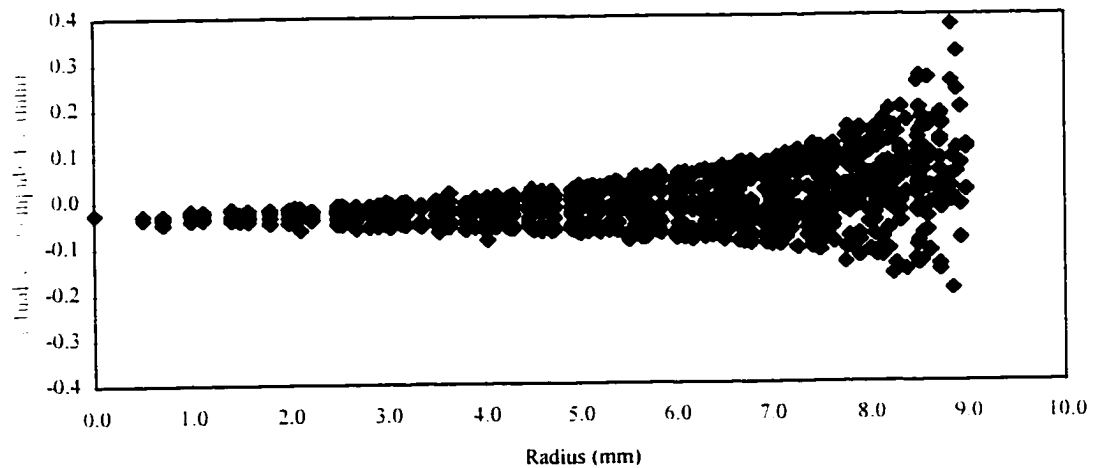
Figure 4-5: a) R_y versus actual y position of wire. b) R_y versus y position of wire as calculated by fitted equation.

Actual x Position – Computed x Position of Wire vs. Radial Position of Wire



a)

Actual y Position – Computed y Position of Wire vs. Radial Position of Wire



b)

Figure 4-6: a) Difference between actual x position of wire and that calculated from the fitted equation versus radial position of the wire. b) Difference between actual y position of wire and that calculated from the fitted equation versus the radial position of the wire.

calculated from (4-1) using the fitted constants. Figure 4-5 is the same as Figure 4-4, but for the y direction. Figure 4-6 shows the difference between the calculated and actual values of x and y versus the radial position of the wire, demonstrating sub-millimeter resolution.

4.4.2 Quadrupole calibration

To calibrate the BPM to measure the quadrupole moment, $\langle x^2 \rangle_{\text{BPM}} - \langle y^2 \rangle_{\text{BPM}}$, one might be tempted to fit equation (1-16) to the BPM map data. As when calibrating for the beam centroid, however, this would give poor results because of the differences between the BPM electrodes. An equation that takes into account their differences must be derived.

The wire used in the apparatus depicted in Figure 4-1 is very thin. It represents a beam that is essentially a delta function in x and y. Therefore, for a wire positioned at (x, y) , equations (1-9), (1-10), (1-11) and (1-12) become

$$A_R = a_{0R} + a_{1R}x + a_{2R}(x^2 - y^2) + a_{3R}(x^3 - 3xy^2) + a_{4R}(x^4 - 6x^2y^2 + y^4) + \dots +$$

$$A_L = a_{0L} - a_{1L}x + a_{2L}(x^2 - y^2) - a_{3L}(x^3 - 3xy^2) + a_{4L}(x^4 - 6x^2y^2 + y^4) + \dots +$$

$$A_T = a_{0T} + a_{1T}y - a_{2T}(x^2 - y^2) - a_{3T}(3x^2y - y^3) + a_{4T}(x^4 - 6x^2y^2 + y^4) + \dots +$$

and

$$A_B = a_{0B} - a_{1B}y - a_{2B}(x^2 - y^2) + a_{3B}(3x^2y - y^3) + a_{4B}(x^4 - 6x^2y^2 + y^4) + \dots +$$

where terms out to fourth order have been kept instead of just the first three. The a_{iR} 's, a_{iL} 's, a_{iT} 's and a_{iB} 's are all constants. In (1-9), (1-10), (1-11) and (1-12) their values

were written explicitly in terms of the BPM radius and the angular width of the electrodes. Now, however, it is assumed that the BPM electrodes are not identical.

Therefore

$$a_{iR} \neq a_{iL} \neq a_{iT} \neq a_{iB}.$$

One does expect, though, that the constants are almost equal. That is

$$a_{iR} \cong a_{iL} \cong a_{iT} \cong a_{iB}.$$

Making the definition

$$Q \equiv \frac{A_R + A_L - A_T - A_B}{A_R + A_L + A_T + A_B} \quad (4-5)$$

it can be shown that, to fourth order, the quadrupole moment, $x^2 - y^2$ for the thin wire, is given by

$$\begin{aligned} x^2 - y^2 = & C_0 + C_1 Q + C_2 (1 - Q)x + C_3 (1 + Q)y + C_4 x^4 + C_5 Qx^4 + C_6 y^4 + C_7 Qy^4 \\ & + C_8 x^2 y^2 + C_9 Qx^2 y^2 + C_{10} (1 - Q)x^3 + C_{11} (1 - Q)xy^2 \\ & + C_{12} (1 + Q)x^2 y + C_{13} (1 + Q)y^3. \end{aligned} \quad (4-6)$$

where the C_j 's are combinations of the a_{iR} 's, a_{iL} 's, a_{iT} 's and a_{iB} 's. Fitting the BPM map data to (4-6) yields

$$C_0 = 4.01 \text{ mm}^2.$$

$$C_1 = 88.9 \text{ mm}^2.$$

$$C_2 = -0.181 \text{ mm}.$$

$$C_3 = 0.129 \text{ mm}.$$

$$C_4 = -0.00013 \text{ mm}^{-2}.$$

$$C_5 = 0.0029 \text{ mm}^{-2}.$$

$$C_6 = -0.00086 \text{ mm}^{-2}.$$

$$C_7 = 0.0024 \text{ mm}^{-2}.$$

$$C_8 = 0.00087 \text{ mm}^{-2}.$$

$$C_9 = -0.0096 \text{ mm}^{-2}.$$

$$C_{10} = -0.0012 \text{ mm}^{-1}.$$

$$C_{11} = 0.0014 \text{ mm}^{-1}.$$

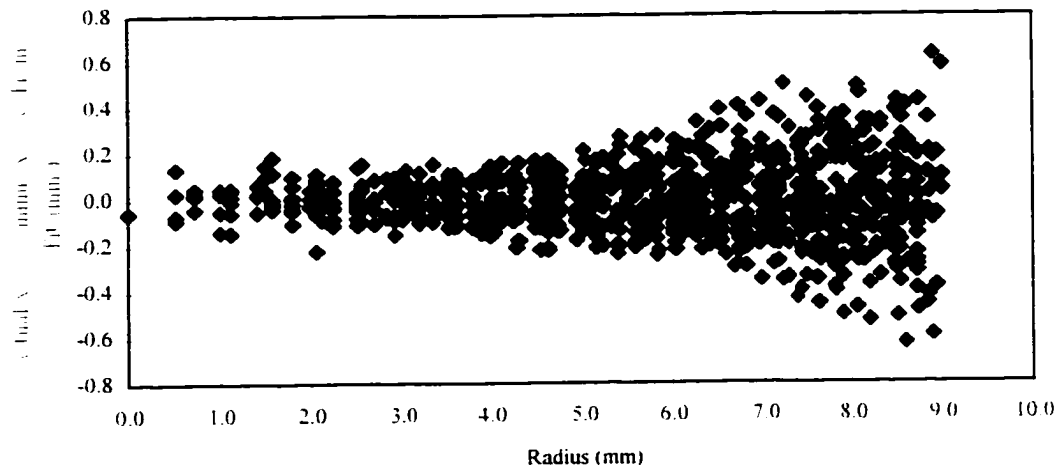
$$C_{12} = -0.0015 \text{ mm}^{-1}$$

and

$$C_{13} = 0.0012 \text{ mm}^{-1}.$$

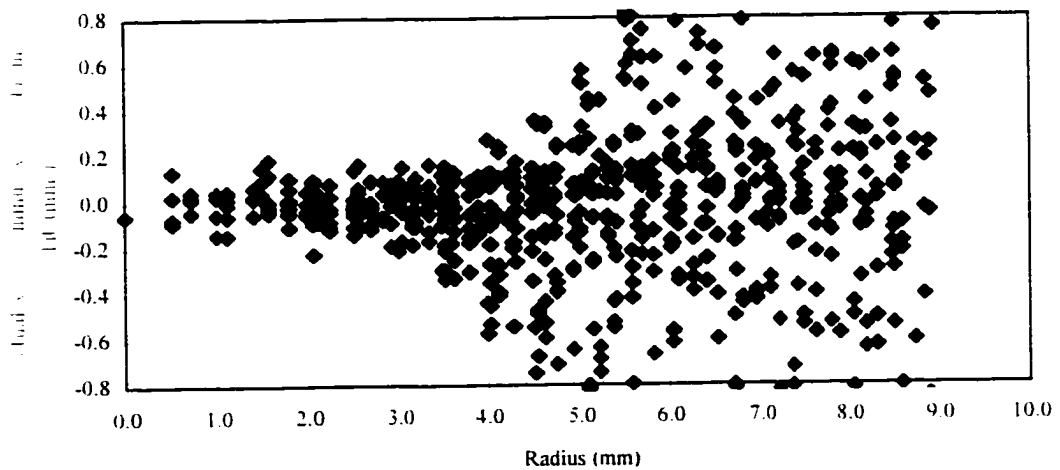
Figure 4-7a shows the results of using this equation, plotting the difference between the actual value of $x^2 - y^2$ and the value obtained with (4-6) and the fitted constants. The results are quite good, being correct to within $\pm 0.6 \text{ mm}^2$. (The wire was moved as far away from the BPM axis as 9.0 mm. Therefore, the maximum value of $x^2 - y^2$ is 81.0 mm^2 .) However, the obvious flaw with this equation is that, when making measurements on a real beam, only x , y and Q , from (4-1), (4-2) and (4-5), will be known. The higher order terms in (4-6), x^4 , y^4 etc., are unknown. Therefore, it would seem that (4-6) is useless when making real beam measurements. We get around this problem by recognizing that, when the beam is close to the axis of the beam pipe, the higher order terms are very small. Figure 4-7b is a plot of the difference between the actual value of $x^2 - y^2$ and the value obtained from the fit using the equation

Difference between Actual $x^2 - y^2$ and $x^2 - y^2$ From Fit vs. Radial Position of Wire



a)

Difference between Actual $x^2 - y^2$ and $x^2 - y^2$ From Fit vs. Radial Position of Wire



b)

Figure 4-7: a) Plot of the difference between actual value of $x^2 - y^2$ and its calculated value using the fit of Equation (4-6) . and b) using Equation (4-7).

$$x^2 - y^2 = C_0 + C_1 Q + C_2(1 - Q)x + C_3(1 + Q)y \quad (4-7)$$

where the constants C_0 , C_1 , C_2 and C_3 are the same as those from (4-6). As can be seen, the results from (4-7) are comparable to those from (4-6) out to a radius of about 4 mm. Therefore, the quadrupole moment of a real beam can be measured quite accurately if the beam is kept within a 4 mm radius of the beam pipe center, a reasonable constraint.

4.5 Simulating a diffuse beam

There are two problems with using a thin wire to calibrate a BPM. First, the wire has no width. Therefore,

$$\langle x^2 \rangle - \langle y^2 \rangle = 0$$

and the quadrupole moment reduces to

$$\langle x^2 \rangle_{\text{BPM}} - \langle y^2 \rangle_{\text{BPM}} = \langle x^2 \rangle - \langle y^2 \rangle + \bar{x}^2 - \bar{y}^2 = x^2 - y^2$$

where x and y are the positions of the wire. Second, the current signal on the wire is not nearly as intense as an actual beam. The BPM maps in Figures 4-2 and 4-3 show that the amplitude of the signals from the BPM electrodes peak at a little less than 6 mV. The signal induced by our electron beam will easily be 20 to 100 times greater than this.

Based on the calibration done in the last section, we can expect to measure the quadrupole moment to $\pm 0.6 \text{ mm}^2$ or better. However, when measuring the emittance, we need to determine $\langle x^2 \rangle - \langle y^2 \rangle$ by subtracting $\bar{x}^2 - \bar{y}^2$ away from the quadrupole moment. How accurately this can be done is hard to judge with the pulsed wire

measurement because $\langle x^2 \rangle - \langle y^2 \rangle$ is zero and because the signal is much less than what we get with an electron beam.

To simulate a diffuse beam where $\langle x^2 \rangle - \langle y^2 \rangle$ is not zero, we can employ the principle of superposition. In Figure 4-8 a square grid is superimposed upon the schematic of a BPM. Using the apparatus in Figure 4-1, the wire is moved to each grid location and the signals from the BPM electrodes are measured. The principle of superposition tells us that the sum of the signals recorded for a particular electrode is the signal one would get from that electrode if all the pencil beams were present concurrently. By manipulating the size and shape of the grid, the value of $\langle x^2 \rangle - \langle y^2 \rangle$ is changed. By shifting its position, different values for \bar{x} and \bar{y} result.

In addition to changing the size and shape of the grid in Figure 4-8, $\langle x^2 \rangle - \langle y^2 \rangle$ can also be modified by assigning a weighting value based upon some superimposed distribution function to each point in the grid. For example, the signal on the right lobe due to the diffuse beam that is represented by all the wire positions would be

$$A_R = \sum_i c_i A_{Ri}$$

where A_{Ri} is the signal on the right electrode for the wire at the i^{th} position and c_i is a weighting value. The value of c_i is determined by the distribution function one chooses to overlay on the grid of points.

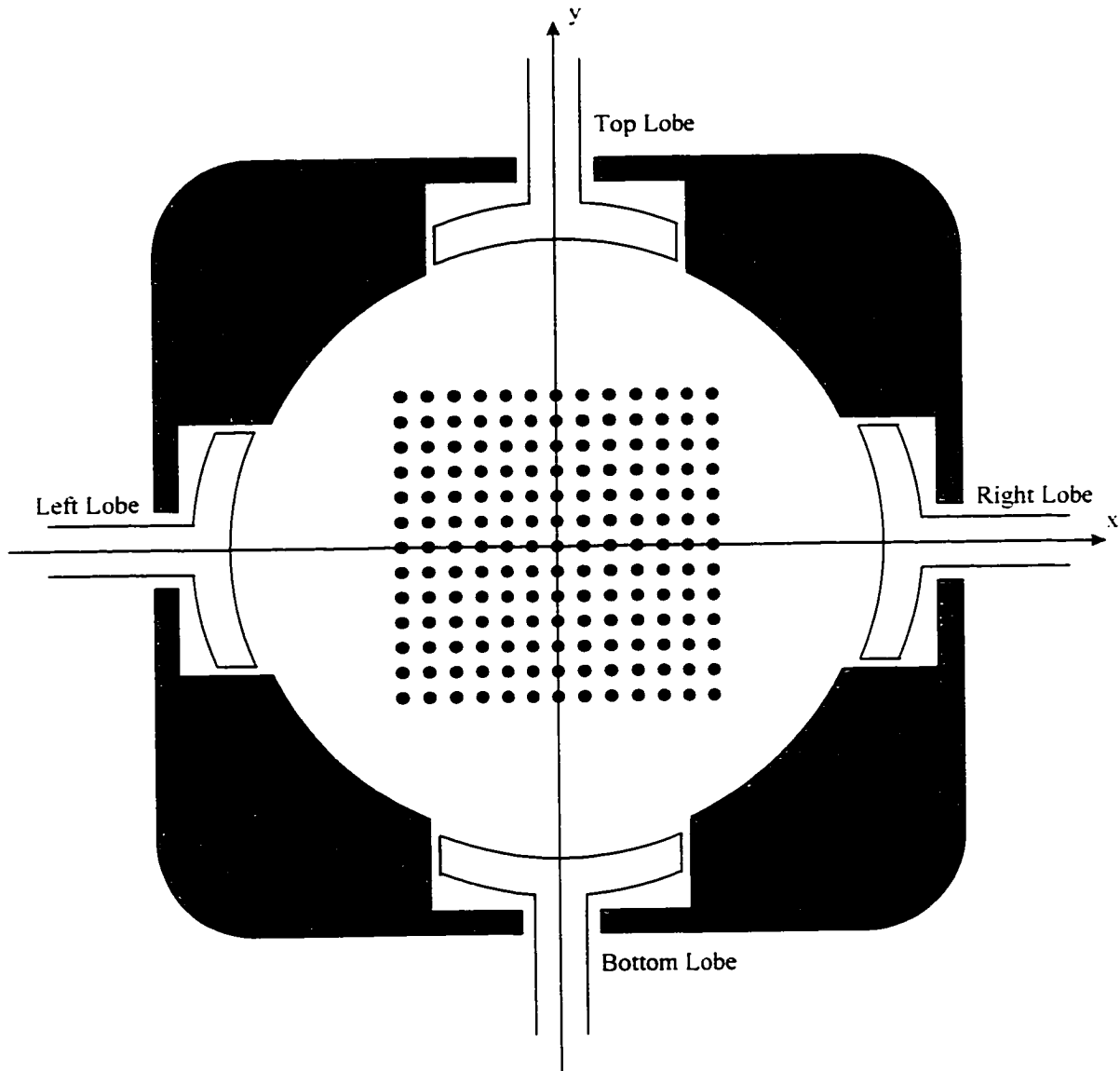


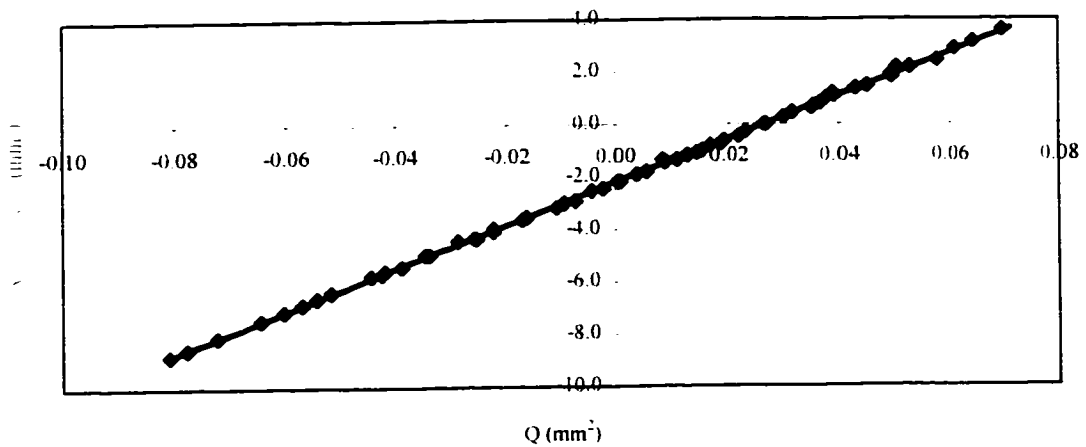
Figure 4-8: Schematic showing grid points for simulation of diffuse beam with a single pulsed wire.

4.5.1 Interpolation versus measurement

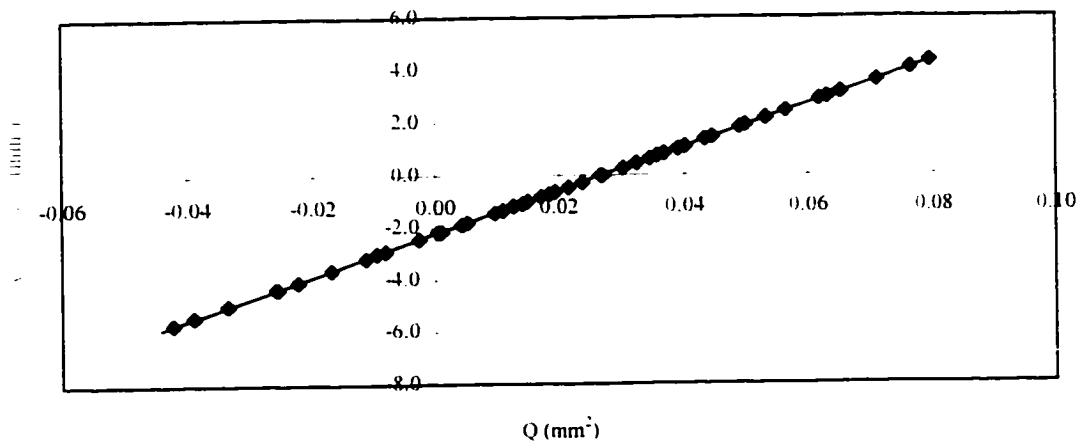
To simulate diffuse beams, the response of the BPM electrodes must be determined for arbitrary wire positions. With the apparatus in Figure 4-1 this is quite easy. The wire is simply moved to the desired location and the response of the electrodes is measured. However, this is also very time consuming, even though the entire process is computer controlled. A much faster method is to predict the response of the BPM electrodes at arbitrary wire positions by interpolating between the grid points in the BPM maps shown in Figures 4-2 and 4-3. To show that this is valid, an experiment was done to compare the two methods.

In Figure 4-9, two sets of data are shown. Each point in the two plots represents a single, simulated, diffuse beam. Each beam has for its center $\bar{x} = 0$ and $\bar{y} = 0$. The value of $\langle x^2 \rangle - \langle y^2 \rangle$ is different for each beam and is calculated from the known wire positions. The grid for each beam consists of 225 wire positions. A Gaussian distribution is superimposed on each grid. In Figure 4-9a the response of the BPM for each wire position is measured using the apparatus in Figure 4-1. In Figure 4-9b the response of the BPM for each wire position is predicted by interpolating between the points of the grid of the BPM maps. (It should be noted that the BPM used for this experiment, although of the same type, was not the same one whose maps are shown in Figures 4-2 and 4-3.)

Because all the beam centers are at zero, (4-6) says that plotting the value of $\langle x^2 \rangle - \langle y^2 \rangle$ versus the value of Q , from (4-5), should be a straight line. As can be seen from the fitted lines in Figures 19a and 19b this is true. Using the fitted line, the

$\langle x^2 \rangle - \langle y^2 \rangle$ vs. Q, Data From Pulsed Wire Apparatus

a) Slope = 81.7 ± 0.21 . Intercept = $-2.165 \pm 0.0082 \text{ mm}^2$

 $\langle x^2 \rangle - \langle y^2 \rangle$ vs. Q, Data From Interpolation

b) Slope = 82.02 ± 0.075 . Intercept = $-2.212 \pm 0.0028 \text{ mm}^2$

Figure 4-9: a) Plot of $\langle x^2 \rangle - \langle y^2 \rangle$ versus Q for a number of simulated beams ($\bar{x} = \bar{y} = 0$) using the apparatus in Figure 4-1. b) Identical to a) except that the responses of the BPM electrodes for the individual grid points are interpolated from BPM maps.

predicted values of $\langle x^2 \rangle - \langle y^2 \rangle$ match the actual values to within $\pm 0.1 \text{ mm}^2$ for both sets of data.

The slope of the line in Figure 4-9a is 81.7 ± 0.21 and its intercept is $-2.165 \pm 0.0082 \text{ mm}^2$. In Figure 4-9b the line has slope 82.02 ± 0.075 and intercept $-2.212 \pm 0.0028 \text{ mm}^2$. The properties of the two lines are very close, indicating the two methods, although not identical, produce very similar results. These discrepancies can largely be attributed to errors in the program that controlled the wire position in the apparatus of Figure 4-1. This error was later corrected, but access to the equipment was lost before this experiment could be repeated.

4.5.2 Check of BPM accuracy for measuring $\langle x^2 \rangle - \langle y^2 \rangle$

As a check to verify that $\langle x^2 \rangle - \langle y^2 \rangle$, and the beam center, can be measured accurately with a BPM, several simulated, diffuse beams were created. Ten of these, arbitrarily chosen, are shown in Table 4-1. Each beam consists of approximately 121 wire positions. The table shows the actual values of \bar{x} , \bar{y} and $\langle x^2 \rangle - \langle y^2 \rangle$, as calculated from the known wire positions that make up the simulated beam, and the values as calculated from the signals from the BPM electrodes. The BPM used for this experiment is the one that was used to measure the emittance in the next Chapter and is the BPM whose calibration constants are shown in this chapter.

Figure 4-10 is created by taking a single, simulated beam and moving its center radial outward from the BPM's center. The value of $\langle x^2 \rangle - \langle y^2 \rangle$ is held constant and 121 wire

Table 4-1: Table comparing the values of \bar{x} , \bar{y} and $\langle x^2 \rangle - \langle y^2 \rangle$ as measured by a BPM to their actual values for several simulated, diffuse beams.

Actual \bar{x} (mm)	\bar{x} Measured by BPM (mm)	Actual \bar{y} (mm)	\bar{y} Measured by BPM (mm)	Actual $\langle x^2 \rangle - \langle y^2 \rangle$ (mm ²)	$\langle x^2 \rangle - \langle y^2 \rangle$ Measured by BPM (mm ²)
0.00	0.05	0.00	0.03	-3.74	-3.78
-1.91	-1.87	-1.29	-1.24	0.75	0.75
2.52	2.60	1.63	1.64	2.23	2.04
0.54	0.60	-3.86	-3.89	-1.27	-0.87
0.14	0.19	-0.99	-0.97	-1.31	-1.37
0.45	0.50	-0.23	-0.20	1.25	1.20
-0.29	-0.25	1.47	1.48	3.00	3.09
-0.34	0.28	-0.37	-0.37	-12.5	-12.7
1.83	1.97	-0.81	-0.79	6.04	5.83
0.25	0.29	0.05	0.08	-0.94	-0.95

positions were used to create each beam. Figure 4-10 is a plot of the difference between the actual value of $\langle x^2 \rangle - \langle y^2 \rangle$ and that calculated from the BPM signals. It shows the expected decrease in accuracy as the radius increases.

Although only a few examples are shown here, numerous simulation of these diffuse beams indicate that the BPM can measure the value of $\langle x^2 \rangle - \langle y^2 \rangle$ to $\pm 0.2 \text{ mm}^2$ reliably, if the conditions are right. That means the beam must be stable, be well centered in the BPM aperture and the data acquisition system must have sufficient accuracy. Typically these conditions are not met with SPA, especially the beam stability requirement. Therefore, when making error estimates, it was generally assumed that the BPM would have an accuracy of $\pm 0.5 \text{ mm}^2$ when measuring $\langle x^2 \rangle - \langle y^2 \rangle$.

4.6 Concerns with calibration method

Using a pulsed wire apparatus like that described here is a very common way to calibrate BPMs. However, there are some concerns with its efficacy. The rf signal on the wire is a single frequency sine wave. Our electron beam, on the other hand, consists of a continuum of frequencies. Obviously, then, there is a possibility that the two signals are not equivalent. In fact, it is not at all uncommon for the electrical center of the BPM to change depending upon the frequency of the sine wave used to calibrate it[28]. This calls into question the accuracy of the pulsed wire calibration.

An ideal calibration scheme would use the electron beam that the BPM is intended to monitor instead of the pulsed wire. At the moment, it is not clear how this would be done and in any case, as will be shown in Chapter 5, the SPA electron beam is currently too

unstable for the task. Hopefully, future work will better this stability, allowing for clever experiments to calibrate BPMs with the electron beam and eliminate any ambiguity that might exist from the pulsed wire calibration.

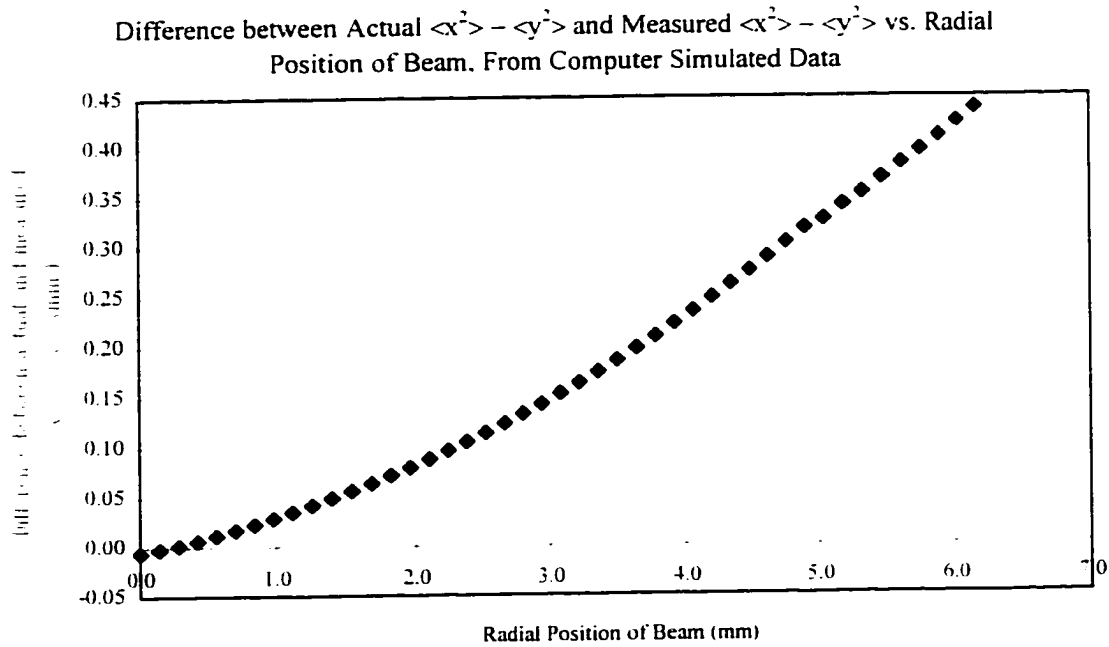


Figure 4-10: Plot of the difference between the actual value of $\langle x^2 \rangle - \langle y^2 \rangle$ and that calculated from the BPM signals in mm^2 for a single simulated beam as it is move radial outward from the BPM center.

Chapter 5

EXPERIMENTAL RESULTS

5.1 Introduction

In this chapter are presented the results of beam experiments intended to demonstrate Miller's technique for measuring the x and y rms emittances using a BPM. The chapter begins by describing the experimental apparatus and the data acquisition system. It then moves on to describe three different experiments: the first is a check of the electron beam stability, the second is a verification of the BPM calibration done in Chapter 4 and the third demonstrates Miller's emittance measurement.

5.2 Experimental apparatus and data acquisition

This section describes the experimental apparatus and the data acquisition system.

5.2.1 Experimental apparatus

The experimental apparatus is merely the end section of the SPA beam line shown in Figure I-2. A schematic of this end section is shown in Figure 5-1. It consists of quadrupoles 7 and 8, a steering coil, a BPM, the spectrometer and the drifts between the magnets. (The fast deflector cavity, because it is not used, is left out of the figure.)

Quadrupoles 7 and 8 are identical. They are electromagnetic, have a pole length of

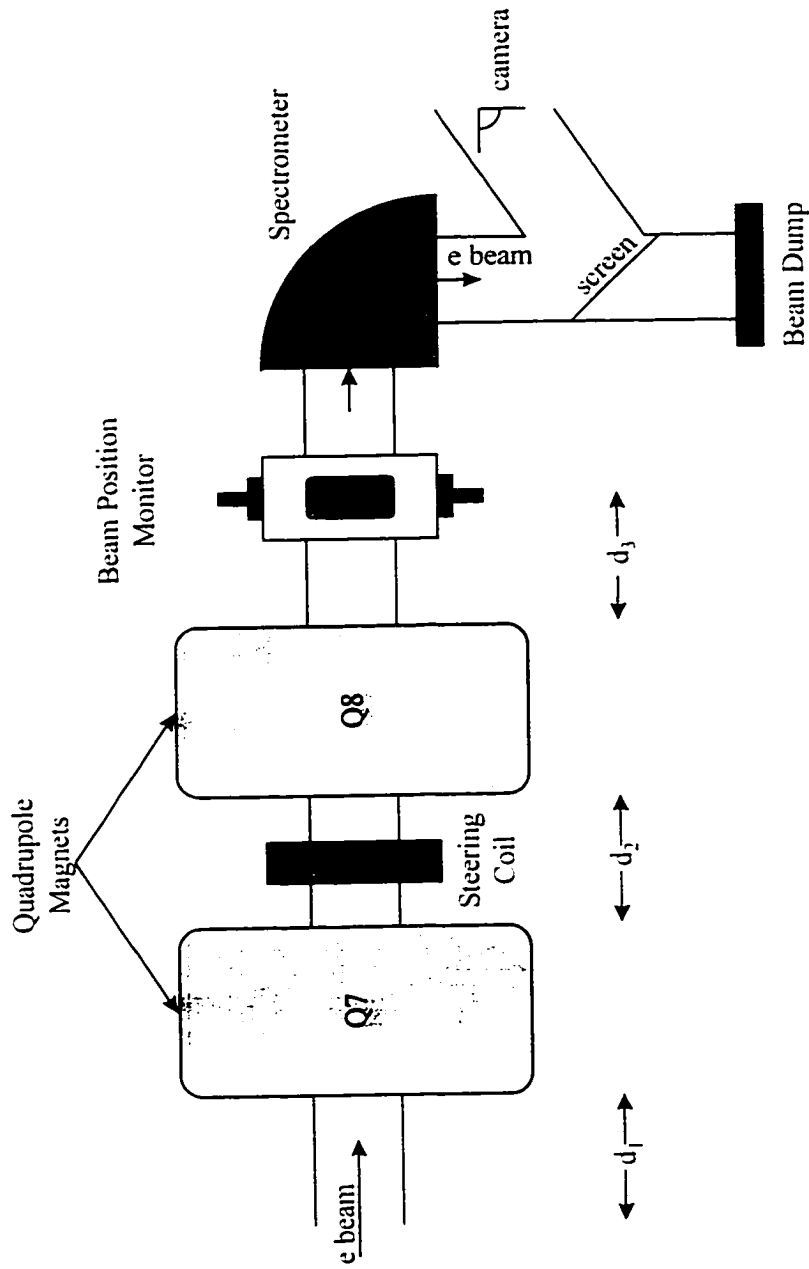


Figure 5-1: Schematic of end section of SPA beam line.

2.75 inches and a gap radius of one inch. The fields of these quadrupoles have been simulated and measured. From this it has been determined that their effective length is 86 mm and that, at a radius of 1 cm, the multipole components of the field are less than 1 percent of the quadrupole field. Attached to one pole of each magnet is a small Hall probe. The Hall probe voltages have been correlated to the gradients of the quadrupole fields. During beam operation, monitoring these voltages enables us to determine these gradients to within a percent.

The steering coil is used for positioning the beam inside the BPM aperture. It is electromagnetic, of a standard design and is capable of deflecting the 8 MeV electron beam several mrad. Its field has not been characterized.

The BPM is the same BPM whose calibration is discussed in Chapter 4.

The spectrometer is an electromagnetic dipole magnet that bends the beam 90°. Its edge angles are such that it focuses the beam on the screen shown in Figure 5-1. The average energy of the beam is determined by adjusting the current of the magnet until the beam spot is centered on the screen. Measuring the width of the beam spot determines the energy spread of the beam. The spectrometer has been calibrated so that the average energy can be determined to within 2 percent accuracy.

The three drifts in Figure 5-1 have the following lengths:

$$d_1 = 496 \text{ mm} .$$

$$d_2 = 425 \text{ mm}$$

and

$$d_3 = 237 \text{ mm} .$$

5.2.2 Capturing BPM signals

A schematic of the data acquisition system for capturing the signals from the BPM electrodes is shown in Figure 5-2. The signals from the four BPM electrodes travel down 50 Ohm, coaxial Heliac™ cables of equal length to 300 MHz, low-pass filters. From there they go to two, dual channel HP™ 54111D digitizing oscilloscopes. The oscilloscope digitizers operate at 1 giga-sample per second with six bit accuracy. Linked to the oscilloscopes via GPIB is a PC running a control program written in LabView® from National Instruments™. The PC stores the digitized BPM signals in binary files. It can capture the signals from up to 99 individual beam shots. Each beam shot consists of several (usually less than 10) beam bunches traveling one after the other.

5.2.3 Analyzing digitized BPM signals

The digitized BPM signals are read into the IDL® data analysis software from Research Systems, Inc. Here, each electrode signal is processed with a 250 MHz digital filter. Utilizing the sampling theorem[29], the signals are filled in by interpolating ten additional points for each data point taken to obtain a voltage versus time signal like that shown in Figure 5-3. This trace shows two full beam bunches and part of a third from a typical beam shot.

After the electrode signals are reconstructed, the peak-to-peak voltage of each beam bunch is determined. This is defined as the voltage difference between the first negative peak and the first positive peak of the bunch. The peak-to-peak voltage is only dependent

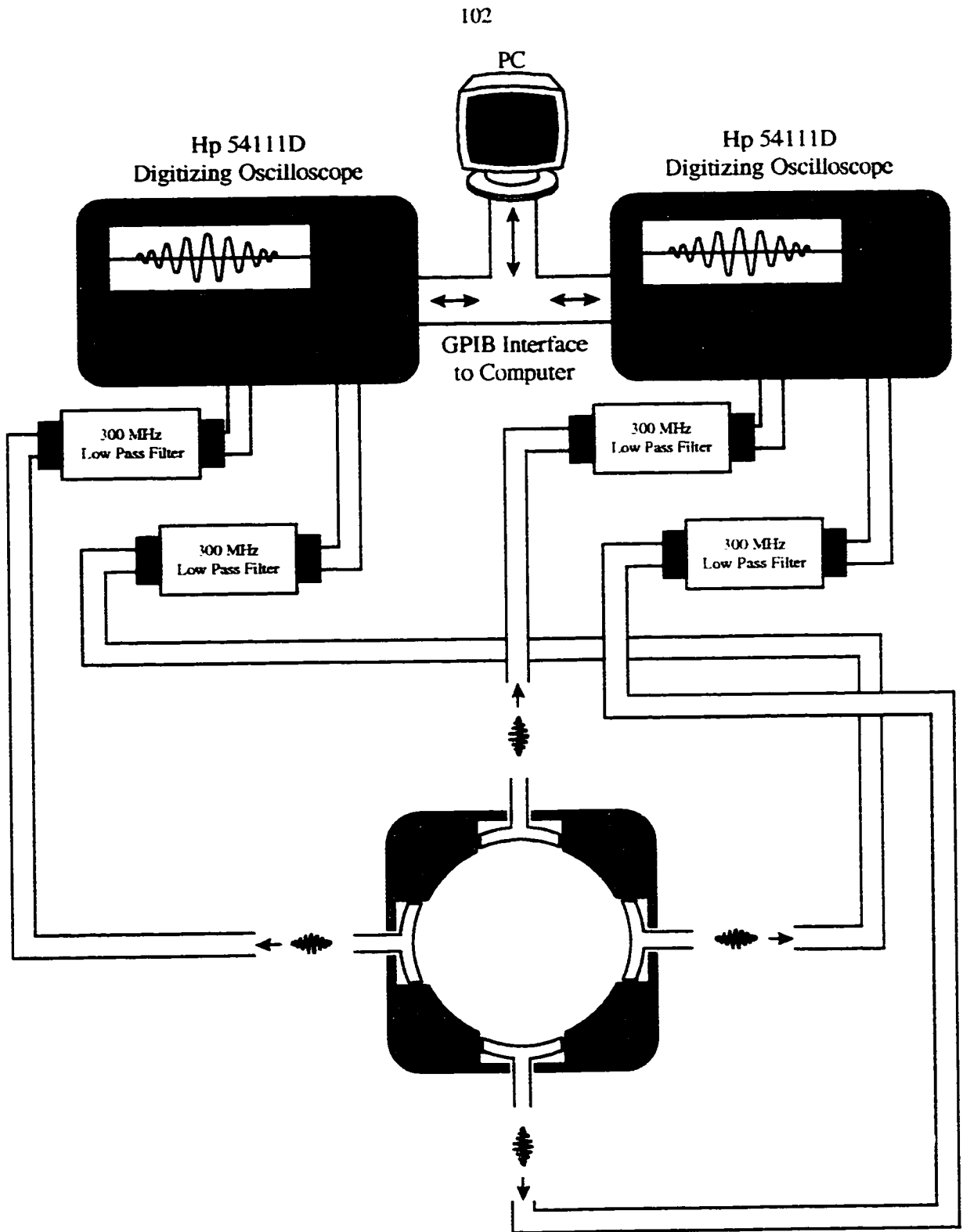


Figure 5-2: Schematic of data acquisition system for capturing BPM signals.

Voltage vs. Time for a Typical Beam Shot

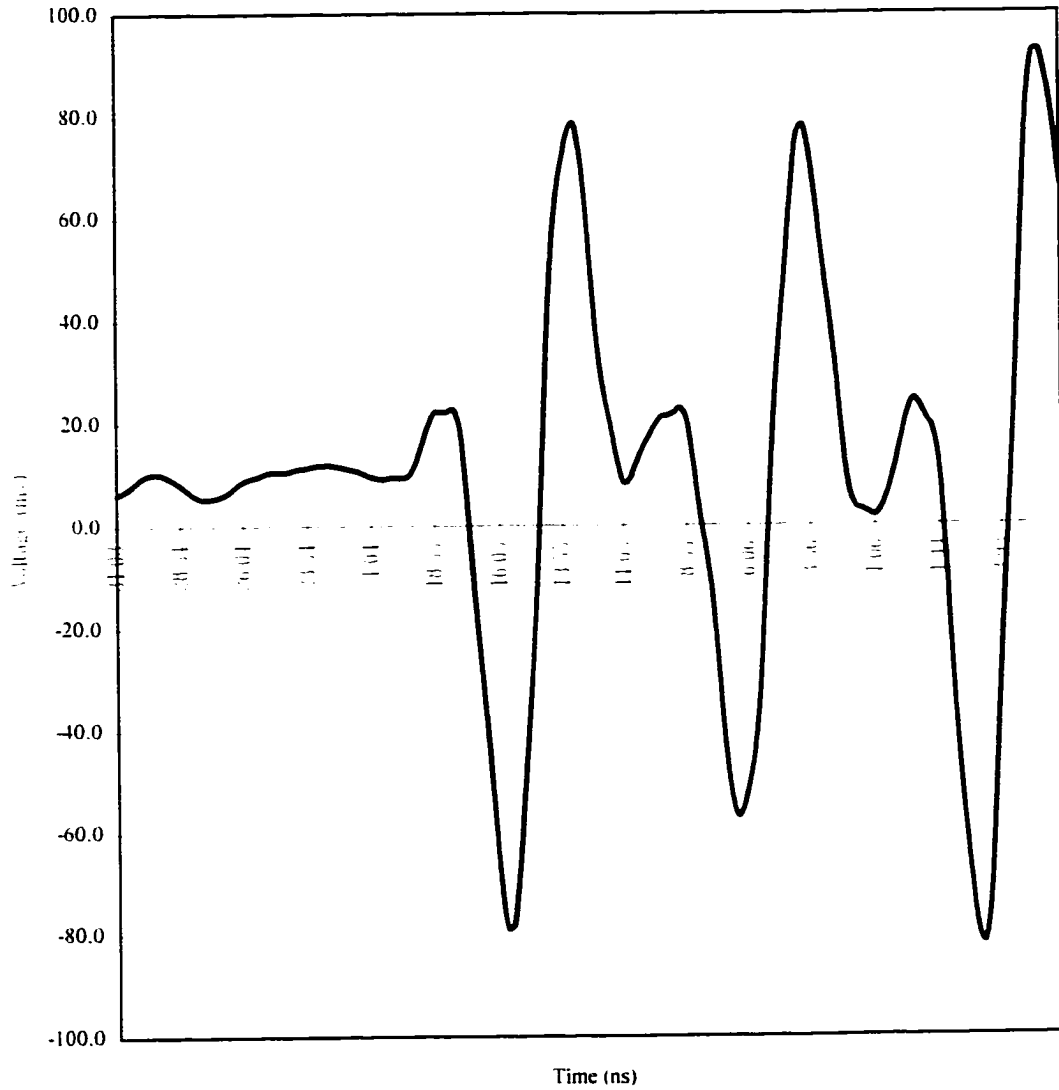


Figure 5-3: Voltage versus time signal from BPM electrode for a typical beam shot.

There are two full beam bunches and part of a third displayed.

upon the amplitude of the signal and has the property that any dc bias that might be present is eliminated. Once the peak-to-peak voltages are determined, the values of \bar{x} , \bar{y} and $\langle x^2 \rangle - \langle y^2 \rangle$ for the desired number of beam bunches are determined according to equations (4-1), (4-2) and (4-7) using the calibration constants determined in Chapter 4.

5.3 Stability experiment

The electron beam from SPA is not very stable beam-shot to beam-shot. This is due, mainly, to fluctuations in the drive laser beam that strips the electrons from the photo-cathode. This first experiment is meant as a check of this stability.

The drive laser is located a considerable distance from the accelerator vault. The laser beam is transported several hundred feet from the laser location to its injection point in the accelerator beam line via an evacuated pipe using multiple mirrors and lenses. There are two stability issues associated with the technology used to create the drive laser beam: amplitude fluctuations and pointing instabilities. The amplitude fluctuations are changes in the amount of light energy contained in each laser pulse, causing corresponding amplitude fluctuations in the electron beam. The pointing instabilities are small changes in the location on the photo-cathode where the drive laser beam strikes. These are due to small deflections of the laser beam caused by air currents and vibrations in the optics. Because of the great distance the laser beam travels, these small deflections are greatly amplified. This translates into position fluctuations in the electron beam and, because the photo-cathode surface does not emit electrons uniformly, amplitude fluctuations as well.

To test how severe the electron beam instability is, two BPM experiments were done.

In the first, the stability of the beam shot-to-shot was investigated by measuring the intensity of the beam (sum of all four BPM electrodes), \bar{x} , \bar{y} and $\langle x^2 \rangle - \langle y^2 \rangle$ for 99 successive beam shots. In the second experiment, the average stability of the beam was observed by taking the average intensity, average beam center and average value of $\langle x^2 \rangle - \langle y^2 \rangle$ over 99 successive beam shots. This was done for multiple sets of 99 beam shots to determine if the average values of these quantities change over time scales on the order of about one hour.

There are also long term (days) stability questions arising from changes to the photo-cathode. The photo-cathode material used in SPA is Cs₂Te, a fairly reactive substance. Although the accelerator is maintained at a pressure on the order of 10⁻⁹ Torr, the photo-cathode surface is slowly contaminated over time. Also, breakdown in the accelerator cavities often results in electrical arcs that damage the photo-cathode surface. The end result is a slow degradation of the photo-cathode performance. We attempt to neutralize this effect by replacing the cathode every few months (when possible) and by increasing the laser power to maintain constant charge levels. However, the effect of photo-cathode aging on the electron beam has not been investigated.

5.3.1 Shot-to-shot stability

In the first experiment, the electron beam was first transported to the position of the BPM in Figure 5-1. To ensure that the majority of the beam that exits the accelerator arrives at the BPM position, the intensity of the beam at the BPM at the beginning of the SPA beam line (Figure I-2) was compared to the intensity of the beam at the BPM in

Figure 5-1. Using this diagnostic, and adjusting the strength of the focusing elements, nearly 100 percent transmission of the electron beam from the accelerator exit to the experimental BPM was achieved. This procedure was followed as a precursor to all the experiments described in this chapter.

Once good beam transport was established, up to 99 successive beam shot signals were captured using the data acquisition apparatus shown in Figure 5-2. This was done without changing the focusing or steering of the beam. For each shot, the BPM signals were processed to extract \bar{x} , \bar{y} , the intensity (sum of the four electrodes) and $\langle x^2 \rangle - \langle y^2 \rangle$. A typical result is shown in Figures 5-4 and 5-5.

As can be seen in the figures, the shot-to-shot stability of the beam is not very good. This is especially true of the $\langle x^2 \rangle - \langle y^2 \rangle$ measurement, which is the most susceptible to error. These fluctuations have two possible origins: actual changes to the electron beam from shot-to-shot and the limited accuracy of the oscilloscope digitizers.

The digitizers operate with 6 bit accuracy and there was some concern that this limited precision was responsible for the observed beam instability. The rms scatter that is introduced by the digitizers can be estimated and compared to the observed scatter.

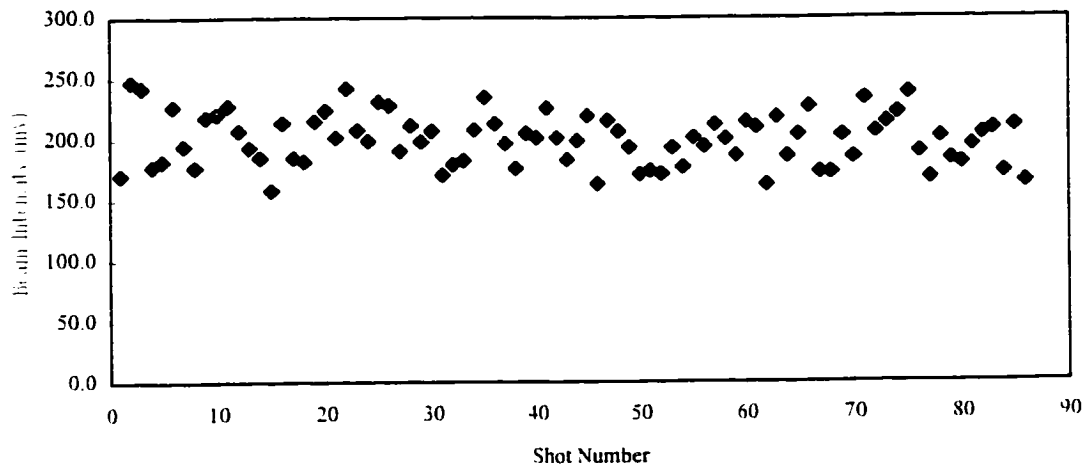
In Figure 5-4a, the rms scatter of the beam intensity versus shot number is calculated to be

$$\sigma = \pm 17.4 \text{ mV} .$$

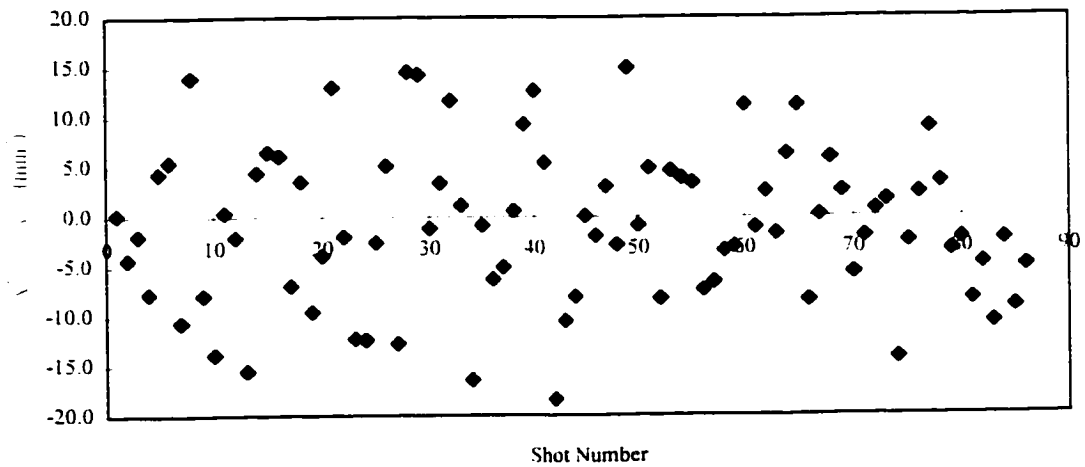
A simple calculation of the scatter due to the limited accuracy of the digitizers yields

$$\sigma_{\text{Digitizers}} = \pm \frac{\text{Average Intensity}}{2^{\text{Number of bits}}} = \pm 3.1 \text{ mV} .$$

Beam Intensity vs. Shot Number



a)

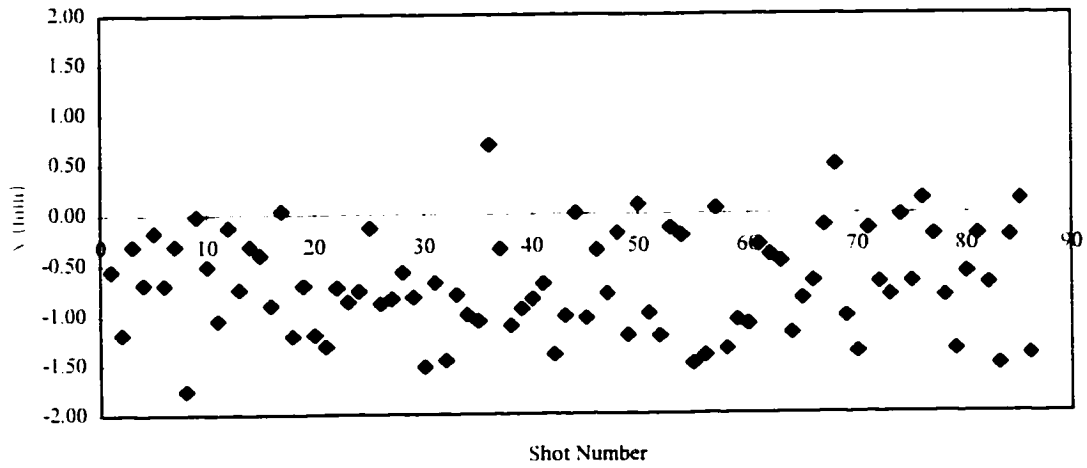
 $\langle x^2 \rangle - \langle y^2 \rangle$ vs. Shot Number

b)

Figure 5-4: a) Intensity (sum of four BPM electrodes) versus successive beam shots. b)

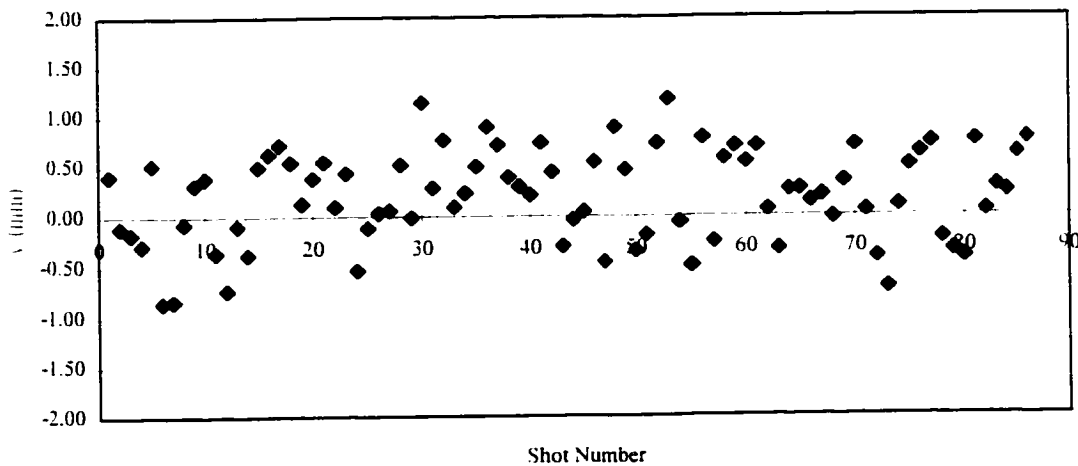
 $\langle x^2 \rangle - \langle y^2 \rangle$ versus successive beam shots.

x Position of Beam Center vs. Shot Number



a)

y Position of Beam Center vs. Shot Number



b)

Figure 5-5: a) x position of beam center versus successive beam shots. b) y position of beam center versus successive beam shots.

Assuming the scatter due to the beam and the scatter due to the 6 bit digitizers add in quadrature, the scatter due to the beam is found to be

$$\sigma_{\text{Beam}} = \pm 17.2 \text{ mV} .$$

This indicates that beam fluctuations are the dominate source of noise for the intensity measurement.

In Figure 5-5, the rms scatter for the x position of the beam versus shot number is calculated to be

$$\sigma = \pm 0.41 \text{ mm}$$

and for the y position

$$\sigma = \pm 0.38 \text{ mm} .$$

The scatter due to the digitizers is calculated to be

$$\sigma_{\text{Digitizers}} = \pm \frac{20}{\ln 10} \frac{2\sqrt{2}}{2^{\text{Number of bits}}} S_x = \pm 0.14 \text{ mm}$$

in x and

$$\sigma_{\text{Digitizers}} = \pm \frac{20}{\ln 10} \frac{2\sqrt{2}}{2^{\text{Number of bits}}} S_y = \pm 0.14 \text{ mm}$$

in y. S_x and S_y are the calibration constants found in Chapter 4. Therefore, the scatter due to beam fluctuations is

$$\sigma_{\text{Beam}} = \pm 0.38 \text{ mm}$$

in x and

$$\sigma_{\text{Beam}} = \pm 0.35 \text{ mm}$$

in y.

In Figure 5-4b, the rms scatter of $\langle x^2 \rangle - \langle y^2 \rangle$ versus shot number is calculated to be

$$\sigma = \pm 6.2 \text{ mm}^2.$$

An estimate of the scatter due to the accuracy of the oscilloscope digitizers yields

$$\sigma_{\text{Digitizers}} = \pm \frac{C_1}{2^{\text{Number of bits}}} = \pm 1.4 \text{ mm}^2.$$

where C_1 is the calibration constant determined in Chapter 4. Therefore, the scatter due to the beam fluctuations is

$$\sigma_{\text{Beam}} = \pm 6.0 \text{ mm}^2.$$

The estimates of the scatter due to the 6 bit digitizers are accurate to about a factor of 2 for the four plots. Therefore, it is apparent that the dominate source of noise in these measurements is beam related. Oscilloscopes with more accurate digitizers would have been nice, if they had been available. But they are not necessary. The error introduced by the oscilloscopes is effectively swamped by beam noise.

5.3.2 Average stability

To check the average stability of the electron beam, a similar experiment was performed. Again, good transport of the beam to the BPM in Figure 5-1 was achieved first. In this experiment, sets of up 99 beam shots were captured using the apparatus in Figure 5-2. Typically, each beam shot contained 5 beam bunches. For each set of 99 shots, the average values of \bar{x} , \bar{y} , the intensity and $\langle x^2 \rangle - \langle y^2 \rangle$ were calculated for each beam bunch. This was done for successive sets of 99 beam shots without changing the beam focusing or steering. The time lapse between measurements was 2 to 5 minutes.

Because the focusing remains constant, the average value of $\langle x^2 \rangle - \langle y^2 \rangle$ should not change if the beam is stable.

The average stability of the beam was tested several times on different days using different focusing and different amounts of charge per beam bunch. Figure 5-6 and 5-7 show the results of one of these experiments for a single beam bunch. Comparing these to Figures 5-4 and 5-5, it is apparent that the average stability is better than the shot-to-shot stability. However, it is still poor. Figure 5-8 shows the results of a similar experiment done on a different day at different charge and different focusing. Obviously, the beam was more erratic when this data was taken than it was for the data shown in Figures 5-6 and 5-7.

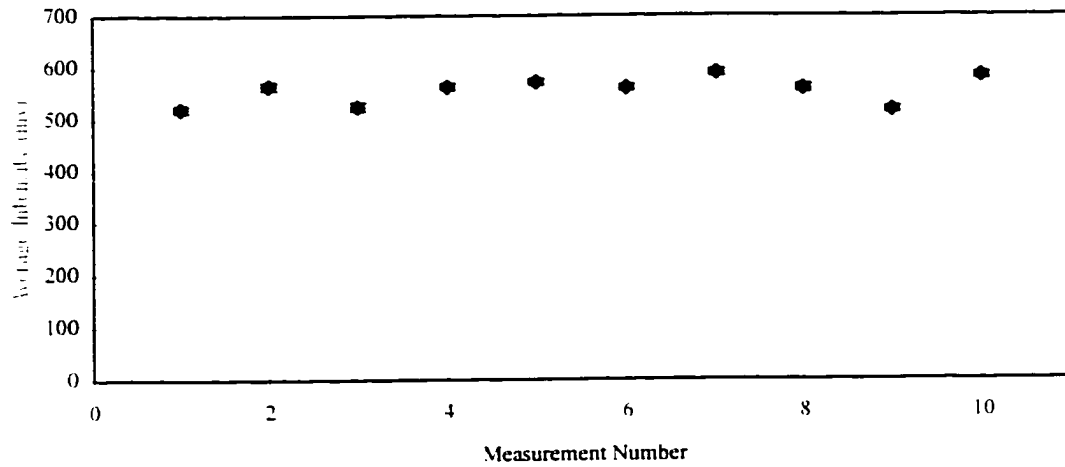
These experiments demonstrate that the stability of the SPA electron beam is not very good. This adversely impacts the precision with which one can expect to measure the emittance using Miller's technique.

5.4 Experiments to check BPM calibration

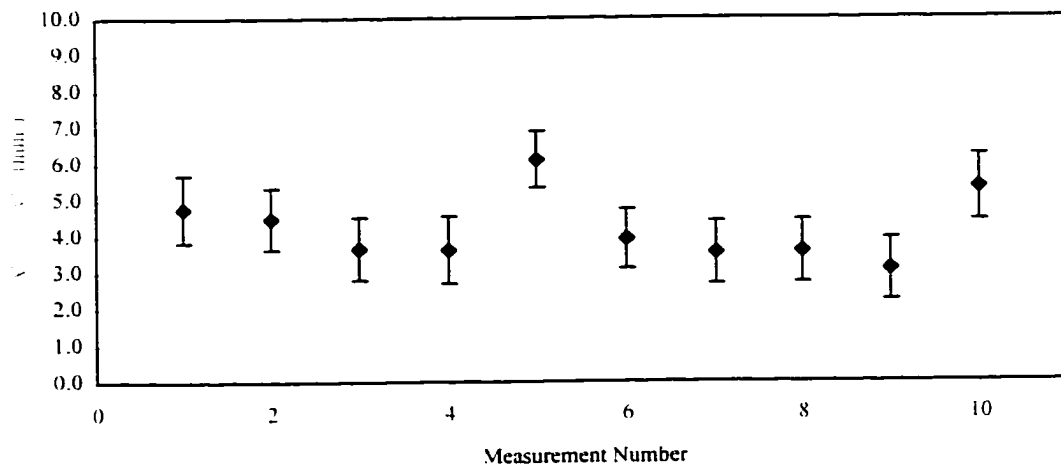
Using the pulsed wire technique described in Chapter 4, the BPM was calibrated to measure \bar{x} , \bar{y} and $\langle x^2 \rangle - \langle y^2 \rangle$. To check that this calibration is valid for a real electron beam, the following experiment was performed.

This experiment is very similar to the one described in the previous section. Again, good transport of the beam to the location of the BPM in Figure 5-1 was first established. Then, without changing the upstream focusing, the electron beam was steered to different transverse locations inside the BPM aperture using the steering coil shown in Figure 5-1.

Average Intensity vs. Measurement Number



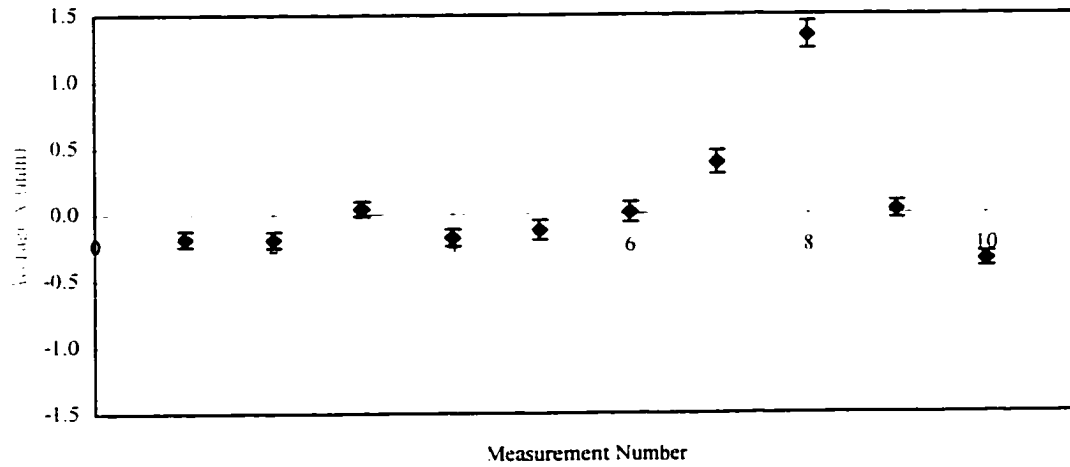
a)

Average Value of $\langle x^2 \rangle - \langle y^2 \rangle$ vs. Measurement Number

b)

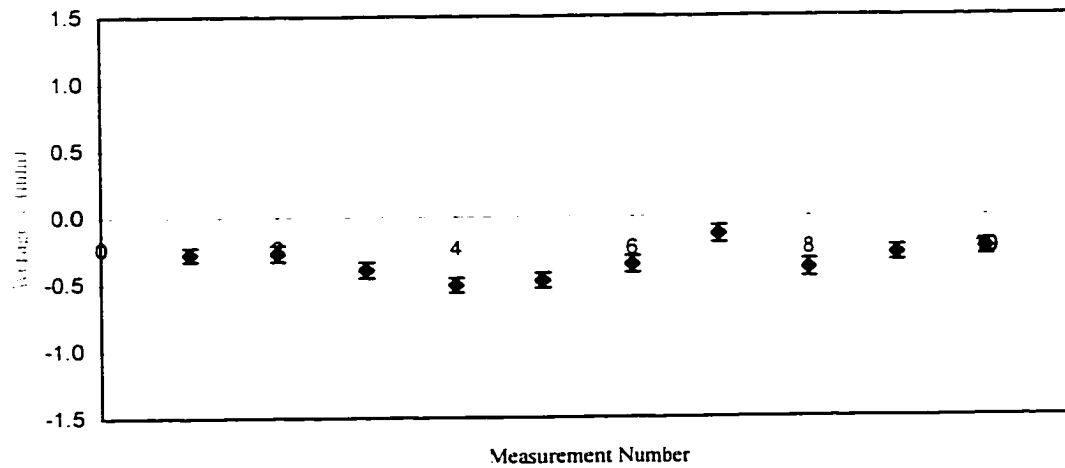
Figure 5-6: a) Average intensity (sum of four BPM electrodes) of beam bunch versus measurement number. b) Average value of $\langle x^2 \rangle - \langle y^2 \rangle$ versus measurement number. Each measurement is the average over 99 consecutive beam shots.

Average x Position of Beam Center vs. Measurement Number



a)

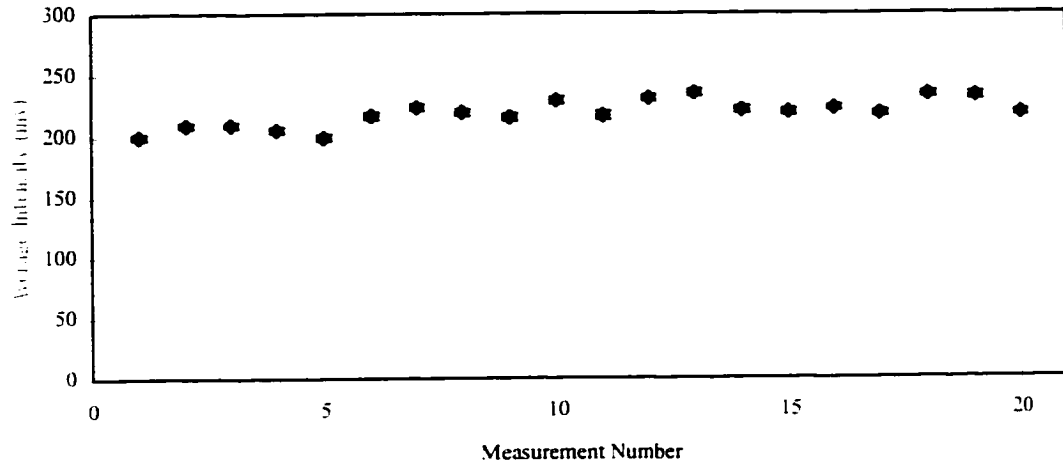
Average y Position of Beam Center vs. Measurement Number



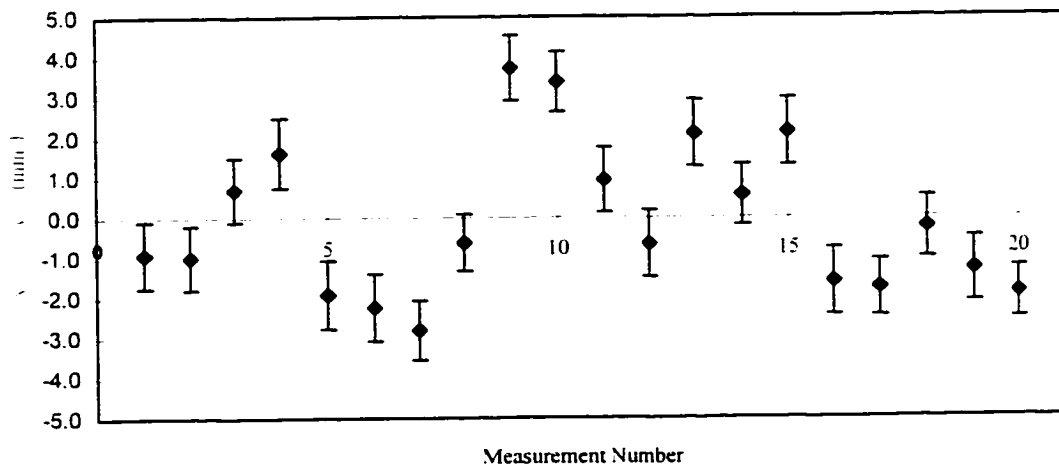
b)

Figure 5-7: a) Average value of x position of beam bunch center versus measurement number. b) Average value of y position of beam bunch center versus measurement number. Each measurement is the average over 99 consecutive beam shots.

Average Intensity vs. Measurement Number



a)

Average Value of $\langle x^2 \rangle - \langle y^2 \rangle$ vs. Measurement Number

b)

Figure 5-8: a) Another example of the average intensity (sum of four BPM electrodes) of a beam bunch versus measurement number. b) Another example of the average value of $\langle x^2 \rangle - \langle y^2 \rangle$ versus measurement number.

At each location, the signals from 99 beam shots are captured with the apparatus of Figure 5-2. Each beam shot consisted of 5 beam bunches. For each beam location, the average values of $\bar{x}^2 - \bar{y}^2$, the quadrupole moment and $\langle x^2 \rangle - \langle y^2 \rangle$ were calculated for each beam bunch.

In Chapter 4, the BPM was calibrated (Equation 4-7) to measure

$$\langle x^2 \rangle_{\text{BPM}} - \langle y^2 \rangle_{\text{BPM}} = \langle x^2 \rangle - \langle y^2 \rangle + \bar{x}^2 - \bar{y}^2.$$

Recall from Chapter 1 that this is called the quadrupole moment of the BPM signal. In this experiment, because the focusing is kept constant, the value of $\langle x^2 \rangle - \langle y^2 \rangle$ should stay constant. (Even though the experiments from the last section show that this is not necessarily true for the SPA electron beam, we will assume that it is for the present circumstances.) Therefore, the only change in the quadrupole moment is due to the change in the value of $\bar{x}^2 - \bar{y}^2$ that occurs when the beam is moved to different locations within the BPM aperture. The value of this term is known because the ability of the BPM to measure \bar{x} and \bar{y} accurately has been verified on a similar electron accelerator[16]. Therefore, if the calibration constants in Equation 4-7 are correct, a plot of the quadrupole moment versus $\bar{x}^2 - \bar{y}^2$ should be a straight line with slope equal to 1.0. Figure 5-9 shows the results of one of these experiments.

The slope of the line in Figure 5-9a is 0.95. This is close to 1.0, suggesting that the calibration is fairly accurate. Repetitions of this experiment indicate that a slope of 0.95 is typical.

It is tempting to try to correct the calibration so that the small error that is indicated is eliminated. However, because of the instability of the electron beam, illustrated by Figure

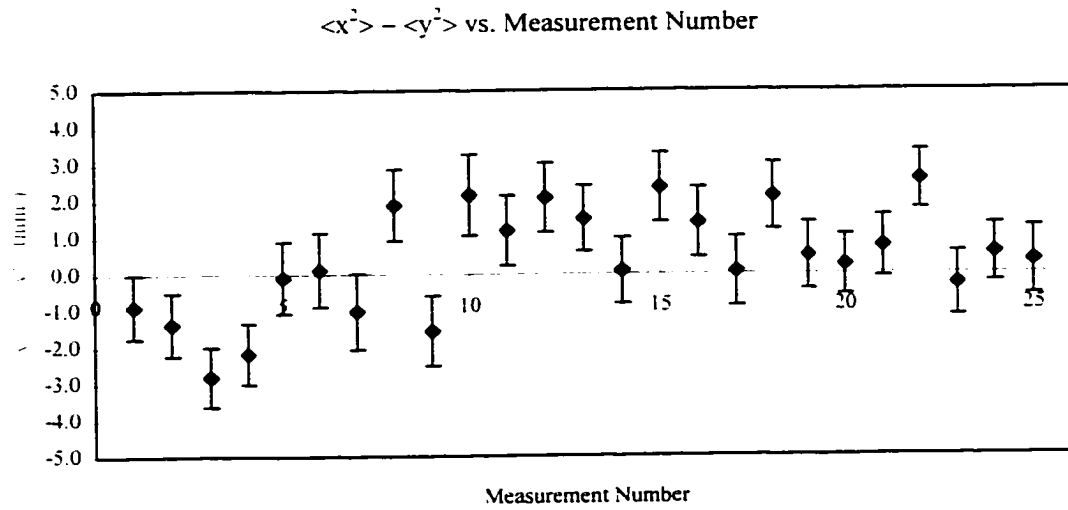
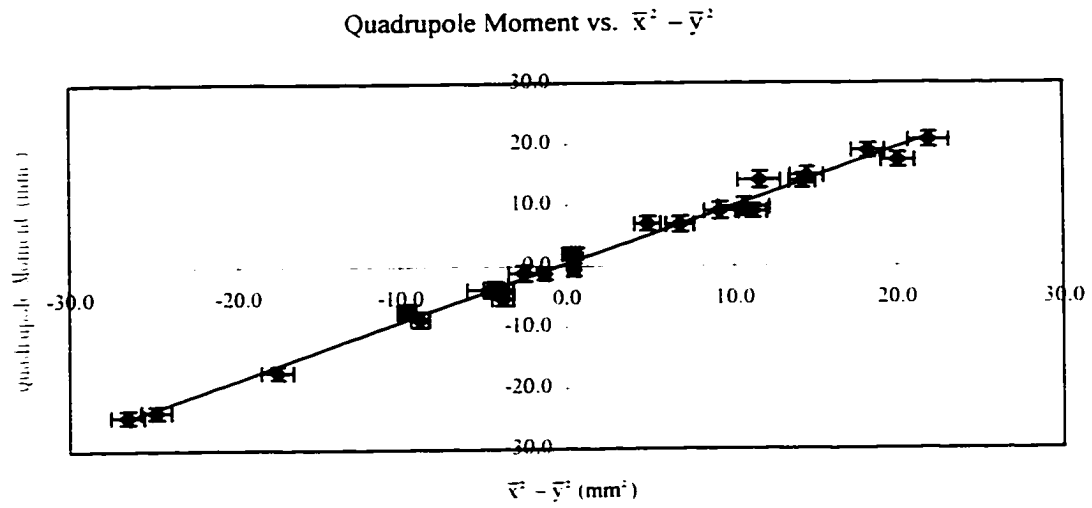


Figure 5-9: a) Quadrupole moment versus $\bar{x}^2 - \bar{y}^2$. The slope of the fit line is 0.95 ± 0.021 . b) $\langle x^2 \rangle - \langle y^2 \rangle$ versus measurement number for the same data points shown in a). Each point is the average of 99 beam shots.

5-8b and the previous section, it is uncertain how much faith one can put into this calibration check. Also, this experiment says nothing about the constant term in Equation 4-7. Therefore, no change to the calibration found in Chapter 4 was made.

One other note. This experiment was performed several times and in each case the data yielded plots very much like that shown in Figure 5-9, even though the amount of charge per bunch varied by as much as a factor of 20. This demonstrates the BPM's expected insensitivity to charge when measuring the beam position and quadrupole moment.

5.5 Emittance measurements

The final experiments presented in this chapter are intended to verify that the emittance of the beam can be measured by Miller's technique utilizing the BPM and the beam line components shown in Figure 5-1. The main difficulty is that there is no independent verification that the emittance numbers obtained this way are, in fact, correct. As was discussed in the Introduction, one of the main reasons this method is being pursued is that there are no other satisfactory approaches to measuring the rms emittance of photo-injector electron beams. The validity of Miller's technique must be inferred by looking at the numerical error estimates and the behavior of the emittance as beam parameters are changed.

The first part of this section goes through the approach to a single emittance measurement. This will serve as an example and it can be assumed that all other emittance measurements are done in the same manner. The second part of this section shows the results of measuring the emittance of the beam with different amounts of

charge per bunch. It is expected that the emittance will increase as the charge is increased. The third part of this section shows the results of measuring the emittance with different amounts of magnetic flux on the photo-cathode. It can be shown that the emittance changes in a predictable way as the strength of the magnetic field in the photo-cathode region is changed [6], [30]. All of the emittance measurements presented here were done at an average beam energy of 7.77 MeV with an energy spread of less than 1 percent.

5.5.1 Single emittance measurement

To measure the emittance with Miller's technique, the first thing that needed to be done was to find focusing settings for quadrupoles 7 and 8 in Figure 5-1 that resulted in a stable matrix equation. This subject was discussed at length in Chapter 2 where it was concluded that a quadrupole triplet was a very good optics configuration for performing this measurement. As can be seen in Figure 5-1, however, only two quadrupoles were used in this experiment. Initially, three quadrupoles were used. However, it became apparent early on that the emittance of the SPA electron beam was not as good as was predicted by simulation. (This will be discussed later.) Because of this, the beam size tended to be bigger than anticipated and there was a substantial problem with the beam intercepting the beam pipe walls when the triplet configuration was used. To minimize this problem, just the two quadrupoles were used. Although this does not provide as good a resolution as the triplet configuration, it proved to be adequate.

Utilizing the ideas presented in Chapter 2, 18 settings for quadrupoles 7 and 8 that produced a stable matrix equation with sufficient resolution were determined. Added to

these 18 settings is one more that is known to transport 100 percent of the electron beam from the accelerator exit to the experimental BPM. This 19th quadrupole setting allows one to determine if a significant amount of the beam is intercepting the beam pipe wall for any of the other 18. The matrix $\bar{\bar{A}}$ that results is shown in Figure 5-10. The figure of merit (FOM), as defined by Equation 2-9, for this matrix is

$$\text{FOM} = 0.30$$

This shows that these quadrupoles settings result in a matrix equation that is sufficiently stable.

After choosing the quadrupole settings that produce the matrix in Figure 5-10, considerable time was spent focusing the beam as it entered the section of beam line where the emittance measurements occurred (Figure 5-1). The goal was to adjust the properties of the entering electron beam so no beam was lost in the diagnostic section of beam line (Figure 5-1) for any of the 19 quadrupole settings chosen for the emittance measurement. Again, this was done by comparing the intensity of the beam at the BPM at the start of the SPA beam line to the intensity of the beam at the BPM in Figure 5-1. This task was complicated by the unstable nature of the beam intensity (Figure 5-6a and Figure 5-8a) and, in the end, was not accomplished with complete success. Very often measurements were discarded when too much scraping of the beam occurred.

When making an emittance measurement, the quadrupoles in Figure 5-1 were set to each of the 19 settings in turn and the beam was approximately centered in the BPM aperture using the steering coil. For each setting, 99 beam shots were captured and stored on the computer. Each beam shot typically contained 5 beam bunches. Each of these 5

$$\bar{\mathbf{A}} = \begin{bmatrix} 1.1450 & 2.9264 & 1.8697 & -0.8651 & -2.4034 & -1.6693 \\ 8.1735 & -0.3626 & 0.0040 & -0.0073 & 0.0060 & -0.0013 \\ 5.0447 & -1.4027 & 0.0975 & -0.0478 & -0.1145 & -0.0686 \\ 2.8484 & -1.7965 & 0.2833 & 0.2306 & -0.4483 & -0.2179 \\ 0.0033 & 0.1852 & 2.5660 & -0.0260 & 0.0067 & -0.0004 \\ 0.0578 & 0.7794 & 2.6251 & -0.0014 & -0.0140 & -0.0360 \\ 0.1694 & 1.3450 & 2.6699 & -0.0461 & -0.1495 & -0.1212 \\ 0.0127 & -0.0032 & 0.0002 & -9.1505 & -0.1079 & -0.0003 \\ 0.0048 & 0.0208 & 0.0227 & -6.0285 & 1.1742 & -0.0572 \\ 0.2427 & 0.4643 & 0.2221 & -3.3388 & 1.6799 & -0.2113 \\ 0.0289 & -0.0036 & 0.0001 & -0.0092 & 0.2934 & -2.3290 \\ 0.0016 & 0.0150 & 0.0350 & -0.0078 & -0.2723 & -2.3836 \\ 0.1237 & 0.3197 & 0.2067 & -0.0596 & -0.7340 & -2.2605 \\ 0.0643 & -0.0039 & 0.0001 & -5.3022 & -12.7231 & -7.6325 \\ 0.0184 & -0.0350 & 0.0167 & -4.6875 & -11.3255 & -6.8409 \\ 0.0001 & -0.0050 & 0.0668 & -4.0891 & -9.9595 & -6.0643 \\ 6.8308 & 15.4086 & 8.6894 & -0.0934 & -0.0209 & -0.0012 \\ 6.0439 & 13.7133 & 7.7786 & -0.0381 & 0.0330 & 0.0071 \\ 5.2439 & 11.9836 & 6.8464 & -0.0052 & 0.0313 & -0.0469 \end{bmatrix}$$

Figure 5-10: $\bar{\mathbf{A}}$ matrix associated with settings for quadrupoles in Figure 5-1 used to measure the electron beam emittance.

bunches were analyzed to find the intensity, \bar{x} , \bar{y} , and $\langle x^2 \rangle - \langle y^2 \rangle$. Any beam outside a 4 mm radius of the BPM center was then discarded because the BPM calibration for the quadrupole moment is not valid in this range (Chapter 4). Of the remaining beam shots, the average value of the intensity and $\langle x^2 \rangle - \langle y^2 \rangle$ was calculated for each quadrupole setting.

A typical result of such a measurement is shown in Figure 5-11 and Table 5-1. The charge per bunch was approximately 0.2 nC*. Figure 5-11 is a plot of the average beam intensity for each of the 19 quadrupole settings. The second column of Table 5-1 presents the average measured value of $\langle x^2 \rangle - \langle y^2 \rangle$ for each of the 19 quadrupole settings for one of the beam bunches. Using this data and the matrix $\bar{\bar{A}}$ shown in Figure 5-10, one can solve for the rms beam parameters as described in Chapter 2, yielding:

$$\langle x^2 \rangle = 3.46 \text{ mm}^2 \pm 0.408 \text{ mm}^2 .$$

$$\langle xx' \rangle = -3.51 \text{ mm mrad} \pm 0.582 \text{ mm mrad} .$$

$$\langle x'^2 \rangle = 4.26 \text{ mrad}^2 \pm 1.004 \text{ mrad}^2 .$$

$$\langle y^2 \rangle = 0.95 \text{ mm}^2 \pm 0.333 \text{ mm}^2 .$$

$$\langle yy' \rangle = -0.22 \text{ mm mrad} \pm 0.582 \text{ mm mrad} .$$

and

$$\langle y'^2 \rangle = 1.42 \text{ mrad}^2 \pm 0.933 \text{ mrad}^2 .$$

The error estimates are obtained from the well known covariance matrix as derived in Appendix F and assume the measurement errors are normally distributed.

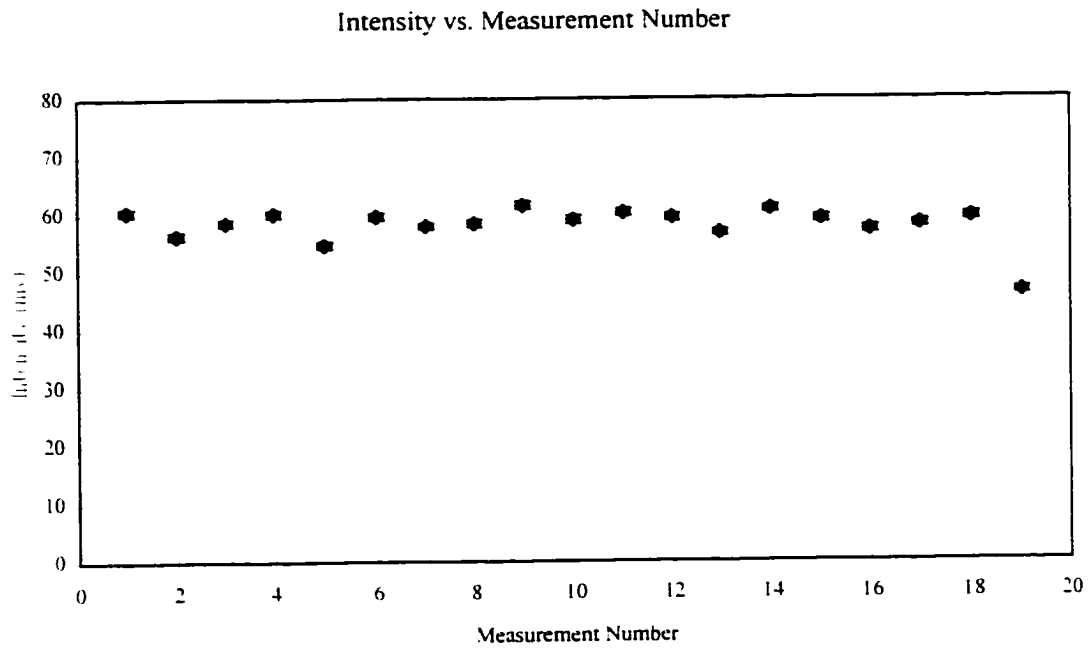


Figure 5-11: Average beam intensity (sum of four BPM electrodes) at BPM versus measurement number for emittance measurement a charge equal to approximately 0.2 nC/bunch.

Table 5-1: Average measured value of $\langle x^2 \rangle - \langle y^2 \rangle$, predicted value of $\langle x^2 \rangle - \langle y^2 \rangle$ (from fit) and the difference between them for each quadrupole setting in emittance measurement for charge equal to approximately 0.2 nC/bunch*.

Measurement Number	Average value of $\langle x^2 \rangle - \langle y^2 \rangle$ (mm ²)	Error estimate. σ . for average value of $\langle x^2 \rangle - \langle y^2 \rangle$ (mm ²)	Predicted value of $\langle x^2 \rangle - \langle y^2 \rangle$ (mm ²)	Difference between predicted value and measured value (mm ²)
1	-2.6	± 0.90	-1.0	-1.6
2	23.1	± 0.95	29.6	-6.4
3	26.3	± 0.82	22.7	3.6
4	23.3	± 0.91	16.9	6.3
5	6.6	± 0.87	10.3	-3.7
6	8.3	± 0.81	8.6	-0.3
7	7.5	± 0.89	7.1	0.5
8	-8.6	± 0.82	-8.6	0.1
9	-7.1	± 0.86	-6.1	-1.0
10	-2.7	± 0.77	-3.7	1.0
11	-2.9	± 0.76	-3.3	0.3
12	-3.7	± 0.83	-3.2	-0.5
13	-2.6	± 0.81	-2.9	0.3
14	-12.5	± 0.77	-12.8	0.3
15	-11.8	± 0.85	-11.4	-0.4
16	-10.0	± 0.80	-10.0	0.0
17	11.3	± 0.82	6.5	4.8
18	11.2	± 0.86	5.9	5.3
19	-6.0	± 0.85	5.2	-11.1

Using (2-1) and (2-2), the x and y rms emittances can be calculated, yielding

$$\varepsilon_x = 1.6 \text{ mm mrad} \pm 0.49 \text{ mm mrad}$$

and

$$\varepsilon_y = 1.1 \text{ mm mrad} \pm 0.36 \text{ mm mrad} .$$

Multiplying these number by the relativistic factor $\beta\gamma$ to obtain the normalized emittances (Equations 2-3 and 2-4) gives

$$\varepsilon_{xn} = 25.2 \text{ mm mrad} \pm 7.94 \text{ mm mrad}$$

and

$$\varepsilon_{yn} = 18.5 \text{ mm mrad} \pm 5.89 \text{ mm mrad} .$$

The formulas for the error estimates are derived in Appendix F. Again, normally distributed measurement errors are assumed.

After performing the fit to estimate the rms beam parameters, one can then use those estimates to calculate the predicted values of $\langle x^2 \rangle - \langle y^2 \rangle$, shown in column 4 of Table 5-1. In column 5 of Table 5-1 is shown the difference between the average measured value of $\langle x^2 \rangle - \langle y^2 \rangle$ and the predicted value. From this column, the value of σ , the error in the measurements, is estimated to be $\pm 4.71 \text{ mm}^2$ (See Appendix F). This is much different from the values of σ in column 2 of Table 5-1. It is apparent that there is often poor agreement between the measured and predicted values.

To improve the fit to the data, data points where excessive beam scraping occurred need to be eliminated. For instance, in Figure 5-11, the intensity for measurement 19 is obviously much lower than the rest. The electron beam, for whatever reason, changed, or, more likely, was intercepting the beam pipe walls during this measurement. So, this

data point is thrown away. Although less obvious, the same is true for measurements 2, 3 and 5. Now, doing a fit without these data points yields

$$\langle x^2 \rangle = 5.34 \text{ mm}^2 \pm 0.250 \text{ mm}^2 .$$

$$\langle xx' \rangle = -4.07 \text{ mm mrad} \pm 0.169 \text{ mm mrad} .$$

$$\langle x'^2 \rangle = 4.37 \text{ mrad}^2 \pm 0.270 \text{ mrad}^2 .$$

$$\langle y^2 \rangle = 0.97 \text{ mm}^2 \pm 0.069 \text{ mm}^2 .$$

$$\langle yy' \rangle = -0.20 \text{ mm mrad} \pm 0.121 \text{ mm mrad} .$$

and

$$\langle y'^2 \rangle = 1.41 \text{ mrad}^2 \pm 0.194 \text{ mrad}^2 .$$

The emittances are now calculated to be:

$$\varepsilon_x = 2.60 \text{ mm mrad} \pm 0.079 \text{ mm mrad}$$

and

$$\varepsilon_y = 1.15 \text{ mm mrad} \pm 0.067 \text{ mm mrad} .$$

Or,

$$\varepsilon_{xn} = 42.1 \text{ mm mrad} \pm 1.29 \text{ mm mrad}$$

and

$$\varepsilon_{yn} = 18.6 \text{ mm mrad} \pm 1.08 \text{ mm mrad} .$$

The estimated error in these beam parameters is much lower than it was before.

Taking the new estimated rms beam parameters, one can again predicted the value of $\langle x^2 \rangle - \langle y^2 \rangle$ for each of the measurements kept. The result is Table 5-2. From column 5 the value of σ , the error in the measurements, is now estimated to be $\pm 0.98 \text{ mm}^2$ (See

Table 5-2: Same as Table 5-1, but measurements 2, 3, 5 and 19 are all discarded because of beam scraping.

Measurement Number	Average value of $\langle x^2 \rangle - \langle y^2 \rangle$ (mm ²)	Error estimate. σ , for average value of $\langle x^2 \rangle - \langle y^2 \rangle$ (mm ²)	Predicted value of $\langle x^2 \rangle - \langle y^2 \rangle$ (mm ²)	Difference between predicted value and measured value (mm ²)
1	-2.6	± 0.90	-0.3	-2.3
4	23.3	± 0.91	23.3	0.0
6	8.3	± 0.81	8.7	-0.4
7	7.5	± 0.89	7.1	0.4
8	-8.6	± 0.82	-9.3	0.7
9	-7.1	± 0.86	-5.7	-1.4
10	-2.7	± 0.77	-4.0	1.3
11	-2.9	± 0.76	-3.4	0.5
12	-3.7	± 0.83	-3.3	-0.4
13	-2.6	± 0.81	-2.7	0.1
14	-12.5	± 0.77	-12.8	0.3
15	-11.8	± 0.85	-11.3	-0.5
16	-10.0	± 0.80	-10.3	0.3
17	11.3	± 0.82	10.8	0.5
18	11.2	± 0.86	10.2	1.0

Appendix F). This is much closer to the values of σ given in column 3 than the is previous value of $\pm 4.71 \text{ mm}^2$.

It might be argued that there is no reason to expect that the estimated value of σ from the fit be anywhere near the values of σ in column 3. Based on the stability experiments presented in the previous sections it should be much bigger. However, obtaining a smaller estimated value of σ was not the reason that data points were discarded. That was based solely on concerns that the beam was scraping. The fact that the estimated value of σ did approach the values of σ in column 3 is quite remarkable. In fact, this was a typical behavior. Based on observation, whatever beam fluctuations that caused the large changes in the average value of $\langle x^2 \rangle - \langle y^2 \rangle$ shown in the stability experiments seemed to be damped when quadrupoles 7 and 8 were set to their measurement values. Unfortunately, no experiments were done during this run cycle to verify this quantitatively

5.5.2 On the question of beam scraping

The last section presented an example of a fairly typical emittance measurement using Miller's method on SPA. However, when analyzing the data certain data points were discarded to improve the fit to the model. As it turns out, this was also typical. Sometimes, as was the case with measurement 19 in the example, discarding a data point was easily justifiable. Obviously, some kind of beam scraping had occurred. However, as is the case with at least one of the other three data points that were thrown away, arguing that the beam was intercepting the beam pipe is not always so easy. As can be

seen by comparing Figures 5-8a and 5-11, the fluctuations in intensity seen in the emittance measurement (Figure 5-11) are not so different from the fluctuations in intensity when no focusing changes are made (Figure 5-8a).

The risk one takes when throwing away “bad” data points is that the fault may not be in the data, but in the model used to fit it. By throwing out data to make the fit better, one could be ignoring a physical effect that the model does not take into account.

To verify that this is not true here, Miller’s emittance measurement was simulated using the particle code PARMELA[21]. First, a beam bunch containing 20,000 particles and having a Gaussian distribution was generated. Its rms beam parameters were

$$\langle x^2 \rangle = 5.26 \text{ mm}^2 .$$

$$\langle xx' \rangle = -3.97 \text{ mm mrad} .$$

$$\langle x'^2 \rangle = 4.31 \text{ mrad}^2 .$$

$$\langle y^2 \rangle = 1.08 \text{ mm}^2 .$$

$$\langle yy' \rangle = -0.25 \text{ mm mrad} .$$

and

$$\langle y'^2 \rangle = 1.39 \text{ mrad}^2 .$$

The beam bunch has an energy spread of 1 percent and a FWHM length of 3 mm longitudinally. This is about what is expected of the SPA beam. The rms beam parameters were chosen to be close to those measured in the example from the last section. The charge was assumed to be 1 nC in order to exaggerate the space charge effect, if any. A Gaussian distribution was used because the point of this exercise is to

simulate a diffuse beam, not because that is the expected distribution of the SPA beam. The distribution of the SPA beam is generally unknown.

PARMELA takes this beam bunch and moves the particles down a simulation of the beam line shown in Figure 5-1 and includes non-linear effects as it does so. The simulation was run twice, one with a boundary where the real beam pipe should be and one without. When a particle in the first simulation "hit" the beam pipe, it was discarded.

After running both simulations for each of the 19 quadrupole settings, the value of $\langle x^2 \rangle - \langle y^2 \rangle$ was calculated for each. Also, for the first simulation, the number of particles left at the BPM position was recorded. A plot of this number versus measurement looks like Figure 5-12. As can be seen, the way in which the beam intensity increases from measurement 2 to 4 is very similar to that seen in Figure 5-11 for the real data.

Fitting the data from the first simulation and keeping all the data points yields Table 5-3 and the rms beam parameters in Table 5-4. Comparing the predicted values of $\langle x^2 \rangle - \langle y^2 \rangle$ for measurements 2 through 4 to the values calculated from the simulation, there is a similarity to the relationship between the predicted and measured values of $\langle x^2 \rangle - \langle y^2 \rangle$ in Table 5-1: the predicted value of $\langle x^2 \rangle - \langle y^2 \rangle$ for measurement 2 is larger than the measured value, the predicted value for measurement 3 is about right and the predicted value for measurement 4 is too small.

When the values of $\langle x^2 \rangle - \langle y^2 \rangle$ from the second simulation, where there is no beam pipe, were fit, the predicted values matched the simulated values. Also, if measurements

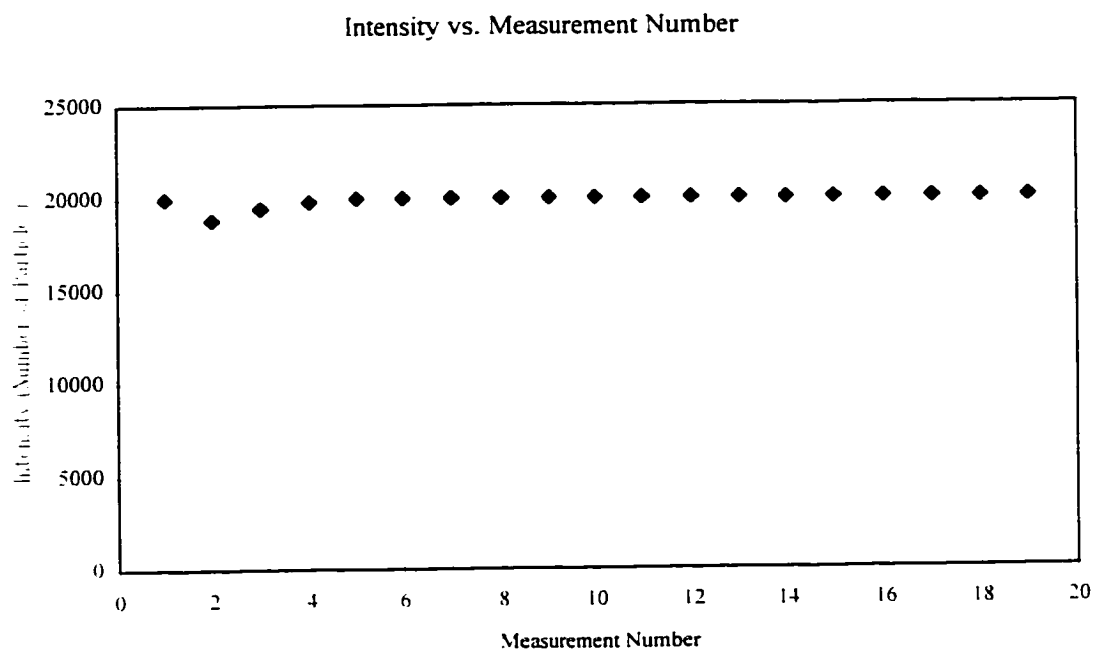


Figure 5-12: Intensity vs. measurement number for simulated emittance measurement.

Table 5-3: Value of $\langle x^2 \rangle - \langle y^2 \rangle$ from simulation, predicted value of $\langle x^2 \rangle - \langle y^2 \rangle$ (from fit) and the difference between them for each quadrupole setting in simulated emittance measurement with beam pipe.

Measurement Number	Calculated value of $\langle x^2 \rangle - \langle y^2 \rangle$ (mm ²) from simulation	Predicted value of $\langle x^2 \rangle - \langle y^2 \rangle$ (mm ²)	Difference between predicted value and simulated value (mm ²)
1	-0.3	-0.1	-0.2
2	32.7	34.8	-2.1
3	27.3	25.9	1.4
4	21.2	18.8	2.4
5	10.4	10.8	-0.4
6	8.6	9.2	-0.6
7	7.0	7.8	-0.8
8	-9.5	-9.5	0.0
9	-6.7	-6.6	-0.1
10	-3.8	-3.9	0.1
11	-3.6	-3.6	0.0
12	-3.6	-3.6	0.0
13	-3.1	-3.1	0.0
14	-14.1	-14.1	0.0
15	-12.6	-12.6	0.0
16	-11.1	-11.0	-0.1
17	13.1	12.9	0.2
18	11.8	11.6	0.2
19	10.2	10.1	0.1

Table 5-4: Values of the RMS beam parameters for different fits in simulated emittance measurements.

RMS Beam parameters	Actual values	Predicted values from fit using data from simulation with beam pipe	Predicted values from fit using data from simulation with beam pipe, but discarding data points 2 and 3	Predicted values from fit using data from simulation with beam pipe, but discarding data points 2, 3 and 4	Predicted values from fit using data from simulation without beam pipe
$\langle x^2 \rangle$ (mm ²)	5.26	4.10	4.84	5.28	5.26
$\langle xx' \rangle$ (mm mrad)	-3.97	-3.51	-3.71	-3.93	-3.92
$\langle x'^2 \rangle$ (mrad ²)	4.31	4.49	4.29	4.34	4.34
$\langle y^2 \rangle$ (mm ²)	1.08	1.05	1.05	1.05	1.06
$\langle yy' \rangle$ (mm mrad)	-0.25	-0.25	-0.25	-0.24	-0.24
$\langle y'^2 \rangle$ (mrad ²)	1.39	1.58	1.57	1.57	1.57

2 through 4 are discarded from the first simulation. then the fit to that simulated data is also very good. Table 5-4 shows the results for the rms beam parameters for several scenarios.

What the simulation without beam pipe boundaries shows is that there are no unexpected discrepancies between the model and what is really going on in the beam dynamics. The linear model is quite good, even at a relatively high charge of 1 nC per beam bunch.

What is apparent from the first simulation, where the beam pipe was present, is that the beam intercepting the pipe wall is a problem. From this one can conclude that throwing away data points because it is suspected that beam scraping has taken place is acceptable. In fact, from simulation, a good rule of thumb is that, when $\langle x^2 \rangle - \langle y^2 \rangle$ gets bigger than about $\pm 20 \text{ mm}^2$, beam scraping should be looked for carefully.

What this simulation does not address is the difficulty of distinguishing beam scraping from the inherent instability of the electron beam. As has already been established, changes in beam parameters and intensity are to be expected as a normal property of the beam. Determining which changes are due to the beam intercepting the wall is often arbitrary. This is not a very satisfactory solution, but until improvements to the stability of the electron beam are made it is unavoidable.

5.5.3 Emittance versus bunch charge

To verify that this method for measuring the emittance actually works is difficult. We would like to compare the numbers from this technique to others. However, as has

already been discussed, there are no other methods that we trust because of the unique qualities of a photoinjector beam. This limits us to more a more indirect approach.

One way to verify Miller's technique is to vary the emittance in a predictable way. For instance, as the charge per beam bunch is increased, we expect the emittance to increase. By measuring the emittance at different charge levels, a definite trend should emerge. In this experiment, the emittance of the beam is measured versus the charge per bunch of the beam. The charge per bunch is the only variable changed. The focusing elements upstream from the experimental section are kept constant. The emittance at each charge level was measured using the method described in section 5.5.1. Each beam shot contained 5 bunches. The emittance for each bunch was measured at each charge level. The average of these 5 emittances at each charge level is plotted in Figure 5-13. The x emittance shows a definite upward trend, as expected. The trend for the y emittance is less clear, although it does seem to increase as well.

5.5.4 Emittance versus magnetic field

A better check of the efficacy of Miller's emittance measurement is to measure the emittance as the magnetic field on the cathode is changed. In Figure I-1, three solenoids are shown around the front end of the SPA photoinjector. The two large solenoids are used to focus the beam as it is accelerated. The smaller bucking coil is used to cancel the magnetic fields of the two larger solenoids in the region of the photo-cathode. What will be shown is that, as the current through the bucking coil is moved away from its proper value, the emittance of the electron beam will increase.

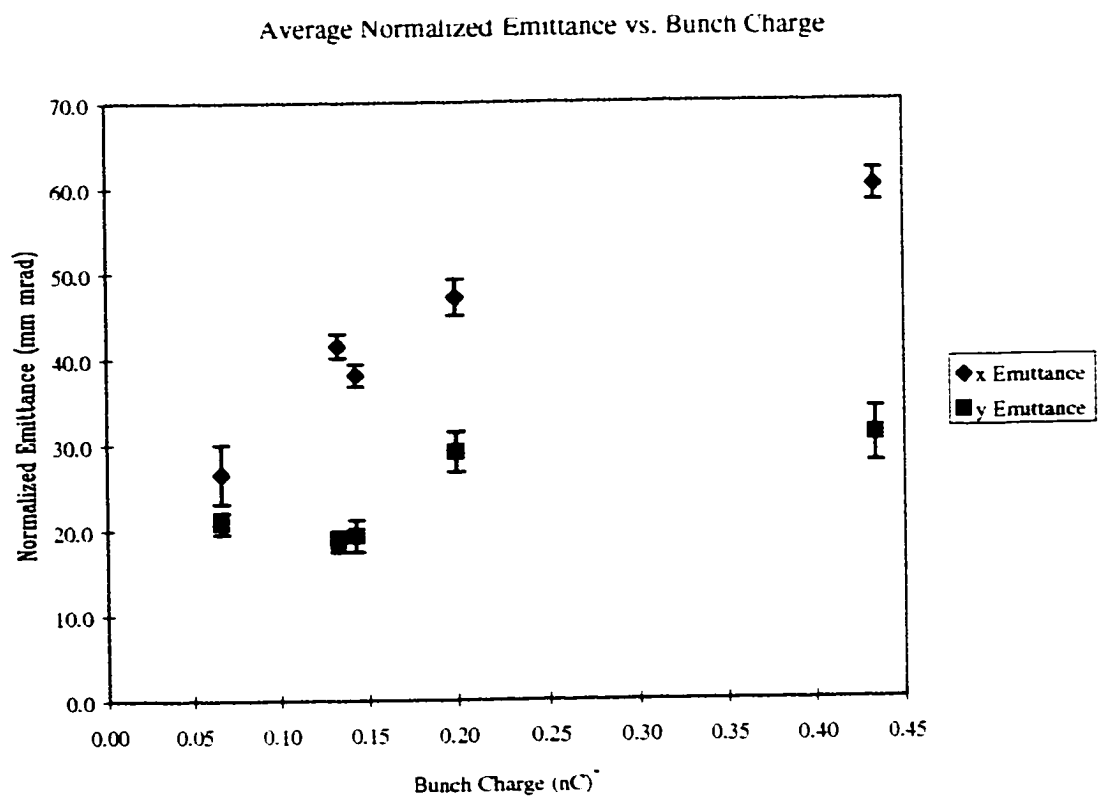


Figure 5-13: A plot of normalized emittance versus bunch charge.

The front end of the SPA photoinjector is designed so that the electric and magnetic fields are cylindrically symmetric about the axis that runs through the center of the cathode. Therefore,

$$\frac{\partial \phi}{\partial \theta} = \frac{\partial \bar{\mathbf{A}}}{\partial \theta} = 0. \quad (5-1)$$

where ϕ is the scalar potential and $\bar{\mathbf{A}}$ is the vector potential. The equations of motion for a charged particle in cylindrical coordinates are

$$\begin{aligned} \frac{d}{dt}(\gamma m \dot{r}) - \gamma m r \dot{\theta}^2 &= q(E_r + r\dot{\theta}B_z - \dot{z}B_\theta), \\ \frac{1}{r} \frac{d}{dt}(\gamma m r^2 \dot{\theta}) &= q(E_\theta + \dot{z}B_r - r\dot{z}B_z), \end{aligned} \quad (5-2)$$

and

$$\frac{d}{dt}(\gamma m \dot{z}) = q(E_z + r\dot{\theta}B_\theta - r\dot{\theta}B_r) [6].$$

Using (5-1), we have

$$E_\theta = -\frac{\partial A_\theta}{\partial t},$$

$$B_r = -\frac{\partial A_\theta}{\partial z}$$

and

$$B_z = \frac{1}{r} \frac{\partial}{\partial r}(rA_\theta).$$

Substituting these into Equation 5-2 gives

$$\frac{1}{r} \frac{d}{dt}(\gamma m r^2 \dot{\theta}) = q \left(\frac{\partial A_\theta}{\partial t} + \dot{r} \frac{\partial A_\theta}{\partial r} + \dot{z} \frac{\partial A_\theta}{\partial z} + \frac{\dot{r} A_\theta}{r} \right)$$

or

$$\frac{d}{dt}(\gamma m r^2 \dot{\theta} + q r A_{\theta}) = 0.$$

Therefore,

$$\gamma m r^2 \dot{\theta} + q r A_{\theta} = \text{constant} . \quad (5-3)$$

This is equivalent to saying that the canonical angular momentum in the Hamiltonian formalism is a conserved quantity when the system has cylindrical symmetry.

The magnetic flux through the circle defined by the radial position of the particle is

$$\psi = \int \vec{B} \cdot d\vec{S} = \int (\nabla \times \vec{A}) \cdot d\vec{S} = \oint \vec{A} \cdot d\vec{l} = 2\pi r A_{\theta} \quad [6].$$

Therefore (5-3) can be rewritten as

$$\gamma m r^2 \dot{\theta} + \frac{q}{2\pi} \psi = \text{constant} . \quad (5-4)$$

This is known as Busch's theorem [6].

The bucking coil on the SPA photoinjector was incorporated in the design in order to nullify the magnetic fields from the other two solenoids on the surface of the cathode so that ψ in (5-4) is zero. When its current is not properly set, however, there will be a magnetic field perpendicular to the photocathode surface that is nearly constant with radius. Then ψ will be given by

$$\psi = \pi r_c^2 B_c .$$

where B_c is the magnetic field on the cathode and r_c is the radial position of the electron at the cathode. Equation (5-4) now becomes

$$\gamma m r_c^2 \dot{\theta} - \frac{e r_c^2 B_c}{2} = \text{constant} .$$

This is significant because, when the electrons are emitted from the cathode surface, their angular velocity will be very small. So, we can say that

$$\gamma m r^2 \dot{\theta} + \frac{q}{2\pi} \psi \cong -\frac{e r_c^2 B_c}{2}, \quad (5-5)$$

where r is the radial position of the electron at some point downstream.

As the beam is accelerated away from the cathode, the magnetic fields, and therefore the magnetic flux, from the solenoids decrease to zero. According to (5-5) the angular velocities of the electrons grow to compensate. This leads to an increase in the x and y momenta of the electrons as they pass into the field free region downstream from the cathode, enlarging the area of the beam in x and y phase space. Since the x and y rms emittances are proportional to this area, they also increase.

An analysis of the beam envelope equation [6], [30], shows that the emittance increases with the magnetic field on the cathode according to

$$\varepsilon_n = \sqrt{\varepsilon_i^2 + \left(\frac{e R_c^2 B_c}{4mc}\right)^2} \quad (5-6)$$

where ε_n is the normalized rms emittance, ε_i is some intrinsic emittance and R_c is the radius of the cathode. This equation holds for both the x and y directions although the intrinsic emittance will be different for each. By moving the current of the bucking coil away from its proper value and using Miller's technique to measure the emittance, a distinct curve that follows (5-6) should emerge. The results of such an experiment are shown in Figure 5-14.

The fitted curves in Figure 5-14 are slightly different. The magnetic field dependent term was slightly bigger (20%) for the x direction than it was in the y direction for a

given magnetic field. However, the fits to (5-6) are quite good considering the simple model used to obtain the dependence of the emittance on the magnetic field.

According to Figure 5-14, the x emittance is determined with better accuracy than the y emittance. This is not a failure of the technique, but a problem with the signal to noise ratio. The poor stability of the electron beam limits the resolution of Miller's emittance measurement. It would appear that oftentimes the value of the y emittance falls beneath this resolution. With improvements to the beam, better values with smaller error bars for the y emittance will result.

*The charge per bunch was measured using a wall current monitor. Recent experiments have call into question its calibration. Therefore all charge measurements are not accurate to better than a factor of two.

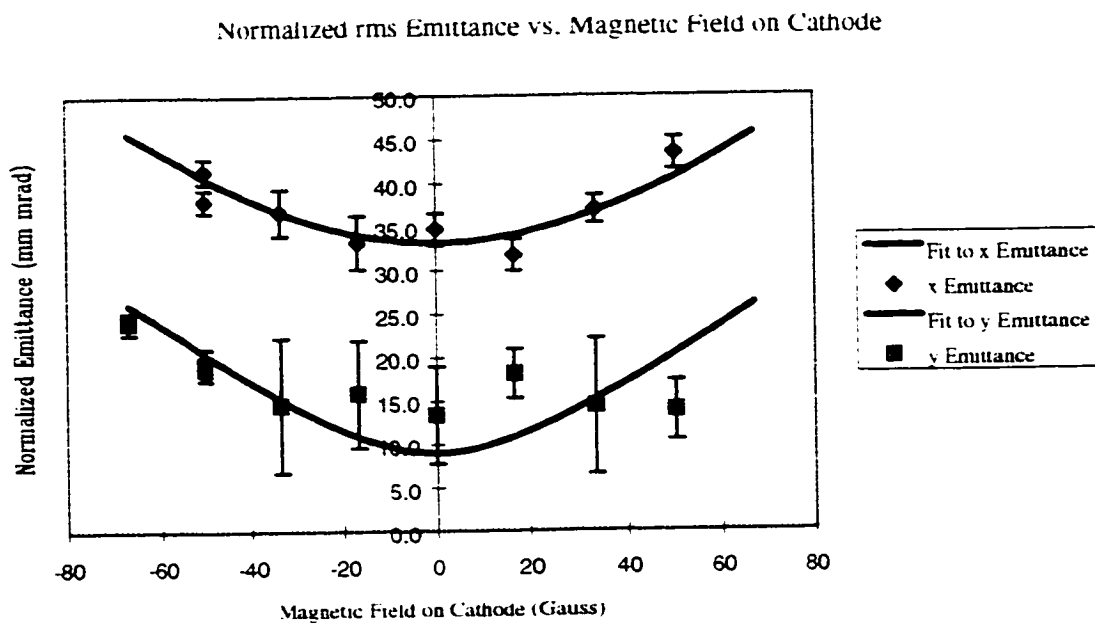


Figure 5-14: Emittance versus magnetic field on photo-cathode.

CONCLUSION

The goal of this thesis was to present a sound theoretical basis for measuring both the rms emittance and the rms pulse length using BPMs and to demonstrate Miller's emittance measurement technique experimentally. This has been achieved. However, in the process some questions were raised and problems encountered.

The poor stability of the SPA electron beam presented the greatest obstacle to implementing Miller's emittance measurement successfully. The hope we have is to use Miller's method as a routine emittance measurement. To do this, however, the beam stability must be improved. At the time of this writing, changes are being made that should improve the stability considerably.

As was mentioned briefly in Chapter 5, the measured x and y emittances of the SPA beam were greater than anticipated. Simulations of the machine show that, at 1 nC per beam bunch, the normalized emittances should be about 10 mm mrad. At 0.2 nC per beam bunch, the normalized x emittance was three to four times this value. The normalized y emittance was, perhaps, more reasonable. It is not yet known why this discrepancy exists. Possible reasons are that the simulations are wrong, something in the beam line is causing the emittance to grow, the emittance measurement is flawed or, quite simply, we are not running the accelerator in an optimal fashion.

In its previous incarnation as the injector for the HIBAF facility[14], PARMELA

simulations of the injector and experiments agreed quite well. For this reason, we have great faith in PARMELA to accurately predict the performance of SPA. For the simulations to be incorrect, a substantial physical effect would have to be neglected.

In our PARMELA simulations of SPA, it is assumed by the code that the photo-cathode emits electrons uniformly when struck by the laser beam. However, we know that this is not true in the real accelerator. When fabricated, a photo-cathode's surface does not have a uniform quantum efficiency. This is a result of the fabrication process. These discrepancies are small, and simulations done in the past indicate that they do not degrade the beam quality significantly. However, it is not clear what happens to the photo-cathode surface over time after it is placed inside the accelerator.

Because of limited access to the photo-cathode preparation equipment, the photo-cathode that was in place when the emittance measurements presented here were performed was well over one year old and had been inside the accelerator for nine months. This is longer than any cathode of this type has been used. During this time the cathode was damaged by arcing in the accelerator cavities, it was poisoned on one occasion when a vacuum pump failed and its average quantum efficiency degraded by a factor of 20. It is unknown what this abuse did to the cathode surface. It is possible that the initial shape of the beam, because of the damage to the cathode, is the cause of the larger emittance.

There is also a possibility that some part of the SPA beam line is producing nonlinear forces that are causing substantial emittance growth. This is unlikely. However, the possibility should also be investigated.

There is also a chance that the emittance measurement is flawed somehow. However, I consider this to be the least likely explanation. Presented in this thesis is ample evidence that Miller's emittance method is sound. Also, based on the poor behavior of the beam, there is no reason to think that the emittance is any better than what was measured. The difficulties in transporting the beam and beam spot size on the two screens in the beam line tend to support the higher numbers.

The simplest explanation for the higher numbers is that the accelerator is not being run optimally. That is, the currents in the solenoids are such that the emittance of the beam is not minimized. The simulations are run such that the magnetic fields from the solenoids are very close to their optimum value. Hence, if the currents in the real solenoids are not set properly, simulation and experiment will not agree. Since the magnetic fields from the solenoids have never been mapped, setting their currents properly is not automatic. With experience, this condition should improve.

Appendices

Appendix A

Appendix A

CHARGE DISTRIBUTION INDUCED ON INNER SURFACE OF BEAM PIPE DUE TO RELATIVISTIC ELECTRON BEAM

A.1 Introduction

Consider Figure A-1. An electron bunch that is described in the lab frame by the density distribution $\rho_L(\vec{x})$ traveling with a relativistic velocity, v , inside a metal pipe with radius a . The distribution function $\rho_L(\vec{x})$ is referenced to the coordinate system whose origin corresponds to the pipe center. The electric potential, Φ , is defined to be zero on the pipe. In the metal walls of the pipe, the electron bunch induces an image charge. A relationship between the bunch density distribution and this image charge will be derived.

The problem will be broken down into two parts. First, the problem is solved in the beam frame where $v = 0$. Then, to find the solution in the lab frame, a relativistic transformation is made.

A.2 Solution in beam frame

In the beam bunch's rest frame it has a density distribution that will be denoted by $\rho_B(\vec{x})$. To find the image charge distribution that is induced by the bunch, Poisson's equation must be solved,

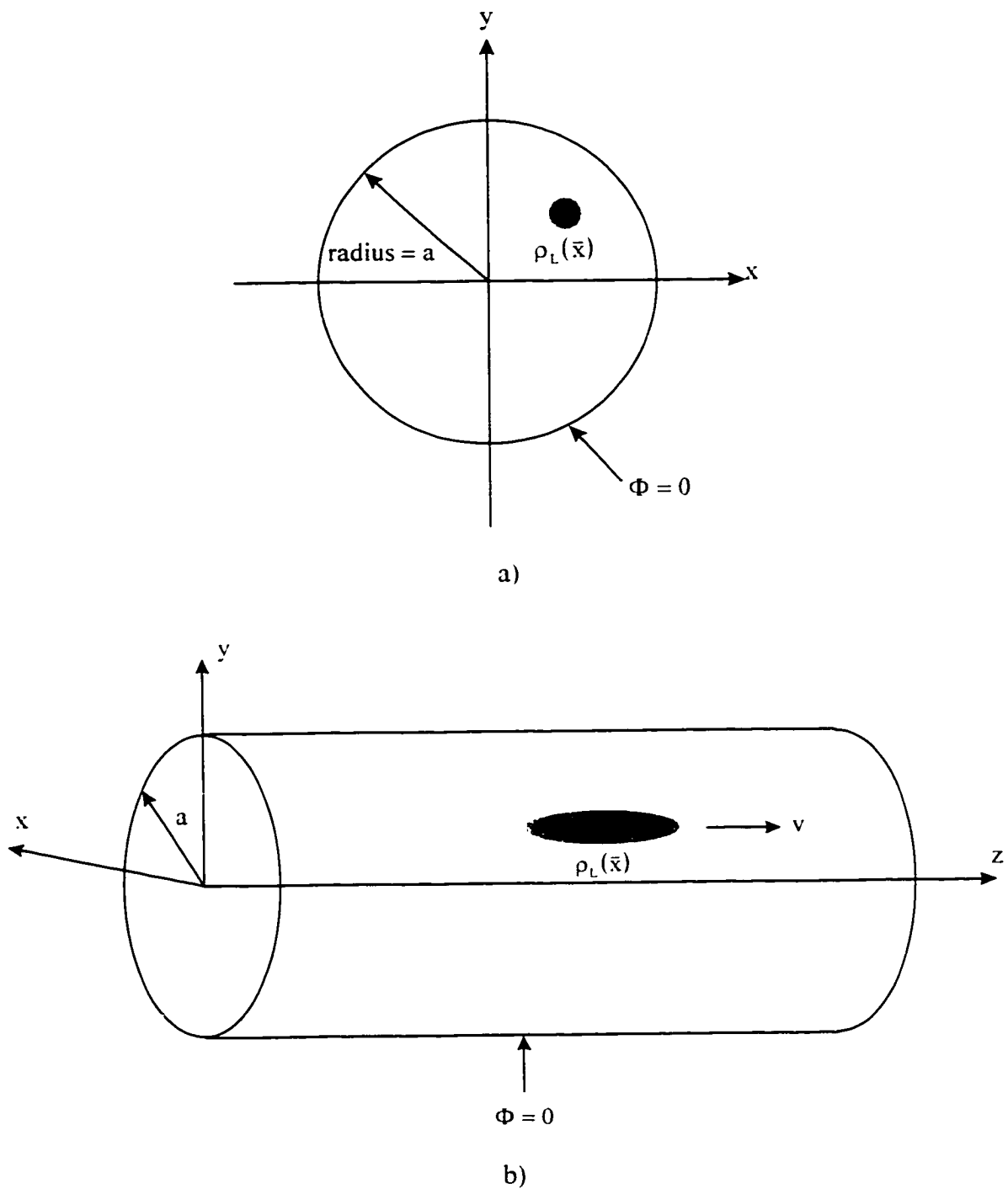


Figure A-1: Relativistic electron beam pulse in metal pipe: a) cross sectional view, b) longitudinal view.

$$\nabla^2 \Phi(\bar{x}) = 4\pi\rho_B(\bar{x}).$$

for the potential $\Phi(\bar{x})$ using the proper boundary conditions. This problem was first done by Smythe[31]. The image charge distribution on the pipe walls is then given by

$$\begin{aligned} \sigma(\theta, z) &= -\frac{1}{4\pi} \hat{n} \cdot \bar{E} \Big|_{r=a}, \quad \hat{n} = \hat{r} \\ &= -\frac{1}{4\pi} E_r \Big|_{r=a} = \frac{1}{4\pi} \frac{\partial \Phi(r, \theta, z)}{\partial r} \Big|_{r=a}. \end{aligned} \quad (\text{A-1})$$

In cylindrical coordinates, Poisson's equation becomes

$$\frac{\partial^2 \Phi(\bar{x})}{\partial r^2} + \frac{1}{r} \frac{\partial \Phi(\bar{x})}{\partial r} + \frac{1}{r^2} \frac{\partial^2 \Phi(\bar{x})}{\partial \theta^2} + \frac{\partial^2 \Phi(\bar{x})}{\partial z^2} = 4\pi\rho_B(\bar{x}). \quad (\text{A-2})$$

The boundary conditions on $\Phi(\bar{x})$ are

$$\Phi(\bar{x}) \Big|_{r=a} = 0 \quad (\text{A-3})$$

and

$$\Phi(\bar{x}) \Big|_{z \rightarrow \pm\infty} = 0. \quad (\text{A-4})$$

To solve for the potential, the Green's function, $G(\bar{x}, \bar{x}')$, is found. Then

$$\Phi(\bar{x}) = \int_{\text{Volume}} \rho_B(\bar{x}') G(\bar{x}, \bar{x}') d^3x' - \frac{1}{4\pi} \oint_{\text{Surface}} \Phi(\bar{x}') \frac{\partial G(\bar{x}, \bar{x}')}{\partial n'} da' \quad [32]. \quad (\text{A-5})$$

By evaluating the surface integral over the boundary where the potential is zero. (A-3)

and (A-4), (A-5) becomes

$$\Phi(\bar{x}) = \int_{\text{Volume}} \rho_B(\bar{x}') G(\bar{x}, \bar{x}') d^3x'. \quad (\text{A-6})$$

By definition, the Green's function has the following properties:

$$G(\bar{x}, \bar{x}') = G(\bar{x}', \bar{x}). \quad (\text{A-7})$$

$$\nabla^2 G(\bar{x}, \bar{x}') = -4\pi\delta(\bar{x} - \bar{x}') \quad (\text{A-8})$$

and $G(\bar{x}, \bar{x}')$ has the same boundary conditions as $\Phi(\bar{x})$. Therefore, from (A-3) and (A-4)

$$G(\bar{x}, \bar{x}') \Big|_{r=a} = 0 \quad (\text{A-9})$$

and

$$G(\bar{x}, \bar{x}') \Big|_{z \rightarrow z \pm \infty} = 0. \quad (\text{A-10})$$

In cylindrical coordinates, the Dirac delta function is given by

$$\delta(\bar{x} - \bar{x}') = \frac{1}{r} \delta(r - r') \delta(\theta - \theta') \delta(z - z').$$

Therefore, from (A-8),

$$\nabla^2 G(\bar{x}, \bar{x}') = -4\pi \frac{1}{r} \delta(r - r') \delta(\theta - \theta') \delta(z - z'). \quad (\text{A-11})$$

It is known that

$$\frac{1}{\pi} \int_0^{2\pi} \cos[n(\theta - \theta')] \cos[n'(\theta - \theta')] d\theta = \delta_{n,n'}. \quad (\text{A-12})$$

$$\frac{1}{\pi} \int_0^{2\pi} \sin[n(\theta - \theta')] \sin[n'(\theta - \theta')] d\theta = \delta_{n,n'}$$

and

$$\frac{2}{a^2 J_{\nu+1}^2(x_{\nu m})} \int_0^a r J_{\nu}\left(x_{\nu m} \frac{r}{a}\right) J_{\nu}\left(x_{\nu m'} \frac{r}{a}\right) dr = \delta_{m,m'} \quad (\text{A-13})$$

where $\nu \geq -1$ and $x_{\nu m}$ is the Bessel function zero[33]. Therefore, we can expand the function

$$\frac{1}{r} \delta(r - r') \delta(\theta - \theta')$$

in the following series[32]:

$$\begin{aligned} \frac{1}{r} \delta(r - r') \delta(\theta - \theta') = \sum_{n=0}^{\infty} a_n \sum_{m=1}^{\infty} J_n \left(x_{nm} \frac{r}{a} \right) \{ & A_{nm} \cos[n(\theta - \theta')] \\ & + B_{nm} \sin[n(\theta - \theta')] \} \end{aligned} \quad (\text{A-14})$$

where

$$a_n = \begin{cases} \frac{1}{2} & n = 0 \\ 1 & n \neq 0 \end{cases}.$$

$$\begin{aligned} A_{nm} &= \frac{2}{\pi a^2 J_{n+1}^2(x_{nm})} \int_0^{2\pi} d\theta \int_0^a dr r \frac{1}{r} \delta(r - r') \delta(\theta - \theta') J_n \left(x_{nm} \frac{r}{a} \right) \cos[n(\theta - \theta')] \\ &= \frac{2 J_n \left(x_{nm} \frac{r'}{a} \right)}{\pi a^2 J_{n+1}^2(x_{nm})}. \end{aligned}$$

and

$$\begin{aligned} B_{nm} &= \frac{2}{\pi a^2 J_{n+1}^2(x_{nm})} \int_0^{2\pi} d\theta \int_0^a dr r \frac{1}{r} \delta(r - r') \delta(\theta - \theta') J_n \left(x_{nm} \frac{r}{a} \right) \sin[n(\theta - \theta')] \\ &= 0. \end{aligned}$$

Expanding the Green's function in a similar fashion yields

$$G(\bar{x}, \bar{x}') = \sum_{n=0}^{\infty} a_n \sum_{m=1}^{\infty} Z_{nm}(z, z') J_n \left(x_{nm} \frac{r}{a} \right) A_{nm} \cos[n(\theta - \theta')]. \quad (\text{A-15})$$

The constants are the same as in (A-12) and $Z_{nm}(z, z')$ contains the z dependence of $G(\bar{x}, \bar{x}')$. (The sin term is dropped because $G(\bar{x}, \bar{x}') = G(\bar{x}', \bar{x})$ and $\sin[n(\theta - \theta')] \neq \sin[n(\theta' - \theta)]$). Therefore, it is expected that the sin term coefficients

should, in fact, be zero.) Substituting (A-15) into (A-11) yields

$$\begin{aligned} \nabla^2 G(\bar{x}, \bar{x}') &= \frac{\partial^2 G}{\partial r^2} + \frac{1}{r} \frac{\partial G}{\partial r} + \frac{1}{r^2} \frac{\partial^2 G}{\partial \theta^2} + \frac{\partial^2 G}{\partial z^2} = -4\pi \frac{1}{r} \delta(r-r') \delta(\theta-\theta') \delta(z-z'). \\ \sum_{n=0}^{\infty} a_n \cos[n(\theta-\theta')] \sum_{m=1}^{\infty} A_{nm} &\left\{ Z_{nm}(z, z') \left[\frac{\partial^2 J_n\left(x_{nm} \frac{r}{a}\right)}{\partial r^2} + \frac{1}{r} \frac{\partial J_n\left(x_{nm} \frac{r}{a}\right)}{\partial r} \right. \right. \\ &\left. \left. - \frac{n^2}{r^2} J_n\left(x_{nm} \frac{r}{a}\right) \right] + J_n\left(x_{nm} \frac{r}{a}\right) \frac{\partial^2 Z_{nm}(z, z')}{\partial z^2} \right\} = -4\pi \frac{1}{r} \delta(r-r') \delta(\theta-\theta') \delta(z-z'). \end{aligned}$$

Making the definition

$$x \equiv x_{nm} \frac{r}{a}.$$

this expression becomes

$$\begin{aligned} \sum_{n=0}^{\infty} a_n \cos[n(\theta-\theta')] \sum_{m=1}^{\infty} A_{nm} &\left\{ Z_{nm}(z, z') \left(\frac{x_{nm}}{a}\right)^2 \left[\frac{\partial^2 J_n(x)}{\partial x^2} + \frac{1}{x} \frac{\partial J_n(x)}{\partial x} - \frac{n^2}{x^2} J_n(x) \right] \right. \\ &\left. + J_n\left(x_{nm} \frac{r}{a}\right) \frac{\partial^2 Z_{nm}(z, z')}{\partial z^2} \right\} = -4\pi \frac{1}{r} \delta(r-r') \delta(\theta-\theta') \delta(z-z'). \end{aligned}$$

By using Bessel's equation.

$$\frac{\partial^2 J_n(x)}{\partial x^2} + \frac{1}{x} \frac{\partial J_n(x)}{\partial x} + \left(1 - \frac{n^2}{x^2}\right) J_n(x) = 0.$$

this becomes

$$\begin{aligned} \sum_{n=0}^{\infty} a_n \cos[n(\theta-\theta')] \sum_{m=1}^{\infty} A_{nm} J_n\left(x_{nm} \frac{r}{a}\right) &\left[\frac{\partial^2 Z_{nm}(z, z')}{\partial z^2} - \left(\frac{x_{nm}}{a}\right)^2 Z_{nm}(z, z') \right] \\ &= -4\pi \frac{1}{r} \delta(r-r') \delta(\theta-\theta') \delta(z-z'). \end{aligned}$$

Multiplying both sides of the equation by

$$\frac{1}{\pi} \cos[n'(\theta - \theta')] r J_{n'}\left(x_{n'm'} \frac{r}{a}\right)$$

and integrating over r and θ from 0 to a and 0 to 2π respectively gives

$$\begin{aligned} & \sum_{n=0}^{\infty} a_n \frac{1}{\pi} \int_0^{2\pi} \cos[n(\theta - \theta')] \cos[n'(\theta - \theta')] d\theta \sum_{m=1}^{\infty} A_{nm} \int_0^a r J_n\left(x_{nm} \frac{r}{a}\right) J_{n'}\left(x_{n'm'} \frac{r}{a}\right) dr \\ & \otimes \left[\frac{\partial^2 Z_{nm}(z, z')}{\partial z^2} - \left(\frac{x_{nm}}{a}\right)^2 Z_{nm}(z, z') \right] \\ & = -4\pi \frac{1}{\pi} \int_0^{2\pi} \int_0^a \cos[n'(\theta - \theta')] r J_{n'}\left(x_{n'm'} \frac{r}{a}\right) \frac{1}{r} \delta(r - r') \delta(\theta - \theta') \delta(z - z') dr d\theta. \end{aligned}$$

Using (A-12) and (A-13) yields

$$\begin{aligned} & a_n \frac{a^2 J_{n'+1}^2(x_{n'm'})}{2} A_{n'm'} \left[\frac{\partial^2 Z_{n'm'}(z, z')}{\partial z^2} - \left(\frac{x_{n'm'}}{a}\right)^2 Z_{n'm'}(z, z') \right] \\ & = -4 J_{n'}\left(x_{n'm'} \frac{r'}{a}\right) \delta(z - z'). \end{aligned}$$

From (A-14)

$$a_n \frac{a^2 J_{n'+1}^2(x_{n'm'})}{2} A_{n'm'} = J_{n'}\left(x_{n'm'} \frac{r'}{a}\right).$$

leaving the equation

$$\frac{\partial^2 Z_{nm}(z, z')}{\partial z^2} - \left(\frac{x_{nm}}{a}\right)^2 Z_{nm}(z, z') = -4\pi \delta(z - z') \quad (\text{A-16})$$

where the primes on n and m have been dropped for convenience.

To solve this differential equation, first simplify the notation by making the definition

$$k \equiv \frac{x_{nm}}{a}.$$

Then.

$$\frac{\partial^2 Z_{nm}(z, z')}{\partial z^2} - k^2 Z_{nm}(z, z') = -4\pi\delta(z - z').$$

Multiplying both sides of the equation by $\frac{\partial Z_{nm}(z, z')}{\partial z}$ and integrating, gives

$$\frac{1}{2}(Z'_{nm}(z))^2 - k^2 \frac{(Z_{nm}(z, z'))^2}{2} = -4\pi Z'_{nm}(z', z') + \text{constant}.$$

Equation (A-10) requires that, as $z \rightarrow \pm\infty$, Z goes to zero, and, as a consequence, so does its derivative. Therefore.

$$4\pi Z'_{nm}(z', z') + \text{constant} = 0.$$

leaving

$$\frac{(Z'_{nm}(z, z'))^2}{2} - k^2 \frac{(Z_{nm}(z, z'))^2}{2} = 0.$$

Therefore

$$Z_{nm}(z, z') = e^{\pm kz - C},$$

where C is some constant.

To determine the final form of the function $Z_{nm}(z, z')$, first rewrite the constant C in the following way:

$$C \rightarrow Ae^C.$$

This gives

$$Z_{nm}(z, z') = Ae^{\pm kz - C}.$$

From (A-10) and (A-7)

$$Z_{nm}(z, z') \Big|_{z \rightarrow \pm\infty} \rightarrow 0 \quad (\text{A-17})$$

and

$$Z_{nm}(z, z') = Z_{nm}(z', z). \quad (\text{A-18})$$

Now, consider the special case of a point charge located at \bar{x}_0 .

$$\Phi(\bar{x}) = \int_V \rho_B(\bar{x}') G(\bar{x}, \bar{x}') d^3x' = \int_V q \delta(\bar{x}' - \bar{x}_0) G(\bar{x}, \bar{x}') d^3x' = qG(\bar{x}, \bar{x}_0).$$

Therefore, z' can be considered the longitudinal position of the point charge. Given the symmetry of this problem, it is expected that the function $Z_{nm}(z, z')$ will be symmetric about that position. This, combined with (A-17) and (A-18) leads to the solution

$$Z_{nm}(z, z') = Ae^{-k|z-z'|}.$$

To find the amplitude, A , first take into account the discontinuity at $z = z'$. To do this, recall (A-16) and do the integration

$$\int_{z'-\epsilon}^{z'+\epsilon} \left[\frac{d^2 Z_{nm}(z, z')}{dz^2} - k^2 Z_{nm}(z, z') \right] dz = -4\pi \int_{z'-\epsilon}^{z'+\epsilon} \delta(z - z')$$

where $\epsilon \rightarrow 0$. This becomes

$$A(-k)e^{-k(z'-\epsilon-z')} - A(+k)e^{-k(z'-z'+\epsilon)} = -4\pi.$$

When $\epsilon \rightarrow 0$

$$A = \frac{2\pi}{k}.$$

Therefore

$$Z_{nm}(z, z') = \frac{2\pi a}{x_{nm}} e^{-\frac{x_{nm}}{a}(z-z')} \quad (\text{A-19})$$

Combining (A-19) and (A-15) results in

$$G(\bar{x}, \bar{x}') = \frac{4}{a} \sum_{n=0}^{\infty} a_n \cos[n(\theta - \theta')] \sum_{m=1}^{\infty} \frac{J_n\left(x_{nm} \frac{r'}{a}\right) J_n\left(x_{nm} \frac{r}{a}\right)}{x_{nm} J_{nm}^2(x_{nm})} e^{-\frac{x_{nm}}{a}(z-z')}$$

for the Green's function. Substituting this into (A-6) to find the potential and then putting the potential into (A-1) gives

$$\begin{aligned} \sigma(\theta, z) &= \frac{1}{\pi a} \int_{\mathcal{V}} \rho_B(\bar{x}') \sum_{n=0}^{\infty} a_n \cos[n(\theta - \theta')] \\ &\quad \otimes \sum_{m=1}^{\infty} \left(\frac{x_{nm}}{a}\right) \frac{J_n\left(x_{nm} \frac{r'}{a}\right) J'_n(x_{nm})}{x_{nm} J_{n+1}^2(x_{nm})} e^{-\frac{x_{nm}}{a}(z-z')} d^3x' \end{aligned}$$

Using

$$J'_n(x_{nm}) = -J_{n+1}(x_{nm}) [33],$$

and the final expression for the image charge in the beam rest frame is

$$\sigma(\theta, z) = \frac{-1}{\pi a^2} \int_{\mathcal{V}} \rho_B(\bar{x}') \sum_{n=0}^{\infty} a_n \cos[n(\theta - \theta')] \sum_{m=1}^{\infty} \frac{J_n\left(x_{nm} \frac{r'}{a}\right)}{J_n(x_{nm})} e^{-\frac{x_{nm}}{a}(z-z')} d^3x' \quad (\text{A-20})$$

where

$$a_n = \begin{cases} \frac{1}{2}, & n = 0 \\ 1, & n \neq 0 \end{cases}.$$

A.3 Surface charge distribution in lab frame

Now that the problem has been solved in the beam frame, a relativistic transformation is made to the lab frame. The situation is that depicted in Figure A-2. K is the lab frame, where one wishes to know the surface charge distribution and K' is the beam frame, where the surface charge distribution is already known. The frame K' moves with velocity, v , relative to the K frame in the z direction. In K' , the surface charge, from (A-20), is

$$\sigma'(\theta', z') = \frac{-1}{\pi a^2} \int \rho_B(\bar{x}'') \sum_{n=0}^{\infty} a_n \cos[n(\theta' - \theta'')].$$

$$\otimes \sum_{m=1}^{\infty} \frac{J_n\left(x_{nm} \frac{r''}{a}\right)}{J_n(x_{nm})} e^{-\frac{x_{nm}}{a} z' - z''} d^3 x'' \quad (\text{A-21})$$

To get the charge distribution in the lab frame, K , make the following transformations:

$$E_r = \gamma E'_r \Rightarrow \sigma = \gamma \sigma'$$

$$r' \rightarrow r.$$

$$\theta' \rightarrow \theta.$$

$$r'' \rightarrow r''.$$

$$\theta'' \rightarrow \theta''.$$

$$z' \rightarrow \gamma(z - \beta ct).$$

$$z'' \rightarrow \gamma(z'' - \beta ct).$$

$$d^3 x'' \rightarrow r'' dr'' d\phi'' \gamma dz'' = \gamma d^3 x''.$$

and

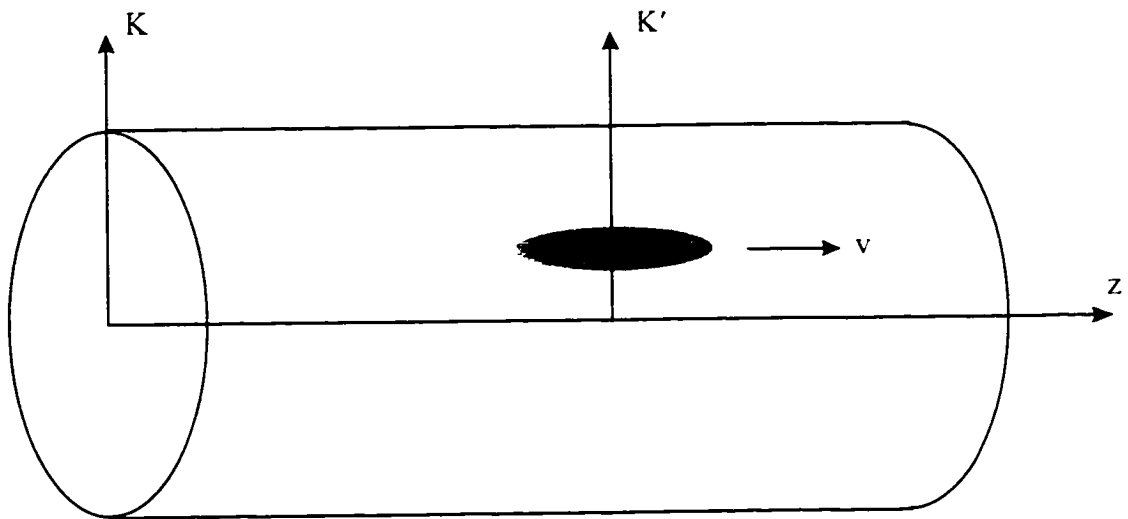


Figure A-2: Lab and beam frame for relativistic electron beam bunch traveling down beam pipe.

$$\rho_B(\bar{x}'') \rightarrow \rho_B(r'', \theta'', \gamma(z'' - \beta ct))$$

where

$$\beta = \frac{v}{c}$$

and

$$\gamma = \frac{1}{\sqrt{1 - \beta^2}}.$$

Substituting these into (A-21) gives

$$\begin{aligned} \sigma(\theta, z, t) = \frac{-\gamma^2}{\pi a^2} \int \rho_B(r'', \theta'', \gamma(z'' - \beta ct)) \sum_{n=0}^{\infty} a_n \cos[n(\theta - \theta'')] \\ \otimes \sum_{m=1}^{\infty} \frac{J_n\left(x_{nm} \frac{r''}{a}\right)}{J_n(x_{nm})} e^{-\frac{x_{nm}}{a} z - z''} d^3 x''. \end{aligned} \quad (\text{A-22})$$

In the lab frame, the bunch density distribution will be different from the bunch density distribution in the beam frame in two ways: the lab density distribution will be shorter because of length contraction, and, because of conservation of charge, it will also be more peaked. Therefore

$$\gamma \rho_B(r', \theta', \gamma(z' - \beta ct)) = \rho_L(r', \theta', z', t) \quad (\text{A-23})$$

where $\rho_L(r', \theta', z', t)$ is just the bunch density distribution in the lab frame. K. Substituting this into (A-22) and making the double primes single primes for convenience yields the final expression for the surface charge distribution in the lab frame.

$$\sigma(\theta, z, t) = \frac{-\gamma}{\pi a^2} \int_V \rho_L(r', \theta', z', t) \sum_{n=0}^{\infty} a_n \cos[n(\theta - \theta')] \otimes \sum_{m=1}^{\infty} \frac{J_n\left(x_{nm} \frac{r'}{a}\right)}{J_n(x_{nm})} e^{-\frac{x_{nm}}{a} z - z'} d^3x' \quad (\text{A-24})$$

where

$$a_n = \begin{cases} \frac{1}{2}, & n = 0 \\ 1, & n \neq 0 \end{cases}.$$

A.4 Relativistic approximation

As a final note, a useful approximation is derived that is valid when the electron beam is highly relativistic.

One definition of the Dirac delta function is

$$\delta(x - x') \equiv \lim_{\varepsilon \rightarrow 0} \frac{e^{-\frac{x-x'}{\varepsilon}}}{2\varepsilon}.$$

Making the definition

$$\varepsilon \equiv \frac{a}{\gamma x_{nm}}$$

gives

$$e^{-\frac{x_{nm}}{a} z - z'} = \frac{a}{\gamma x_{nm}} \frac{e^{-\frac{z-z'}{\frac{a}{\gamma x_{nm}}}}}{\frac{a}{\gamma x_{nm}}} = 2 \frac{a}{\gamma x_{nm}} \frac{e^{-\frac{z-z'}{\varepsilon}}}{2\varepsilon}.$$

When γ is large, then, one can make the approximation

$$e^{-\gamma \frac{x_{nm}}{a} |z-z'|} \cong 2 \frac{a}{\gamma x_{nm}} \delta(z-z').$$

Substituting this into (A-24) gives

$$\sigma(\theta, z, t) = \frac{-2}{\pi a} \int_{\text{area of pipe}} \rho_L(r', \theta', z', t) \sum_{n=0}^{\infty} a_n \cos[n(\theta - \theta')].$$

$$\otimes \sum_{m=1}^{\infty} \frac{J_n\left(x_{nm} \frac{r'}{a}\right)}{x_{nm} J_{nm}(x_{nm})} r' dr' d\theta'. \quad (\text{A-25})$$

From (A-13) any function of r can be expanded in the series

$$f(r) = \sum_{m=1}^{\infty} A_{vm} J_v\left(x_{vm} \frac{r}{a}\right)$$

where

$$A_{nm} = \frac{2}{a^2 J_{n-1}^2(x_{nm})} \int_0^a r f(r) J_n\left(x_{nm} \frac{r}{a}\right) dr.$$

Expanding the function

$$f(r) = \left(\frac{r}{a}\right)^n.$$

the relation

$$\left(\frac{r}{a}\right)^n = 2 \sum \frac{J_n\left(x_{nm} \frac{r}{a}\right)}{x_{nm} J_{n+1}(x_{nm})}$$

results. Therefore, (A-25) can be approximated by

$$\sigma(\theta, z, t) \cong \frac{-1}{2\pi a} \int_{\text{area of pipe}} \rho_L(r', \theta', z, t) \left\{ 1 + 2 \sum_{n=1}^{\infty} \left(\frac{r'}{a}\right)^n \cos[n(\theta - \theta')] \right\} r' dr' d\theta'.$$

The term inside the parentheses is the distribution function of an infinite line charge. (See Appendix B) This is a result of the well known "pan-caking" effect when charges become highly relativistic. The electric field lines become almost perpendicular to the direction of motion.

Appendix B

Appendix B

SURFACE CHARGE DISTRIBUTION ON INNER SURFACE OF CYLINDRICAL METAL PIPE DUE TO AN INFINITE LINE CHARGE INSIDE THE PIPE AND PARALLEL TO ITS AXIS

B.1 Introduction

In this appendix, the distribution function for the image charge induced on the inner surface of an infinite metal pipe due to an infinite line charge is calculated. The line charge is inside the pipe and parallel to its axis.

B.2 Constant potential surfaces due to two infinite line charges in free space

To begin, the constant potential surfaces that occur in the presence of two infinite line charges in free space are calculated. The line charges are parallel to each other.

Figure B-1 shows two infinite line charges perpendicular to the page and parallel to the z axis. One has a charge per unit length of λ and the other $-\lambda$. They are positioned at $(0,0)$ and $(0,d)$ respectively. The electric potential due to these line charges at some point (x,y) is given by

$$\Phi(x,y) = -2\lambda \ln r_1 + 2\lambda \ln r_2 \quad (\text{B-1})$$

where

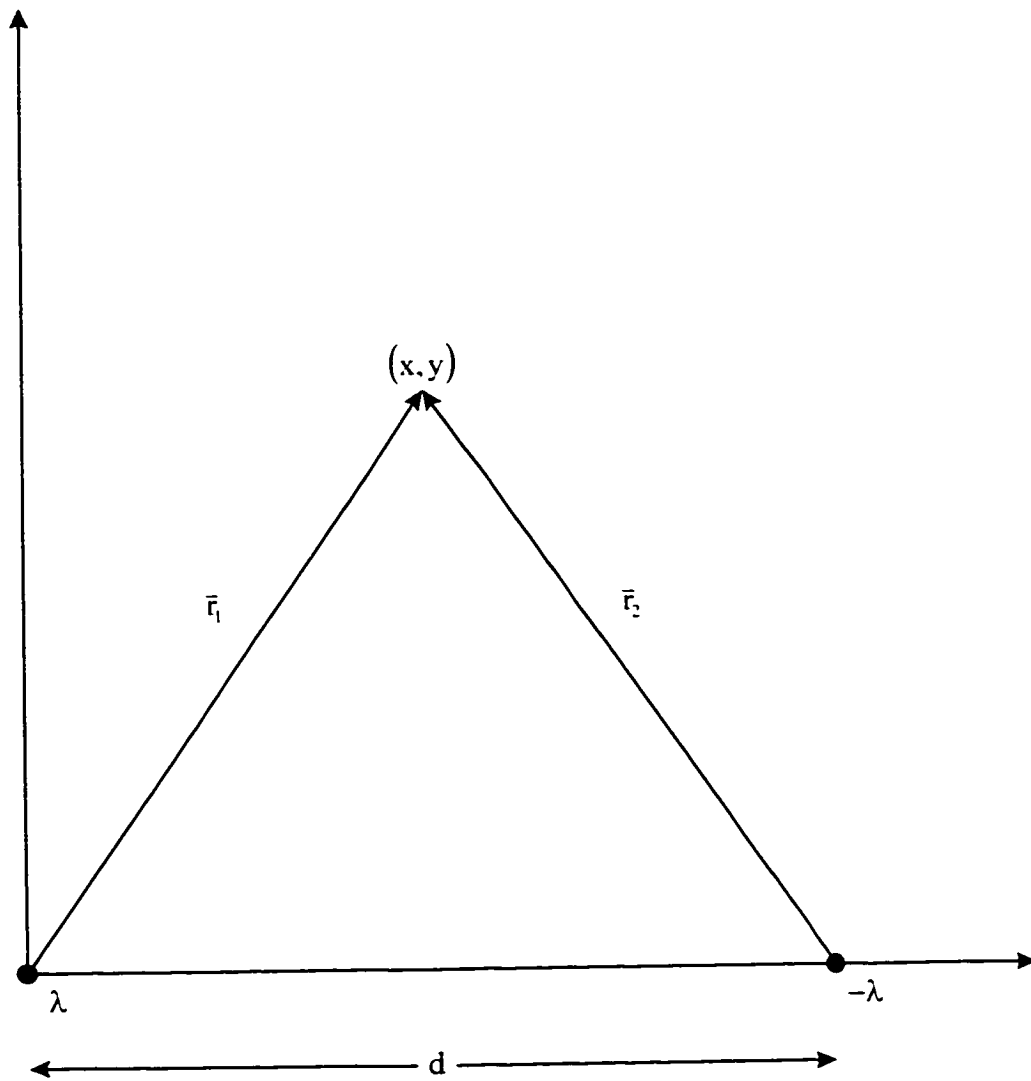


Figure B-1: Two infinite line charges parallel to the z axis with charge per unit length λ and $-\lambda$, respectively.

$$r_1^2 = x^2 + y^2 \quad (\text{B-2})$$

and

$$r_2^2 = (x - d)^2 + y^2. \quad (\text{B-3})$$

The constant potential surfaces occur when

$$\frac{r_1}{r_2} = k$$

where k is some constant. Squaring this expression leads to

$$r_1^2 = k^2 r_2^2.$$

Using (B-2) and (B-3) yields

$$x^2 + y^2 = k^2(x - d)^2 + k^2 y^2.$$

$$x^2 + y^2 = k^2 x^2 - 2k^2 dx + k^2 d^2 + k^2 y^2.$$

$$x^2(1 - k^2) + 2k^2 dx + y^2(1 - k^2) = k^2 d^2.$$

$$x^2 + 2x \frac{k^2 d}{1 - k^2} + y^2 = \frac{k^2 d^2}{1 - k^2}.$$

$$x^2 + 2x \frac{k^2 d}{1 - k^2} + \frac{k^4 d^2}{(1 - k^2)^2} + y^2 = \frac{k^2 d^2}{1 - k^2} + \frac{k^4 d^2}{(1 - k^2)^2}.$$

$$\left(x + \frac{k^2 d}{1 - k^2}\right)^2 + y^2 = \frac{k^2 d^2 - k^4 d^2 + k^4 d^2}{(1 - k^2)^2}.$$

$$\left(x + \frac{k^2 d}{1 - k^2}\right)^2 + y^2 = \frac{k^2 d^2}{(1 - k^2)^2}.$$

This is the equation for a circle with its center at

$$x_0 = -\frac{k^2 d}{1 - k^2} \quad (\text{B-4})$$

and

$$y_0 = 0.$$

The radius is

$$R = \frac{kd}{1 - k^2}. \quad (\text{B-5})$$

B.3 Electric potential from infinite line charge inside an infinite metal pipe

It proves necessary to calculate the electric potential for an infinite line charge inside an infinite metal pipe before the image charge distribution can be determined. The line charge is parallel to the pipe axis. In this section, using the results just derived, the electric potential for an arbitrary point is determined for the given situation.

In Figure B-2 an infinite line charge with a charge per unit length λ is placed in a metal pipe of radius a . The line charge is parallel to the pipe axis and is located at (r', θ') . Because the potential on the pipe must be a constant, an image line charge of opposite sign appears at (R, θ') .

In the primed coordinate system, the potential on the pipe is constant if r' is set equal to the result in (B-4),

$$x'_0 = r' = -\frac{k^2 d}{1 - k^2} \quad (\text{B-6})$$

and the radius of the pipe is set equal to the result in (B-5)

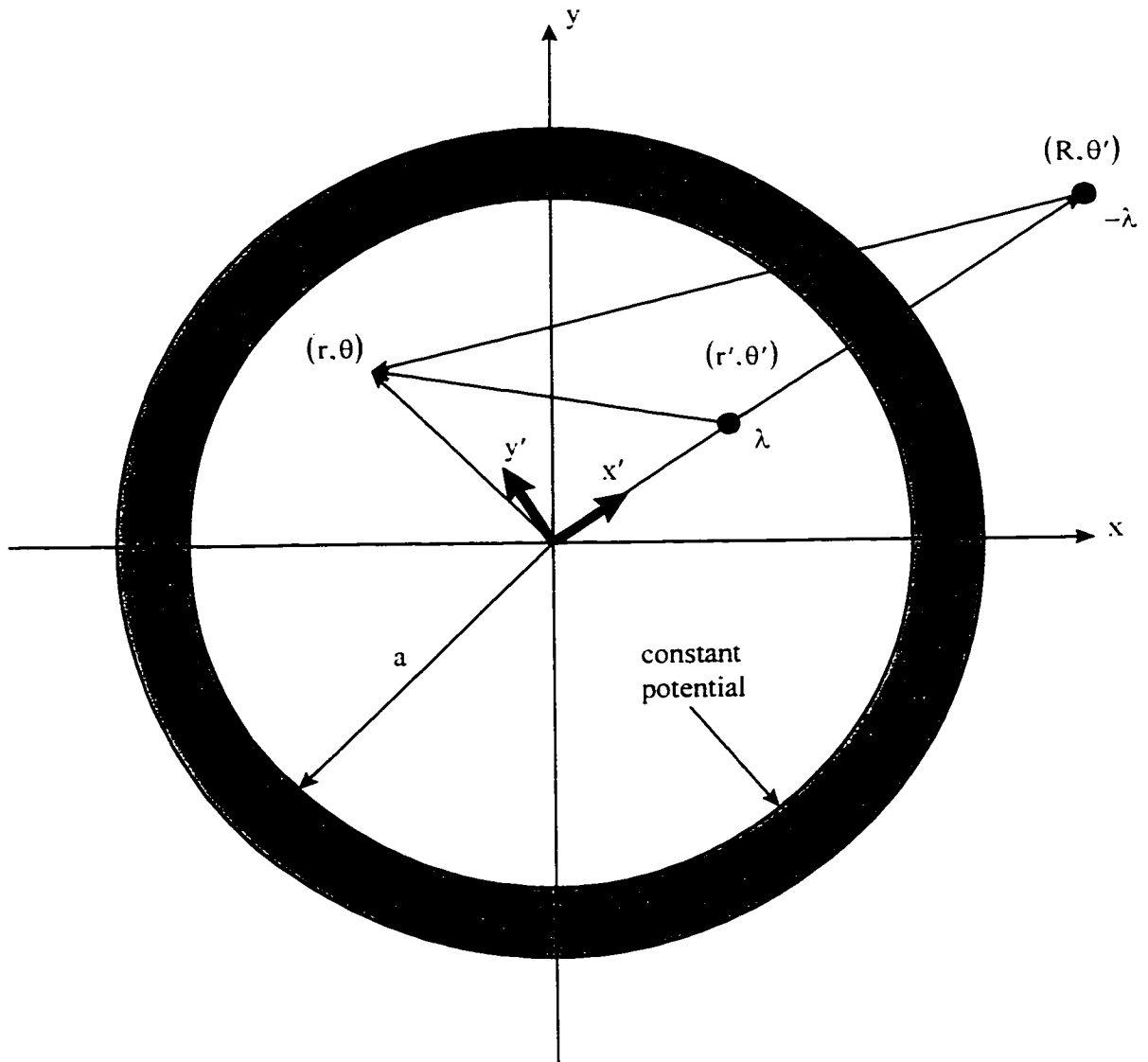


Figure B-2: Infinite line charge inside an infinite metal pipe.

$$a = \frac{kd}{1 - k^2}. \quad (\text{B-7})$$

Using (B-6) and (B-7) to solve for k and d yields

$$k = \frac{r'}{a} \quad (\text{B-8})$$

and

$$d = \frac{a^2 - r'^2}{r'}. \quad (\text{B-9})$$

Using (B-9) the radial position of the line charge $-\lambda$ is given by

$$R = r' + d = r' + \frac{a^2 - r'^2}{r'} = \frac{a^2}{r'}. \quad (\text{B-10})$$

The distances from the line charges λ and $-\lambda$ to some point (r, θ) can be determined by the law of cosines. Identifying these distances as r_λ and $r_{-\lambda}$, we have

$$r_\lambda^2 = r'^2 + r^2 - 2r r' \cos(\theta - \theta') \quad (\text{B-11})$$

and

$$r_{-\lambda}^2 = R^2 + r^2 - 2rR \cos(\theta - \theta').$$

Substituting (B-10) into the last expression gives

$$r_{-\lambda}^2 = \frac{a^4}{r'^2} + r^2 - 2r \frac{a^2}{r'} \cos(\theta - \theta'). \quad (\text{B-12})$$

The electric potential at (r, θ) can be calculated using (B-1), (B-11) and (B-12).

$$\Phi(r, \theta) = -2\lambda \ln \left(\frac{r_\lambda}{r_{-\lambda}} \right)$$

$$\begin{aligned}
&= -2\lambda \left\{ \ln[r'^2 + r^2 - 2rr' \cos(\theta - \theta')]^{1/2} - \ln \left[\frac{a^4}{r'^2} + r^2 - 2r \frac{a^2}{r'} \cos(\theta - \theta') \right]^{1/2} \right\} \\
\Phi(r, \theta) &= -\lambda \left\{ \ln[r'^2 + r^2 - 2rr' \cos(\theta - \theta')] \right. \\
&\quad \left. - \ln \left[\frac{a^4}{r'^2} + r^2 - 2r \frac{a^2}{r'} \cos(\theta - \theta') \right] \right\} \quad (B-13)
\end{aligned}$$

B.4 Surface charge distribution from infinite line charge inside infinite metal pipe

B.4.1 Image charge distribution

Now that the electric potential is known, (B-13), the induced surface charge, $\sigma(\theta)$, on the inside of the pipe is given by

$$\begin{aligned}
\sigma(\theta) &= -\frac{1}{4\pi} \hat{n} \cdot \vec{E} \Big|_{r=a}, \quad \hat{n} = \hat{r} \\
&= -\frac{1}{4\pi} E_r \Big|_{r=a} = \frac{1}{4\pi} \frac{\partial \Phi(r, \theta)}{\partial r} \Big|_{r=a}.
\end{aligned}$$

From (B-13),

$$\frac{\partial \Phi(r, \theta)}{\partial r} = -\lambda \left\{ \frac{2r - 2r' \cos(\theta - \theta')}{r'^2 + r^2 - 2rr' \cos(\theta - \theta')} - \frac{2r - 2 \frac{a^2}{r'} \cos(\theta - \theta')}{\frac{a^4}{r'^2} + r^2 - 2r \frac{a^2}{r'} \cos(\theta - \theta')} \right\}$$

Therefore,

$$\sigma(\theta) = -\frac{\lambda}{2\pi} \left\{ \frac{a - r' \cos(\theta - \theta')}{r'^2 + a^2 - 2ar' \cos(\theta - \theta')} - \frac{a - \frac{a^2}{r'} \cos(\theta - \theta')}{\frac{a^2}{r'^2} [r'^2 + a^2 - 2ar' \cos(\theta - \theta')]} \right\}$$

$$\sigma(\theta) = -\frac{\lambda}{2\pi} \left\{ \frac{a - r' \cos(\theta - \theta') - \frac{r'^2}{a} + r' \cos(\theta - \theta')}{r'^2 + a^2 - 2ar' \cos(\theta - \theta')} \right\}$$

$$\sigma(\theta) = -\frac{\lambda}{2\pi a} \frac{a^2 - r'^2}{r'^2 + a^2 - 2ar' \cos(\theta - \theta')} \quad (\text{B-14})$$

B.4.2 Expansion of image charge distribution in Fourier series

It will prove useful to expand (B-14) in a Fourier series. Making the definitions

$$x \equiv \frac{r'}{a} \leq 1$$

and

$$\alpha \equiv \theta - \theta'$$

yields

$$f(x, \alpha) = \frac{1 - x^2}{1 + x^2 - 2x \cos \alpha} = \frac{a_0}{2} + \sum_{n=1}^{\infty} (a_n \cos n\alpha + b_n \sin n\alpha) \quad (\text{B-15})$$

where

$$a_n = \frac{1}{\pi} \int_0^{2\pi} f(x, \alpha) \cos(n\alpha) d\alpha$$

and

$$b_n = \frac{1}{\pi} \int_0^{2\pi} f(x, \alpha) \sin(n\alpha) d\alpha.$$

Evaluating the first integral.

$$\begin{aligned} a_n &= \frac{(1-x^2)^{2\pi}}{\pi} \int_0^{2\pi} \frac{\cos(n\alpha)d\alpha}{1+x^2-2x\cos\alpha} \\ &= \frac{(1-x^2)}{\pi} 2 \int_0^\pi \frac{\cos(n\alpha)d\alpha}{1+x^2-2x\cos\alpha} \\ a_n &= \frac{(1-x^2)}{\pi} 2 \frac{\pi x^n}{|1-x^2|} \text{ (From Tables).} \end{aligned}$$

Since x is less than or equal to 1.

$$1-x^2 = |1-x^2|.$$

Therefore

$$a_n = \frac{(1-x^2)}{\pi} 2 \frac{\pi x^n}{(1-x^2)} = 2x^n. \quad (\text{B-16})$$

The second integral is

$$\begin{aligned} b_n &= \frac{(1-x^2)^{2\pi}}{\pi} \int_0^{2\pi} \frac{\sin(n\alpha)d\alpha}{1+x^2-2x\cos\alpha} \\ b_n &= -\frac{(1-x^2)}{\pi} \left[\ln(1+x^2-2x\cos\alpha) \right]_0^{2\pi} = 0. \end{aligned} \quad (\text{B-17})$$

Substituting the results in (B-16) and (B-17) and the definitions of x and α into (B-15)

yields

$$\sigma(\theta) = -\frac{\lambda}{2\pi a} \frac{a^2 - r'^2}{r'^2 + a^2 - 2ar' \cos(\theta - \theta')} = -\frac{\lambda}{2\pi a} \left\{ 1 + 2 \sum_{n=1}^{\infty} \left(\frac{r'}{a} \right)^n \cos[n(\theta - \theta')] \right\}.$$

Appendix C

Appendix C

VOLTAGE SIGNAL GENERATED ON OSCILLOSCOPE FROM BEAM POSITION MONITOR SIGNAL TRANSMITTED THROUGH TRANSMISSION LINE

C.1 Introduction

As an electron beam bunch passes through a BPM, it generates a signal on the BPM's electrodes. This signal is transmitted by a transmission line, passed through a low-pass filter and displayed on an oscilloscope. In this appendix, an expression for the voltage signal on the oscilloscope is derived. The coupling between the electron beam and the BPM electrodes is modeled with a simple electrical circuit.

C.2 General Solution

In this section, the voltage signal seen by the oscilloscope is derived. This is done using a simple circuit model and the results from Appendix A.

C.2.1 Solution to circuit model

The coupling of the BPM electrodes to the beam image charge can be modeled by the circuit in Figure C-1[17]. The image charge is represented by the current, i_b . Z_c is the characteristic impedance of the transmission line and C_p is the capacitance of the BPM

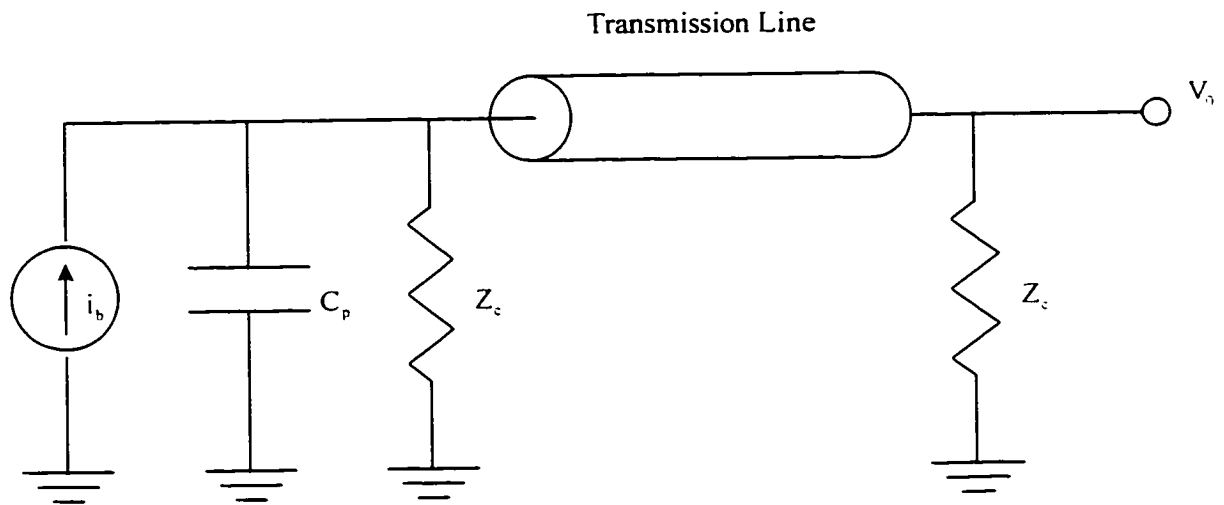


Figure C-1: Circuit model of BPM electrode coupling to electron beam. C_p is the capacitance of the BPM electrode. Z_c is the characteristic impedance of the transmission line. i_b represents the image induced image charge from the passing electron beam.

electrodes. In the frequency domain, this model is accurate to approximately 2 GHz[16]. Beyond this, it breaks down.

The relationship between voltage signal into the transmission line, v_T , and the current, i_b , is

$$i_b = \frac{v_T}{Z_c} + C_p \frac{dv_T}{dt}.$$

Taking the Fourier transform of both sides of this equation, yields

$$I_b(\omega) = \frac{V_T(\omega)}{Z_c} + C_p j\omega V_T(\omega)$$

where the well known Fourier transform of a function is given by

$$F(\omega) = \int_{-\infty}^{\infty} f(t)e^{-j\omega t} dt.$$

Solving for $V_T(\omega)$ gives

$$V_T(\omega) = \frac{Z_c I_b(\omega)}{1 + j\omega C_p Z_c}. \quad (C-1)$$

Because the beam bunches generated by SPA are very short, a large part of the signal content is at very high frequencies. Since the model is inaccurate above 2 GHz, low-pass filters are placed on the oscilloscope inputs in order to ensure that we are far from that regime. The end result is that the original signal is modified significantly by the time it is displayed on the oscilloscope. Therefore, transfer functions are assigned in the frequency domain: $\sigma(\omega)$ for the transmission line and $A(\omega)$ for the combination low pass filter and oscilloscope. The resulting voltage signal is given by simply multiplying equation (C-1) by these transfer functions, yielding

$$V_{\text{osc}}(\omega) = \frac{Z_c I_b(\omega)}{1 + j\omega C_p Z_c} \sigma(\omega) A(\omega).$$

Taking the inverse Fourier transform of this function gives

$$v_{\text{osc}}(t) = \frac{1}{2\pi} \int_{-\infty}^{\infty} \frac{Z_c I_b(\omega)}{1 + j\omega C_p Z_c} \sigma(\omega) A(\omega) e^{j\omega t} d\omega. \quad (\text{C-2})$$

C.2.2 Expression for beam current

To find an expression for $I_b(\omega)$, one first finds the current generated by the image charge, $i_b(t)$. It is given by the time derivative of the total amount of charge on the BPM electrode, or,

$$i_b(t) = \frac{d}{dt} \int_{\text{Area of Electrode}} \sigma(\theta, z, t) da.$$

The surface charge distribution for a highly relativistic beam is known from Appendix A.

$$\sigma(\theta, z, t) = \frac{-1}{2\pi a} \int_{\text{area of pipe}} \rho_L(r', \theta', z, t) \left\{ 1 + 2 \sum_{n=1}^{\infty} \left(\frac{r'}{a} \right)^n \cos[n(\theta - \theta')] \right\} r' dr' d\theta'.$$

The BPMs used on SPA have square electrodes. The electrodes have longitudinal length L , longitudinal location z_0 , angular width 2α and angular location θ_0 . Integrating the expression for the surface charge distribution over the surface area of the electrodes gives

$$i_b(t) = \frac{-1}{2\pi a} \frac{d}{dt} \int_{\theta_0 - \alpha}^{\theta_0 + \alpha} \int_{z_0}^{z_0 + L} \int_{\text{area of pipe}} \rho_L(r', \theta', z, t) \left\{ 1 + 2 \sum_{n=1}^{\infty} \left(\frac{r'}{a} \right)^n \cos[n(\theta - \theta')] \right\} da'.$$

The integral over θ is simple and results in

$$i_b(t) = \frac{-1}{2\pi} \frac{d}{dt} \int_{z_0}^{z_0+L} dz \int_{\text{area of pipe}} \rho_L(r', \theta', z, t) \left\{ 2\alpha + 4 \sum_{n=1}^{\infty} \left(\frac{r'}{a} \right)^n \frac{\sin n\alpha}{n} \cos[n(\theta - \theta')] \right\} da'.$$

Taking the Fourier transform yields

$$I_b(\omega) = \frac{-1}{2\pi} \int_{-\infty}^{\infty} dt e^{-j\omega t} \frac{d}{dt} \int_{z_0}^{z_0+L} dz \int_{\text{area of pipe}} \rho_L(r', \theta', z, t) \otimes \left\{ 2\alpha + 4 \sum_{n=1}^{\infty} \left(\frac{r'}{a} \right)^n \frac{\sin n\alpha}{n} \cos[n(\theta - \theta')] \right\} da'. \quad (C-3)$$

Inside equation (C-3) is the expression

$$\frac{d}{dt} \int_{z_0}^{z_0+L} \rho_L(r', \theta', z, t) dz \quad (C-4)$$

Recall from equation (A-23) that z and t occur in the charge distribution together as $z - \beta ct$. In other words, the density distribution function can be rewritten as

$$\rho_L(r', \theta', z, t) = \rho_L(r', \theta', z - \beta ct).$$

Taking the time derivative of the distribution gives

$$\frac{d}{dt} \rho_L(r', \theta', z, t) = -\beta c \frac{d}{dz} \rho_L(r', \theta', z - \beta ct).$$

Therefore, if the time derivative is moved inside the integral given in (C-4) then

$$\int_{z_0}^{z_0+L} \frac{d}{dt} \rho_L(r', \theta', z, t) dz = -\beta c \left[\rho_L(r', \theta', z_0 + L - \beta ct) - \rho_L(r', \theta', z_0 - \beta ct) \right].$$

Then (C-3) becomes

$$I_b(\omega) = \frac{\beta c}{2\pi} \int_{-\infty}^{\infty} dt e^{-j\omega t} \int \left[\rho_L(r', \theta', z_0 + L - \beta ct) - \rho_L(r', \theta', z_0 - \beta ct) \right] \otimes \left\{ 2\alpha + 4 \sum_{n=1}^{\infty} \left(\frac{r'}{a} \right)^n \frac{\sin n\alpha}{n} \cos[n(\theta - \theta')] \right\} da' . \quad (C-5)$$

As was just done for the z integral in equation (C-3), the time integral can be isolated from (C-5) leaving

$$\begin{aligned} I &= \int_{-\infty}^{\infty} e^{-j\omega t} \left[\rho_L(r', \theta', z_0 + L - \beta ct) - \rho_L(r', \theta', z_0 - \beta ct) \right] dt \\ &= \int_{-\infty}^{\infty} e^{-j\omega t} \left[e^{j\omega \frac{z_0 + L}{\beta c}} e^{-j\omega \frac{z_0 + L}{\beta c}} \rho_L(r', \theta', z_0 + L - \beta ct) - e^{j\omega \frac{z_0}{\beta c}} e^{-j\omega \frac{z_0}{\beta c}} \rho_L(r', \theta', z_0 - \beta ct) \right] dt \\ &= e^{-j\frac{\omega}{\beta c}(z_0 + L)} \int_{-\infty}^{\infty} e^{j\frac{\omega}{\beta c}(z_0 + L - \beta ct)} \rho_L(r', \theta', z_0 + L - \beta ct) dt \\ &\quad - e^{-j\frac{\omega}{\beta c}z_0} \int_{-\infty}^{\infty} e^{j\frac{\omega}{\beta c}(z_0 - \beta ct)} \rho_L(r', \theta', z_0 - \beta ct) dt . \end{aligned}$$

Making the definitions:

$$z' \equiv z_0 + L - \beta ct$$

and

$$z'' \equiv z_0 - \beta ct .$$

gives

$$I = \frac{-e^{-j\frac{\omega}{\beta c}(z_0 + L)}}{\beta c} \int_{-\infty}^{\infty} e^{j\frac{\omega}{\beta c}z'} \rho_L(r', \theta', z') dz' + \frac{e^{-j\frac{\omega}{\beta c}z_0}}{\beta c} \int_{-\infty}^{\infty} e^{j\frac{\omega}{\beta c}z''} \rho_L(r', \theta', z'') dz'' .$$

Recognizing that the two integrals are identical yields

$$I = \frac{e^{-j\frac{\omega}{\beta c}z_0}}{\beta c} \left(1 - e^{-j\frac{\omega}{\beta c}L}\right) \int_{-\infty}^{+\infty} e^{j\frac{\omega}{\beta c}z'} \rho_L(r', \theta', z') dz'.$$

Substituting this back into (C-5) gives

$$I_b(\omega) = \frac{e^{-j\frac{\omega}{\beta c}z_0}}{2\pi} \left(1 - e^{-j\frac{\omega}{\beta c}L}\right) \int_{\text{area of pipe}} da' \int_{-\infty}^{+\infty} dz' e^{j\frac{\omega}{\beta c}z'} \rho_L(r', \theta', z')$$

$$\otimes \left\{ 2\alpha + 4 \sum_{n=1}^{\infty} \left(\frac{r'}{a}\right)^n \frac{\sin n\alpha}{n} \cos[n(\theta - \theta')] \right\}. \quad (C-6)$$

C.2.3 Solution

Now that an expression for the current has been found, one can write the complete general solution for the voltage signal seen by the oscilloscope. Substituting (C-6) into (C-2) yields

$$v_{\text{osc}}(t) = \frac{1}{4\pi^2} \int_{-\infty}^{+\infty} \frac{Z_c \sigma(\omega) A(\omega)}{1 + j\omega C_p Z_c} \left\{ e^{-j\frac{\omega}{\beta c}z_0} \left(1 - e^{-j\frac{\omega}{\beta c}L}\right) \int_{\text{area of pipe}} da' \int_{-\infty}^{+\infty} dz' e^{j\frac{\omega}{\beta c}z'} \rho_L(r', \theta', z') \right.$$

$$\left. \otimes \left\{ 2\alpha + 4 \sum_{n=1}^{\infty} \left(\frac{r'}{a}\right)^n \frac{\sin n\alpha}{n} \cos[n(\theta - \theta')] \right\} \right\} e^{j\omega t} d\omega. \quad (C-7)$$

C.3 Approximate solution for short beam pulse

In general, the analytical forms for the charge distribution and the transfer functions $\sigma(\omega)$ and $A(\omega)$ will be unknown. What is known, however, is that the electron beam bunches from SPA are very short. The maximum expected full width at half maximum length (FWHM) is 6 mm, or 20 ps. Because of the low-pass filter that signal passes

through, the beam pulse is essentially a delta function longitudinally for all frequencies of interest:

$$\int_{-\infty}^{\infty} dz' e^{-j\frac{\omega}{\beta c}z'} \rho_L(r', \theta', z') \cong \int_{-\infty}^{\infty} dz' \rho_L(r', \theta', z') \quad (C-8)$$

to high accuracy. Substituting this into (C-7) gives

$$v_{osc}(t) = \frac{1}{4\pi^2} \int_{\text{area of pipe}} da' \int_{-\infty}^{\infty} dz' \rho_L(r', \theta', z') \left\{ 2\alpha + 4 \sum_{n=1}^{\infty} \left(\frac{r'}{a}\right)^n \frac{\sin n\alpha}{n} \cos[n(\theta - \theta')] \right\} \\ \otimes \int_{-\infty}^{\infty} \frac{e^{-j\frac{\omega}{\beta c}z_1}}{2\pi} \left(1 - e^{-j\frac{\omega}{\beta c}L} \right) \frac{Z_c \sigma(\omega) A(\omega)}{1 + j\omega C_p Z_c} e^{j\omega t} d\omega. \quad (C-9)$$

C.4 Gaussian beam

To demonstrate that (C-8) is a reasonable approximation, we will demonstrate it using a Gaussian longitudinal distribution.

If the beam bunches have a Gaussian distribution longitudinally, the total beam pulse distribution is

$$\rho_L(r', \theta', z') \rightarrow \rho_L(r', \theta') \frac{e^{-\frac{z'^2}{2\sigma^2}}}{\sqrt{2\pi\sigma}}.$$

From (C-8) two integrals can be defined:

$$I_1 = \int_{-\infty}^{\infty} dz' \rho_L(r', \theta', z') = \rho_L(r', \theta')$$

and

$$I_2 = \int_{-\infty}^{\infty} dz' e^{-j\frac{\omega}{\beta c} z'} \rho_L(r', \theta', z') = \rho_L(r', \theta') \int_{-\infty}^{\infty} dz' e^{-j\frac{\omega}{\beta c} z'} \frac{e^{-\frac{z'^2}{2\sigma^2}}}{\sqrt{2\pi\sigma}}.$$

Therefore, to show that (C-8) is valid, it is enough to show that a third integral.

$$I_3 = \int_{-\infty}^{\infty} dz' e^{-j\frac{\omega}{\beta c} z'} \frac{e^{-\frac{z'^2}{2\sigma^2}}}{\sqrt{2\pi\sigma}}.$$

is very close to one for all frequencies of interest.

To do I_3 , first complete the square:

$$I_3 = \frac{1}{\sqrt{2\pi\sigma}} \int_{-\infty}^{\infty} dz' e^{-\left(\frac{1}{\sqrt{2}\sigma} z' + j\frac{1}{\sqrt{2}} \frac{\omega}{\beta c} \sigma\right)^2} e^{-\frac{1}{2} \left(\frac{\omega}{\beta c} \sigma\right)^2}.$$

Making the definition

$$x \equiv \frac{1}{\sqrt{2}\sigma} z' + j\frac{1}{\sqrt{2}} \frac{\omega}{\beta c} \sigma$$

yields

$$I_3 = \frac{e^{-\frac{1}{2} \left(\frac{\omega}{\beta c} \sigma\right)^2}}{\sqrt{2\pi\sigma}} \int_{-\infty}^{\infty} dx \sqrt{2}\sigma e^{-x^2} = \frac{\sqrt{2\pi\sigma} e^{-\frac{1}{2} \left(\frac{\omega}{\beta c} \sigma\right)^2}}{\sqrt{2\pi\sigma}} = e^{-\frac{1}{2} \left(\frac{\omega}{\beta c} \sigma\right)^2}.$$

To see how close I_3 is to one, the function $e^{-\frac{1}{2} \left(\frac{\omega}{\beta c} \sigma\right)^2}$ versus frequency is plotted in Figure C-2 for a beam bunch with a FWHM length of 6 mm, or 20 ps. This is the approximate maximum length beam bunch expected. The relationship between σ , the rms width of the pulse, and the FWHM for a Gaussian pulse is

$$\sigma = \frac{\text{FWHM}}{2\sqrt{\ln 4}} \cong \frac{\text{FWHM}}{2.35}.$$

As can be seen, even at 1 GHz this function is very close to one.

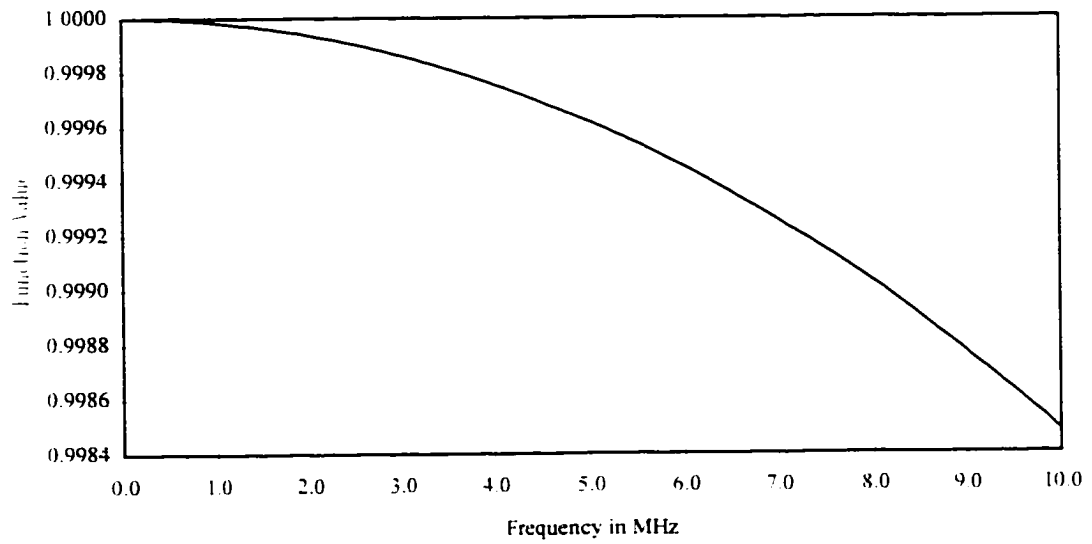


Figure C-2: The function $e^{-\frac{1}{2}\left(\frac{\omega}{\beta c}\sigma\right)^2}$ vs. frequency for a 6 mm. or 20 ps. FWHM long electron pulse.

Appendix D

Appendix D

EXPANSION OF BPM SIGNAL AMPLITUDE IN CARTESIAN COORDINATES

D.1 Introduction

In Appendix C an expression, equation (C-9), was derived for the voltage signal seen by an oscilloscope due to the signal generated in a BPM electrode by an electron beam bunch. In fact, it is the amplitude of this voltage time signal we are interested in.

In this appendix, the first few terms of the amplitude in (C-9) are converted to Cartesian coordinates. These few terms are then shown to be important beam parameters. In Chapter 1, it is demonstrated how the BPM electrode signals can be exploited to measure them.

D.2 Expansion of amplitude in Cartesian coordinates

The amplitude in equation (C-9) is

$$A = \frac{1}{4\pi^2} \int_{\text{area of pipe}} da' \int_{-\infty}^{\infty} dz' \rho_L(r', \theta', z') \left\{ 2\alpha + 4 \sum_{n=1}^{\infty} \left(\frac{r'}{a} \right)^n \frac{\sin n\alpha}{n} \cos[n(\theta - \theta')] \right\} \quad (\text{D-1})$$

in cylindrical coordinates. To change to Cartesian coordinates, start by making the substitution

$$\rho_L(r', \theta', z') \rightarrow \rho_L(x', y', z').$$

Then, for simplicity, change the bounds on the transverse integral from being just over the beam pipe area to $\pm \infty$ in x and y . This is justified because the beam is, by necessity, confined to the interior of the pipe. Including areas outside the pipe by going to $\pm \infty$ will contribute nothing to the integral. Therefore, (D-1) becomes

$$A = \frac{1}{4\pi^2} \int_{-\infty}^{+\infty} \int_{-\infty}^{+\infty} \int_{-\infty}^{+\infty} \rho_L(x', y', z') \otimes \left\{ 2\alpha + 4 \sum_{n=1}^{\infty} \left(\frac{r'}{a} \right)^n \frac{\sin n\alpha}{n} \cos[n(\theta - \theta')] \right\} dx' dy' dz' \quad (D-2)$$

D.2.1 Expansion of summation term in Cartesian coordinates

Looking at the summation in (D-2) out to $n = 3$ gives

$$2\alpha + 4 \sum_{n=1}^{\infty} \left(\frac{r'}{a} \right)^n \frac{\sin n\alpha}{n} \cos[n(\theta - \theta')] = 2\alpha + 4 \sin \alpha \frac{r'}{a} \cos(\theta - \theta') \\ + 2 \sin 2\alpha \left(\frac{r'}{a} \right)^2 \cos[2(\theta - \theta')] + \frac{4}{3} \sin 3\alpha \left(\frac{r'}{a} \right)^3 \cos[3(\theta - \theta')] + O\left(\frac{1}{a^4}\right).$$

Exploiting the relationships

$$x' = r' \cos \theta'$$

and

$$y' = r' \sin \theta'.$$

these terms can be written in Cartesian coordinates.

Term 1: 2α

$$\text{Term 2: } 4 \sin \alpha \frac{r'}{a} \cos(\theta - \theta') = \frac{4 \sin \alpha}{a} r' [\cos \theta' \cos \theta + \sin \theta' \sin \theta]$$

$$= \frac{4 \sin \alpha}{a} (x' \cos \theta + y' \sin \theta)$$

$$\begin{aligned} \text{Term 3: } 2 \sin 2\alpha \left(\frac{r'}{a} \right)^2 \cos[2(\theta - \theta')] &= \frac{2 \sin 2\alpha}{a^2} r'^2 [\cos 2\theta' \cos 2\theta + \sin 2\theta' \sin 2\theta] \\ &= \frac{2 \sin 2\alpha}{a^2} r'^2 [(\cos^2 \theta' - \sin^2 \theta') \cos 2\theta + 2 \sin \theta' \cos \theta' \sin 2\theta] \\ &= \frac{2 \sin 2\alpha}{a^2} [(x'^2 - y'^2) \cos 2\theta + 2x'y' \sin 2\theta] \end{aligned}$$

$$\begin{aligned} \text{Term 4: } \frac{4}{3} \sin 3\alpha \left(\frac{r'}{a} \right)^3 \cos[3(\theta - \theta')] &= \frac{4 \sin 3\alpha}{3 a^3} r'^3 [\cos 3\theta' \cos 3\theta + \sin 3\theta' \sin 3\theta] \\ &= \frac{4 \sin 3\alpha}{3 a^3} r'^3 [(\cos^3 \theta' - 3 \cos \theta' \sin^2 \theta') \cos 3\theta + (3 \cos^2 \theta' \sin \theta' - \sin^3 \theta') \sin 3\theta] \\ &= \frac{4 \sin 3\alpha}{3 a^3} [(x'^3 - 3x'y'^2) \cos 3\theta + (3x'^2y' - y'^3) \sin 3\theta] \end{aligned}$$

Therefore, (D-2) becomes

$$\begin{aligned} A &= \frac{1}{4\pi^2} \int_{-\infty}^{+\infty} \int_{-\infty}^{+\infty} \int_{-\infty}^{+\infty} \rho_L(x', y', z') \left\{ 2\alpha + \frac{4 \sin \alpha}{a} (x' \cos \theta + y' \sin \theta) \right. \\ &\quad + \frac{2 \sin 2\alpha}{a^2} [(x'^2 - y'^2) \cos 2\theta + 2x'y' \sin 2\theta] \\ &\quad + \frac{4 \sin 3\alpha}{3 a^3} [(x'^3 - 3x'y'^2) \cos 3\theta + (3x'^2y' - y'^3) \sin 3\theta] \\ &\quad \left. + O\left(\frac{1}{a^4}\right) \right\} dx' dy' dz'. \end{aligned} \tag{D-3}$$

D.2.2 Expressing amplitude as a sum of moments

In Chapter 1, two averages were defined. The first is called an ensemble average.

This is the average of a quantity over the beam distribution in the coordinate system

whose origin corresponds to the center of the beam. An ensemble average is denoted by angled brackets:

$$\langle \text{quantity} \rangle \equiv \frac{\iiint \text{quantity} \times \rho(\bar{x}) dV}{\iiint \rho(\bar{x}) dV} \quad (\text{D-4})$$

Origin corresponds to beam center
Origin corresponds to beam center

where $\rho(\bar{x})$ describes the electron beam's spatial distribution. By definition

$$\langle x \rangle = \langle y \rangle = \langle z \rangle = 0.$$

The second average defines the transverse, or xy, origin to correspond with the center of the beam pipe. The longitudinal, or z, origin corresponds to the longitudinal center of the beam bunch. This average will be referred to as a BPM average and is denoted in the following way:

$$\langle \text{quantity} \rangle_{\text{BPM}} \equiv \frac{\iiint \text{quantity} \times \rho(\bar{x}) dV}{\iiint \rho(\bar{x}) dV} \quad (\text{D-5})$$

xy origin corresponds to beam pipe center, z origin to beam bunch center
xy origin corresponds to beam pipe center, z origin to beam bunch center

The average values of x and y with this definition yield the x and y position of the center of the beam with respect to the beam pipe and

$$\langle z \rangle = 0.$$

The first integral in (D-3) is

$$\int_{-\infty}^{+\infty} \int_{-\infty}^{+\infty} \int_{-\infty}^{+\infty} \rho_L(x', y', z') dx' dy' dz' = q,$$

where q is the total charge in the pulse. This is by definition of the beam bunch distribution function. The other integrals in (D-3) are BPM averages defined by (D-5) and multiplied by q. That is

$$\begin{aligned}
A = \frac{1}{4\pi^2} & \left\{ 2\alpha + \frac{4\sin\alpha}{a} \left(q\langle x \rangle_{\text{BPM}} \cos\theta + q\langle y \rangle_{\text{BPM}} \sin\theta \right) \right. \\
& + \frac{2\sin 2\alpha}{a^2} \left[q\left(\langle x^2 \rangle_{\text{BPM}} - \langle y^2 \rangle_{\text{BPM}} \right) \cos 2\theta + 2q\langle xy \rangle_{\text{BPM}} \sin 2\theta \right] \\
& + \frac{4\sin 3\alpha}{3a^3} \left[q\left(\langle x^3 \rangle_{\text{BPM}} - 3\langle xy^2 \rangle_{\text{BPM}} \right) \cos 3\theta + q\left(3\langle x^2y \rangle_{\text{BPM}} - \langle y^3 \rangle_{\text{BPM}} \right) \sin 3\theta \right] \\
& \left. + O\left(\frac{1}{a^4} \right) \right\}.
\end{aligned}$$

The primes have been dropped for convenience. Typically, the x and y center positions of the beam, given by $\langle x \rangle_{\text{BPM}}$ and $\langle y \rangle_{\text{BPM}}$ are denoted by \bar{x} and \bar{y} , respectively.

Therefore, this becomes

$$\begin{aligned}
A = \frac{q}{4\pi^2} & \left\{ 2\alpha + \frac{4\sin\alpha}{a} (\bar{x} \cos\theta + \bar{y} \sin\theta) \right. \\
& + \frac{2\sin 2\alpha}{a^2} \left[(\langle x^2 \rangle_{\text{BPM}} - \langle y^2 \rangle_{\text{BPM}}) \cos 2\theta + 2\langle xy \rangle_{\text{BPM}} \sin 2\theta \right] \\
& + \frac{4\sin 3\alpha}{3a^3} \left[(\langle x^3 \rangle_{\text{BPM}} - 3\langle xy^2 \rangle_{\text{BPM}}) \cos 3\theta + (3\langle x^2y \rangle_{\text{BPM}} - \langle y^3 \rangle_{\text{BPM}}) \sin 3\theta \right] \\
& \left. + O\left(\frac{1}{a^4} \right) \right\}. \tag{D-6}
\end{aligned}$$

The term $\langle x^2 \rangle_{\text{BPM}} - \langle y^2 \rangle_{\text{BPM}}$ in (D-6) is given special treatment. Let us look at the integral of x^2 over the beam bunch density distribution.

$$\begin{aligned}
\int_{-\infty}^{+\infty} \int_{-\infty}^{+\infty} \int_{-\infty}^{+\infty} x^2 \rho_L(x, y, z) dx dy dz &= \int_{-\infty}^{+\infty} \int_{-\infty}^{+\infty} \int_{-\infty}^{+\infty} (x^2 - 2x\bar{x} + 2x\bar{x} + \bar{x}^2 - \bar{x}^2) \rho_L(x, y, z) dx dy dz \\
&= \int_{-\infty}^{+\infty} \int_{-\infty}^{+\infty} \int_{-\infty}^{+\infty} [(x - \bar{x})^2 + 2x\bar{x} - \bar{x}^2] \rho_L(x, y, z) dx dy dz
\end{aligned}$$

$$= q \left[\langle (x - \bar{x})^2 \rangle_{\text{BPM}} + \bar{x}^2 \right].$$

Because of the definitions of the ensemble and BPM averages given in (D-4) and (D-5), subtracting the term \bar{x} from x inside the angle brackets changes the BPM average to an ensemble average. That is

$$q \langle x^2 \rangle_{\text{BPM}} = q \left[\langle (x - \bar{x})^2 \rangle_{\text{BPM}} + \bar{x}^2 \right] = q \left(\langle x^2 \rangle + \bar{x}^2 \right).$$

Similarly

$$q \langle y^2 \rangle_{\text{BPM}} = q \left[\langle (y - \bar{y})^2 \rangle_{\text{BPM}} + \bar{y}^2 \right] = q \left(\langle y^2 \rangle + \bar{y}^2 \right).$$

Therefore,

$$\langle x^2 \rangle_{\text{BPM}} - \langle y^2 \rangle_{\text{BPM}} = \langle x^2 \rangle - \langle y^2 \rangle + \bar{x}^2 - \bar{y}^2.$$

Appendix E

Appendix E

FIRST ORDER CALCULATION OF THE TRAJECTORY OF AN ELECTRON DUE TO IDEAL FAST DEFLECTOR FIELDS

E.1 Introduction

A fast deflector is a cylindrical cavity operating in a TM_{110} mode. In this mode the dominant field is a time varying dipole field transverse to the z direction. This is shown to be true in the first part of this appendix. In the second part the trajectory of a relativistic electron through this dipole field is calculated to first order.

E.2 Electric and magnetic fields of fast deflector

The fast deflector is a cylindrical cavity that operates in a TM_{110} mode. A schematic is shown in Figure E-1. The ideal electric and magnetic fields are

$$E_z = E_0 J_1(k_{11}r) \cos\theta \cos(\omega t + \phi), \quad (E-1)$$

$$B_r = \omega \frac{a^2}{x_{11}^2 r c^2} E_0 J_1(k_{11}r) \sin\theta \sin(\omega t + \phi) \quad (E-2)$$

and

$$B_\theta = \omega \frac{a}{x_{11} c^2} E_0 J_1'(k_{11}r) \cos\theta \sin(\omega t + \phi). \quad (E-3)$$

All other field components are zero. The constant k_{11} is defined as

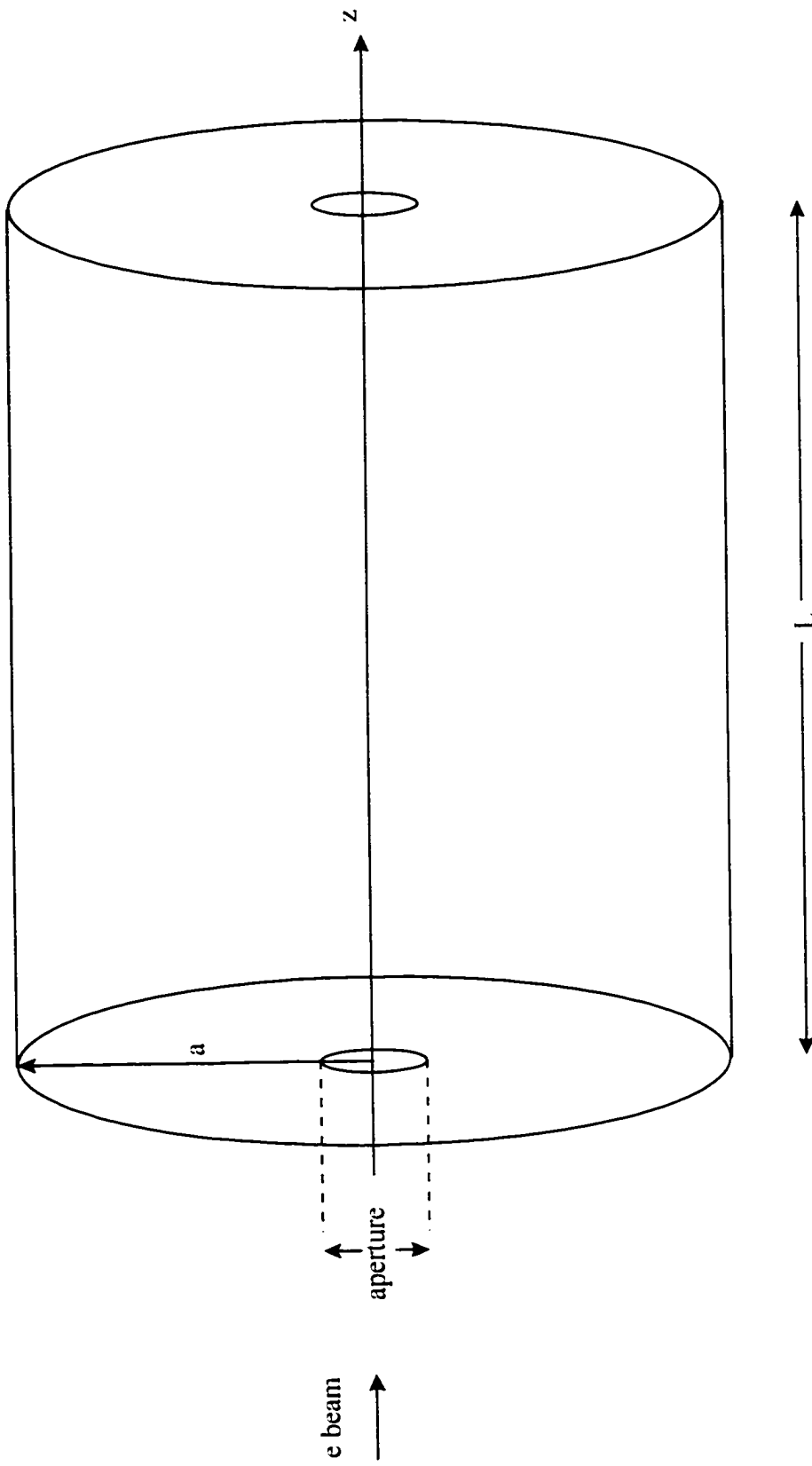


Figure B-1: Schematic of fast deflector cavity.

$$k_{11} \equiv \frac{x_{11}}{a}$$

where x_{11} , equal to 3.8317, is the first zero of the first Bessel function and a is the radius of the cavity. The angular frequency, ω , is given by

$$\omega = 2\pi f$$

where the frequency, f , is 1300 MHz for our cavity. The relationship between the angular frequency and the geometrical properties of the cavity is

$$\omega = k_{11}c.$$

Therefore, the cavity radius is

$$a = \frac{x_{11}c}{\omega} = \frac{x_{11}c}{2\pi f} = 0.14 \text{ m}.$$

The length of the cavity, L , is independent of frequency and on SPA measures 14.48 cm.

The maximum amplitude of the electric field, E_0 , is 24MV/m. from measurement. The kinetic energy of the electrons as they enter the cavity will be approximately 8 MeV. The aperture of the cavity, the opening that the beam travels through, is one inch in diameter, or 1.27 cm in radius.

E.3 Transformation of fields to Cartesian coordinates

The magnetic field vector is given by

$$\vec{B} = B_r \hat{r} + B_\theta \hat{\theta} + B_z \hat{z} = B_r \hat{r} + B_\theta \hat{\theta}$$

where $B_z = 0$. The relationships between the cylindrical coordinate unit vectors and the Cartesian unit vectors are

$$\hat{r} = \hat{x} \cos\theta + \hat{y} \sin\theta$$

and

$$\hat{\theta} = -\hat{x} \sin\theta + \hat{y} \cos\theta.$$

Therefore,

$$\begin{aligned}\bar{\mathbf{B}} &= B_r(\hat{x} \cos\theta + \hat{y} \sin\theta) + B_\theta(-\hat{x} \sin\theta + \hat{y} \cos\theta) \\ &= \hat{x}(B_r \cos\theta - B_\theta \sin\theta) + \hat{y}(B_r \sin\theta + B_\theta \cos\theta).\end{aligned}$$

This gives

$$B_x = B_r \cos\theta - B_\theta \sin\theta \quad (\text{E-4})$$

and

$$B_y = B_r \sin\theta + B_\theta \cos\theta. \quad (\text{E-5})$$

Substituting (E-2) and (E-3) into (E-4) gives

$$\begin{aligned}B_x &= \left[\omega \frac{a^2}{x_{11}^2 r c^2} J_1(k_{11} r) E_0 \sin\theta \cos\theta - \omega \frac{a}{x_{11} c^2} J_1'(k_{11} r) E_0 \sin\theta \cos\theta \right] \sin(\omega t + \phi) \\ &= \frac{a\omega}{2x_{11} c^2} E_0 \sin 2\theta \left[\frac{a}{x_{11} r} J_1(k_{11} r) - J_1'(k_{11} r) \right] \sin(\omega t + \phi).\end{aligned}$$

A property of Bessel functions is

$$xJ_1'(x) = J_1(x) - xJ_2(x) [33].$$

Therefore,

$$J_1'(x) = \frac{J_1(x)}{x} - J_2(x).$$

Remembering that

$$k_{11} \equiv \frac{x_{11}}{a}.$$

$$\begin{aligned} \frac{a}{x_{11}r} J_1(k_{11}r) - J_1'(k_{11}r) &= \frac{J_1(k_{11}r)}{k_{11}r} - \frac{J_1(k_{11}r)}{k_{11}r} + J_2(k_{11}r) \\ &= J_2(k_{11}r). \end{aligned}$$

Therefore

$$B_x = \frac{a\omega}{x_{11}c^2} J_2(k_{11}r) E_0 \sin 2\theta \sin(\omega t + \phi). \quad (\text{E-6})$$

Substituting (E-2) and (E-3) into (E-5) gives

$$\begin{aligned} B_y &= \left[\omega \frac{a^2}{x_{11}^2 r c^2} E_0 J_1(k_{11}r) \sin^2 \theta + \omega \frac{a}{x_{11}c^2} E_0 J_1'(k_{11}r) \cos^2 \theta \right] \sin(\omega t + \phi) \\ &= \frac{\omega a}{x_{11}c^2} E_0 \left(\frac{a}{x_{11}r} J_1(k_{11}r) \sin^2 \theta + J_1'(k_{11}r) \cos^2 \theta \right) \sin(\omega t + \phi). \end{aligned}$$

Using

$$J_1'(k_{11}r) = \frac{a}{x_{11}r} J_1(k_{11}r) - J_2(k_{11}r)$$

gives

$$\begin{aligned} B_y &= \frac{\omega a}{x_{11}c^2} E_0 \left(\frac{a}{x_{11}r} J_1(k_{11}r) \sin^2 \theta \right. \\ &\quad \left. + \frac{a}{x_{11}r} J_1(k_{11}r) \cos^2 \theta - J_2(k_{11}r) \cos^2 \theta \right) \sin(\omega t + \phi) \\ B_y &= \frac{\omega a}{x_{11}c^2} E_0 \left(\frac{a}{x_{11}r} J_1(k_{11}r) - J_2(k_{11}r) \cos^2 \theta \right) \sin(\omega t + \phi). \quad (\text{E-7}) \end{aligned}$$

The Bessel functions $J_1(k_{11}r)$ and $J_2(k_{11}r)$ can be written as infinite series. The first

terms of these series are

$$\frac{k_{11}r}{2}$$

and

$$\frac{1}{8}(k_{11}r)^2.$$

respectively. The value of k_{11} is

$$k_{11} = \frac{x_{11}}{a} = 0.2737 \text{ cm}^{-1}.$$

The electrons are limited to the region defined by the aperture through which they enter the cavity. If these two functions are plotted versus radius as in Figure E-2, it is apparent that the first term is a very good approximation of the full Bessel function in each case when the maximum value of the radius is limited to the value of the aperture radius, 1.27 cm. Therefore, (E-1), (E-6) and (E-7) become

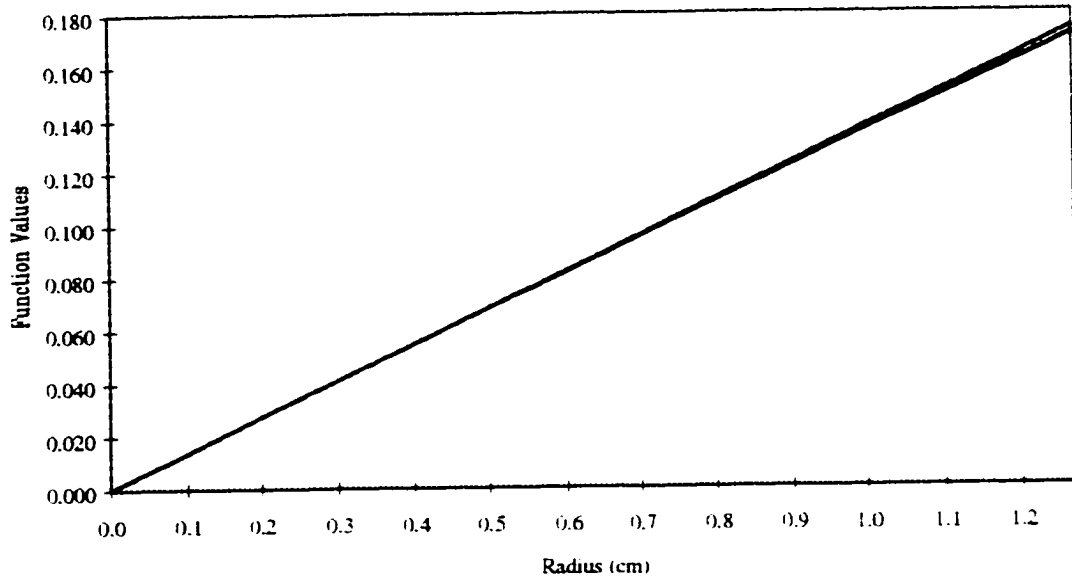
$$E_z \cong E_0 \frac{k_{11}}{2} x \cos(\omega t + \phi). \quad (\text{E-8})$$

$$B_x \cong \frac{a\omega}{x_{11}c^2} E_0 \frac{1}{4} k_{11}^2 xy \sin(\omega t + \phi) = \frac{\omega x_{11}}{4ac^2} E_0 xy \sin(\omega t + \phi) \quad (\text{E-9})$$

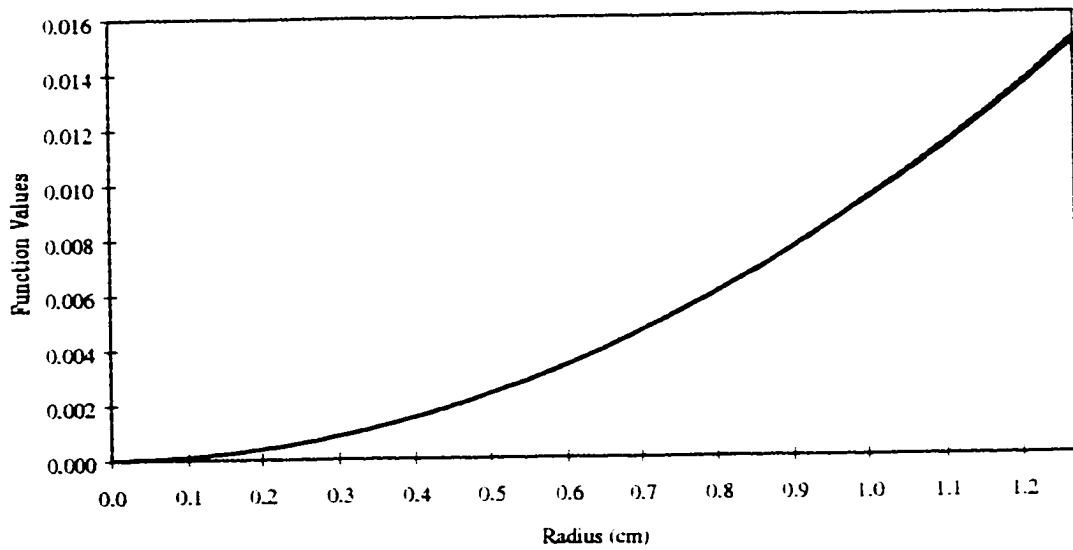
and

$$B_y \cong \frac{\omega a}{2x_{11}c^2} E_0 \left(1 - \frac{x_{11}^2}{4a^2} x^2 \right) \sin(\omega t + \phi). \quad (\text{E-10})$$

The y magnetic field, given in (E-10), has a small quadratic term. However, as can be seen in Figure E-3, this results in, perhaps, a three percent variation in field strength along



a)



b)

Figure E-2: a) $J_1(k_{11}r)$ (blue) and $\frac{k_{11}r}{2}$ (red) versus radius, b) $J_2(k_{11}r)$ (blue) and

$\frac{1}{8}(k_{11}r)^2$ (red) versus radius.

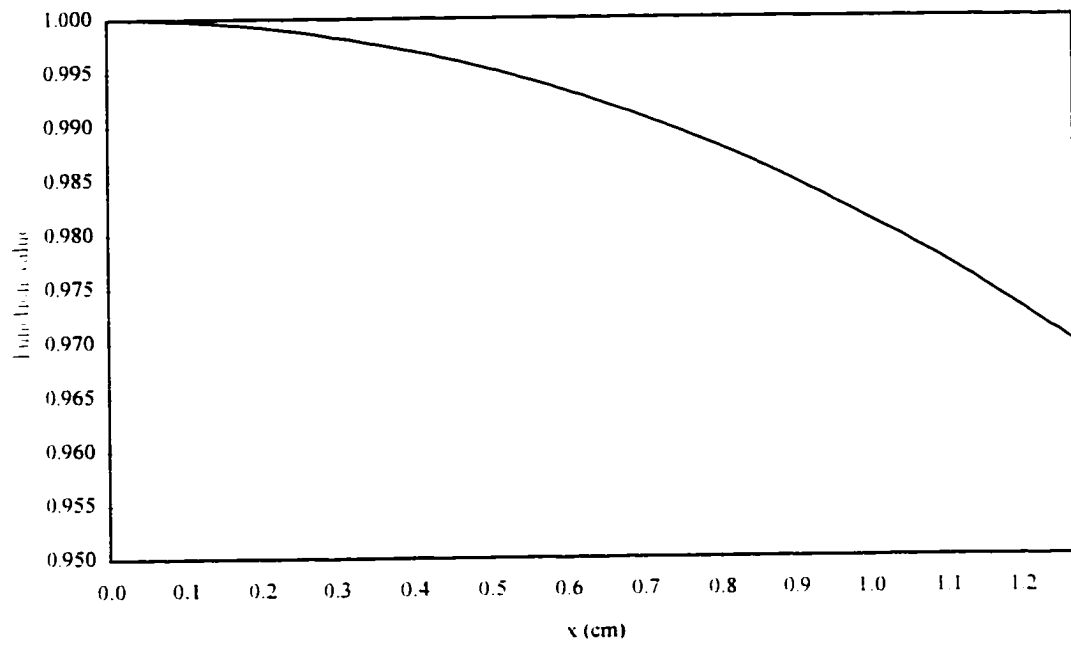


Figure E-3: $\left(1 - \frac{x_{11}^2}{4a^2} x^2\right)$ vs. x (cm).

the x axis. Therefore, this term will also be dropped, leaving

$$B_y \cong \frac{\omega a}{2x_{11}c^2} E_0 \sin(\omega t + \phi). \quad (\text{E-11})$$

E.4 Demonstration of dominant field

Of the three field components present inside the fast deflector cavity, it is the y magnetic field given in (E-11) that has the dominant effect. This can be seen if we first calculate the magnitude of the ratio of the x magnetic field to the y magnetic field. Using (E-9) and (E-11) this is

$$\left| \frac{B_x}{B_y} \right| \leq \frac{\frac{\omega x_{11}}{8ac^2} E_0 x_{\max} y_{\max}}{\frac{\omega a}{2x_{11}c^2} E_0} = \frac{x_{11}^2 r_{\max}^2}{2a^2} = \frac{(3.8317)^2 (1.27\text{cm})^2}{4(14.0\text{cm})^2} = 0.03.$$

Therefore, the x magnetic field magnitude will be, at most, three percent of the y magnetic field. Therefore, the x magnetic field can be ignored.

To demonstrate that the electric field can also be ignored, an estimate of an electron's energy change as it passes through the cavity is necessary. Since the fast deflector cavity is not intended to give, or take, energy from the electrons, it is expected that this change will be slight.

The equation of motion for the longitudinal direction is

$$\frac{d}{dt}(\gamma m \dot{z}) = qE_z = -eE_z$$

Since the electron are already highly relativistic, the longitudinal velocity will not change substantially. Therefore,

$$\frac{dz}{dt} = 0$$

leaving

$$m\dot{z} \frac{d\gamma}{dt} = -eE_z.$$

Using

$$\dot{z} = \beta c$$

and substituting (E-8) for E_z gives

$$\frac{d\gamma}{dt} = -\frac{eE_0 k_{11} x}{2\beta c m} \cos(\omega t + \phi).$$

To estimate the energy change, the time dependence of x will be assumed to be constant. This makes integrating this equation trivial:

$$\int_{t_{in}}^{t_{out}} \frac{d\gamma}{dt} dt = \gamma_{out} - \gamma_{in} \equiv \Delta\gamma \cong -\frac{eE_0 k_{11} x}{2\beta c m} \frac{\sin(\omega t + \phi)}{\omega} \Big|_{t_{in}}^{t_{out}}.$$

The time that an electron exits the cavity, t_{out} , is equal to the time that it enters the cavity, t_{in} , plus the time it takes for it to traverse the fast deflector. Therefore

$$t_{out} = t_{in} + \frac{L}{\beta c}$$

and

$$\Delta\gamma \cong -\frac{eE_0 k_{11} x}{2\beta c m \omega} \left\{ \sin \left[\omega \left(t_{in} + \frac{L}{\beta c} \right) + \phi \right] - \sin(\omega t_{in} + \phi) \right\}. \quad (E-12)$$

For a given electric field amplitude, it is easy to find the maximum energy change from (E-12). Figure E-4 shows the maximum relative change in gamma versus x for an 8 MeV electron when E_0 is set to its maximum value of 24 MV/m. The largest relative energy

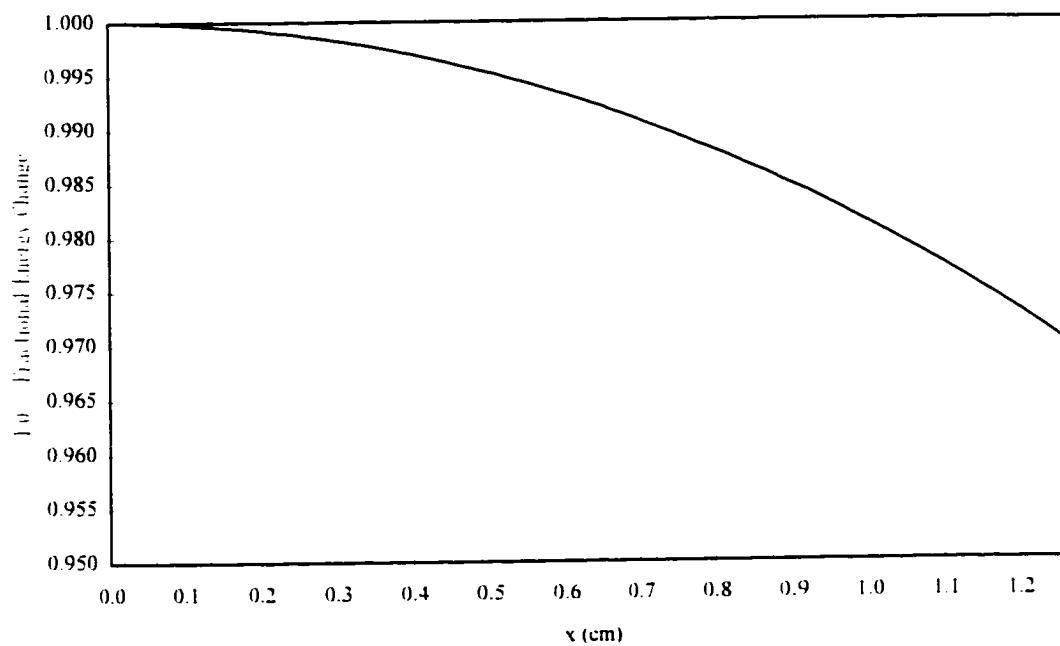


Figure E-4: $\left| \frac{\Delta\gamma}{\gamma} \right|$ vs. x (cm) for an 8 MeV electron.

change is about four percent near the edge of the aperture. Since the energy change will generally be much smaller than this, the electric field can also be neglected.

E.5 Solution to the first order equations of motion

If only the y magnetic field in (E-11) is kept, we are left with a simple equation of motion:

$$\frac{d}{dt}(\gamma m \dot{x}) = -qzB_y = e\dot{z}B_y.$$

Substituting (E-11) into this equation and setting

$$\dot{\gamma} = 0$$

yields

$$\gamma m \ddot{x} = e\dot{z} \frac{\omega a}{2x_{11}c^2} E_0 \sin(\omega t + \phi). \quad (\text{E-13})$$

To solve (E-13), we will first change to more useful coordinates. First,

$$\frac{d}{dt} = \frac{dz}{dt} \frac{d}{dz} = \dot{z} \frac{d}{dz} = \beta c \frac{d}{dz}.$$

Therefore

$$\gamma m (\beta c)^2 \frac{d^2 x}{dz^2} = e\beta c \frac{\omega a}{2x_{11}c^2} E_0 \sin(\omega t + \phi).$$

or

$$x'' = \frac{e}{\beta \gamma m c} \frac{\omega a}{2x_{11}c^2} E_0 \sin(\omega t + \phi).$$

The value of t is given by

$$t = \frac{z}{\beta c},$$

where z is the electron's longitudinal location and βc its longitudinal velocity. It will be defined that z equal to zero is the entrance to the fast deflector cavity. Therefore

$$x'' = \frac{e}{\beta \gamma m c} \frac{\omega a}{2x_{11} c^2} E_0 \sin\left(\frac{\omega z}{\beta c} + \phi\right). \quad (\text{E-14})$$

It is easy to integrate (E-14). Doing this yields

$$x'(z) = -\frac{e}{\gamma m} \frac{a}{2x_{11} c^2} E_0 \cos\left(\frac{\omega z}{\beta c} + \phi\right) + c_1, \quad (\text{E-15})$$

where c_1 is a constant. Integrating again gives

$$x(z) = -\frac{e}{\gamma m} \frac{a}{2x_{11} c^2} E_0 \frac{\beta c}{\omega} \sin\left(\frac{\omega z}{\beta c} + \phi\right) + c_1 z + c_2, \quad (\text{E-16})$$

where c_2 is also a constant.

The position and divergence of the electron at the fast deflector cavity entrance are defined as

$$x_i \equiv x(0)$$

and

$$x'_i \equiv x'(0).$$

Substituting these values into (E-15) and (E-16) and solving for the constants c_1 and c_2 results in

$$c_1 = x'_i + \frac{e}{\gamma m} \frac{a}{2x_{11} c^2} E_0 \cos \phi \quad (\text{E-17})$$

and

$$c_2 = x_i + \frac{e}{\gamma m} \frac{a}{2x_{11}c^2} E_0 \frac{\beta c}{\omega} \sin \phi. \quad (\text{E-18})$$

E.6 Electron position and divergence at exit of fast deflector cavity

In practice, we are not concerned very much with the trajectory of the electrons through the fast deflector. It is the final trajectory, at the cavity exit, that is more important. Also, since the electrons will always be part of a beam bunch, the notation used to this point needs to be modified slightly.

At the exit to the fast deflector cavity, z is equal to L , the cavity length. Using (E-15) and (E-16), the position and divergence of the electron at the cavity exit are given by

$$x_L = x(L) = -\frac{e}{\gamma m} \frac{a}{2x_{11}c^2} E_0 \frac{\beta c}{\omega} \sin\left(\frac{\omega L}{\beta c} + \phi\right) + c_1 L + c_2 \quad (\text{E-19})$$

and

$$x'_L = x'(L) = -\frac{e}{\gamma m} \frac{a}{2x_{11}c^2} E_0 \cos\left(\frac{\omega L}{\beta c} + \phi\right) + c_1. \quad (\text{E-20})$$

The phase angle, ϕ , can be rewritten as

$$\phi = \phi_0 + \Delta\phi + \phi_z.$$

The angle $\phi_0 + \Delta\phi$ is defined as the phase of the beam bunch center with respect to the cavity fields. The angle $\Delta\phi$ is included for calibration purposes. Its magnitude is defined to be much less than one. The angle ϕ_z is defined as the phase of a particular electron in the bunch with respect to $\phi_0 + \Delta\phi$.

As mentioned in Chapter 1, the beam bunches on SPA are 6 mm FWHM in length or less. This is a time duration of 20 ps. At the frequency 1300 MHz, then, the magnitude

of ϕ_z will be

$$|\phi_z| \leq (10 \text{ ps})(2\pi f) = 0.082 .$$

Therefore,

$$|\Delta\phi + \phi_z| \ll 1$$

and one can make the following approximations:

$$\begin{aligned} \cos\left(\frac{\omega L}{\beta c} + \phi_0 + \Delta\phi + \phi_z\right) &= \cos\left(\frac{\omega L}{\beta c} + \phi_0\right) \cos(\Delta\phi + \phi_z) \\ &\quad - \sin\left(\frac{\omega L}{\beta c} + \phi_0\right) \sin(\Delta\phi + \phi_z). \\ &\cong \cos\left(\frac{\omega L}{\beta c} + \phi_0\right) \left[1 - (\Delta\phi + \phi_z)^2\right] - \sin\left(\frac{\omega L}{\beta c} + \phi_0\right) \left[(\Delta\phi + \phi_z) - (\Delta\phi + \phi_z)^3\right] \\ \cos\left(\frac{\omega L}{\beta c} + \phi_0 + \Delta\phi + \phi_z\right) &\cong \cos\left(\frac{\omega L}{\beta c} + \phi_0\right) - (\Delta\phi + \phi_z) \sin\left(\frac{\omega L}{\beta c} + \phi_0\right). \end{aligned} \quad (\text{E-21})$$

$$\begin{aligned} \sin\left(\frac{\omega L}{\beta c} + \phi_0 + \Delta\phi + \phi_z\right) &= \sin\left(\frac{\omega L}{\beta c} + \phi_0\right) \cos(\Delta\phi + \phi_z) \\ &\quad + \cos\left(\frac{\omega L}{\beta c} + \phi_0\right) \sin(\Delta\phi + \phi_z). \\ \sin\left(\frac{\omega L}{\beta c} + \phi_0 + \Delta\phi + \phi_z\right) &\cong \sin\left(\frac{\omega L}{\beta c} + \phi_0\right) + (\Delta\phi + \phi_z) \cos\left(\frac{\omega L}{\beta c} + \phi_0\right). \end{aligned} \quad (\text{E-22})$$

$$\cos\phi = \cos(\phi_0 + \Delta\phi + \phi_z) = \cos\phi_0 \cos(\Delta\phi + \phi_z) - \sin\phi_0 \sin(\Delta\phi + \phi_z).$$

$$\cos\phi \cong \cos\phi_0 - (\Delta\phi + \phi_z) \sin\phi_0 \quad (\text{E-23})$$

and

$$\sin \phi = \sin(\phi_0 + \Delta\phi + \phi_z) = \sin \phi_0 \cos(\Delta\phi + \phi_z) + \sin(\Delta\phi + \phi_z) \cos \phi_0.$$

$$\sin \phi \cong \sin \phi_0 + (\Delta\phi + \phi_z) \cos \phi_0. \quad (\text{E-24})$$

Substituting (E-21), (E-22), (E-23) and (E-24) into (E-17), (E-18), (E-19) and (E-20) yields

$$\begin{aligned} x_L = & -\frac{e}{\gamma m} \frac{a}{2x_{11}c^2} E_0 \frac{\beta c}{\omega} \left[\sin\left(\frac{\omega L}{\beta c} + \phi_0\right) + (\Delta\phi + \phi_z) \cos\left(\frac{\omega L}{\beta c} + \phi_0\right) \right] \\ & + L \left[x'_i + \frac{e}{\gamma m} \frac{a}{2x_{11}c^2} E_0 (\cos \phi_0 - (\Delta\phi + \phi_z) \sin \phi_0) \right] \\ & + x_i + \frac{e}{\gamma m} \frac{a}{2x_{11}c^2} E_0 \frac{\beta c}{\omega} (\sin \phi_0 + (\Delta\phi + \phi_z) \cos \phi_0) \end{aligned}$$

$$\begin{aligned} x_L = & x_i + Lx'_i + \frac{e}{\gamma m} \frac{a}{2x_{11}c^2} E_0 \frac{\beta c}{\omega} \left\{ \sin \phi_0 + \frac{\omega L}{\beta c} \cos \phi_0 - \sin\left(\frac{\omega L}{\beta c} + \phi_0\right) \right. \\ & \left. + (\Delta\phi + \phi_z) \left[\cos \phi_0 - \frac{\omega L}{\beta c} \sin \phi_0 - \cos\left(\frac{\omega L}{\beta c} + \phi_0\right) \right] \right\}. \end{aligned}$$

and

$$\begin{aligned} x'_L = & x'_i + \frac{e}{\gamma m} \frac{a}{2x_{11}c^2} E_0 \left\{ \cos \phi_0 - \cos\left(\frac{\omega L}{\beta c} + \phi_0\right) \right. \\ & \left. + (\Delta\phi + \phi_z) \left[\sin\left(\frac{\omega L}{\beta c} + \phi_0\right) - \sin \phi_0 \right] \right\}. \end{aligned}$$

Appendix F

Appendix F
COVARIANCE MATRIX AND THE STANDARD ERROR IN THE
CALCULATION OF THE EMITTANCE

F.1 Introduction

As demonstrated in Chapter 2, the rms beam parameters, $\langle x^2 \rangle$, $\langle x'^2 \rangle$, $\langle xx' \rangle$, $\langle y^2 \rangle$, $\langle y'^2 \rangle$ and $\langle yy' \rangle$, are determined by inverting a matrix equation. The x and y rms emittances are then calculated according to

$$\varepsilon_x \equiv \sqrt{\langle x^2 \rangle \langle x'^2 \rangle - \langle xx' \rangle^2} \quad (\text{F-1})$$

and

$$\varepsilon_y \equiv \sqrt{\langle y^2 \rangle \langle y'^2 \rangle - \langle yy' \rangle^2} . \quad (\text{F-2})$$

In this appendix, expressions for the standard errors for the rms beam parameters and the x and y rms emittances are derived.

The standard errors in rms beam parameters are determined from the well known covariance matrix[34]. The expressions for the standard errors for the x and y rms emittances were first demonstrated by Miller et al.[12].

F.2 Estimating measurement errors

In this section, an estimate for the measurement errors in a linear set of equations is derived. It is assumed that these errors are normally distributed.

Assume the general matrix equation,

$$\bar{\bar{\mathbf{A}}}\bar{\bar{\mathbf{x}}} = \bar{\bar{\mathbf{b}}},$$

where $\bar{\bar{\mathbf{A}}}$ has m rows and n columns, $\bar{\bar{\mathbf{x}}}$ has dimension n and $\bar{\bar{\mathbf{b}}}$ has dimension m . The vector $\bar{\bar{\mathbf{b}}}$ is determined by measurement. Therefore, there will be some standard error, σ , associated with the individual entries of $\bar{\bar{\mathbf{b}}}$. Although it might be true that the value of this error is well known from the measurement process, it can also be estimated from the data.

Assume that $m > n$ and $\bar{\bar{\mathbf{A}}}$ is of rank n . To solve for $\bar{\bar{\mathbf{x}}}$, first multiply both sides by the transpose of $\bar{\bar{\mathbf{A}}}$, leaving

$$\bar{\bar{\mathbf{A}}}^T \bar{\bar{\mathbf{A}}}\bar{\bar{\mathbf{x}}} = \bar{\bar{\mathbf{A}}}^T \bar{\bar{\mathbf{b}}}.$$

$\bar{\bar{\mathbf{A}}}^T \bar{\bar{\mathbf{A}}}$ is a positive definite square matrix and can be inverted. Multiplying both sides of the equation by its inverse gives

$$\bar{\bar{\mathbf{x}}} = \left(\bar{\bar{\mathbf{A}}}^T \bar{\bar{\mathbf{A}}} \right)^{-1} \bar{\bar{\mathbf{A}}}^T \bar{\bar{\mathbf{b}}}.$$

The matrix $\bar{\bar{\mathbf{A}}}^T \bar{\bar{\mathbf{A}}}$ has a set of n eigenvectors $\bar{\bar{\mathbf{v}}}_i$ defined by

$$\bar{\bar{\mathbf{v}}}_i \cdot \bar{\bar{\mathbf{v}}}_j = \delta_{ij}$$

and

$$\bar{\bar{\mathbf{A}}}^T \bar{\bar{\mathbf{A}}}\bar{\bar{\mathbf{v}}}_i = \lambda_i \bar{\bar{\mathbf{v}}}_i$$

where λ_i is the corresponding eigenvalue. The set of $\bar{\mathbf{v}}_i$'s form an orthonormal basis in the space spanned by $\bar{\mathbf{x}}$. Therefore, one can write $\bar{\mathbf{x}}$ and the vector $\bar{\bar{\mathbf{A}}}^T \bar{\mathbf{b}}$ as linear combinations of the eigenvectors:

$$\bar{\mathbf{x}} = \sum_{i=1}^n c_i \bar{\mathbf{v}}_i \quad (\text{F-3})$$

where the constants, c_i , are defined by the dot product

$$c_i \equiv \bar{\mathbf{x}} \cdot \bar{\mathbf{v}}_i,$$

and

$$\bar{\bar{\mathbf{A}}}^T \bar{\mathbf{b}} = \sum_{i=1}^n d_i \bar{\mathbf{v}}_i$$

where

$$d_i \equiv \bar{\bar{\mathbf{A}}}^T \bar{\mathbf{b}} \cdot \bar{\mathbf{v}}_i.$$

This gives,

$$\bar{\bar{\mathbf{A}}}^T \bar{\bar{\mathbf{A}}} \bar{\mathbf{x}} = \bar{\bar{\mathbf{A}}}^T \bar{\bar{\mathbf{A}}} \sum_{i=1}^n c_i \bar{\mathbf{v}}_i = \sum_{i=1}^n c_i \lambda_i \bar{\mathbf{v}}_i = \bar{\bar{\mathbf{A}}}^T \bar{\mathbf{b}} = \sum_{i=1}^n d_i \bar{\mathbf{v}}_i.$$

Dotting $\bar{\mathbf{v}}_j$ into both sides,

$$\bar{\mathbf{v}}_j \cdot \left(\sum_{i=1}^n c_i \lambda_i \bar{\mathbf{v}}_i \right) = c_j \lambda_j = \bar{\mathbf{v}}_j \cdot \left(\sum_{i=1}^n d_i \bar{\mathbf{v}}_i \right) = d_j,$$

substituting in the expression for d_j and solving for c_j gives

$$c_j = \frac{(\bar{\bar{\mathbf{A}}}^T \bar{\mathbf{b}}) \cdot \bar{\mathbf{v}}_j}{\lambda_j}.$$

Using (F-3) gives

$$\bar{\mathbf{x}} = \sum_{j=1}^n \frac{(\bar{\bar{\mathbf{A}}}^T \bar{\mathbf{b}}) \cdot \bar{\mathbf{v}}_j}{\lambda_j} \bar{\mathbf{v}}_j. \quad (\text{F-4})$$

The vector $\bar{\mathbf{b}}$ can be rewritten as

$$\bar{\mathbf{b}} = \bar{\mathbf{b}}_0 + \bar{\mathbf{e}}_b.$$

The vector $\bar{\mathbf{b}}_0$ is the ideal value of $\bar{\mathbf{b}}$. The vector $\bar{\mathbf{e}}_b$ contains the errors associated with $\bar{\mathbf{b}}$. Substituting this into (F-4) gives

$$\bar{\mathbf{x}} = \bar{\mathbf{x}}_0 + \bar{\mathbf{e}}_x = \sum_{j=1}^n \frac{[\bar{\bar{\mathbf{A}}}^T (\bar{\mathbf{b}}_0 + \bar{\mathbf{e}}_b)] \cdot \bar{\mathbf{v}}_j}{\lambda_j} \bar{\mathbf{v}}_j = \sum_{j=1}^n \frac{(\bar{\bar{\mathbf{A}}}^T \bar{\mathbf{b}}_0) \cdot \bar{\mathbf{v}}_j}{\lambda_j} \bar{\mathbf{v}}_j + \sum_{j=1}^n \frac{(\bar{\bar{\mathbf{A}}}^T \bar{\mathbf{e}}_b) \cdot \bar{\mathbf{v}}_j}{\lambda_j} \bar{\mathbf{v}}_j.$$

So, the ideal value of $\bar{\mathbf{x}}$ is

$$\bar{\mathbf{x}}_0 = \sum_{j=1}^n \frac{(\bar{\bar{\mathbf{A}}}^T \bar{\mathbf{b}}_0) \cdot \bar{\mathbf{v}}_j}{\lambda_j} \bar{\mathbf{v}}_j$$

and its error is given by

$$\bar{\mathbf{e}}_x = \sum_{j=1}^n \frac{(\bar{\bar{\mathbf{A}}}^T \bar{\mathbf{e}}_b) \cdot \bar{\mathbf{v}}_j}{\lambda_j} \bar{\mathbf{v}}_j. \quad (\text{F-5})$$

Because $\bar{\mathbf{e}}_b$ is unknown, $\bar{\mathbf{e}}_x$ is also unknown. However, $\bar{\mathbf{e}}_x$ can be estimated. To do this, start by recognizing that

$$\begin{aligned} (\bar{\bar{\mathbf{A}}}\bar{\mathbf{v}}_i) \cdot (\bar{\bar{\mathbf{A}}}\bar{\mathbf{v}}_j) &= (\bar{\bar{\mathbf{A}}}\bar{\mathbf{v}}_i)^T (\bar{\bar{\mathbf{A}}}\bar{\mathbf{v}}_j), \\ &= \bar{\mathbf{v}}_i^T \bar{\bar{\mathbf{A}}}^T \bar{\bar{\mathbf{A}}}\bar{\mathbf{v}}_j = \lambda_j \bar{\mathbf{v}}_i^T \bar{\mathbf{v}}_j. \end{aligned}$$

$$(\bar{\bar{\mathbf{A}}}\bar{\mathbf{v}}_i) \cdot (\bar{\bar{\mathbf{A}}}\bar{\mathbf{v}}_j) = \lambda_j \delta_{ij}.$$

Now, we make the definition that there is a set of m orthonormal vectors, $\bar{\mathbf{g}}_i$, that span the space of $\bar{\mathbf{b}}$. The first n of these vectors are defined by

$$\bar{\mathbf{g}}_i \equiv \frac{\bar{\bar{\mathbf{A}}}\bar{\mathbf{v}}_i}{\left|\bar{\bar{\mathbf{A}}}\bar{\mathbf{v}}_i\right|} = \frac{\bar{\bar{\mathbf{A}}}\bar{\mathbf{v}}_i}{\sqrt{\lambda_i}}. \quad (\text{F-6})$$

Therefore, one can write

$$\bar{\mathbf{e}}_b = \sum_{i=1}^m a_i \bar{\mathbf{g}}_i \quad (\text{F-7})$$

where

$$a_i \equiv \bar{\mathbf{e}}_b \cdot \bar{\mathbf{g}}_i.$$

Substituting this into (F-5) gives

$$\bar{\mathbf{e}}_x = \sum_{j=1}^n \frac{\left(\bar{\bar{\mathbf{A}}}^T \sum_{i=1}^m a_i \bar{\mathbf{g}}_i\right) \cdot \bar{\mathbf{v}}_j}{\lambda_j} \bar{\mathbf{v}}_j. \quad (\text{F-8})$$

By definition

$$\left(\bar{\bar{\mathbf{A}}}^T \bar{\mathbf{g}}_i\right) \cdot \bar{\mathbf{v}}_j = \bar{\mathbf{g}}_i^T \bar{\bar{\mathbf{A}}}\bar{\mathbf{v}}_j = \frac{\bar{\mathbf{v}}_i^T \bar{\bar{\mathbf{A}}}^T \bar{\bar{\mathbf{A}}}\bar{\mathbf{v}}_j}{\sqrt{\lambda_i}}.$$

$$\left(\bar{\bar{\mathbf{A}}}^T \bar{\mathbf{g}}_i\right) \cdot \bar{\mathbf{v}}_j = \frac{\lambda_j \bar{\mathbf{v}}_i^T \bar{\mathbf{v}}_j}{\sqrt{\lambda_i}} = \sqrt{\lambda_i} \delta_{ij}$$

when $i \leq n$ and

$$\left(\bar{\bar{\mathbf{A}}}^T \bar{\mathbf{g}}_i\right) \cdot \bar{\mathbf{v}}_j = 0$$

when $i > n$. Substituting these results into (F-8) gives

$$\bar{\mathbf{e}}_x = \sum_{j=1}^n \sum_{i=1}^n a_i \frac{\delta_{ij} \sqrt{\lambda_i}}{\lambda_j} \bar{\mathbf{v}}_j = \sum_{j=1}^n \frac{a_j \bar{\mathbf{v}}_j}{\sqrt{\lambda_j}}. \quad (\text{F-9})$$

Each element of $\bar{\mathbf{e}}_b$ is the error in the measurement of the corresponding element of $\bar{\mathbf{b}}$. Assume that these errors are normal and, on average, equal. Then the magnitude of

the vector $\bar{\mathbf{e}}_b$ is

$$|\bar{\mathbf{e}}_b| = \sqrt{\bar{\mathbf{e}}_b \cdot \bar{\mathbf{e}}_b} \cong \sqrt{m\sigma^2} = \sigma\sqrt{m}$$

where σ is the average measurement error. Using (F-9) one gets

$$\bar{\mathbf{e}}_b \cdot \bar{\mathbf{e}}_b = \left(\sum_{i=1}^m a_i \bar{\mathbf{g}}_b \right) \cdot \left(\sum_{j=1}^m a_j \bar{\mathbf{g}}_b \right) = \sum_{j=1}^m a_j^2 \cong m\sigma^2.$$

Therefore, on average,

$$a_j^2 \cong (\bar{\mathbf{e}}_b \cdot \bar{\mathbf{g}}_i)^2 \cong \sigma^2. \quad (\text{F-10})$$

The vector $\bar{\mathbf{b}}$ can also be expanded as a sum of $\bar{\mathbf{g}}_i$'s.

$$\bar{\mathbf{b}} = \sum_{i=1}^m (\bar{\mathbf{b}} \cdot \bar{\mathbf{g}}_i) \bar{\mathbf{g}}_i.$$

$$\sum_{i=1}^m (\bar{\mathbf{b}} \cdot \bar{\mathbf{g}}_i) \bar{\mathbf{g}}_i = \sum_{i=1}^m [(\bar{\mathbf{b}}_0 + \bar{\mathbf{e}}_b) \cdot \bar{\mathbf{g}}_i] \bar{\mathbf{g}}_i.$$

$$\sum_{i=1}^m (\bar{\mathbf{b}} \cdot \bar{\mathbf{g}}_i) \bar{\mathbf{g}}_i = \sum_{i=1}^n [(\bar{\mathbf{b}}_0 + \bar{\mathbf{e}}_b) \cdot \bar{\mathbf{g}}_i] \bar{\mathbf{g}}_i + \sum_{i=n+1}^m [(\bar{\mathbf{b}}_0 + \bar{\mathbf{e}}_b) \cdot \bar{\mathbf{g}}_i] \bar{\mathbf{g}}_i.$$

Because $\bar{\mathbf{b}}_0$ is perpendicular to $\bar{\mathbf{g}}_i$ when $i > m$.

$$\sum_{i=1}^m (\bar{\mathbf{b}} \cdot \bar{\mathbf{g}}_i) \bar{\mathbf{g}}_i = \sum_{i=1}^n (\bar{\mathbf{b}} \cdot \bar{\mathbf{g}}_i) \bar{\mathbf{g}}_i + \sum_{i=n+1}^m (\bar{\mathbf{e}}_b \cdot \bar{\mathbf{g}}_i) \bar{\mathbf{g}}_i.$$

or

$$\bar{\mathbf{b}} - \sum_{i=1}^n (\bar{\mathbf{b}} \cdot \bar{\mathbf{g}}_i) \bar{\mathbf{g}}_i = \sum_{i=n+1}^m (\bar{\mathbf{e}}_b \cdot \bar{\mathbf{g}}_i) \bar{\mathbf{g}}_i.$$

Taking the square of both sides and using (F-10) yields

$$\left[\bar{\mathbf{b}} - \sum_{i=1}^n (\bar{\mathbf{b}} \cdot \bar{\mathbf{g}}_i) \bar{\mathbf{g}}_i \right]^2 = \sum_{i=n+1}^m (\bar{\mathbf{e}}_b \cdot \bar{\mathbf{g}}_i)^2 \cong (m-n)\sigma^2.$$

Therefore

$$\sigma^2 \equiv \frac{1}{m-n} \left[\bar{\mathbf{b}} - \sum_{i=1}^n (\bar{\mathbf{b}} \cdot \bar{\mathbf{g}}_i) \bar{\mathbf{g}}_i \right]^2 \quad (\text{F-10})$$

By the definition in (F-6),

$$\begin{aligned} (\bar{\mathbf{b}} \cdot \bar{\mathbf{g}}_i) \bar{\mathbf{g}}_i &= (\bar{\mathbf{g}}_i \cdot \bar{\mathbf{b}}) \bar{\mathbf{g}}_i = \frac{[(\bar{\bar{\mathbf{A}}}\bar{\mathbf{v}}_i) \cdot \bar{\mathbf{b}}](\bar{\bar{\mathbf{A}}}\bar{\mathbf{v}}_i)}{\lambda_i} \\ (\bar{\mathbf{b}} \cdot \bar{\mathbf{g}}_i) \bar{\mathbf{g}}_i &= \frac{[(\bar{\bar{\mathbf{A}}}\bar{\mathbf{v}}_i) \cdot (\bar{\bar{\mathbf{A}}}\bar{\mathbf{x}})](\bar{\bar{\mathbf{A}}}\bar{\mathbf{v}}_i)}{\lambda_i} = \frac{[(\bar{\bar{\mathbf{A}}}\bar{\mathbf{x}}) \cdot (\bar{\bar{\mathbf{A}}}\bar{\mathbf{v}}_i)](\bar{\bar{\mathbf{A}}}\bar{\mathbf{v}}_i)}{\lambda_i} \\ (\bar{\mathbf{b}} \cdot \bar{\mathbf{g}}_i) \bar{\mathbf{g}}_i &= \frac{[\bar{\bar{\mathbf{x}}}\bar{\bar{\mathbf{A}}}^T \bar{\bar{\mathbf{A}}}\bar{\mathbf{v}}_i](\bar{\bar{\mathbf{A}}}\bar{\mathbf{v}}_i)}{\lambda_i} = \frac{[\bar{\bar{\mathbf{x}}}^T \lambda_i \bar{\mathbf{v}}_i](\bar{\bar{\mathbf{A}}}\bar{\mathbf{v}}_i)}{\lambda_i} \\ (\bar{\mathbf{b}} \cdot \bar{\mathbf{g}}_i) \bar{\mathbf{g}}_i &= [\bar{\bar{\mathbf{x}}}^T \bar{\mathbf{v}}_i](\bar{\bar{\mathbf{A}}}\bar{\mathbf{v}}_i). \end{aligned}$$

Since $\bar{\bar{\mathbf{x}}}^T \bar{\mathbf{v}}_i$ is a constant,

$$\begin{aligned} (\bar{\mathbf{b}} \cdot \bar{\mathbf{g}}_i) \bar{\mathbf{g}}_i &= (\bar{\bar{\mathbf{A}}}\bar{\mathbf{v}}_i) \bar{\bar{\mathbf{x}}}^T \bar{\mathbf{v}}_i = \bar{\bar{\mathbf{A}}}\bar{\mathbf{v}}_i \bar{\mathbf{v}}_i^T \bar{\bar{\mathbf{x}}} = \bar{\bar{\mathbf{A}}}(\bar{\mathbf{v}}_i \cdot \bar{\mathbf{v}}_i) \bar{\bar{\mathbf{x}}} \\ (\bar{\mathbf{b}} \cdot \bar{\mathbf{g}}_i) \bar{\mathbf{g}}_i &= \bar{\bar{\mathbf{A}}}\bar{\bar{\mathbf{x}}}. \end{aligned}$$

Putting this into (F-10) yields

$$\sigma^2 \equiv \frac{1}{m-n} \left[\bar{\mathbf{b}} - \bar{\bar{\mathbf{A}}}\bar{\bar{\mathbf{x}}} \right]^2 \quad (\text{F-11})$$

F.3 Covariance matrix

In this section the Covariance matrix is defined and its relationship with the estimated errors in the components of $\bar{\mathbf{x}}$ is established

To begin, define the matrix

$$\bar{\bar{\mathbf{E}}} \equiv (\bar{\bar{\mathbf{A}}^T \bar{\bar{\mathbf{A}}})^{-1}.$$

The n eigenvectors of the matrix $\bar{\bar{\mathbf{A}}^T \bar{\bar{\mathbf{A}}}$ can be written as

$$\bar{\mathbf{v}}_i = \begin{pmatrix} v_{i1} \\ v_{i2} \\ \vdots \\ v_{in} \end{pmatrix}.$$

This allows $\bar{\bar{\mathbf{E}}}$ to be written as

$$\bar{\bar{\mathbf{E}}} = \begin{bmatrix} v_{11} & v_{21} & \dots & v_{n1} \\ v_{12} & \cdot & \cdot & v_{n2} \\ \cdot & \cdot & \cdot & \cdot \\ \cdot & \cdot & \cdot & \cdot \\ v_{1n} & v_{2n} & \dots & v_{nn} \end{bmatrix} \begin{bmatrix} 1/\lambda_1 & 0 & \dots & 0 \\ 0 & 1/\lambda_2 & \cdot & \cdot \\ \cdot & \cdot & \cdot & \cdot \\ \cdot & \cdot & \cdot & 0 \\ 0 & \cdot & \cdot & 0 & 1/\lambda_n \end{bmatrix} \begin{bmatrix} v_{11} & v_{12} & \dots & v_{1n} \\ v_{21} & \cdot & \cdot & v_{2n} \\ \cdot & \cdot & \cdot & \cdot \\ \cdot & \cdot & \cdot & \cdot \\ v_{n1} & v_{n2} & \dots & v_{nn} \end{bmatrix} \quad [20].$$

Multiplying this out, one gets the symmetric matrix

$$\bar{\bar{\mathbf{E}}} = \begin{bmatrix} \sum_{i=1}^n \frac{v_{i1}^2}{\lambda_i} & \sum_{i=1}^n \frac{v_{i1} v_{i2}}{\lambda_i} & \cdot & \cdot & \cdot & \sum_{i=1}^n \frac{v_{i1} v_{in}}{\lambda_i} \\ \sum_{i=1}^n \frac{v_{i1} v_{i2}}{\lambda_i} & \sum_{i=1}^n \frac{v_{i2}^2}{\lambda_i} & \cdot & \cdot & \cdot & \cdot \\ \cdot & \cdot & \cdot & \cdot & \cdot & \cdot \\ \cdot & \cdot & \cdot & \cdot & \cdot & \cdot \\ \cdot & \cdot & \cdot & \cdot & \cdot & \sum_{i=1}^n \frac{v_{i(n-1)} v_{in}}{\lambda_i} \\ \sum_{i=1}^n \frac{v_{i1} v_{in}}{\lambda_i} & \cdot & \cdot & \cdot & \sum_{i=1}^n \frac{v_{i(n-1)} v_{in}}{\lambda_i} & \sum_{i=1}^n \frac{v_{in}^2}{\lambda_i} \end{bmatrix}. \quad (\text{F-12})$$

The covariance matrix is defined as

$$\bar{\bar{\mathbf{C}}} \equiv \sigma^2 \bar{\bar{\mathbf{E}}} \quad (\text{F-13})$$

where σ^2 is given by (F-11).

Equation (F-9) is an expression for the error vector \bar{e}_x :

$$\bar{e}_x = \sum_{j=1}^n \sum_{i=1}^n a_i \frac{\delta_{ij} \sqrt{\lambda_i}}{\lambda_j} \bar{v}_j = \sum_{j=1}^n \frac{a_j \bar{v}_j}{\sqrt{\lambda_j}}.$$

The estimated value of a_j is given in (F-10). Therefore, the errors in the individual components of \bar{x} is given by

$$(e_{x_i})^2 \cong \sigma^2 \sum_{j=1}^n \frac{v_{ji}^2}{\lambda_j} \quad (\text{F-14})$$

where e_{x_i} is the error in the i^{th} element of \bar{e}_x and v_{ji} is the i^{th} element of the j^{th} eigenvector of $\bar{A}^T \bar{A}$. The expression in (F-14) is just the expression for the diagonal entries of the covariance matrix defined in (F-12) and (F-13). Therefore, the magnitude of the error in the i^{th} element of \bar{x} is

$$|e_{x_i}| \cong \sqrt{C_{ii}}. \quad (\text{F-15})$$

F.4 Estimated error in calculation of the emittance

For the particular set of linear equations dealt with in Chapter 1, $n = 6$ and

$$\bar{x} \cong \begin{pmatrix} \langle x^2 \rangle \\ \langle xx' \rangle \\ \langle x'^2 \rangle \\ \langle y^2 \rangle \\ \langle yy' \rangle \\ \langle y'^2 \rangle \end{pmatrix}. \quad (\text{F-16})$$

From the elements of \bar{x} , the x and y rms emittances are calculated according to (F-1) and

(F-2). In this section the errors in the emittances are estimated.

To begin, from (F-1), the x emittance squared is

$$\varepsilon_x^2 = \langle x^2 \rangle \langle x'^2 \rangle - \langle xx' \rangle^2 = x_1 x_3 - x_2^2$$

where x_1 , x_2 and x_3 are the first three elements of the vector \bar{x} given in (F-16). Recall that we can write

$$\bar{x} = \bar{x}_0 + \bar{e}_x.$$

then

$$\varepsilon_x^2 = (x_{01} + e_{x1})(x_{03} + e_{x3}) - (x_{02} + e_{x2})^2.$$

Multiplying this out,

$$\varepsilon_x^2 = x_{01}x_{03} - x_{02}^2 + x_{01}e_{x3} + x_{03}e_{x1} + e_{x1}e_{x3} - 2x_{02}e_{x2} - e_{x2}^2. \quad (\text{F-17})$$

The first two terms in give the actual, or ideal, emittance

$$\varepsilon_{x0}^2 = x_{01}x_{03} - x_{02}^2.$$

The remaining terms give the error in the emittance estimate.

To find a value for the emittance error, first make the substitutions

$$x_{01} \rightarrow x_1,$$

$$x_{02} \rightarrow x_2$$

and

$$x_{03} \rightarrow x_3.$$

Since x_{01} , x_{02} and x_{03} are unknown, they are replaced with x_1 , x_2 and x_3 , the best estimate of their values. Then, from (F-17), the error in the emittance squared is

$$\text{err}_{\varepsilon_x^2} \cong x_1 e_{x3} + x_3 e_{x1} + e_{x1} e_{x3} - 2x_2 e_{x2} - e_{x2}^2.$$

This can be divided into two terms:

$$\text{err}_{\mathbf{e}_i} \cong \text{term1} + \text{term2}, \quad (\text{F-18})$$

where

$$\text{term1} = \mathbf{e}_{x1}\mathbf{e}_{x3} - \mathbf{e}_{x2}^2 \quad (\text{F-19})$$

and

$$\text{term2} = x_1\mathbf{e}_{x3} + x_3\mathbf{e}_{x1} - 2x_2\mathbf{e}_{x2}. \quad (\text{F-20})$$

From (F-9).

$$\bar{\mathbf{e}}_x = \begin{pmatrix} \mathbf{e}_{x1} \\ \mathbf{e}_{x2} \\ \cdot \\ \cdot \\ \cdot \\ \mathbf{e}_6 \end{pmatrix} = \sum_{j=1}^6 \frac{\mathbf{a}_j \bar{\mathbf{v}}_j}{\sqrt{\lambda_j}}.$$

Substituting this into (F-19) and (F-20) gives

$$\text{term1} = \left[\sum_{j=1}^6 \frac{\mathbf{a}_j \mathbf{v}_{j1}}{\sqrt{\lambda_j}} \right] \left[\sum_{j=1}^6 \frac{\mathbf{a}_j \mathbf{v}_{j3}}{\sqrt{\lambda_j}} \right] - \left[\sum_{j=1}^6 \frac{\mathbf{a}_j \mathbf{v}_{j2}}{\sqrt{\lambda_j}} \right]^2$$

and

$$\text{term2} = x_1 \left[\sum_{j=1}^6 \frac{\mathbf{a}_j \mathbf{v}_{j3}}{\sqrt{\lambda_j}} \right] + x_3 \left[\sum_{j=1}^6 \frac{\mathbf{a}_j \mathbf{v}_{j1}}{\sqrt{\lambda_j}} \right] - 2x_2 \left[\sum_{j=1}^6 \frac{\mathbf{a}_j \mathbf{v}_{j2}}{\sqrt{\lambda_j}} \right].$$

For term1, we have

$$\text{term1} = \left[\sum_{j=1}^6 \frac{\mathbf{a}_j \mathbf{v}_{j1}}{\sqrt{\lambda_j}} \right] \left[\sum_{j=1}^6 \frac{\mathbf{a}_j \mathbf{v}_{j3}}{\sqrt{\lambda_j}} \right] - \left[\sum_{j=1}^6 \frac{\mathbf{a}_j \mathbf{v}_{j2}}{\sqrt{\lambda_j}} \right]^2$$

$$\begin{aligned}
&= \sum_{j=1}^6 \sum_{i=1}^6 \frac{a_j v_{j1}}{\sqrt{\lambda_j}} \frac{a_i v_{i3}}{\sqrt{\lambda_i}} - \sum_{j=1}^6 \sum_{i=1}^6 \frac{a_j v_{j2}}{\sqrt{\lambda_j}} \frac{a_i v_{i2}}{\sqrt{\lambda_i}} \\
&= \sum_{j=1}^6 \sum_{i=1}^6 \frac{a_j}{\sqrt{\lambda_j}} \frac{a_i}{\sqrt{\lambda_i}} (v_{j1} v_{i3} - v_{j2} v_{i2}).
\end{aligned}$$

Since one can only estimate the magnitude of a_j and a_i using (F-10), term1 cannot be reduced any further. However, its magnitude can be estimated by adding in quadrature.

That is

$$\begin{aligned}
\text{term1}^2 &\cong \sum_{j=1}^6 \sum_{i=1}^6 \frac{a_j^2}{\lambda_j} \frac{a_i^2}{\lambda_i} (v_{j1} v_{i3} - v_{j2} v_{i2})^2 \\
&\cong \sum_{j=1}^6 \sum_{i=1}^6 \frac{\sigma^4}{\lambda_j \lambda_i} (v_{j1}^2 v_{i3}^2 - 2v_{j1} v_{i3} v_{j2} v_{i2} + v_{j2}^2 v_{i2}^2) \\
&\cong \left(\sigma^2 \sum_{j=1}^6 \frac{v_{j1}^2}{\lambda_j} \right) \left(\sigma^2 \sum_{i=1}^6 \frac{v_{i3}^2}{\lambda_i} \right) - 2 \left(\sigma^2 \sum_{j=1}^6 \frac{v_{j1} v_{j2}}{\lambda_j} \right) \left(\sigma^2 \sum_{i=1}^6 \frac{v_{i2} v_{i3}}{\lambda_i} \right) \\
&\quad + \left(\sigma^2 \sum_{j=1}^6 \frac{v_{j2}^2}{\lambda_j} \right) \left(\sigma^2 \sum_{i=1}^6 \frac{v_{i2}^2}{\lambda_i} \right).
\end{aligned}$$

The terms in parentheses can be identified as elements of the covariance matrix. (F-13).

Therefore

$$\text{term1}^2 \cong C_{11} C_{33} - 2C_{12} C_{23} + C_{22} C_{22} = C_{11} C_{33} + C_{22}^2 - 2C_{12} C_{23}. \quad (\text{F-21})$$

For term2 we have

$$\begin{aligned}
\text{term2} &= x_1 \left[\sum_{j=1}^6 \frac{a_j v_{j3}}{\sqrt{\lambda_j}} \right] + x_3 \left[\sum_{j=1}^6 \frac{a_j v_{j1}}{\sqrt{\lambda_j}} \right] - 2x_2 \left[\sum_{j=1}^6 \frac{a_j v_{j2}}{\sqrt{\lambda_j}} \right] \\
&= \sum_{j=1}^6 \frac{a_j}{\sqrt{\lambda_j}} (x_1 v_{j3} + x_3 v_{j1} - 2x_2 v_{j2}).
\end{aligned}$$

This can also be estimated by adding in quadrature:

$$\begin{aligned}
 \text{term2}^2 &\equiv \sum_{j=1}^6 \frac{a_j^2}{\lambda_j} (x_1 v_{j3} + x_3 v_{j1} - 2x_2 v_{j2})^2 \\
 &\equiv \sum_{j=1}^6 \frac{\sigma^2}{\lambda_j} (x_1^2 v_{j3}^2 + 2x_1 v_{j3} x_3 v_{j1} - 4x_1 v_{j3} x_2 v_{j2} + x_3^2 v_{j1}^2 - 4x_3 v_{j1} x_2 v_{j2} + 4x_2^2 v_{j2}^2) \\
 &\equiv x_1^2 \left(\sigma^2 \sum_{j=1}^6 \frac{v_{j3}^2}{\lambda_j} \right) + 2x_1 x_3 \left(\sigma^2 \sum_{j=1}^6 \frac{v_{j1} v_{j3}}{\lambda_j} \right) - 4x_1 x_2 \left(\sigma^2 \sum_{j=1}^6 \frac{v_{j2} v_{j3}}{\lambda_j} \right) \\
 &\quad + x_3^2 \left(\sigma^2 \sum_{j=1}^6 \frac{v_{j1}^2}{\lambda_j} \right) - 4x_2 x_3 \left(\sigma^2 \sum_{j=1}^6 \frac{v_{j1} v_{j2}}{\lambda_j} \right) + 4x_2^2 \left(\sigma^2 \sum_{j=1}^6 \frac{v_{j2}^2}{\lambda_j} \right).
 \end{aligned}$$

The summation terms can again be identified as elements of the covariance matrix, \bar{C} , yielding

$$\text{term2}^2 \equiv x_1^2 C_{33} + x_3^2 C_{11} + 4x_2^2 C_{22} + 2x_1 x_2 C_{13} - 4x_1 x_2 C_{23} - 4x_2 x_3 C_{12}. \quad (\text{F-22})$$

Since (F-21) and (F-22) are estimates of the magnitude of term1 and term2, they cannot be substituting into (F-18) to get the error in the emittance squared. However, by again adding in quadrature, the magnitude of $\text{err}_{\epsilon_x^2}$ can be estimated:

$$\begin{aligned}
 \text{err}_{\epsilon_x^2}^2 &\equiv \text{term1}^2 + \text{term2}^2 \\
 &\equiv x_1^2 C_{33} + x_3^2 C_{11} + 4x_2^2 C_{22} + 2x_1 x_2 C_{13} - 4x_1 x_2 C_{23} - 4x_2 x_3 C_{12} \\
 &\quad + C_{11} C_{33} + C_{22}^2 - 2C_{12} C_{23}
 \end{aligned}$$

Therefore,

$$\epsilon_x^2 = x_1 x_3 - x_2^2 \pm \sqrt{\text{err}_{\epsilon_x^2}^2}.$$

$$\begin{aligned}\varepsilon_x^2 = & \langle x^2 \rangle \langle x'^2 \rangle - \langle xx' \rangle^2 \pm \left(\langle x^2 \rangle^2 C_{33} + \langle x'^2 \rangle^2 C_{11} + 4 \langle xx' \rangle^2 C_{22} + 2 \langle x^2 \rangle \langle x'^2 \rangle C_{13} \right. \\ & \left. - 4 \langle x^2 \rangle \langle xx' \rangle C_{23} - 4 \langle xx' \rangle \langle x'^2 \rangle C_{12} + C_{11} C_{33} + C_{22}^2 - 2 C_{12} C_{23} \right)^{\frac{1}{2}}\end{aligned}$$

The emittance is then

$$\begin{aligned}\varepsilon_x &= \sqrt{\langle x^2 \rangle \langle x'^2 \rangle - \langle xx' \rangle^2} \pm \text{err}_{\varepsilon_x^2} \\ \varepsilon_x &= \sqrt{\langle x^2 \rangle \langle x'^2 \rangle - \langle xx' \rangle^2} \sqrt{1 \pm \frac{\text{err}_{\varepsilon_x^2}}{\langle x^2 \rangle \langle x'^2 \rangle - \langle xx' \rangle^2}}.\end{aligned}$$

When the emittance is significantly bigger than the error.

$$\begin{aligned}\varepsilon_x &= \sqrt{\langle x^2 \rangle \langle x'^2 \rangle - \langle xx' \rangle^2} \left[1 \pm \frac{\text{err}_{\varepsilon_x^2}}{2(\langle x^2 \rangle \langle x'^2 \rangle - \langle xx' \rangle^2)} \right] \\ \varepsilon_x &= \sqrt{\langle x^2 \rangle \langle x'^2 \rangle - \langle xx' \rangle^2} \pm \frac{1}{2\sqrt{\langle x^2 \rangle \langle x'^2 \rangle - \langle xx' \rangle^2}} \left(\langle x^2 \rangle^2 C_{33} + \langle x'^2 \rangle^2 C_{11} \right. \\ & \quad \left. + 4 \langle xx' \rangle^2 C_{22} + 2 \langle x^2 \rangle \langle x'^2 \rangle C_{13} - 4 \langle x^2 \rangle \langle xx' \rangle C_{23} - 4 \langle xx' \rangle \langle x'^2 \rangle C_{12} \right. \\ & \quad \left. + C_{11} C_{33} + C_{22}^2 - 2 C_{12} C_{23} \right)^{\frac{1}{2}}.\end{aligned}$$

Through a similar procedure, the y emittance can be found to be

$$\begin{aligned}\varepsilon_y &= \sqrt{\langle y^2 \rangle \langle y'^2 \rangle - \langle yy' \rangle^2} \pm \frac{1}{2\sqrt{\langle y^2 \rangle \langle y'^2 \rangle - \langle yy' \rangle^2}} \left(\langle y^2 \rangle^2 C_{66} + \langle y'^2 \rangle^2 C_{44} \right. \\ & \quad \left. + 4 \langle yy' \rangle^2 C_{55} + 2 \langle y^2 \rangle \langle y'^2 \rangle C_{46} - 4 \langle y^2 \rangle \langle yy' \rangle C_{56} - 4 \langle yy' \rangle \langle y'^2 \rangle C_{45} \right. \\ & \quad \left. + C_{44} C_{66} + C_{55}^2 - 2 C_{45} C_{56} \right)^{\frac{1}{2}}.\end{aligned}$$

REFERENCES

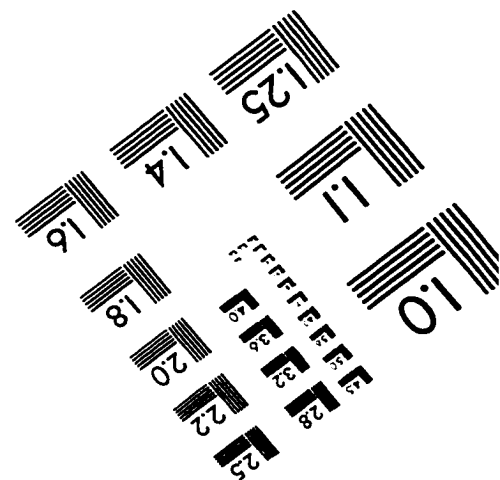
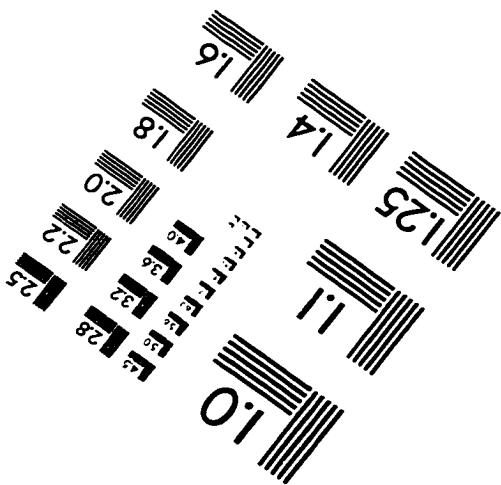
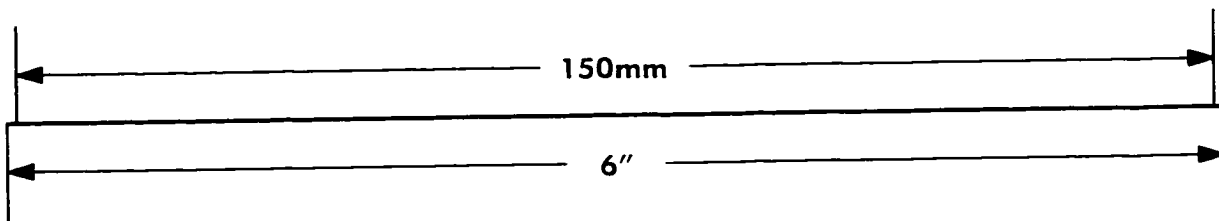
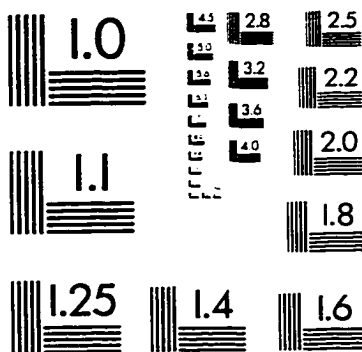
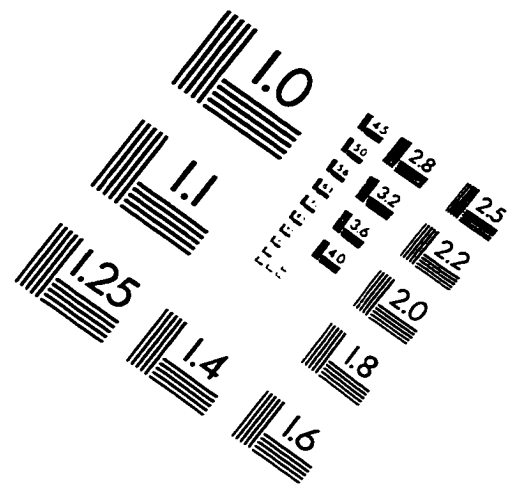
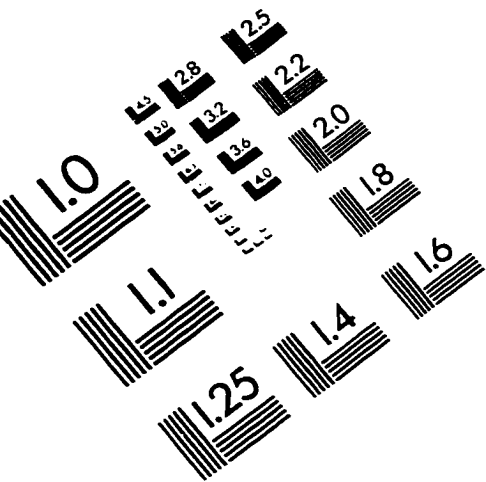
REFERENCES

- [1] R. Warren. "Star Wars and The FEL." (private communication).
- [2] C. A. Brau. *Free-Electron Lasers*. (Academic Press. Sand Diego, CA. 1990).
- [3] J. M. J. Madey. "Stimulated Emission of Bremsstrahlung in a Periodic Magnetic Field." *J. Appl. Phys.* **42**, 1906 (1971).
- [4] J. S. Fraser, R. L. Sheffield, E. R. Gray, P. M. Giles, R. W. Springer and V. A. Loeb. "Photocathodes in Accelerator Applications." *Proceedings of the 1987 Particle Accelerator Conference*, IEEE catalog No. 87CH2387-9, 1705 (IEEE, New York, 1987).
- [5] J. S. Fraser and Richard L. Sheffield. "High-Brightness Injectors for RF-Driven Free-Electron Lasers." *IEEE J. Quantum Electron.* **23**, 1489 (1987).
- [6] M. Reiser, *Theory and Design of Charged Particle Beams*. (John Wiley & Sons, New York, NY, 1994).
- [7] P. J. Tallerico and Jean-Pierre Coulon. "Computer Simulation of the Lasertron With a Ring Model." *Proceedings of the 1987 Particle Accelerator Conference*, IEEE catalog No. 87CH2387-9, 1806 (IEEE, New York, 1987).
- [8] B. E. Carlsten and S. J. Russell. "Subpicosecond compression of 0.1-1 nC electron bunches with a magnetic chicane at 8 MeV." *Phys. Rev. E* **53**, 2072 (1996).
- [9] B. E. Carlsten, J. C. Goldstein, P. G. O'Shea and E. J. Pitcher. "Measuring Emittance of Non-thermalized Electron Beams From Photoinjectors." *Nucl. Instrum. Phys. Res. A* **331**, 791 (1993).
- [10] K. Kim. "RF and Space Charge Effects in Laser-driven RF Electron Guns." *Nucl. Instrum. Phys. Res. A* **275**, 201 (1989).
- [11] R. T. Avery, A. Faltens and E. C. Hartwig. "Non-intercepting Monitor for Beam Current and Position." *IEEE Tans. Nucl. Sci.* **18**, 920 (1971).

- [12] R. H. Miller, J. E. Clendenin, M. B. James, J. C. Sheppard. "Non-intercepting Emittance Monitor." *Proceedings of the 12th International Conference on High Energy Accelerators*, 602 (Fermilab, 1983).
- [13] B. E. Carlsten, S. J. Russell, J. M. Kinross-Wright, M. Weber, J. G. Plato, M. L. Milder, R. Cooper and R. Sturges. "Subpicosecond Compression Experiments at Los Alamos National Laboratory." *Proceedings of the Micro Bunches Workshop*, AIP Conf. Proc. 367, 21 (AIP, Upton, NY, 1995).
- [14] W. D. Cornelius, S. Bender, K. Meir, L. E. Thode and J. M. Watson. "The Los Alamos High Brightness Accelerator FEL (HIBAF) Facility." *Nucl. Instrum. Methods Phys. Res. A* **296**, 251 (1990).
- [15] B. E. Carlsten. "Calculation of the noninertial space-charge force and the coherent synchrotron radiation force for short electron bunches in circular motion using the retarded Green's function technique." *Phys. Rev. E* **54**, 838 (1996).
- [16] J. D. Gilpatrick, J. F. Power, R. E. Meyer and C. R. Rose. "Design and Operation of Button-Probe, Beam-Position Measurements." *Proceedings of the 1993 Particle Accelerator Conference*, IEEE catalog No. 93CH3279-7, 2334 (IEEE, New York, 1993).
- [17] J. D. Gilpatrick, H. Marquez, J. Power and V. Yuan. "Design and Operation of a Bunched-Beam, Phase-Spread Measurement". *Proceedings of the 1992 Linear Accelerator Conference*, AECL catalog No. 10728, 359 (AECL Research, Chalk River, Ontario, Canada, 1992).
- [18] K. L. Brown and R. V. Servranckx. "First- and Second-Order Charged Particle Optics." *Presented at the 3rd Summer School on High Energy Particle Accelerators July 6-16*, (Brookhaven National Laboratory, Upton, NY, 1983).
- [19] S. J. Russell and B. E. Carlsten. "Measuring Emittance Using Beam Position Monitors." *Proceedings of the 1993 Particle Accelerator Conference*, IEEE catalog No. 93CH3279-7, 2537 (IEEE, New York, 1993).
- [20] G. Strang, *Linear Algebra and its Applications, Second Edition*, (Academic Press, Orlando, FL, 1980).
- [21] L. M. Young, (private communication).
- [22] K. R. Crandall and D. P. Rusthoi. "Trace3-D Documentation." Los Alamos National Laboratory report, LA-UR-90-4146 (1990).

- [23] J. F. Power, J. D. Gilpatrick, F. Neri and R. B. Shurter, "Characterization of Beam Position Monitors in Two-Dimensions." *Proceedings of the 1992 Linear Accelerator Conference*, AECL catalog No. 10728, 362 (AECL Research, Chalk River, Ontario, Canada, 1992).
- [24] R. E. Shafer, "Beam Position Monitoring," *Proceedings of the 1989 Accelerator Instrumentation Workshop (Brookhaven National Laboratory)*, AIP Conference Proceedings 212, (AIP, Upton, NY, 1989).
- [25] J. D. Gilpatrick, J. Power, F. D. Wells and R. B. Shurter, "Microstrip Probe Electronics." Los Alamos National Laboratory document, LA-CP-89-488 (1989).
- [26] J. D. Gilpatrick and F. D. Wells, "Double Balanced Mixer Operation used as Phase and Synchronous Detector as Applied to Beam Position and Intensity Measurements." Los Alamos National Laboratory document, LA-UR-93-1622 (1992).
- [27] J. D. Gilpatrick, "Microstrip Measurement Algorithms." Los Alamos National Laboratory document, LA-UR-93-1639 (1992).
- [28] P. R. Cameron, M. C. Grau, M. Morvillo, T. J. Shea and R. E. Sikora, "RHIC Beam Position Monitor Characterization." *Proceedings of the 1995 Particle Accelerator Conference and International Conference on High-Energy Accelerators*, IEEE catalog No. 95CH35843, 2458 (IEEE, New York, 1996).
- [29] J. A. Cadzow, *Discrete-Time Systems*, (Prentice-Hall, Inc., Englewood Cliffs, NJ, 1973).
- [30] D. W. Feldman, S. C. Bender, B. E. Carlsten, J. Early, R. B. Feldman, W. J. D. Johnson, A. H. Lumpkin, P. G. O'Shea, W. E. Stein, R. L. Sheffield and L. M. Young, "Experimental Results from the Los Alamos FEL Photoinjector." *IEEE J. Quantum Electron.* **27**, 2636 (1991).
- [31] W. R. Smythe, *Static and Dynamic Electricity*, (McGraw-Hill Book Company, Inc., New York, NY, 1939).
- [32] J. D. Jackson, *Classical Electrodynamics, 2nd Edition*, (John Wiley & Sons, Inc., New York, NY, 1975).
- [33] W. H. Beyer, Editor, *CRC Standard Mathematical Tables and Formulae, 29th Edition*, (CRC Press, Inc., Boca Raton, FL, 1991).
- [34] W. H. Press, S. A. Teukolsky, W. T. Vetterling and B. P. Flannery, *Numerical Recipes in FORTRAN, The Art of Scientific Computing, Second Edition*, (Cambridge University Press, New York, NY, 1992).

IMAGE EVALUATION TEST TARGET (QA-3)



APPLIED IMAGE, Inc
 1653 East Main Street
 Rochester, NY 14609 USA
 Phone: 716/482-0300
 Fax: 716/288-5989

© 1993, Applied Image, Inc., All Rights Reserved